Interactions between ultracold dilute gas of atoms, ions and cavity

Rahul Sawant

Supervisor: Prof. Sadiq Rangwala

Light and Matter Physics Group
Raman Research Institute
Bengaluru - 560080

a thesis submitted to
Jawaharlal Nehru University
for the degree of
Doctor of Philosophy

2017

Declaration

I hereby declare that except where specific reference is made to the work of others, the contents of this dissertation are original and have not been submitted in whole or in part for consideration for any other degree or qualification in this, or any other university. This dissertation is my own work and contains nothing which is the outcome of work done in collaboration with others, except as specified in the text and Acknowledgments. I also declare that I have run it through **Turnitin** plagiarism detection software.

Rahul Sawant

Countersigned:

Prof. Sadiq Rangwala
Light and Matter Physics Group
Raman Research Institute
Bengaluru - 560080

Certification

This is to certify that the thesis titled **"Interactions between ultracold dilute gas of atoms, ions and cavity"** submitted by Rahul Sawant for the award of the degree of Doctor of Philosophy of Jawaharlal Nehru University is a bona-fide work. This has not been submitted to any other university for any other degree, diploma or title.

Prof. Sadiq Rangwala
(Thesis Supervisor)
Light and Matter Physics Group
Raman Research Institute
Bengaluru - 560080

Prof. Ravi Subrahmanyan
Director
Raman Research Institute
Bengaluru - 560080

Acknowledgements

I wish to thank Prof. Sadiq Rangwala for giving me the opportunity to work in an exciting research field, and also for his guidance and constant supervision of my thesis work. This thesis would have not been completed without his support and insights.

I thank Dr. Andal Narayanan and Prof. Joseph Samuel who were part of my thesis advisory committee for advising me and assessing my thesis work. I thank Dr. Sourav Dutta for sharing his knowledge and experimental skills when working on the ion-atom experiment which was performed in collaboration with him. My special thanks SAAC for helping me with my problems.

I thank all the students and faculty members of the LAMP group for sharing instruments and optical components. My thanks to the administrative department of Raman Research Institute (RRI) whose support is essential for the scientific activities in the institute. I gratefully acknowledge the technical support provided by the members of the general and precision workshops. I wish to show my gratitude to Harini and Savitha for their help. My special thanks to Shiva and Manju for all their hard work and support. I thank the entire staff of RRI including library, computer department, canteen and E B department who contributed in one way or the other in the accomplishment of the present work. Library staff's pleasant attitude was helpful throughout my PhD work.

My time at RRI was made enjoyable due to many friends especially my friends from the RMV hostel. I thank all my friends for this time. I am indebted to RRI sports group for providing me a stimulating and fun-filled time which gave me an opportunity to de-stress.

Finally, I am grateful to Papa, Aai, my brother Rohit, my loving wife Reena and all other family members for their faith, tremendous support and appreciation for my PhD. I appreciate your honest compliments and criticisms. I hope that this work makes you proud.

Synopsis

To study interactions between atoms, ions, molecules, and light at the quantum level, it is required to cool them in a hybrid trap and detect them such that the interactions between these are measured with precision. Atom cooling and trapping [1] has formed one pillar of modern atomic physics with deep implications for condensed matter physics, precision measurements and is now giving rise to technologies with unprecedented precision. Cold homo-nuclear and hetero-nuclear molecules which are formed via photoassociation (PA) of atoms using resonant light allow the formation of state selected molecules for experiments. Ion trapping has been another pillar of atomic physics for precision measurements and more recently quantum computation and many-body physics [2, 3]. However, very few experiments have combined these individual components to study the interactions between atoms, ions, molecules, and light, in the quantum regime. The objective of this thesis is to start a systematic investigation of combinations of atoms, ions, molecules, and light with an emphasis on the development of new detection techniques for studies of interactions.

For such an experiment to be viable, we need to both cool and trap the various species, simultaneously and with overlap. Cooling eliminates the thermal effects and allows precise state control. Trapping, on the other hand, ensures long study times, reduces observation time related linewidths and provides the opportunity for interactions between few particles of different co-trapped species to be observed over long times. Our experiment allows simultaneously trapping and cooling of atoms, ions, molecules, and light [4]. In this thesis, we develop and explore techniques which will enable the study of interactions between atoms, ions, and molecules. For this, we explore techniques which exploit light coupled to a cavity mode for detection of species and interaction.

To achieve these goals, we need to combine various species together. At the start of this thesis work, the experiment had already incorporated a working magneto-optical trap (MOT) of ^{85}Rb atoms. I developed the techniques to cool and trap potassium atoms in order to add another species to the experiment. Subsequent to this development, a potassium MOT was used to make K^+ ions, which were then used to demonstrate cooling of these ions by ultracold ^{85}Rb atoms. In this experiment, the ion detection technique also resulted in the destruction of the ions.

An optical and non-destructive method to detect these ions and other particles is essential to increase the efficiency and versatility of the experiments. With this possibility in mind, we also explore various interactions between atoms and light trapped inside a Fabry-Pérot cavity. The presence of a cavity greatly enhances the interaction strength of photons with the atoms giving us the ability to detect small interactions between the particles. Hence, various atom-cavity interactions will be studied in this thesis, with the aim of building a universal detection platform. This has resulted in experimental and theoretical studies of switching of light using light, lasing from driven atoms and the consequences of atomic motion on the atom-cavity coupling.

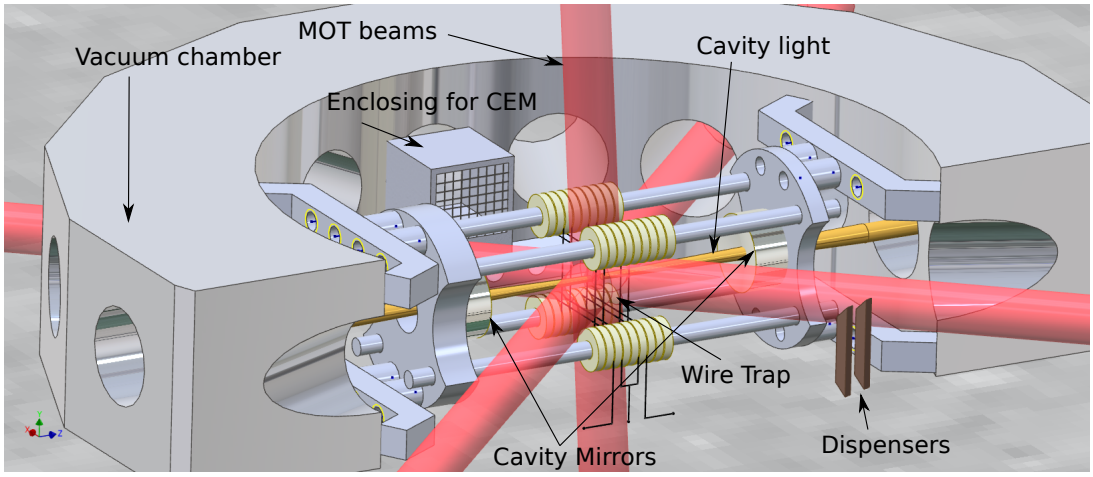

Fig. 1 Experimental chamber. MOT - Magneto-optical trap, CEM - Channel electron multiplier for ion detection. The wire trap is used to trap the ions. Only half vacuum chamber is shown in order for the things inside the chamber to be visible. A pair of anti-Helmholtz coils which produce magnetic field for MOT is not shown, one each is placed on top and bottom of the chamber.

Laser cooling and trapping of potassium atoms

Among the three most abundant isotopes of potassium atoms two are bosonic atoms (^{39}K and ^{41}K) and one is a fermionic atom (^{40}K). The diatomic molecules formed using the atoms ^{39}K and ^{40}K have same electronic structure. However as the constituent atoms follow different quantum statistics, it will be interesting to know how inter-molecule interactions will differ in both the cases. Also, a useful question to ask will be, will the quantum statistics of the molecules depend on the vibrational level in which they are? For this study, cooling and trapping of the potassium atoms is essential as the molecules will be created by combining the atoms. Hence a laser system to cool and trap potassium atoms using a magneto-optical trap (MOT) was developed. The trap is such that we can trap both ^{39}K and ^{40}K with minimal

changes in the optical setup. In the thesis, we present the details of such a trap. Another reason of cooling and trapping potassium atoms is to make positive ions of potassium (K^+) efficiently. These ions are then used for studying cooling of ions using ultracold atoms (^{85}Rb) which are heavier than the ions as discussed below.

Ion cooling using ultracold atoms.

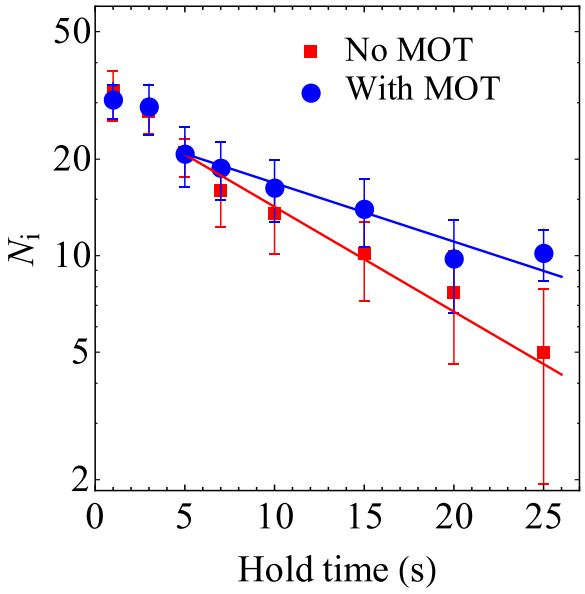

Fig. 2 The number of $^{39}K^+$ ions (N_i) remaining in the ion trap for different values of the hold time either in the presence (blue circles) or the absence (red squares) of the ^{85}Rb MOT. The dotted and the solid lines are single exponential fits for the respective cases. The increase in the survival probability of trapped $^{39}K^+$ ions in the presence of the ^{85}Rb MOT indicates the cooling of $^{39}K^+$ ions. The error bars represent the width (1 s.d.) of the underlying ion number distribution.

Dark ions trapped in an ion trap for which laser cooling is not practical are very hard to cool down. The only feasible way to cool them down is through sympathetic cooling using cold atoms or laser cooled ions of different species. In this thesis, we work towards advancing the technique of cooling trapped ions using ultracold atoms. The technique of cooling a trapped ion using buffer gas of atoms uniformly filled into the vacuum chamber is quite established and was invented a few decades ago [5, 6]. The cooling of the trapped ion in such a technique is only possible when the ion is lighter than the atoms. Precisely, how light the ion should be, depends on ion trap parameters and there are several approaches with varying predictions for it [7–9]. In a different approach, it has been predicted that if the gas of atoms is placed

precisely only near the center of the ion trap, such a restriction on mass does not exist [10, 8]. An experiment to validate this claim was performed. Cooling of $^{39}K^{+}$ ions by a localized ensemble of ultracold ^{85}Rb atoms was demonstrated, and the results are shown in figure 2. The mass of $^{39}K^{+}$ ions is 2.179 times the mass of ^{85}Rb atoms, 2.179 is greater than all the above mentioned predictions for uniform buffer gas cooling and hence is a perfect experiment to validate the above mentioned claim. In the thesis, we present the results of this experiment and the Monte-Carlo simulations performed to explain the experimental results. These simulations are extended, and ways to improve the cooling process are discussed in light of the simulations. In addition, the steady state kinetic energy distributions in the simulations are also discussed. This work is reported in Dutta et.al. [11].

Switching of light using light via the atoms.

Various linear and nonlinear processes can arise due to the collective strong coupling of atoms to the cavity. In the thesis, a theoretical framework for interactions of atoms with the cavity light is provided. Using this framework, we explore the nonlinear phenomenon of optical bistability in multi-level atoms. This is then used to explain experimental observations of Sharma *et.al.* [12] which showed switching of cavity light using an external light, both interacting with the same atoms. The flow of atoms in and out of the cavity mode is also taken into account phenomenologically to explain long transient times in the switching experiment which are dependent on the flow of atoms. This switching experiment was done using an atomic vapor cell at room temperature. Hence, the theory of optical bistability in multi-level atoms was also extended to a localized ensemble of ultracold atoms placed inside a Fabry-Pérot cavity [13]. It is shown that experiments with such ultracold atoms will result in faster switching times and was demonstrated in a recent experiment [14].

Lasing from driven atoms

Most lasers work on the principle of incoherent pumping and gain due to inversion of the atomic population such that more atoms are in a excited state compared to the ground state [15]. There are few other kinds of lasing mechanisms where inversion of the atomic population is not required. One such process is, lasing from atoms which are strongly driven by a coherent light [16]. We investigate experimentally and theoretically such a lasing process when the atoms from a fluorescing MOT strongly couple to a moderate finesse Fabry-Pérot cavity. The coherent driving of the atoms takes place because of the presence of MOT cooling laser. Lasing is observed in this atom cavity system. When the cavity is tuned to the red of the atomic transition, emission of light from the cavity is observed. This light shows threshold

behavior, polarization and spatial mode purity. This kind of lasing is possible because, a part of spontaneously emitted light coupled to the cavity experiences gain. In addition, the atom-cavity system exhibits collective strong coupling and hence greatly enhances the gain process. In an experiment to compliment this observation, external probe light from a laser was coupled to the cavity containing the driven atoms. This probe light showed gain and line narrowing. Using semiclassical theory of atom-cavity interaction, an analysis is done to explain the origin of gain in our system and qualitative agreement is obtained between the experiment and the analysis. The advantage of the lasing studied here is that it is continuous and does not require seed light and the coherent driving light also continuously cools and traps the atoms enabling operation in a steady state.

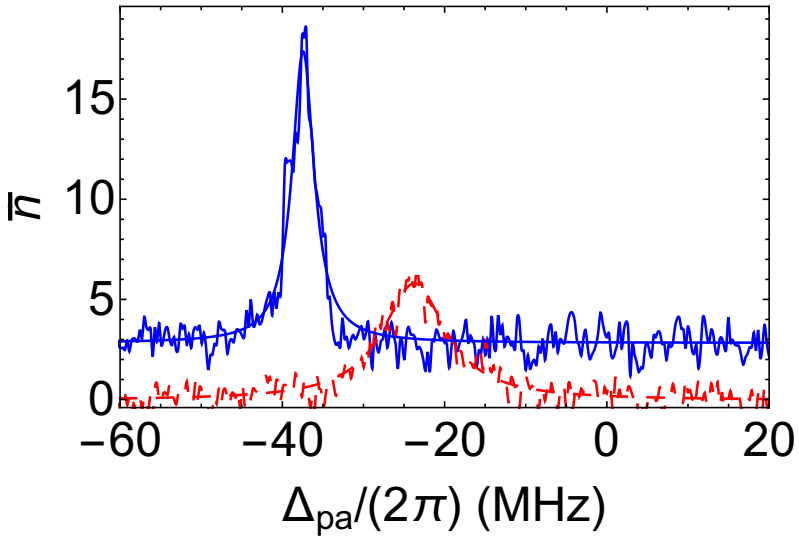

Fig. 3 The line narrowing and gain in a probe coupled to the cavity, when the cavity is tuned to the red side of the atomic transition is shown. A Lorentzian fit to the blue trace gives FWHM of 3.3 MHz and is the blue curve. FWHM of the empty cavity is 9.5 MHz. Line narrowing and gain is signature of lasing. Δ_{ca} is detuning of empty cavity resonance from atomic transition and $\bar{n}$ is average intracavity photon number.

Towards creating molecules inside a cavity

To study interactions between diatomic molecules, we need to have a ultracold ensemble of such molecules. The most efficient way to have such molecules is to create them from the ultracold atoms. A technique called photoassociation is used to create such molecules. In this technique, a laser is used for molecule creation from the atoms. The frequency of photons from this laser is such that it is resonant between the free states of the two atoms and one of the bound vibrational state of the electronically excited molecule. For two atoms which are

appropriately proximate, a photon from this laser creates molecules in an electronically excited state, some of which decay to one of the vibrational levels of the electronic ground state of the molecule. This resonant light for the PA process can be coupled into the cavity enclosing the atoms. Using the cavity serves two purposes, (1) a cavity with very small loss will amplify the intensity of light and (2) a cavity might enhance the strength of coupling of PA light to the molecular excited state. Such an experiment with cavity requires locking the laser to the cavity. The technique of such a lock and other experimental arrangements will be discussed in the thesis. Our experimental signal for molecule formation is the loss of atoms from the MOT, which is detected using the change in fluorescence from the atoms. This fluorescence reduces when the number of atoms becomes less corresponding to molecule formation. In the experiment, we successfully observed photoassociation of molecules via cavity photons. In addition, several surprising observations were made, which indicated the presence of processes other than the process of photoassociation. This has been thoroughly explored experimentally, and preliminary calculations/simulations for understanding the phenomenon are presented in the thesis. A Monte-Carlo simulation allows us to gain an insight into some of the observed processes. The simulations track the motion of atoms inside the high intensity focused light of cavity. We will discuss few plausible explanations for these interesting observations.

Towards studying interaction between molecules

Molecule-molecule interaction where quantum statistics of individual atoms forming the molecules play a role will require major experimental advances. In the last part of the thesis, we discuss briefly the ways to achieve the conditions required to study such an interaction. In such an study, detection of molecules will become very important. Most of the current ways to detect molecule also destroy the molecule. A high fidelity detection of molecules will be necessary to do the above mentioned experiment. As discussed earlier, light inside a high Q cavity can amplify weak signals. Hence we explore the technique of using cavity to detect particles using resonant light. As the molecule does not have a closed optical transition, the detection cannot be through absorption of light. For this reason, we turn to the phenomenon of electromagnetically induced transparency (EIT) using cavity because, for detuning of the probe laser in the cavity, near the EIT resonance, the dispersive effect is very large compared to the absorption and will give a strong signal without bleaching the molecules. Hence, in the thesis, we will discuss the theory for detecting molecules using the phenomenon of cavity EIT.

Summary

Summarizing the work comprising the thesis, we explored interactions of ultracold dilute gas of atoms with ions and with a cavity. The interaction of lighter ions with the localized ensemble of ultracold atoms lead to the observation of cooling of the ions. The interactions of the same atoms with the cavity was then explored. In particular, the use of tunable optical bistability was explored for switching of light using light. Driven atoms placed inside the cavity resulted in the emission of light from the cavity, this light showed features of lasing when the cavity was tuned to the red of the optical transition. Preliminary experiments towards creating molecules inside a cavity were performed and how to distinguish molecular signal from the atomic signal is discussed. Use of a cavity to detect diatomic molecules was also explored. Finally, we conclude the thesis with future directions, which involve observing interactions between ultracold molecules.

Table of contents

Chapter 1

Introduction

1.1 Overview

Advances in the precise manipulation of atoms/ions/molecules using lasers, electric and magnetic fields, have been instrumental in the realization of a large class of experiments. These experiments have aided our understanding of interactions at atomic scale. This is particularly true of two-body interactions, which are quantitatively simple but give a wealth of knowledge regarding the physics of interacting complex systems. In recent times there is increasing emphasis on precise determination of interactions between three and four bodies [17–20].

The precise control and understanding of two-body interactions have enabled access to a variety of tailored many body experiments, which allow an investigation of long standing many-body paradigms. The cooling and trapping of atoms using lasers [1] have resulted in temperatures below mK (ultra-cold regime) and trapping times of more than few seconds in most of the cases. This led to the study of many exotic states of matter where quantum nature of interactions dominate [21]. In addition, a combination of electric fields and magnetic field have enabled the trapping of charged particles [5]. Combining laser cooling with trapping has resulted in unprecedented control of internal and external degrees of freedom for ions. Isolating a single or few ions and studying its quantum properties has become technically accessible [2]. This led to significant advances in fields of precision measurements [22], quantum information [3], and quantum simulation [23]. In this thesis, we study interactions between trapped atoms, ions, and light. To do this, several experiments have been performed to understand specific science problems and the interpretation of the experiments has led to detailed theoretical and numerical work.

A new area of study has emerged over the past decade where these two extensively studied systems (cold atoms and cold ions) are combined to form ion-atom hybrid systems [4, 24]. The long range potential of an ion and ground or excited state atom is of the form $1/r^4$ (ion

+ induced dipole) as opposed to $1/r^6$ in the atom-atom case. Here r is the distance between the ion/atom and atom. In order to have a stable trapped ion-atom system [25], we need to understand how the energy is exchanged between the trapped ions and the cooled and trapped atoms. At the current limit of cooling of trapped ions, the ion temperatures are far greater than the temperature of atoms at quantum degeneracy, or even in very cold magneto-optical traps (MOT). The initial experiments for ion-atom hybrid systems resulted in observations of cooling of trapped ions by ultracold atoms [10, 26–28, 18] and observations of reactive ion-atom collisions [29]. In these experiments, a variety of observations regarding the heating/cooling phenomenon resulted. Briefly, it was found that an ensemble of ultracold atoms localized at the precise center of the ion trap will always cool the ion till the ion is fully immersed in the atomic cloud [10] and atoms were seen to be heating due to collisions with the ions [27]. For a viable hybrid ion-atom system for future experiments, it is imperative that a steady state if not an equilibrium of trapped atoms and ions exist. These results are even more significant for dark ions (ions which cannot be laser cooled) which only cool collisionally with the trapped atoms. In addition to the quest for steady state hybrid systems, there are very interesting theoretical proposals for observing macromolecules in Bose-Einstein condensates (BEC) [30] and hopping conductivity of charge [31] in ultracold mixtures of ion and atoms. The long range nature of ion-atom potential will also give us a chance to study physics beyond two-body interactions as the ion can interact with multiple atoms even in a dilute gas of atoms [18]. These goals provide the motivation for the current effort in experiments around the world including ours to reach low temperatures for ion-atom mixture in order to observe new effects in these ultracold hybrid systems.

Another very useful trap is formed by two highly reflecting mirrors. Two reflecting mirrors form a cavity which is very high Q oscillator for the resonant photons occupying the cavity mode, called Fabry-Pérot cavity which can trap the photons for a long duration of time. This trapping results in the confinement of electric field due to a single photon to a very small volume which enhances the interaction time of the photon with the resonant atoms placed inside the cavity. Experiments involving a single photon and a single atom in a cavity has shed light on many phenomena of quantum mechanics [32–34] like superposition principle and quantum entanglement which defy classical physics intuitions. Cavity photons interacting with many atoms can also lead to interesting linear [35, 36] and nonlinear [37] phenomena. The atom-photon interactions in the cavity mode can be exploited to detect particles and measure change in certain properties due to interactions. Recently, detection of a change in atom-cavity collective strong coupling allowed measurement of the temperature of atomic cloud [38] placed inside the cavity and detection of dark ions interacting with atoms placed inside the cavity in a

demonstration of non-destructive measurement of ion number [39]. So, placing a cavity around an interacting ensemble can be very useful in the development of a tool to detect interactions.

It is a well-known fact that two photons do not interact unless both of them are interacting via a medium. This interaction can be enhanced if one of the two photons is confined to a cavity. An arrangement involving atoms and photons in a cavity and another light beam which is orthogonal to the cavity axis but interacts with the same atoms as the cavity mode can be used to control the intensity of light transmitted by the cavity. These atoms can be either laser-cooled atoms or atoms at room temperature. Such experiments with a system involving a cavity placed around a spectroscopy cell containing thermal vapor of atoms have very modest requirements. This setup was used to show switching of cavity light using the another beam of light in a recent experiment [12, 14].

One level higher in complexity than atoms and ions are diatomic molecules [40]. Currently, the most widely adopted technique to have diatomic molecules at ultracold temperatures is to make them from ultracold atoms. Molecules can be created from atoms using magnetically tunable Feshbach resonances [41] or by photoassociation [42] (PA) using a laser. In this thesis, we study the creation of molecules using PA. One advantage of photoassociation is, the frequency of most of the lasers is tunable continuously over wide range enabling us to create molecules in various excited state vibrational levels. The disadvantage is that molecules are created in the excited electronic state, so they decay either to ground molecular state or into individual atoms reducing the efficiency of molecule creation. There are many motivations for creating ultracold molecules, some of them are, quantum computation with polar molecules [43], exotic phases of matter with long range interaction between particles [44], controlling chemical reactions [45], the study of few body dynamics of identical particles [46], etc. In addition, trapping of polar molecules will enable a study of potentials of the form $1/r^6$ (rotating dipoles), $1/r^3$ (static dipoles) and $1/r^2$ (ion + static dipole) if trapped along with ions. One problem with ultracold molecules is the difficulty in detecting them non-destructively. Existing techniques for detection involves ionizing the molecule and detecting it on an ion detector [47–49] or reconverting the molecules to free atoms and then detecting the atoms [50–53]. By putting a cavity around an ensemble of molecules mixed with resonant atoms we intend in future experiments to enable the non-destructive detection of molecules. This will be possible due to an enhancement of interaction of molecules/atoms with cavity photons in comparison to free space photons. Therefore, creating molecules using light coupled to the cavity mode is important to increase the creation efficiency of the molecules in the cavity mode volume, ensuring its coupling to the cavity mode so that the methods mentioned above which have been successful for atoms can be adapted to molecules.

The experimental apparatus described in this thesis is built to study interactions between all the entities mentioned above or combinations thereof. In this thesis, the emphasis is on ion-atom interactions, atom-cavity interactions, and preparation and detection of molecules using a cavity.

1.2 Motivation and objectives

The motivation for the problems addressed in this thesis is to develop various tools that are necessary to study interactions between different ultracold, trapped, and dilute gases. These gases can be mixtures of atoms, ions, and molecules. One such interaction is atom-ion interaction where the atom is heavier than the ion. There are various theoretical analyses where it is predicted that a uniform buffer gas of atoms cannot cool a trapped ion if the ion is lighter than the atoms [7–9]. In order to see if this holds true when the trapped atoms are heavier than the trapped ions and the atoms are localized at the center of the ion trap, we study trapped potassium ions in the presence of a MOT of rubidium atoms. This allows us to explicitly test our hypothesis that the trapped ion will cool in collisions with a spatially localized reservoir of trapped atoms irrespective of the ion/atom mass ratio.

One major objective of the present thesis is to use the cavity as a detection tool. We explore various phenomena involving the interaction of cavity photons with atoms in order to understand which of these phenomena can be used to study interactions between dilute gases and to detect some of these ultracold dilute gases. We also explore phenomena which might not be useful in studying interactions but offer a glimpse of new physics.

To summarize, the objectives of the thesis are,

- To add evidence to the claim that ions can be cooled by atoms localized at the precise center of the ion trap irrespective of the atom-ion mass ratio. This requires combining atoms and ions of different mass ratio. This is done by combining potassium (K) ions with rubidium (Rb) atoms. This requires building up the laser system for cooling potassium atoms. Dual MOTs of ^{85}Rb and ^{39}K or ^{85}Rb and ^{40}K have to be operated simultaneously to perform the cooling experiment of K^+ ions.

- Perform an experiment to investigate a possibility of cooling potassium ions using localized ultracold rubidium atoms. Perform Monte Carlo simulations to study the role of ion-atom mass ratio and size of atomic cloud in cooling of ions.

- Develop a theoretical model to study various interactions between cavity photons and atoms. Explain an experiment for switching of light using the physics discussed in this

model. Understand the physics and extend the model to the experiments with laser-cooled atoms.

- Perform an experiment to investigate lasing from driven atoms inside the cavity and explain the origin of lasing using a theoretical model.
- Make molecules from ultracold atoms inside cavity using the technique of photoassociation.
- Develop methods to detect molecules using cavity.
- Explore the possibility of studying molecule-molecule collisions at ultracold temperatures.

1.3 Organization of the thesis

In chapter 2 we describe the apparatus which is used to perform the experiments described in this thesis. It starts with a discussion about magneto-optical trap (MOT) and the laser system required for its operation. The MOT is used for cooling and trapping atoms. We will discuss the laser system of ^{40}K, ^{39}K, and ^{85}Rb MOT. Next, we describe the Fabry-Pérot cavity. Later a 3D Paul trap is described. Lastly, the geometry for the combination of all the parts mentioned above and their arrangement in a single vacuum chamber is explained.

Chapter 3 is devoted to the ion-atom interaction where the atom is heavier than the ion. Here we provide experimental evidence for cooling of potassium ions by ultracold atoms. To explain this cooling, Monte Carlo simulations are done which provide intuition for the process. The logic of this simulation will be explained in this chapter. The simulation is further extended to see how the cooling rate varies with atomic size and the ion-atom mass ratio.

A theoretical model for cavity-atom coupling is developed in the fourth chapter. This model is then applied to study switching of cavity light using another light beam. This requires understanding the phenomenon of optical bistability for multi-level atoms. The theory of optical bistability for a 4-level atom is derived and presented. Phenomenologically the flow of atoms in and out of the cavity is incorporated in rate equations to explain long rise times observed in the switching experiment which relates closely to the modeled system.

When a laser driven ensemble of atoms is placed inside a cavity, we observe lasing. In this chapter, we provide multiple evidence through experimental observations for lasing action. We also present theoretical analysis which explains why gain occurs in this case.

In the sixth chapter, the techniques required for the creation of molecules inside a cavity are described. The results of some preliminary experiments are shown. We will also provide an

analysis which helps in separating molecular signal from the atomic signal. This is essential as the presence of photoassociation light will effect the operation of MOT for atoms and change various collective properties of the atomic ensemble.

In the last chapter, we conclude the thesis by giving a summary. Also, a brief overview of future directions in given. We will talk about how molecule-molecule interactions can be studied. In particular, we will talk about changes that will be required to current apparatus if such a study is to take place and the theoretical analysis which will be needed to get an idea of energies involved.

Chapter 2

Overview of experimental concepts, techniques, and apparatus

To perform the experiments enumerated in the introduction, we will be studying systems involving combinations of atoms, ions, cavity photons, and molecules. The experimental study of these systems requires building a complicated apparatus. The requirements on the apparatus are that it should allow laser cooling and trapping of atoms, trapping of atomic ions, the formation of a cavity for light around the laser-cooled atoms, the possibility of creating molecules, and detection of all the entities involved in the studies. For performing the experiments, all the components should be controllable. The simultaneous realization of all these requirements implies a degree of experimental complexity both in the design of the experiment and the implementation of experimental protocols and measurements. It should be emphasized that the present apparatus is unique in its abilities to work with all the key ingredients of atomic, molecular, and optical physics.

In this chapter, we give an overview of all the elements which have gone into the experimental apparatus and which satisfy the requirements stated above. Section 2.1 provides details about MOT concepts and the implementation of these concepts in the laboratory using lasers. Section 2.2 talks about the trapping of ions using oscillating electric fields and the optimal parameters for efficient trapping. In section 2.3, we discuss various properties of light inside an optical cavity. We end this chapter by section 2.4 where we discuss the schematic of the entire apparatus.

2.1 Magneto-optical trap (MOT)

2.1.1 Concepts and theory

Laser cooling

When an atom interacts with light which is resonant with its electronic transition, it absorbs photons from the light and scatters it in random directions. This process can be used to decrease the energy stored in the atom's external motion. Consider a case where a two-level atom moving in the x-direction is illuminated by two beams of laser light, one traveling parallel to $+x$ and another parallel to the $-x$ axis. The momentum kick the atom gets when a photon is absorbed is given by $\hbar\vec{k}$, where $k = |\vec{k}| = 2\pi/\lambda$ is wavenumber and λ the wavelength of light. The absorbed photon is re-emitted in a random direction, hence the momentum kick over large number of re-emissions averages to zero, and so the net transfer of momentum is predominantly in the direction of propagation of the resonant laser beam. The force on the atom from the two beams, $F = F_+ + F_-$ is given by rate of change of momentum due to such scattering events and can be obtained by multiplying total scattering rate by photon momentum. Here,

$$F_\pm = \hbar k \frac{\Gamma}{2}\left[\frac{I_\mathrm{r}}{1+2I_\mathrm{r}+4(\Delta \mp k v_x)^2/\Gamma^2}\right] \tag{2.1}$$

is a force due to $+x$ and $-x$ beam respectively [54]. Γ is excited state decay rate for the atoms, $I_\mathrm{r} = I/I_\mathrm{sat}$ is the ratio of intensity per beam to saturation intensity [55], Δ is detuning of light from resonance, kv_x is detuning due to Doppler shift and v_x is velocity in the x-direction. For very low velocities such that $kv_x \ll \Gamma$ and $kv_x \ll \Delta$, the total force can be expanded in series of kv_x. Keeping only the linear term gives,

$$F = \frac{8\Delta\hbar k^2 I_\mathrm{r} v_x}{\Gamma(1+2I_\mathrm{r}+4\Delta^2/\Gamma^2)^2} \tag{2.2}$$

For negative Δ this force takes the form of frictional force $F = -\beta v_x$, where $\beta = \frac{8|\Delta|\hbar k^2 I_\mathrm{r}}{\Gamma(1+2I_\mathrm{r}+4\Delta^2/\Gamma^2)^2}$. This damping force is responsible for the cooling of atoms.

Trapping

The arrangement mentioned above will only damp the velocity. A restoring force is essential to trap the atoms. For atoms having magnetic sublevels, such a force is provided by a magnetic field gradient. Here we consider a simple case where the total angular momentum of electronic ground state and excited state is zero and one respectively. The degeneracy of magnetic

sublevels will be lifted in the presence of magnetic field. This results in position dependent detuning of the magnetic sublevels with respect to the cooling laser light. The schematic is shown in figure 2.1. This results in an imbalance of force due to light scattering. This imbalance can be manipulated to provide the restoring force. The forces due to the two counter-propagating beams now become,

$$F_{\pm} = \hbar k \frac{\Gamma}{2} \left[\frac{I_{\mathrm{r}}}{1 + 2I_{\mathrm{r}} + 4(\Delta \mp k v_x \mp \mu B(x)/\hbar)^2/\Gamma^2} \right]. \tag{2.3}$$

Here $B(z)$ is the position dependent magnetic field, $\mu = (g_e m_e - g_g m_g)\mu_B$ is the effective magnetic moment, g_e (g_g) is Lande factor of the excited (ground) state, m_e (m_g) is the magnetic number of the excited (ground) state, $\mu B(x)/\hbar$ is the Zeeman shift. For small x and kv_x, a series expansion reduces the total force to, $F = -\beta v_x - \zeta x$ by keeping only linear terms. ζ depends on magnetic gradient and is given by $\zeta = \frac{\partial B(x)}{\partial x}\frac{\mu\beta}{\hbar k}$. This gives a harmonic trap for a constant magnetic gradient, $\frac{\partial B(x)}{\partial x} = B_0$. The argument mentioned above can be expanded to 3-D giving

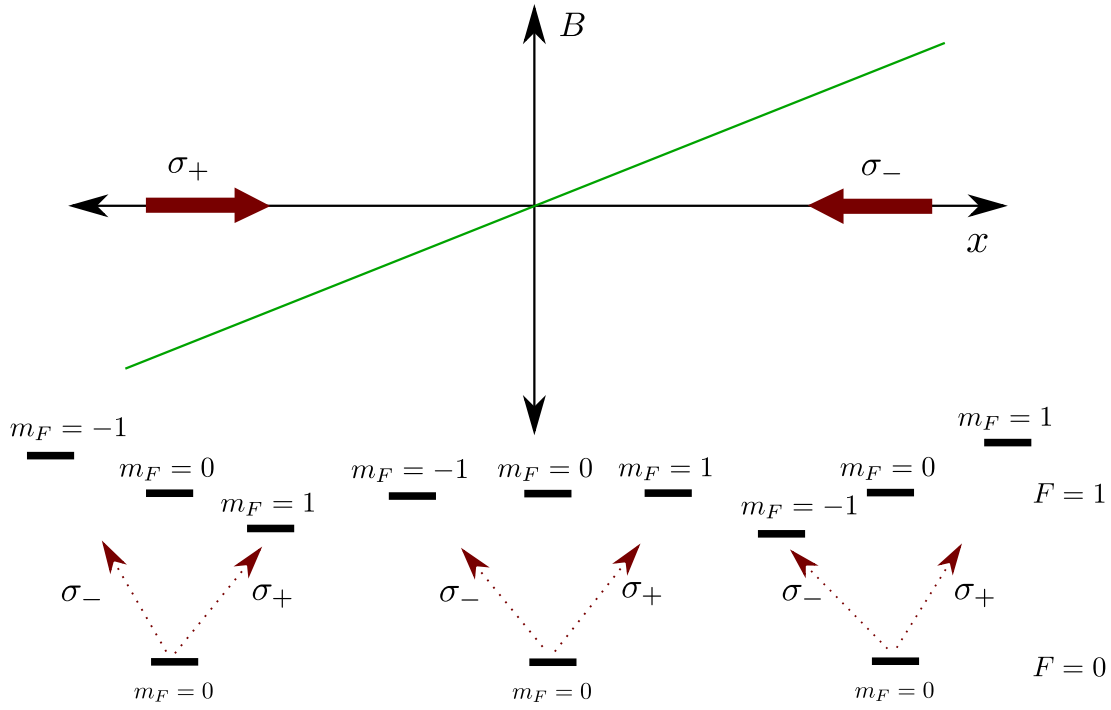

Fig. 2.1 Variation of the magnetic field for MOT and its effect on atomic levels due to Zeeman effect. Towards left (right) the level resonant with σ_+ (σ_-) light comes closer to the laser frequency increasing its push on the atoms. This results in a position-dependent force towards the center of the trap.

the total force as,

$$\vec{F} = -\vec{\beta}_{3D} \circ \vec{v} - \vec{\zeta}_{3D} \circ \vec{r}. \tag{2.4}$$

Here, $\circ$ denotes a Hadamard (element wise) product of the vectors. The only difference between the elements β^i_{3D} for $i \in (x, y, z)$ and β is that the term $6I_r$ in place of $2I_r$. This accounts for saturation effect due to beams in other directions [54]. For MOT assuming equal intensity in all the MOT beams, $\beta^x_{3D} = \beta^y_{3D} = \beta^z_{3D} = \beta_{3D}$. Same holds for the elements ζ^i_{3D}. For more detailed analysis of MOT involving multilevel atoms see [56].

2.1.2 MOT laser system

Here we will discuss the experimental arrangement for magneto-optical cooling and trapping of potassium atoms (^{39}K and ^{40}K) and rubidium atoms (^{85}Rb). We want to cool and trap both the potassium isotopes because ^{39}K is bosonic and ^{40}K is fermionic. Hence preparing a laser system for both of them is a step towards studying the effects of quantum statistics on

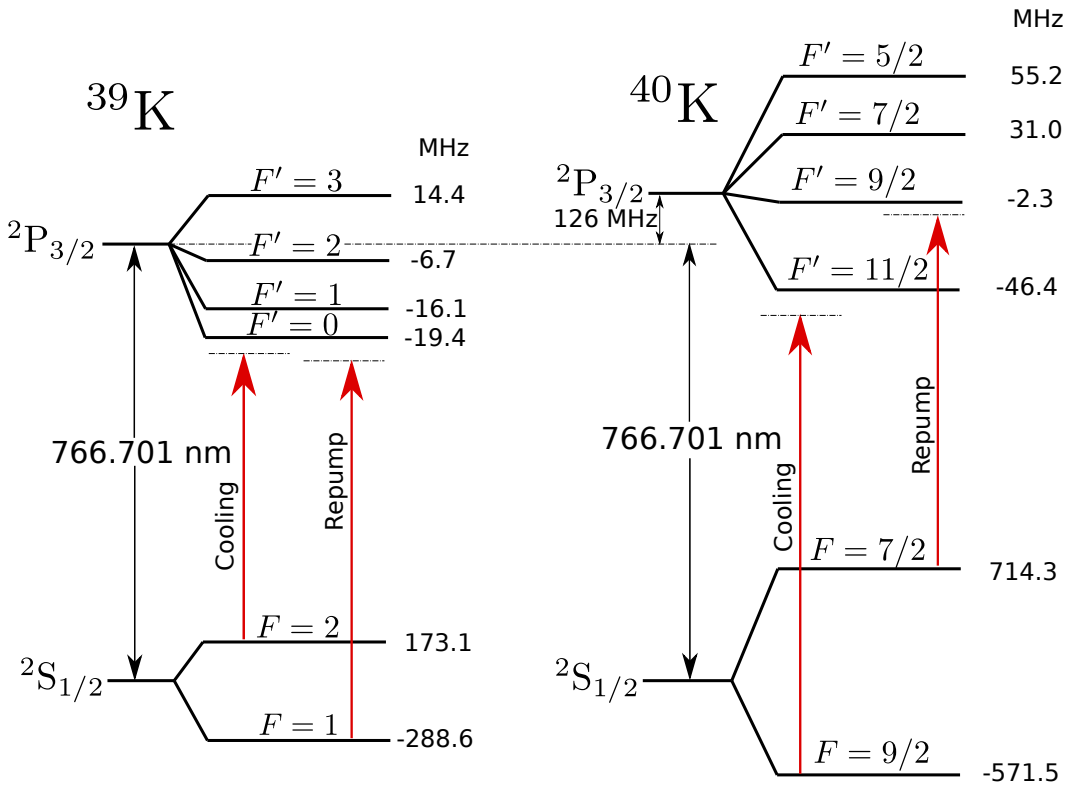

Fig. 2.2 Energy level diagram for the D2 line of ^{39}K and ^{40}K relevant for laser cooling. The numbers to the right of hyperfine (F) levels denote its frequency distance from the fine structure energy level.

interactions. The energy diagram for the potassium atoms is given in figure 2.2. For the present experiment, the laser systems are prepared so that either ^{39}K or ^{40}K can be laser cooled in the experiment at any point in time with minor changes required to switch between isotopes.

For ^{40}K the cooling and trapping light is red detuned from $F = 9/2$ to $F' = 11/2$ transition by 12 MHz. This transition is used because the excited hyperfine level $F' = 11/2$ does not decay back to $F = 7/2$ ground level as it is dipole forbidden. It decays back to $F = 9/2$ with very high probability forming a closed loop essential for continuous cooling of atoms. However, there is a small but finite probability of excitation to $F' = 9/2$ hyperfine level which can decay back to $F = 7/2$ by dipole allowed transition, and therefore the atoms exit the closed cycle where laser cooling is efficient. Hence a small intensity of light is required to pump back the atoms to $F = 9/2$ from $F = 7/2$ which brings the atoms back into the laser cooling cycle. This

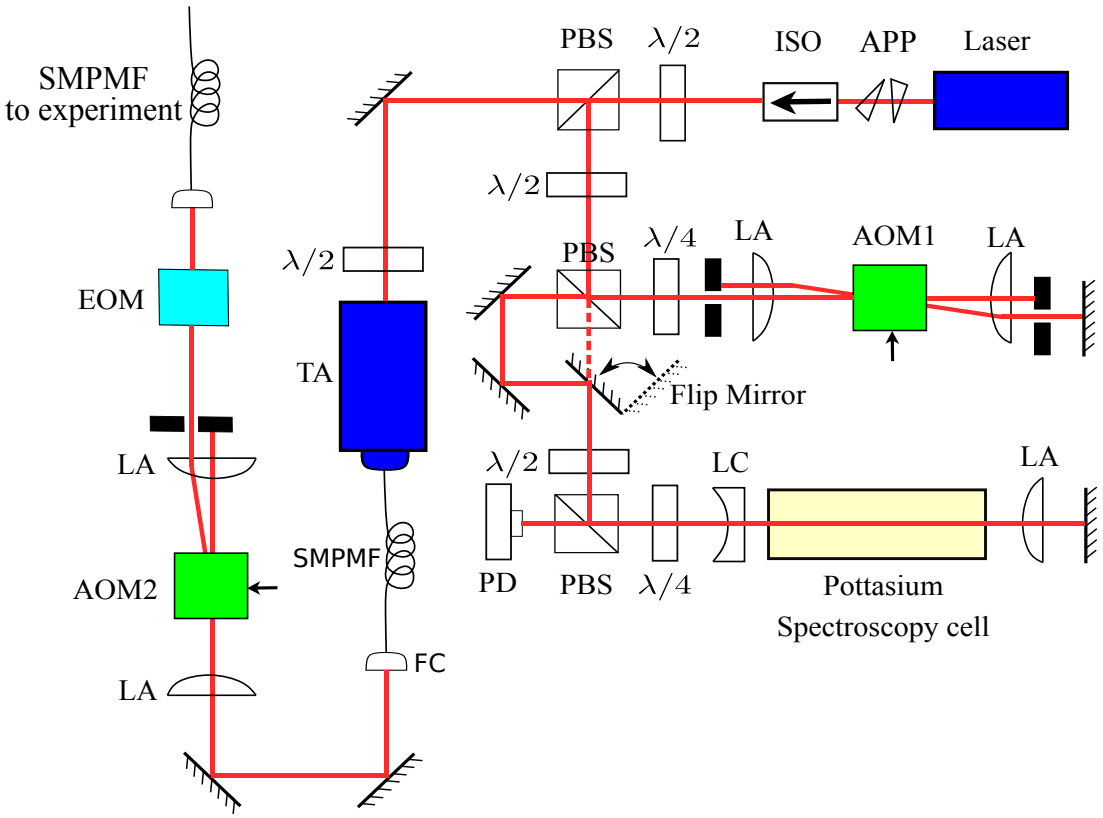

Fig. 2.3 The optical setup for laser cooling and trapping of potassium atoms. PBS - polarizing beam splitter, AOM - acousto-optical modulator, EOM - electro-optical modulator, PD - photo diode, LA - plano convex lens, LC - plano concave lens, APP - anamorphic prism pair, ISO - optical isolator, TA - tapered amplifier, to amplify the power, SMPMF - single mode polarization maintaining fiber, FC- fiber coupling setup, $\lambda/2$ - half wave plate, $\lambda/4$ - quarter wave plate.

is the role of repumping light. The repump light is red detuned from $F = 7/2$ to $F' = 9/2$ transition.

For ^{39}K the excited state hyperfine levels are very closely spaced, hence it is very difficult to form a closed system as neighboring levels also get pumped. The most efficient way is to have both cooling and repump lasers red detuned with respect to the whole excited state manifold [57]. Hence the cooling light is 35 MHz detuned from $F = 2$ to $F' = 3$ transition and the repump light is 18 MHz detuned from $F = 1$ to $F' = 2$ transition.

The cooling and repumping beams mentioned above for magneto-optical trapping of both ^{39}K and ^{40}K are created from a single ECDL laser (Toptica DL100 @ 766.7 nm). The optical setup is such that we can create MOT of both ^{39}K and ^{40}K with only a few minor changes in the setup. The laser is frequency stabilized by locking to the crossover of $F = 2$ to $F' = 3$ and $F = 1$ to $F' = 2$ transitions of ^{39}K. The signal for the cross-over is obtained using saturation absorption spectroscopy (SAS) of ^{39}K contained in a glass cell. The spectroscopy signal is shown in figure 2.4(a). The optical setup is shown in figure 2.3. Two acousto-optical modulators (AOM) are used to shift the frequency. For ^{39}K AOM1 is skipped and the laser is directly locked to the crossover frequency, and AOM2 shifts the frequency by -241.5 MHz. This frequency is used as the cooling frequency. The repump frequency is generated by Electro Optical Modulator (Qubig EO-K39M3) operating at 464 MHz. The EOM creates two sideband frequencies as shown in figure 2.4(b). The higher frequency sideband generated by EOM has frequency required for repumping the atoms. The Radio frequency (RF) power (27 dBm) to

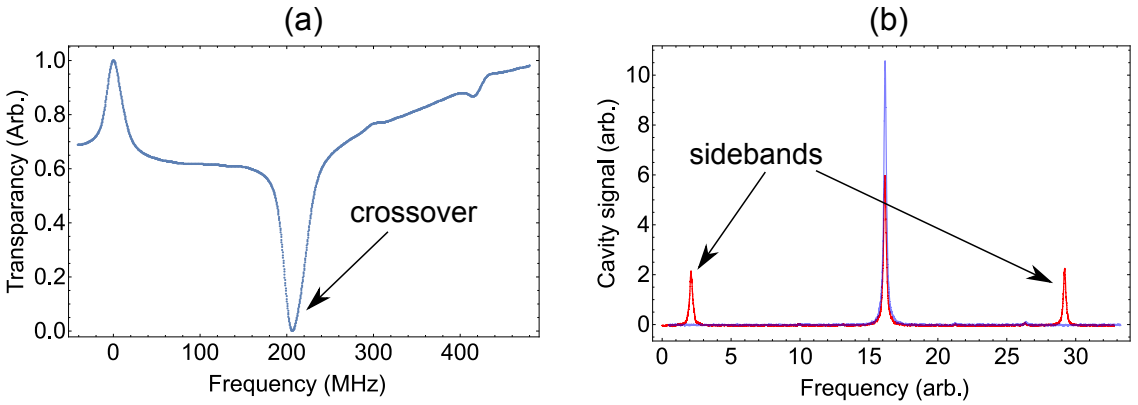

Fig. 2.4 (a) Saturation absorption spectroscopy of potassium atoms. The x-axis shows frequency from $F = 2$ to $F' = 3$ transition of D2 line of ^{39}K atoms (see figure 2.2). (b) This figure shows spectrum of potassium MOT laser when passed through a Fabry-Pérot cavity. The red trace shows spectrum when the light is passed through an EOM and blue trace is spectrum without the EOM.

EOM is such that the optical power at repump frequency is 2/3 of the optical power at cooling frequency.

For ^{40}K MOT AOM1 shifts the frequency by -416 MHz and AOM2 by +176MHz. An EOM (Qubig EO-K40M3) operating at 1230 MHz generates the repump frequency. The ratio of repumping power to cooling power is 1/6 (20 dBm RF power to EOM). The changes which are required to go from ^{39}K MOT to ^{40}K MOT are, change the $\lambda/2$ before AOM1 such that full power is reflected by PBS to AOM1, flip the mirror to send the AOM1 shifted beam to SAS setup, and reverse AOM2 such that the frequency of deflected beam increases and change the EOM. This process ensures minimal change in alignment and gives us the flexibility to work with both the species. Post creation of cooling and repump beams in both the cases, the combined beam is injected into a fiber which takes the beams to the experiment. Figure 2.5 shows a photo of the optical setup of potassium MOT lasers.

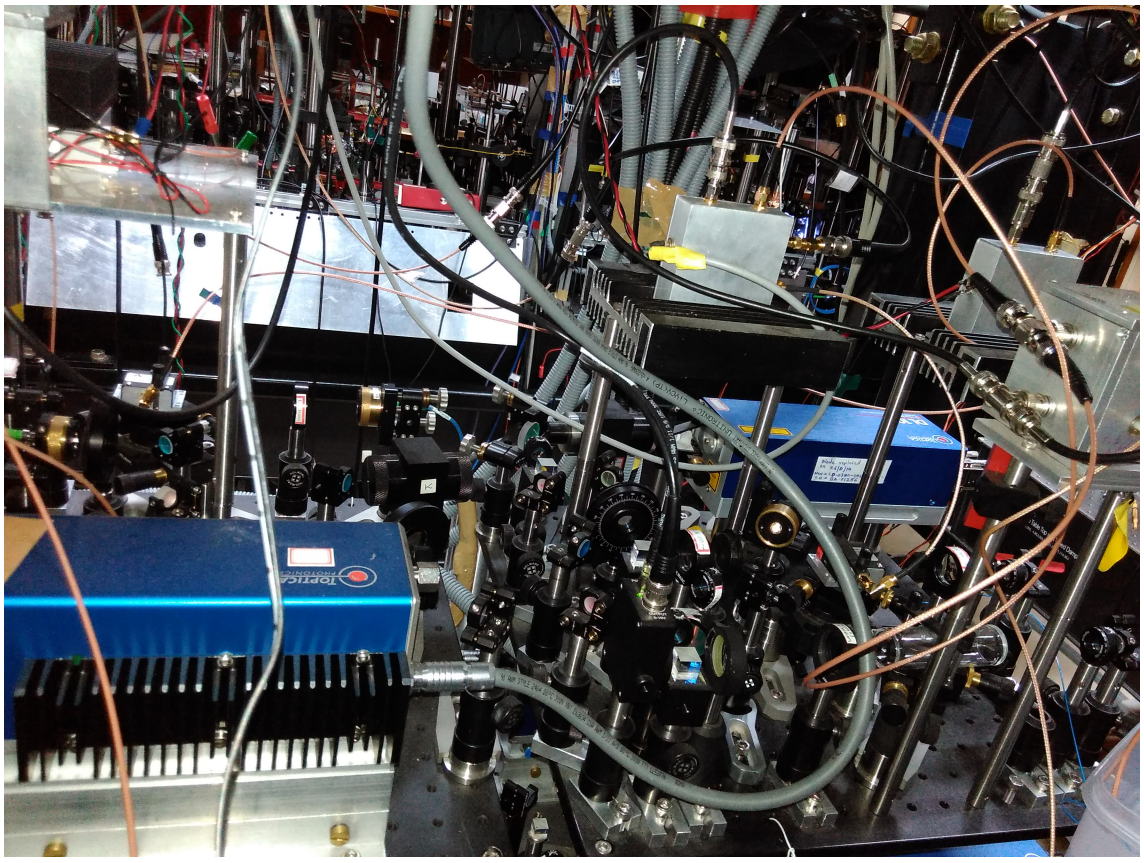

Fig. 2.5 Photo of the optical setup of potassium MOT lasers in our lab.

The experiments described in this thesis also involve ^{85}Rb as one of the cold atom species. The MOT of ^{85}Rb atoms was operational before the start of this thesis. Below we will give an overview of the laser systems involved. The energy level diagram for the ^{85}Rb atom is given

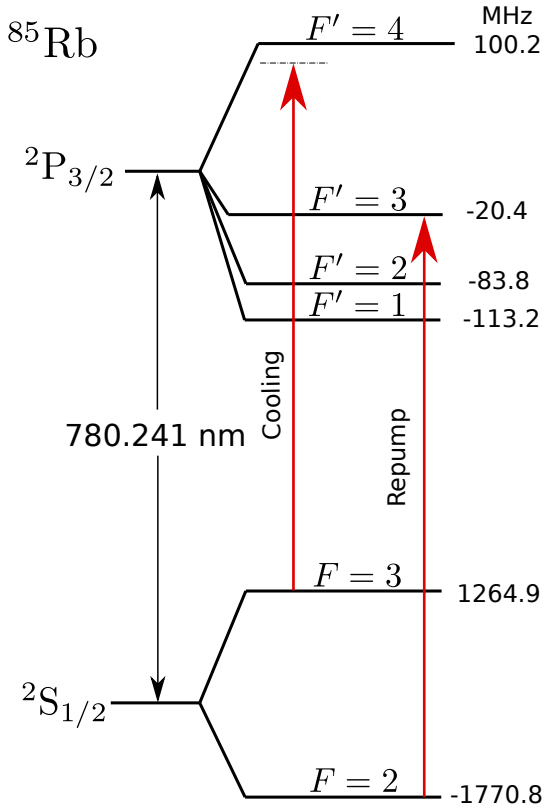

Fig. 2.6 Energy level diagram for the D2 line of ^{85}Rb relevant for laser cooling.

in figure 2.6. Two separate lasers are used for cooling and repumping. The cooling laser is locked $\sim$ 13 MHz red detuned from the $F = 3$ to $F' = 4$ transition. This is a closed transition. The -13 MHz frequency shift is obtained by using two AOMs and locking to the crossover of $F = 3$ to $F' = 4$ and $F = 2$ to $F' = 3$ transitions of ^{85}Rb which is -60 MHz away from $F = 3$ to $F' = 4$ transition. AOM3 shifts the frequency by +227 MHz and AOM4 shifts the frequency by -180MHz making a total shift a +47 MHz (see figure 2.7 for the optical setup). AOM5 is used to switch on and off the cooling laser. The repumping laser is locked to the repumping transition $F = 2$ to $F' = 3$. The setup for this laser is shown in figure 2.8. AOM7 is used for switching on and off the repumping laser and AOM6 is used to cancel the shift due to AOM7 so that the locking point does not change. More details about the laser system for ^{85}Rb MOT can be found in the thesis of Tridib Ray [58] and Jyothi S. [59].

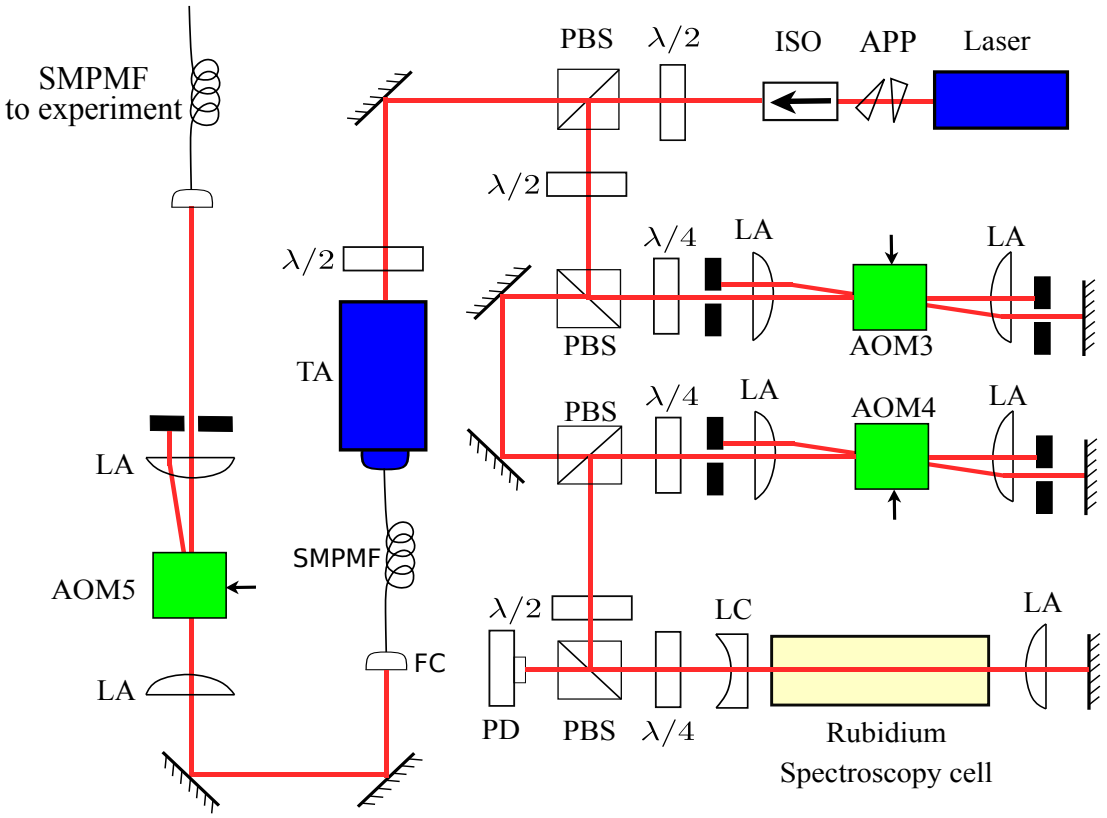

Fig. 2.7 The optical setup for the cooling laser of ^{85}Rb MOT. PBS - polarizing beam splitter, AOM - acousto-optical modulator, PD - photo diode, LA - plano convex lens, LC - plano concave lens, APP - anamorphic prism pair, ISO - optical isolator, TA - tapered amplifier, to amplify the power, SMPMF - single mode polarization maintaining fiber, FC- fiber coupling setup, $\lambda/2$ - half wave plate, $\lambda/4$ - quarter wave plate.

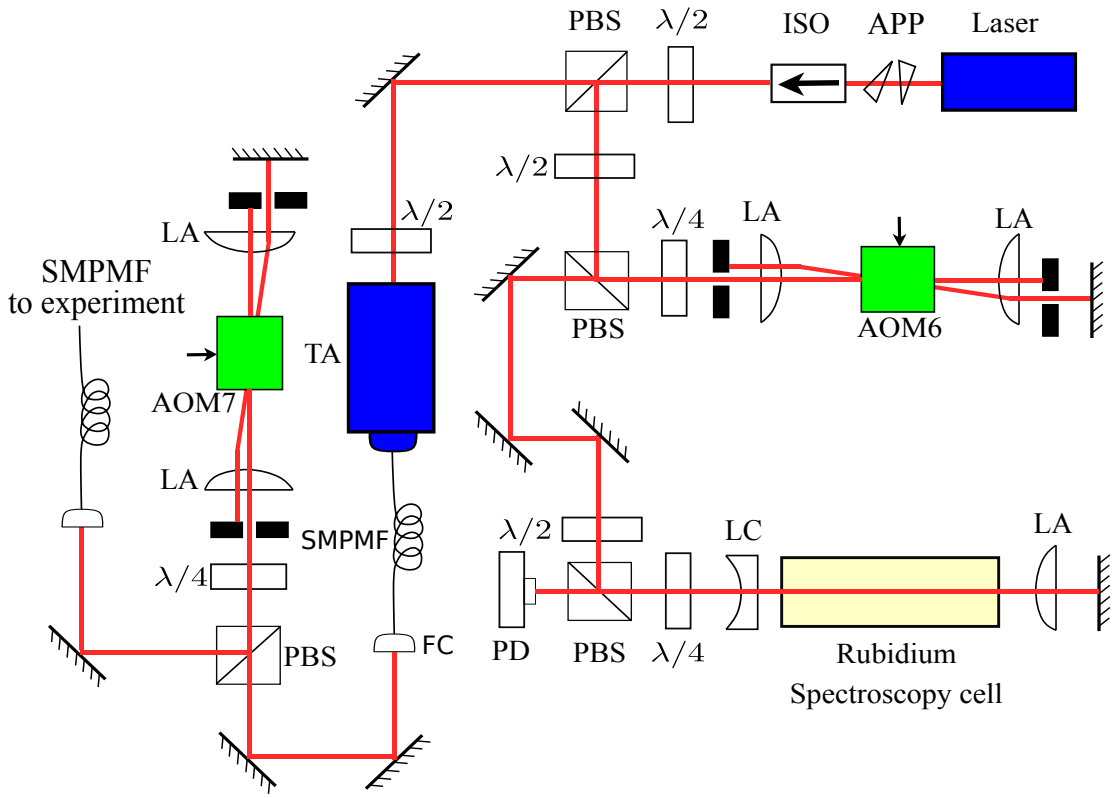

Fig. 2.8 The optical setup for the repumping laser of ^{85}Rb MOT. PBS - polarizing beam splitter, AOM - acousto-optical modulator, PD - photo diode, LA - plano convex lens, LC - plano concave lens, APP - anamorphic prism pair, ISO - optical isolator, TA - tapered amplifier, to amplify the power, SMPMF - single mode polarization maintaining fiber, FC- fiber coupling setup, $\lambda/2$ - half wave plate, $\lambda/4$ - quarter wave plate.

2.1.3 Detection of MOT atoms

The atoms will be continuously scattering light from the MOT lasers. This scattered light (fluorescence) can be detected, and hence the presence of atoms can be inferred from this detected light. The scheme for detection is a spatial filtering arrangement shown in figure 2.9. A combination of 2 lenses is used for imaging. The first lens is at a distance of twice its focal length (f) from the atoms making an image of atoms at a 2f distance on the opposite side of the lens. An aperture is placed at this image plane to filter spatially the light coming from the experimental chamber. Another lens at a 2f distance makes another image of the MOT which is then detected. A 50:50 beam splitter after the second lens splits the power into two parts, one falls on CCD camera forming an image of MOT, and the other part falls on a PMT which detects the total intensity of scattered light. The total number of atoms can be determined using the value of intensity measured. Twice this intensity will be equal to the product of the number

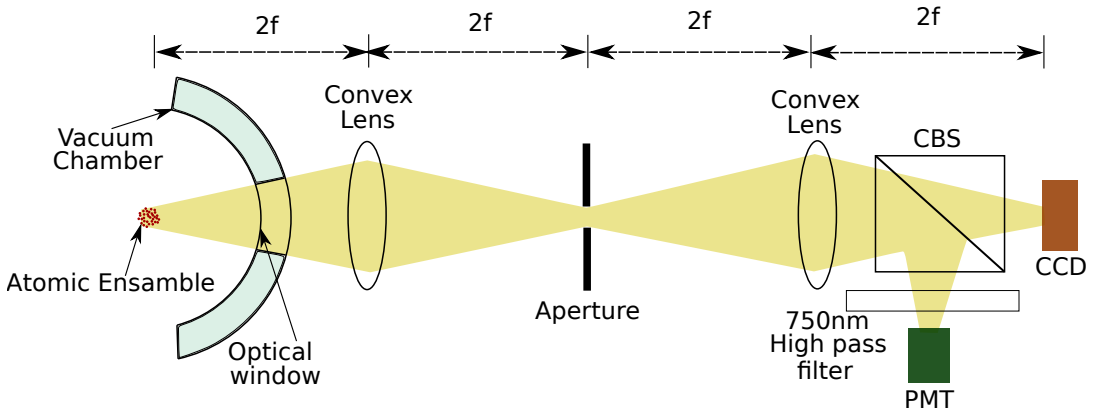

Fig. 2.9 Scheme for detecting atoms. CBS - common (50:50) beam splitter, CCD - charge coupled device camera (Thorlabs DCU224M), PMT - photomultiplier tube (Hamamatsu R636-10). f is the focal length of the two lenses. The 750 nm high pass filter allows light from both Potassium and Rubidium MOTs.

of atoms, the fractional solid angle subtended by most constrained area of the imaging system path, and scattering rate of atoms. The average scattering rate of atoms is given by[1],

$$R = \frac{\Gamma}{2}\left[\frac{I_{\text{tot}}/I_{\text{sat}}}{1 + I_{\text{tot}}/I_{\text{sat}} + 4\Delta^2/\Gamma^2}\right] \tag{2.5}$$

where, I_{tot} is the total intensity of MOT cooling light.

We were able to trap 1.4×10^6 ^{39}K atoms, with 18 mW/cm^2 intensity of cooling light and 12 mW/cm^2 of repumping light. Similarly, for ^{40}K we were able to trap 5×10^5 atoms, with 12 mW/cm^2 intensity of cooling light and 2.4 mW/cm^2 of repumping light. The density profile of both the MOT's is shown in figure 2.10. The ^{39}K MOT is big because the atoms are very hot as a result of inefficient cooling due to a closely spaced hyperfine structure of the excited state manifold. Comparatively the MOT of ^{40}K is smaller in size and also cooler. However, as ^{39}K atoms are the more abundant species ($\sim 90\%$) than ^{40}K (8.4%) the total number of atoms loaded is more for ^{39}K species. The atoms are loaded from background vapor produced by dispenser enriched with ^{40}K atoms (Alvasource AS-3-K40 (8.4%)-5-S).

[1]For ^{39}K, a 2-level model is not valid because of close spaced hyperfine structure. A multilevel model has to be used, details of it can be found in the thesis of Robert Sylvester Williamson III [60].

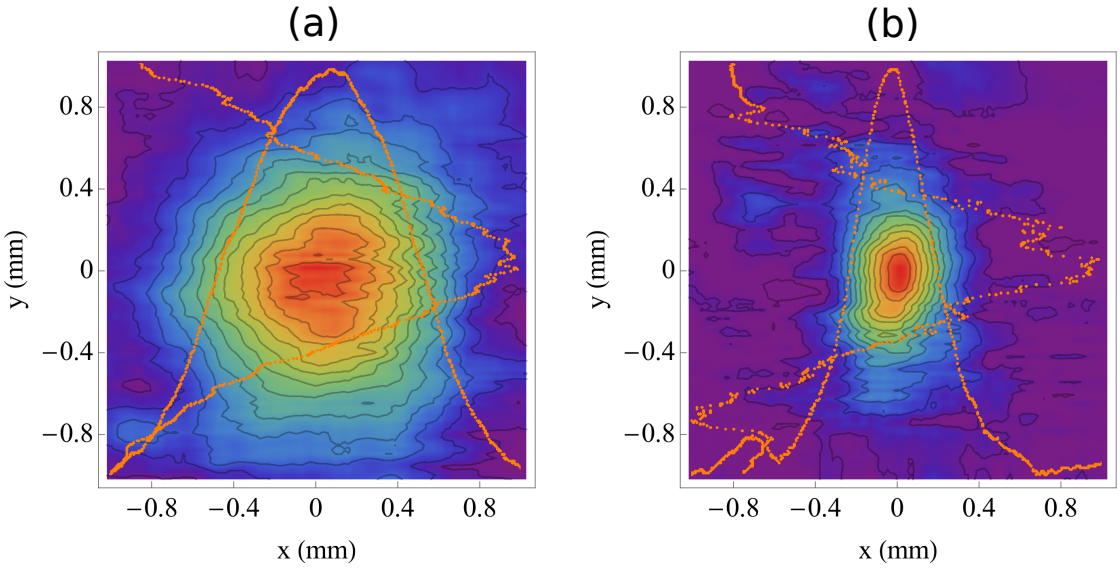

Fig. 2.10 Density profile of (a) ^{39}K MOT and (b) ^{40}K MOT as seen on the CCD camera. The orange curves show 1D density profiles along x and y axes obtained by taking mean along y and x axis respectively. The standard deviations of Gaussian fits to above density profiles are, $\sigma_x = 430\mu m$ & $\sigma_y = 385\mu m$ for ^{39}K and $\sigma_x = 145\mu m$ & $\sigma_y = 225\mu m$ for ^{40}K.

2.2 Ion trap

2.2.1 Concepts of an ideal trap

It is impossible to trap a charged particle with just static electric fields as the electric potential (V) needed to trap the ion would violate Laplace's equation ($\nabla^2 V = 0$) in free space. There are two approaches to circumvent this problem; one uses a static magnetic field in addition to static electric fields and other using oscillating electric fields. The trap which uses the first approach is called Penning trap and ones using the second approach are called Paul traps. In this thesis, we will use 3D Paul trap to confine atomic ions as it is compatible with atom traps.

The potential for an ideal 3D Paul trap [5] is given by,

$$V(x,y,z,t) = \left(\frac{U_0 + V_{\text{rf}}\cos(2\pi f t)}{2d^2}\right)(2z^2 - x^2 - y^2). \tag{2.6}$$

Here U_0 is the dc potential, V_{rf} is potential oscillating at radio frequency (RF) f and, d is a constant signifying the extent of the trap. Using this potential the equations of motion for the

ions are,

$$\frac{d^2x}{dt^2} + [a_x - 2q_x \cos(2\pi ft)]\, x = 0 \tag{2.7a}$$

$$\frac{d^2y}{dt^2} + [a_y - 2q_y \cos(2\pi ft)]\, y = 0 \tag{2.7b}$$

$$\frac{d^2z}{dt^2} + [a_z - 2q_z \cos(2\pi ft)]\, z = 0 \tag{2.7c}$$

where $a_x = a_y = -a_z/2 = \frac{-4QU_0}{m_i d^2 (2\pi f)^2}$ and $q_x = q_y = -q_z/2 = \frac{2QV_{rf}}{m_i d^2 (2\pi f)^2}$ are dimensionless parameters, m_i is the mass of the ion and Q is the charge of the ion. Parameters a_i and q_i for $i \in (x,y,z)$ are usually used to define the stability region of the trap and only a small range of the combination of a_i and q_i is stable [5]. Figure 2.11 shows the typical motion of an ion trapped in an ion trap, along one of the axis. As can be seen from the figure there are two types of motion in the ion trap, one is the usual harmonic motion, and other motion is the fast wiggle on top of this harmonic motion. The harmonic part is called the *secular* motion or *macromotion*, and the high frequency wiggly part is called *micromotion*. The frequency of oscillation for micromotion is same as the RF frequency as this is the response of the ion to the ac electric field applied to the trap electrodes. In the limit $a, q \ll 1$, the motion of ion simplifies to $x(t) = G(1 - 0.5q_x \cos[2\pi ft]) \cos[\omega_x t]$, where G is a constant and $\omega_x/2\pi = 0.5\zeta_x f$ is the secular frequency. $\zeta_x = \sqrt{a_x^2 + 0.5q_x^2}$ is called the stability parameter. Same holds for y and z directions.

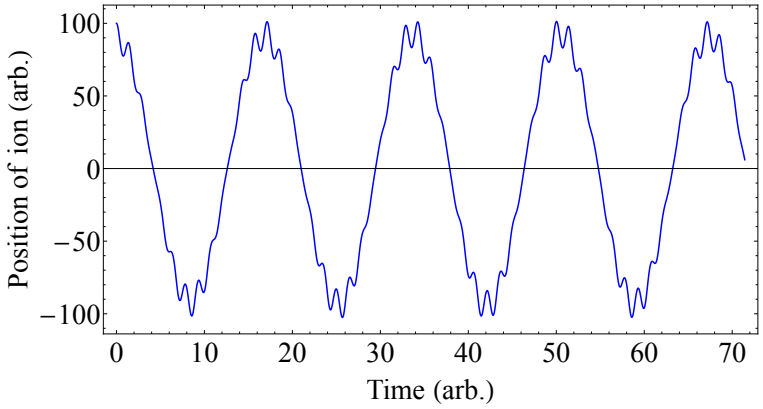

Fig. 2.11 The motion of an ion trapped in an ion trap with time in one dimension.

2.2.2 Wire trap

For our experiments, we use an ion trap made by winding tungsten wires around grooved and cylindrical ceramic sleeves which enclose four metal rods as shown in figure 2.12. There

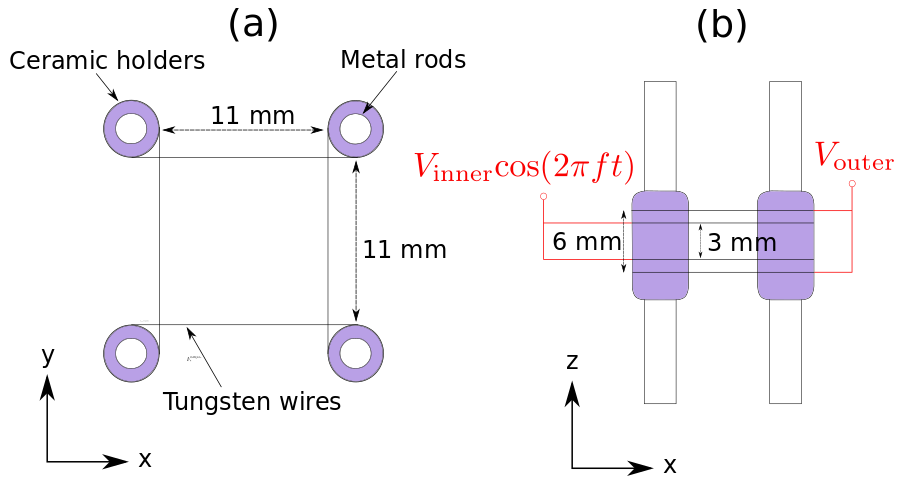

Fig. 2.12 Ion trap made using tungsten wires. (a) x-y cross section and (b) x-z cross-section. Red lines show electrical connections.

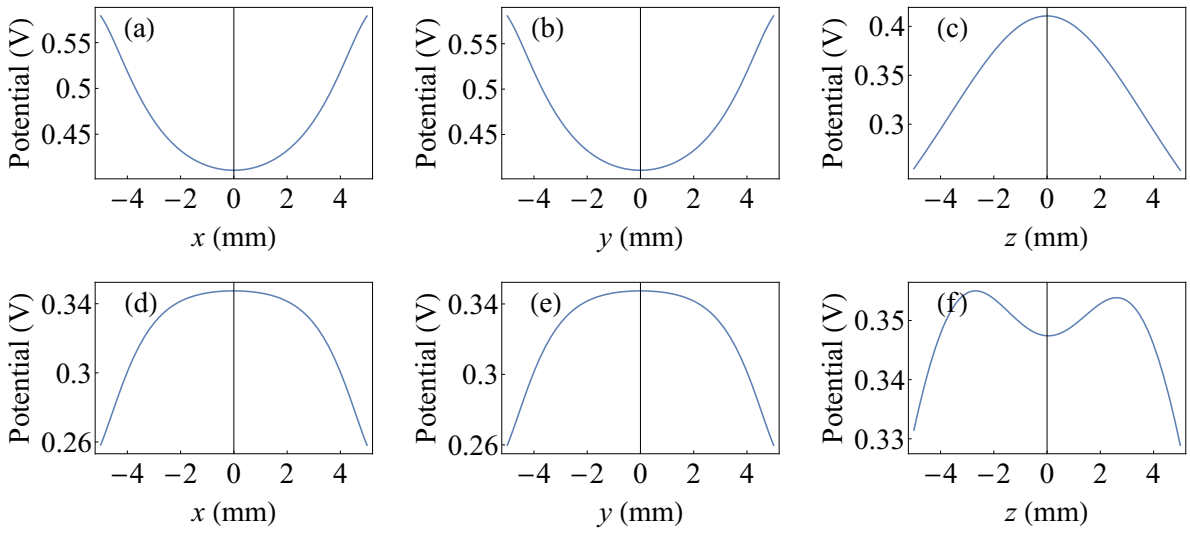

Fig. 2.13 Potential produced by the wires. (a), (b) and (c) are potential curves along x, y, and z axis respectively if 1 volt is applied to the inner pair of wires. (d), (e) and (f) are potential curves along x, y, and z axis respectively if 1 volt is applied to the outer pair of wires.

are four such wires, the inner two form an inner pair of wires to which an oscillating voltage ($V_{\text{inner}}\cos[2\pi ft]$) is applied and an outer two form a outer pair of wires to which a dc voltage (V_{outer}) is applied.

The wires produce confining potentials shown in figure 2.13. These potentials were obtained by numerically solving the Laplace's equation given the geometry and voltage on wires. A software package called SIMION 8.0 was used for such a simulation [59]. For $x < 2$ mm, the

potential can be fitted to a quadratic polynomial giving,

$$V(x,y,z,t) \simeq \left(\frac{V_{\text{outer}}C_2 - V_{\text{inner}}\cos[2\pi ft]}{2d^2}\right)\left(2z^2 - x^2 - y^2\right) + \left(C_1 V_{\text{inner}}\cos[2\pi ft] + V_{\text{outer}}C_2C_3\right). \tag{2.8}$$

Where, $C_1 = 0.41$, $C_2 = 0.21$, $C_3 = 1.7$ and $d = 10$ mm. This is similar to the ideal 3D Paul trap which we discussed in earlier section. In order to estimate various trap parameters like secular frequency, trap depth, trap extent, etc., we perform a numerical integration of equations of motion of the ion in the ion trap (figure 2.11 shows an example of a trajectory obtained from such a simulation). The potential used for this numerical integration is exact (same as shown in figure 2.13) and we make no approximations. The procedure to calculate trap extent in x direction is as follows: we start the ion simulation from some finite distance x_0 and continue for 1000 RF cycles, the minimum distance above which the ion diverges quickly and goes to distance higher than 10 mm from trap center is the trap depth [59]. The same thing can be done with y and z direction. A simulation with $^{39}K^+$ ions performed with parameters $f = 700$ kHz, $V_{\text{outer}} = -5$ V and $V_{\text{inner}} = 85.4$ V gives trap extent of 4.2 mm in x/y direction and 2.8 mm in the z direction. Similarly, trap depth can be found by having a finite initial velocity in one direction keeping all other parameters zero. Such a procedure gives, 0.49 eV in x/y direction and 0.59 eV in the z direction. The secular frequencies can be obtained by Fourier transforming the trajectories of the ion. This gives $\omega_x/2\pi = \omega_y/2\pi = 56$ kHz for x/y and $\omega_z/2\pi = 98$ kHz for z direction as secular/macromotion frequencies. For the potential of the form in the equation 2.8 the secular frequencies can be calculated exactly [5] and are given by $\omega_x/2\pi = \omega_y/2\pi = 0.5\zeta_x f = 53.7$ kHz in x/y direction and $\omega_z/2\pi = 0.5\zeta_z f = 107.5$ kHz in z direction. This shows that the approximate equation 2.8 is quite good. These parameters for trap operation were chosen such that $^{39}K^+$ ions are trapped efficiently, and $^{85}Rb^+$ ions are not. The reason of such a scenario will be clear in section 3.1. The parameters for trapping $^{85}Rb^+$ ions are $f = 500$ kHz, $V_{\text{outer}} = -5$ V and $V_{\text{inner}} = 80$ V.

2.3 Fabry-Pérot cavity

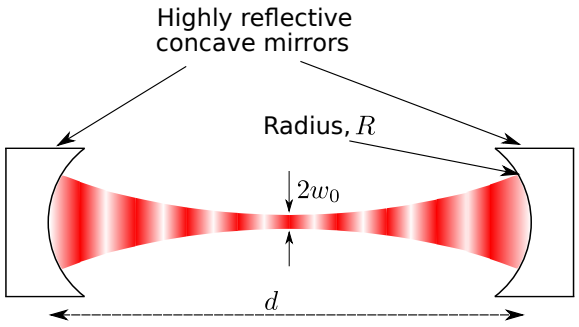

Fig. 2.14 Diagram of a Fabry-Pérot Cavity. The red part is the light confined in the cavity. The color gradient illustrates the intensity variation for a standing wave formed inside the cavity. As the mirrors are concave, the light is also seen focused at the center of the cavity.

To confine the field of a photon to a finite volume, we use two highly reflecting concave mirrors facing each other as shown in figure 2.14.

2.3.1 Spatial mode of the cavity field

For electrical field in vacuum, the wave equation can be written as,

$$\nabla^2 E(\vec{r},t) - \frac{1}{c^2}\frac{\partial^2 E(\vec{r},t)}{\partial t^2} = 0 \tag{2.9}$$

where c is the speed of light. The simplest solution for the above equation is a plane wave. However, the boundary conditions imposed by the cavity mirrors don't allow plane waves as a solution. In paraxial approximation where the rays normal to the wavefronts make very small angle with the optical axis, the electric field can be written as [61, 62], $E(\vec{r},t) = E_0\psi_+(\vec{r})e^{ikz}e^{-i\omega t}$. Where $k = 2\pi/\lambda$ is wavenumber, λ is the wavelength and $\omega/(2\pi)$ is the frequency of the light wave. This is a plane wave traveling in $+z$ direction modulated by the factor $\psi_+(\vec{r})$ which varies slowly along the $+z$ axis. Putting this form in equation 2.9 and keeping only first derivative of $\psi_+(\vec{r})$ with respect to z as the field varies slowly along z compared to the wavelength (λ), we get,

$$\nabla_T^2\psi_+(x,y,z) + 2ik\frac{\partial\psi_+(x,y,z)}{\partial z} = 0 \tag{2.10}$$

where $\nabla_T^2 = \partial^2/\partial x^2 + \partial^2/\partial y^2$ is the Laplacian operator in the transverse direction. This is called paraxial Helmholtz equation. The solution to this equation depends on the boundary conditions, and for optical components with cylindrical symmetry the fundamental solution is given by [62],

$$\psi_+(\vec{r})e^{ikz} = \frac{w_0}{w(z)} e^{-(x^2+y^2)/w(z)^2} e^{ikz - i\tan^{-1}(z/z_0)} e^{\frac{1}{2}ik(x^2+y^2)/R(z)}. \tag{2.11}$$

Here, w_0 is the waist size at the center, $w(z) = w_0\sqrt{1+(z/z_0)^2}$ is waist size at a distance z from the center, $R(z) = z[1+(z_0/z)^2]$ is the radius of curvature, $z_0 = \pi w_0^2/\lambda$ is the Rayleigh range.

For our cavity which is made up of two spherical mirrors, the wavefront of light having the functional form of equation 2.11 should match the curvature of mirrors at the mirror position. This constrains the parameters in the equation 2.11 giving [62],

$$w_0^2 = \frac{\lambda d}{2\pi}\sqrt{\frac{2|R|}{d} - 1} \tag{2.12}$$

where d is the distance between the mirrors and R is the radius of curvature for both the mirrors. There is also a condition for stability of such a resonator [62] given by, $0 < (1 - d/|R|)^2 < 1$.

Similar analysis can be done for a wave traveling in $-z$ direction giving,

$$\psi_-(\vec{r})e^{-ikz} = \frac{w_0}{w(z)} e^{-(x^2+y^2)/w(z)^2} e^{-ikz - i\tan^{-1}(z/z_0)} e^{\frac{1}{2}ik(x^2+y^2)/R(z)}. \tag{2.13}$$

In the cavity, the amplitudes of the two counter-propagating waves will add,

$$\begin{aligned}\psi(\vec{r}) &= \psi_+(\vec{r})e^{ikz} + \psi_-(\vec{r})e^{-ikz} \\ &= \frac{2w_0}{w(z)} e^{-(x^2+y^2)/w(z)^2} \cos[kz] e^{-i\tan^{-1}(z/z_0)} e^{\frac{1}{2}ik(x^2+y^2)/R(z)}.\end{aligned} \tag{2.14}$$

Similarly higher order modes which are stable inside the cavity can be found [62] and are of two types, first ones with rectangular symmetry are called Hermite-Gaussian modes and second ones with cylindrical symmetry are called Laguerre-Gaussian modes. The functional form of Hermite-Gaussian modes is,

$$\begin{aligned}\psi_{mn}(\vec{r}) = &\frac{2w_0}{w(z)} H_m\left(\frac{\sqrt{2}x}{w(z)}\right) H_n\left(\frac{\sqrt{2}y}{w(z)}\right) \\ &e^{-(x^2+y^2)/w(z)^2} \cos[kz] e^{-(m+n+1)i\tan^{-1}(z/z_0)} e^{\frac{1}{2}ik(x^2+y^2)/R(z)}.\end{aligned} \tag{2.15}$$

Where $H_m\left(\frac{\sqrt{2}x}{w(z)}\right)$ is a Hermite polynomial of order m. For Laguerre-Gaussian modes,

$$\psi_{mn}(\vec{r}) = \frac{2w_0}{w(z)}\left[\frac{(x^2+y^2)}{w(z)^2}\right] L_n^m\left(\frac{(x^2+y^2)}{w(z)^2}\right) e^{-im\tan^{-1}(y/x)} \\ e^{-(x^2+y^2)/w(z)^2}\cos[kz] e^{-(m+n+1)i\tan^{-1}(z/z_0)} e^{\frac{1}{2}ik(x^2+y^2)/R(z)}. \tag{2.16}$$

Where $L_n^m\left(\frac{(x^2+y^2)}{w(z)^2}\right)$ is a generalized Laguerre polynomial. m and n are integers.

In frequency domain, the resonance condition for all of these modes is given by [62],

$$\omega_{\text{cv}}/(2\pi) = \nu_{mn} = \nu_{\text{fsr}}\left[q + \frac{1+m+n}{\pi}\cos^{-1}(1-d/|R|)\right]. \tag{2.17}$$

$\nu_{\text{fsr}} = \frac{c}{2d}$ is frequency between $q+1$ and q longitudinal modes and is called the free spectral range (FSR) of the cavity. The modes with different values of m and n are called transverse modes.

2.3.2 Quantized cavity field

The quantized electric field inside the cavity can be written as [55],

$$E(\vec{r},t) = -\sqrt{\frac{\hbar\omega_{\text{cv}}}{2\varepsilon_0}}\left[f(\vec{r})\hat{a}(t) + f^*(\vec{r})\hat{a}^\dagger(t)\right] \tag{2.18}$$

where $f(\vec{r})$ is spatial mode function, $\hat{a}(t)$ and $\hat{a}^\dagger(t)$ are annihilation and creation operators respectively for cavity photons.

From equation 2.14 the normalized spatial mode function can be written as,

$$f(\vec{r}) = \frac{1}{\sqrt{V}}\frac{w_0}{w(z)} e^{-(x^2+y^2)/w(z)^2}\cos[kz] e^{-i\tan^{-1}(z/z_0)} e^{\frac{1}{2}ik(x^2+y^2)/R(z)}. \tag{2.19}$$

Where $V = \pi w_0^2 d/4$ is the volume of the cavity mode and is obtained from the requirement $\int |f(\vec{r})|^2 dr = 1$.

For our cavity the radius of curvature of the concave surface of the mirrors is $|R| = 50$ mm and the distance between the mirrors is $d = 45.7$ mm. Using these quantities, the mode waist at the cavity center becomes $w_0 = 78\mu$m, and the Rayleigh range of the Gaussian mode becomes $z_0 = 24.9$ mm. The interaction of light inside the cavity with the atoms will happen in the region where $z \ll z_0$, hence near the atomic ensemble the spatial mode function can be written

as,

$$f(\vec{r}) = \frac{1}{\sqrt{V}} e^{-(x^2+y^2)/w_0^2} \cos[kz]. \tag{2.20}$$

2.3.3 Rate equation for the cavity field

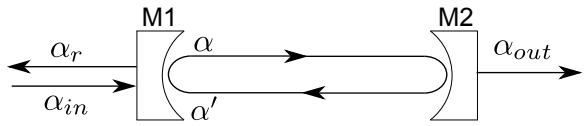

Fig. 2.15 Light fields interacting with the cavity mirrors. M1 - input mirror of the cavity, M2 - output mirror of the cavity, α_{in} - field input to the cavity, α and α' - field inside the cavity, α_{r} - field reflected by the cavity, α_{out} - field transmitted by the cavity.

To calculate the effect of atoms on the cavity field, we first need to calculate the state and dynamics of the field inside an empty cavity. Let $\alpha_{\text{in}}(t)$ be the amplitude of light field incident on the first mirror of the cavity, R_{f} is mirror reflectivity, T_{r} is transitivity of the mirrors and A_{b} is absorption and scattering loss from the mirrors. For fields, the reflectivity, transitivity, and absorptivity become $r_{\text{f}} = \sqrt{R_{\text{f}}}$, $t_{\text{r}} = \sqrt{T_{\text{r}}}$ and $a_{\text{b}} = \sqrt{A_{\text{b}}}$ respectively. The field after reflection by mirror M2 and just before mirror M1 is (see figure 2.15),

$$\alpha'(t) = r_{\text{f}}(1-a_{\text{b}})\alpha(t-\tau)e^{i\pi}e^{-i(2n\pi+\Delta_{\text{cv}}\tau)} \tag{2.21}$$

where $\tau = 2d/c$ is round trip time for the cavity. $\Delta_{\text{cv}} = \omega - \omega_{\text{cv}}$ is detuning of the incident light frequency from nearest cavity mode frequency. The phase π is due to reflection from the mirror and $2n\pi + \Delta_{\text{cv}}\tau$ is relative phase acquired after one round trip where n is an integer. This phase is $2n\pi$ when the light frequency is same as the cavity resonance frequency. Similarly, the intra-cavity field just after the mirror M1 is,

$$\alpha(t) = t_{\text{r}}\alpha_{\text{in}} + r_{\text{f}}(1-a_{\text{b}})\alpha'(t)e^{i\pi}. \tag{2.22}$$

From equations 2.21 and 2.22 and using $e^{-i2n\pi} = 1$,

$$\alpha(t) = t_{\text{r}}\alpha_{\text{in}} + r_{\text{f}}^2(1-a_{\text{b}})^2\alpha(t-\tau)e^{i\pi}e^{-i\Delta_{\text{cv}}\tau}. \tag{2.23}$$

Subtracting $\alpha(t-\tau)$ and dividing by τ on both sides give,

$$\frac{\alpha(t)-\alpha(t-\tau)}{\tau} = \frac{t_{\text{r}}\alpha_{\text{in}}}{\tau} + \frac{r_{\text{f}}^2(1-a_{\text{b}})^2e^{-i\Delta_{\text{cv}}\tau}-1}{\tau}\alpha(t-\tau). \tag{2.24}$$

Let us define rates for transmission and absorption losses as,

$$\kappa_r = (1 - r_f)/(\tau) = (1 - \sqrt{1 - T_r})/(\tau) \approx \frac{T_r}{2\tau} \tag{2.25}$$

$$\kappa_a = a_b/\tau. \tag{2.26}$$

For our cavity, $\kappa_r\tau \ll 1$, $\kappa_a\tau \ll 1$ and $\Delta_{cv}\tau \ll 1$ because all the loss terms are of the order of MHz or less and $1/\tau$ is of the order of GHz. Hence only linear terms are important. In the limit, $\tau \to 0$ we get a rate equation,

$$\frac{d\alpha(t)}{dt} = \eta - (\kappa_t - i\Delta_{cv})\alpha(t) \tag{2.27}$$

where $\eta = \frac{t_r\alpha_{in}}{\tau}$ is the rate at which input field is transmitted into the cavity and $\kappa_t = 2\kappa_r + 2\kappa_a$ is the total loss rate inside the cavity. The limit $\tau \to 0$ is justified because the time scale for all the other relevant processes like cavity decay, atomic decay, and cavity-atom interactions is small compared to τ. In steady state, the intra-cavity intensity then becomes proportional to,

$$|\alpha|^2 = \frac{|\eta|^2}{\Delta_{cv}^2 + \kappa_t^2} \tag{2.28}$$

The intensity of light transmitted by the 2nd mirror is proportional to,

$$\begin{aligned} |\alpha_{out}|^2 = |\alpha|^2 T_r = \frac{|\eta|^2 T_r}{\Delta_{cv}^2 + \kappa_t^2} = \frac{T_r^2|\alpha_{in}|^2}{(\Delta_{cv}^2 + \kappa_t^2)\tau^2} = \frac{4\kappa_r^2|\alpha_{in}|^2}{(\Delta_{cv}^2 + \kappa_t^2)} \\ = T_c|\alpha_{in}|^2. \end{aligned} \tag{2.29}$$

Similarly, the intensity of reflected light is proportional to,

$$|\alpha_r|^2 = \left[\frac{(\kappa_t - 2\kappa_r)^2 + \Delta_{cv}^2}{(\Delta_{cv}^2 + \kappa_t^2)}\right]|\alpha_{in}|^2 = R_c|\alpha_{in}|^2. \tag{2.30}$$

Here T_c and R_c are transitivity and reflectivity of the cavity respectively. The intracavity intensity is a Lorentzian function with the full width at half maxima (FWHM) $\delta\nu = 2\frac{\kappa_t}{2\pi}$. The ratio of cavity FSR to FWHM ($\mathscr{F} = \frac{\nu_{fsr}}{\delta\nu}$) is called the finesse of the cavity. Here $\nu_{fsr} = c/2d = 1/\tau$ is FSR of the cavity. Finesse is usually used to specify the quality of a cavity and can also be defined as the ratio of average time spent by the photon in the cavity to twice cavity round trip time, $\mathscr{F} = \frac{(2\pi/\kappa_t)}{2\tau}$. Hence higher the finesse better the efficiency of trapping the photon. Quality factor ($Q = \frac{\omega_{cv}/2\pi}{\delta\nu}$) is another quantity which is a measure of how good a cavity is. For optical cavities $\omega_{cv}/2\pi \gg \delta\nu$, hence $\mathscr{F}$ is more appropriate quantity to specify.

2.3.4 Estimating the intracavity intensity

For studies of various atom-light interactions inside the cavity, it is important to know the exact value of intracavity intensity. There is no direct way yet to measure the intracavity intensity of many cavity photons without destroying the photons. Only detection of single cavity photon has been demonstrated [63, 64]. However, the intracavity intensity can be estimated by measuring the intensity of light coming out of the cavity which is proportional to the intracavity intensity. Below we describe the procedure to estimate the intracavity intensity. From equation 2.29 it can be seen that this estimation requires the knowledge of total loss rate (κ_t) and the transmission rate (κ_r) of the cavity mirrors. κ_t can be obtained by measuring the linewidth of the transmission spectrum of the cavity. κ_r can be obtained by measuring the absolute value of transmission or reflection using equation 2.29 or 2.30. However, while deriving these equations we assumed that the light transmitted by the first mirror ($|\alpha_{in}|^2$) couples completely to the cavity. This is not practical as the cavity will only accept photons which have same spatial mode as the one supported by the cavity. Even though a mode matching lens is always present before coupling the light to the cavity as shown in figure 2.16, the coupling is never 100%. Hence, only some fraction of the light ($f_r|\alpha_{in}|^2$) will be coupled to the cavity. There are two unknown variables (f_r and κ_r) now. This requires two observations which will be provided by measuring absolute values of transmitted and reflected power. Here, the powers measured by PD1 and PD3 of figure 2.16 will be required. Let us denote by P^t_{out} the power transmitted by the cavity when the laser frequency and cavity resonance match, P^r_1 the power detected by PD1 when laser light is far from cavity resonance, P^r_2 the power detected by PD1 when laser light is on cavity resonance, and P_{in} the power incident on first cavity mirror. Ideally, the transmission (T_c) and reflection (R_c) coefficients will be given by, $\frac{P^t_{out}}{P_{in}}$ and $\frac{P^r_2}{P_{in}}$ respectively if only the model from subsection 2.3.3 is used. Practically, including the mode matching factor the transmission coefficient becomes, $T_c = \frac{P^t_{out}}{f_r P_{in}}$. As can be seen from figure 2.16 the total reflected power does not reach PD1, hence we have to include a loss factor l_r in calculating the reflectivity. Hence, practically $P^r_1 = l_r P_{in}$ and $P^r_2 = l_r R_c f_r P_{in} + l_r(1-f_r)P_{in}$. Here, the second term comes from the assumption that the fraction of power which does not couple to the cavity is reflected back. Dividing P^r_2 by P^r_1 and rearranging gives, $R_c = \frac{P^r_2 - P^r_1(1-f_r)}{P^r_1 f_r}$. Hence calculating the values of κ_r and f_r requires solving the coupled linear equations,

$$\begin{aligned} \frac{4\kappa_r^2}{(\Delta_{cv}^2 + \kappa_t^2)} &= \frac{P^t_{out}}{f_r P_{in}} \\ \frac{(\kappa_t - 2\kappa_r)^2 + \Delta_{cv}^2}{(\Delta_{cv}^2 + \kappa_t^2)} &= \frac{P^r_2 - P^r_1(1-f_r)}{P^r_1 f_r}. \end{aligned} \tag{2.31}$$

Once κ_r is known, the intracavity power can be calculated easily and is given by, $P^t_{out} T_r = 2P^t_{out}\kappa_r$. While deriving the equations, we assumed that the two mirrors are completely identical.

2.3.5 Locking a laser to the cavity

The length of the optical cavity and the frequency of the lasers in our experiment change due to thermal fluctuations. The change in the length of the cavity also changes the resonance frequency of the cavity. So, in order to have a non-fluctuating intensity of light inside the cavity, we have to lock the frequency of the laser to that of the cavity resonance. This ensures the laser is always on the cavity resonance and hence there are no intensity fluctuations. Here, we do not stabilize the cavity length actively because the drift in cavity resonance frequency is of the order of few MHz during our experimental cycle. This drift is small compared to the width of the molecular resonances in the Photoassociation (PA) processes studied in chapter 6. The aim of the experiment studied in chapter 6 which uses this locking technique is to perform PA in a cavity. The optical setup for locking the PA laser is shown in the figure 2.16. The laser is locked to the reflection signal of the cavity using the Pound–Drever–Hall (PDH) technique [65]. In some of the cavity PA experiments, we were required to scan the intensity of PA laser continuously while performing the experiment. This is achieved by attenuating the intensity of laser using a circular variable neutral density filter (VNDF). For a beam of light passing near the circumference of the VNDF, the optical depth changes when the VNDF is rotated around its center. This rotation is achieved by a stepper motor. But, varying the intensity creates problems for the locking of the laser to the cavity. To solve this issue, we pass the reflected light from the cavity through an acousto-optical modulator (AOM8) and lock the laser to the cavity using first order diffraction beam of AOM8. The intensity of this first order beam depends on the input intensity to AOM8 and RF power fed to AOM8. Hence, the intensity on PD1 can be kept constant even when input intensity to AOM8 is varied by controlling the RF power. The intensity on PD1 is actively stabilized using the signal of PD2 and a PID circuit which controls the RF drive driving AOM8. Additionally, the intensity of light coming out of the cavity is monitored using PD3, and the spatial mode of the cavity is monitored using a CCD camera as shown in figure 2.16.

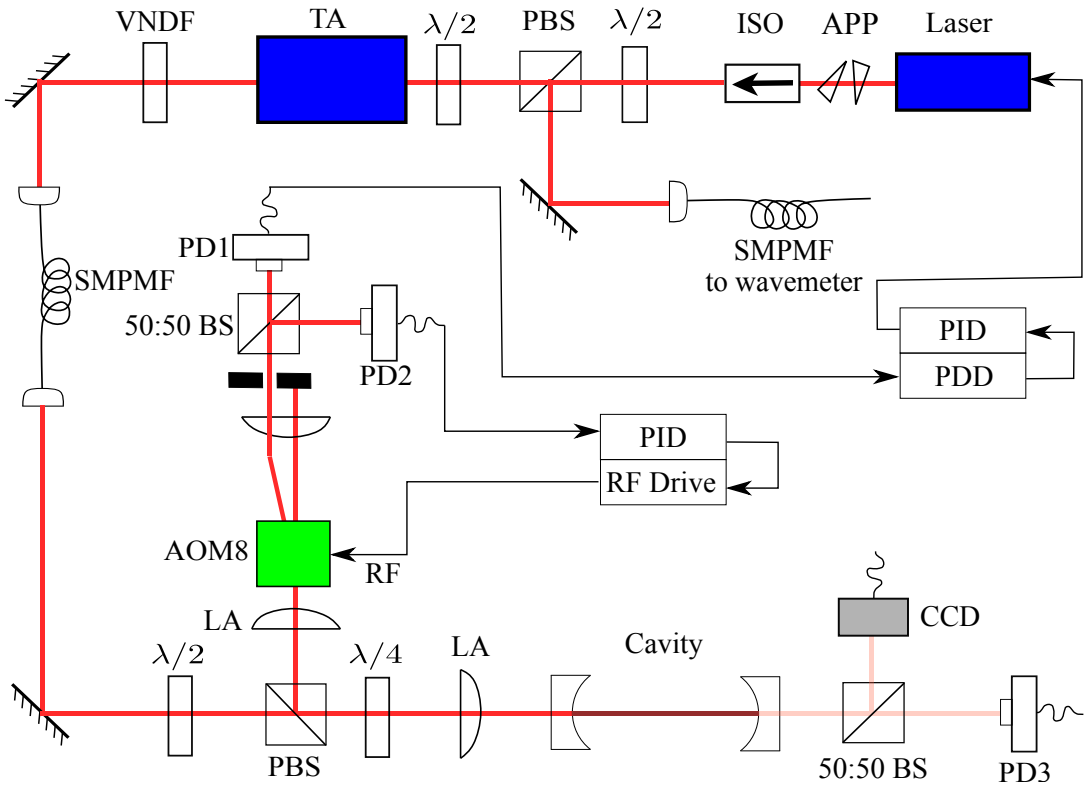

Fig. 2.16 The optical setup for the locking of PA laser to the cavity. VNDF - variable neutral density filter, BS - beam splitter, RF - radio frequency, CCD - charge-coupled device camera, PDD - Pound-Drever-Hall detector, and PID - proportional-integral-differential regulator. For abbreviations of the remaining components see caption of figure 2.3.

2.4 The whole assembly

To study interactions between atoms, ions, and photons all the techniques mentioned above should be integrated together. Figure 2.17 on the last page of this chapter shows a result of such an integration in a single vacuum chamber. The vacuum chamber is made up of stainless steel and is customized model provided by the company Kimball Physics. The chamber has an outer diameter of 17.27 cm, a height of 3.5 cm, and is designed with 16 CF16 and 2 CF100 ports. The vacuum inside the experimental chamber is maintained by an ion pump which is connected to one of its port. This results in a vacuum of $\sim 10^{-10}$ torr when the MOT is operational. The assembly is such that the centers of the ion trap, atom trap, and cavity coincide roughly. Fine adjustment to the center of atomic cloud is done by using the magnetic field of Helmholtz coils placed around the chamber. The ions created in our experiments are detected using a channel electron multiplier (Dr. Sjuts: KBL10RS), the position of it with respect to other

components is shown in the figure 2.17. The atoms are loaded from a thermal vapor created in the experimental chamber using dispensers containing alkali metal salt. The dispensers emit thermal alkali atoms when they are heated by passing few amperes of current through them. There are dispensers of total four elements inside the chamber which can be used to create ultracold atoms. They are, rubidium (72.2% ^{85}Rb and 27.8% ^{87}Rb), enriched potassium (8.4% ^{40}K, 85.42% ^{39}K, and 6.16%^{41}K), cesium (100% ^{133}Cs), and calcium (99.9% ^{40}Ca).

Combining a MOT, an ion trap and a cavity together put many constraints on the components and their arrangements. The ion trapping is done using only electric fields in a modified spherical Paul trap as high magnetic fields required to trap ions in Penning trap will not allow the operation of a MOT for atoms. Also, the size of the MOT beams has to be large and hence occupy large volumes. Hence the Paul trap is created using thin tungsten wires of 80 μm diameter to minimize the blocking and scattering of MOT beams. Additionally, the ions are extracted radially with respect to the Paul trap as axial extraction is not possible due to the presence of the cavity along the axial axis. The finesse of our cavity is not very high because high finesse might result in the build up of high intensity of light inside the cavity due to the coupling of the fluorescence from the MOT atoms to the cavity. This high-intensity light will interfere with the operation of the MOT. Also, the distance between cavity mirrors is kept large to allow for MOT beams to reach the center of the MOT. Increasing the distance between the mirrors results in a decrease in atom-cavity coupling strength (g_0), nevertheless, we are in collective strong coupling regime where the collective interaction of atoms is large enough to be observable. Finally, as was discussed in chapter 1, there are two methods to create molecules from a ultracold ensemble of atoms. One method uses a magnetic field and the other uses lasers to create molecules. As will be seen in chapter 6 we choose to use lasers to create molecules via the process of PA because the large magnetic fields required for Feshbach creation of the molecules will hinder the operation of the MOT. For more details about the assembly and its construction see the thesis of Tridib Ray [58] and S. Jyothi [59].

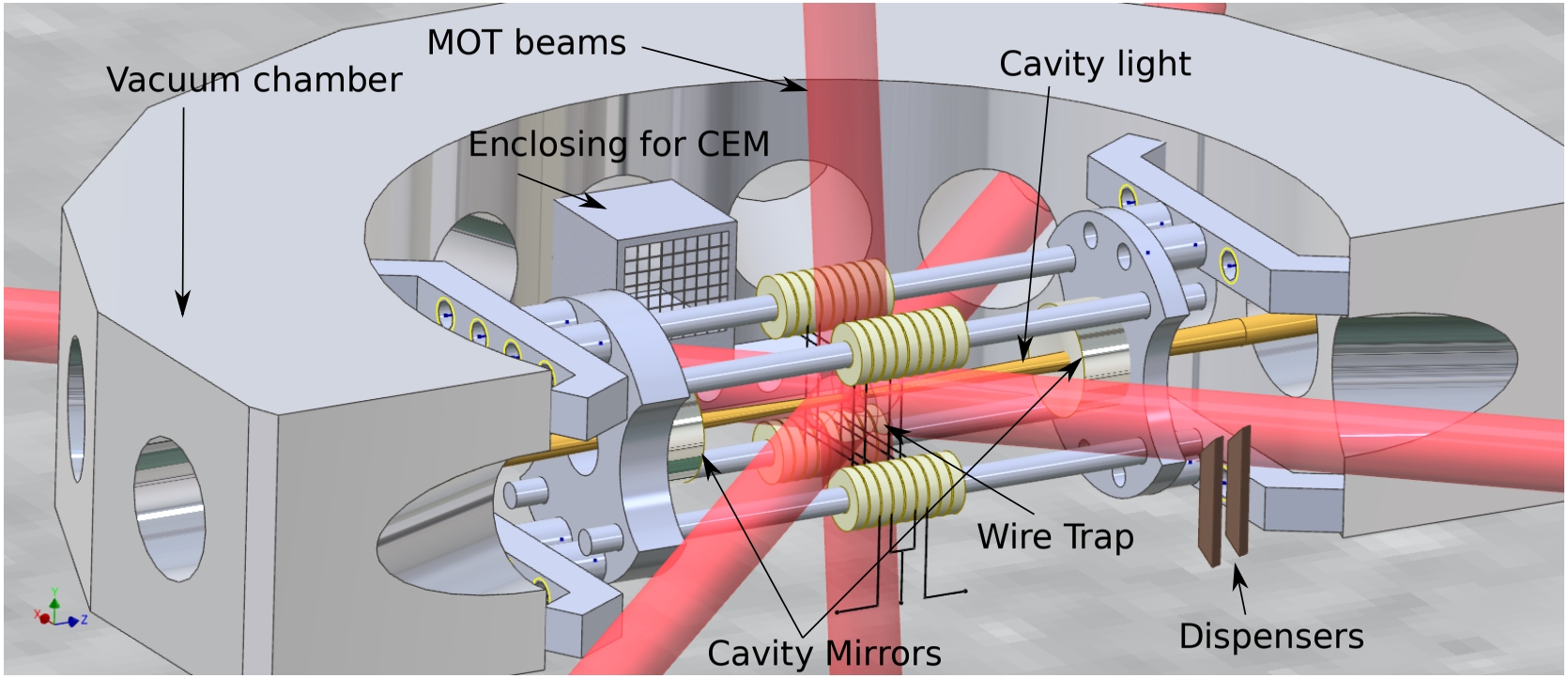

Fig. 2.17 Assembly of components in the experimental chamber. MOT - magneto-optical trap, CEM - channel electron multiplier for ion detection. Only half vacuum chamber is shown in order for the things inside the chamber to be visible. A pair of anti-Helmholtz coils which produce the magnetic field for MOT is not shown, one each is placed on top and bottom of the chamber.

Chapter 3

Collisional cooling of lighter ions by heavier atoms

In the introduction, we enumerated various motivations for combining ion and atom traps. One of the motivation was to see whether we can cool ions using an ensemble of atoms. Uniform buffer gas of atoms lighter than the ion have been extensively used to cool the trapped ions [5, 6]. For such a scenario it was theoretically shown that cooling is not possible when the atoms are heavier than the ions [6–9]. For such a case, the ion will heat as it undergoes collisions with atoms instead of being cooled even if the temperature of the atoms is much lower than that of the ion. In a seminal work on this topic by Major and Dehmelt [6], an estimation for the atom to ion mass ratio of one ($m_r = (m_a/m_i) = 1$) was made above which heating occurs. Here m_a is the mass of atoms and m_i the mass of ions. More recent values of this ratio, called the critical mass ratio (CMR) above which heating occurs has been the topic of many recent articles [7–9]. The CMR values derived by these work are 1.55 [7], 1.47 [8] and 0.95 [9] for our ion trap parameters. In a previous work from our group [10], cooling of ions by atoms of equal mass was experimentally demonstrated and it was theoretically shown that cooling is possible for any mass ratio if the atom-ion collisions are restricted to the center of the trap. Recent theoretical work [66, 67] by another group detailed and extended the description of such a cooling process, and suggest some approaches for making it more efficient in addition to ones discussed in this chapter. An experiment to validate this claim was missing. In the following section, we describe an experiment which shows cooling of K^+ ions using ^{85}Rb atoms. In the later sections, we will talk about simulations that mimic such experiments, and we will provide qualitative interpretations of the results obtained in the experiments.

3.1 Experiments demonstrating cooling of ions

The goal of the experiment described in this section is to show that $^{39}K^{+}$ ions are effectively cooled by ^{85}Rb atoms in a MOT. To create the $^{39}K^{+}$ ions we build a small MOT of ^{39}K from which ions are loaded by two photon ionization near the center of the ion trap and the dense ^{85}Rb MOT. The ions loaded in the trap then interact with ^{85}Rb atoms. The details about ^{39}K MOT is given in section 2.1.

For ^{85}Rb MOT the cooling light is 12 MHz red detuned from the ^{85}Rb ($5^2S_{1/2}$, $F = 3$) $\rightarrow$ ^{85}Rb ($5^2P_{3/2}$, $F' = 4$) transition and the repumping light is on resonance with the ^{85}Rb ($5^2S_{1/2}$, $F = 2$) $\rightarrow$ ^{85}Rb ($5^2P_{3/2}$, $F' = 3$) transition. The total power in the cooling (repumping) beams is 20 mW (1 mW). With a magnetic field gradient of $\sim$ 22 Gauss/cm, a ^{85}Rb MOT with $\sim$ 4×10^5 ultracold ^{85}Rb atoms (FWHM $\sim$ 280 μm and peak density $\sim 10^{10}$ cm^{-3}) is formed at a temperature of 150 μK.

The $^{39}K^{+}$ ions are created by resonant two-photon ionization of ultracold atoms in the ^{39}K MOT, where the first photon (the cooling laser of the ^{39}K MOT, which is 35 MHz red detuned from 2-3$'$ transition of D2 line of ^{39}K atoms) results in the $4^2S_{1/2} \rightarrow 4^2P_{3/2}$ excitation at 767 nm and a second photon is sourced from a collimated light-emitting diode (LED) with its emission centered at 456 nm. The beams for the ^{39}K MOT are combined with those for the ^{85}Rb MOT on a polarizing beam splitter and which then propagate along the same direction.

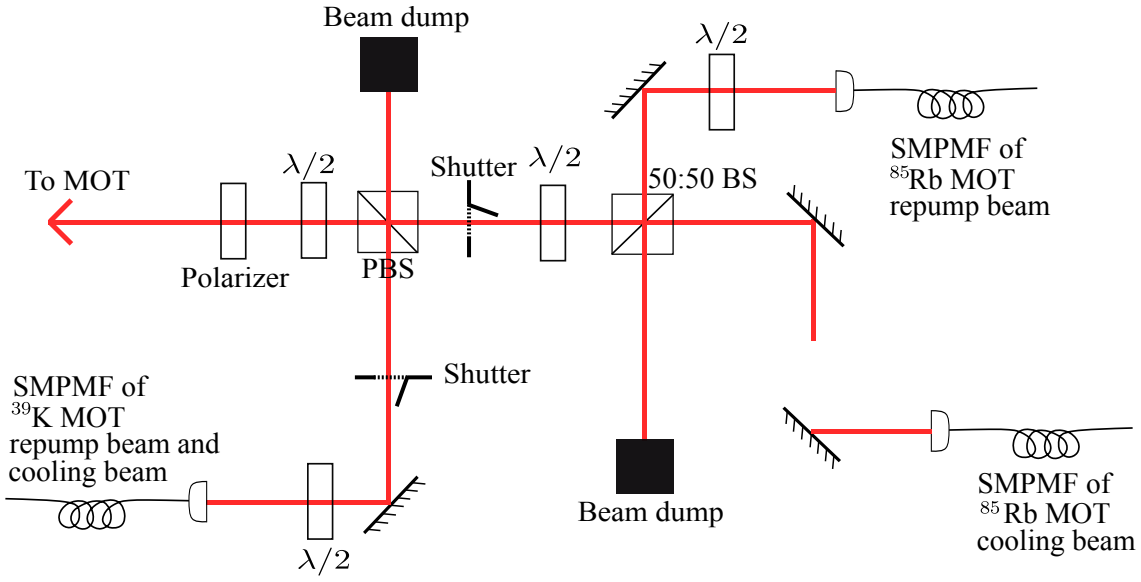

Fig. 3.1 Experimental setup showing the mixing of ^{39}K and ^{85}Rb MOT beams. PBS - polarizing beam splitter, 50:50 BS - 50 % transmission and 50 % reflection beam splitter, SMPMF - single mode polarization maintaining fiber, $\lambda/2$ - half wave plate.

The experimental arrangement for the mixing of the MOT beams is shown in figure 3.1. The two MOTs are formed at the same location and they overlap with the ion trap center. The loading of the two MOTs is independently controlled by mechanical shutters placed in the paths of the respective laser beams as shown in figure 3.1. Both MOT's are vapor-loaded. The parameters for trapping of $^{39}K^{+}$ are given in section 2.2. The counting of trapped ions is done by detecting them using a channel electron multiplier (CEM) which gives a $\sim$ 8 ns pulse of voltage across a resistor whenever an ion makes an impact on the CEM [68]. The extraction of ions from ion trap region to the CEM is done by applying a high voltage (360 V) pulse, which launches them along the axis of a time of flight (ToF) mass spectrometer (MS). This ToF MS between the ion trap and the CEM enables differentiation between $^{39}K^{+}$ and $^{85}Rb^{+}$ ions based on their time of arrival. More details about the extraction process can be found in [68] and [59].

The aim of the experiment is to measure the lifetime of the trapped $^{39}K^{+}$ ions when held with and without the ^{85}Rb MOT atoms. The experimental sequence is given in figure 3.2. The LED light can also ionize ^{85}Rb atoms, hence the ^{85}Rb MOT is operated only after the ionization step is completed. The sequence is: the ^{39}K MOT is loaded, the fields used for ion-trapping are switched on, $^{39}K^{+}$ ions are created by a flash of blue LED, and the light of the ^{39}K MOT is shuttered off in order to remove the remaining atoms from interaction region. In the second stage, either the ^{85}Rb MOT light is allowed to load the ^{85}Rb MOT, or the ^{85}Rb light is kept blocked so that no MOT is loaded. The trapped $^{39}K^{+}$ ions are then held in the ion trap for variable hold times, and are subsequently extracted for detection by a CEM. The pulses generated by the impact of ions are counted, and the number of ions which have survived in the ion trap is recorded as a function of the hold time (t). This is done both in the presence and absence of the ^{85}Rb MOT. Additionally, an experiment to check the localized cooling of ions was separately conducted with $^{85}Rb^{+}$ ions, with a MOT of ^{133}Cs atoms, in a distinct apparatus.

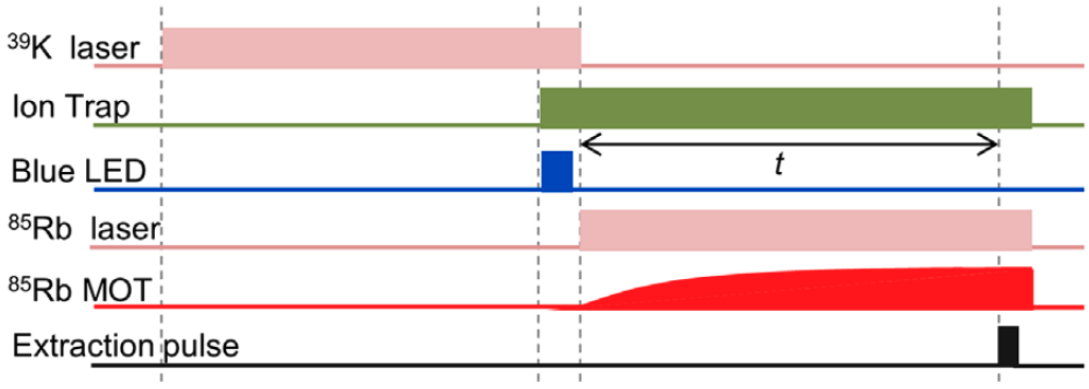

Fig. 3.2 Relative timing sequence for various stages in the experiment.

Results of the experiments

The results of the experiment mentioned above are shown in Fig. 3.3. In Fig. 3.3(a), it can be seen that $^{39}K^{+}$ ions survive longer in the presence of ^{85}Rb MOT atoms. For small hold time intervals, there is not a great difference between surviving ion number with (circles) and without (squares) ^{85}Rb MOT since it takes 5 seconds for the ^{85}Rb MOT to load. After 5 seconds of hold time, the difference starts to emerge, and a clear separation between the two cases can be seen at 25 seconds.

The trapping lifetime of the ions increases because in the presence of ^{85}Rb MOT atoms, the total heating rate of ions is reduced. The reduction in heating rate is possible only due to the cooling effect of the ^{85}Rb MOT atoms [10, 28]. The cooling of $^{39}K^{+}$ ions is made possible because the ^{85}Rb atoms are located precisely at the center of the ion trap, and the volume of the

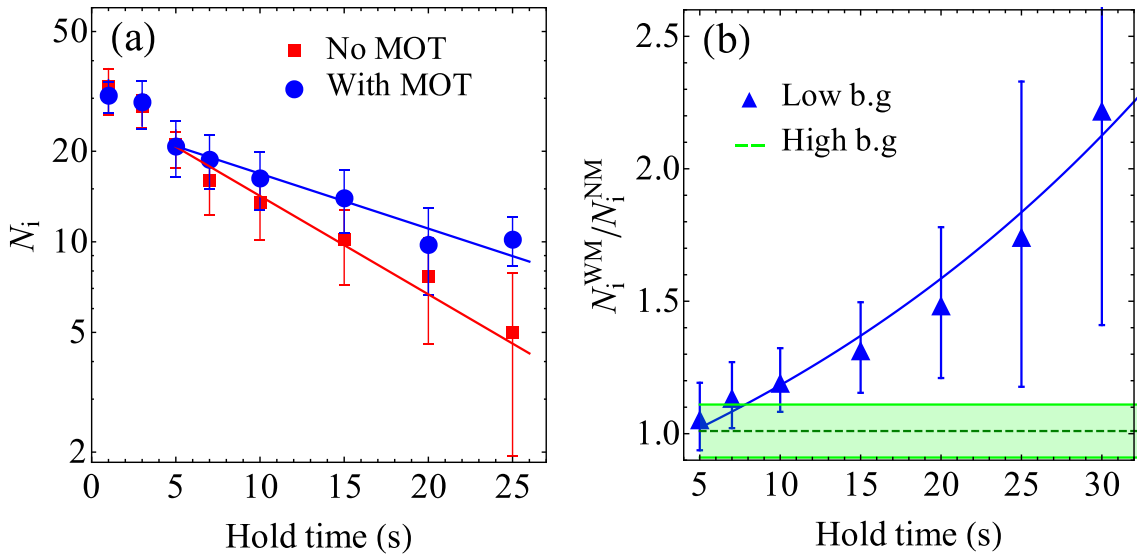

Fig. 3.3 (a) The number of $^{39}K^{+}$ ions (N_i) remaining in the ion trap for different values of the hold time either in the presence (blue circles) or the absence (red squares) of the ^{85}Rb MOT. The blue and the red lines are single exponential fits for the respective cases. The increase in the survival probability of trapped $^{39}K^{+}$ ions in the presence of the ^{85}Rb MOT indicates the cooling of $^{39}K^{+}$ ions. The error bars represent the width (one s.d.) of the underlying ion number distribution. (b) The ratio between the number of trapped $^{39}K^{+}$ ions with ^{85}Rb MOT (N_i^{WM}) and with no ^{85}Rb MOT (N_i^{NM}), for low ($\leq 5.9 \times 10^{-10}$ Torr) background partial pressure of Rb (blue triangles) and high ($\geq 8.3 \times 10^{-10}$ Torr) background partial pressure of Rb (dotted green line). The shaded region represents one s.d. for the measurements at a high background pressure. At a high background pressure, the cooling of ions (indicated by ratios > 1) is not experimentally discernible. The solid line is a fit to an exponential for the low background pressure case. The values of partial pressure for Rb was obtained from the loading rate of the ^{85}Rb MOT [69].

ion trap is much larger than the volume of the atom trap. This localization of atoms ensures that collisions happen near the center of the ion trap, where the energy due to micromotion of ions is negligible [10]. In contrast, for a uniform buffer gas majority of collisions take place near the classical turning points where micromotion is highest [10].

Nine measurements similar to Fig. 3.3(a) were performed all of which showed cooling of $^{39}K^{+}$ in the presence of ^{85}Rb MOT atoms. We can fit a single exponential of the form $N_i(t) = N_i^0 e^{-k(t-5)}$ to the data from all of these nine measurements, where $N_i(t)$ is ion number after a hold time t, N_i^0 is the ion number at 5 seconds hold time and k gives the rate of decay in the number of ions. The mean of k for experiments without ^{85}Rb MOT atoms is $k_1 = 0.089(0.014)\text{s}^{-1}$, and with ^{85}Rb MOT atoms is $k_2 = 0.056(0.018)\text{s}^{-1}$, the values in brackets are standard deviation (s.d) of the means. The lifetimes corresponding to these rates are $\tau_1 = 11.2^{+2.2}_{-1.6}$ s and $\tau_2 = 17.8^{+8.2}_{-4.3}$ s for without and with ^{85}Rb MOT atoms respectively. The triangles in Fig. 3.3(b) show the averages of ratios of number of ions with ^{85}Rb MOT atoms and without ^{85}Rb MOT atoms for the given hold time. As seen in the figure the ratio increases with hold time and a fit of the form $Ae^{k_{\text{eff}}(t-5)}$ gives $k_{\text{eff}} = 0.0293(\pm 0.0024) \approx (k_1 - k_2)$. Fig. 3.3(b) shows the same ratio for a higher background pressure of Rb atoms but with the same number of atoms in ^{85}Rb MOT. Here the ratios for all hold times is near one because a higher density of the uniform gas of Rb atoms will heat the lower mass ion $^{39}K^{+}$ more, completely overpowering the cooling effect of the ^{85}Rb MOT. This observation tells us that the background pressure contributes to heating of the ions in a major way, consistent with the initial predictions of Major and Dehmelt [6] and other recent work [7–9] on buffer gas cooling and heating.

In earlier experiments with $^{85}Rb^{+}$ ions and a ^{85}Rb MOT [10], the cooling of ions was faster compared to this experiment. The cooling rate is higher because $m_r = 1$ for which cooling due to elastic collisions is more efficient plus the cooling by resonant charge exchange (RCE) is likely to have been active [70]. Since K and Rb are different species, RCE is not possible, but nonresonant charge exchange (nRCE) is. However, it is very weak [71] and is not detected in our experiment. The experimental sequence to check for nRCE is as follows,

(a) $^{85}Rb^{+}$ ions are loaded into the ion trap by photoionization of ^{85}Rb atoms from a ^{85}Rb MOT. The $^{85}Rb^{+}$ ions are held in the ion trap with or without the ^{85}Rb MOT for a certain hold time, and are then extracted onto the CEM for detection. The arrival time distribution of $^{85}Rb^{+}$ ions is recorded.

(b) Keeping the ion trap voltages identical, $^{39}K^{+}$ ions are loaded into the ion trap by photoionization of ultracold ^{39}K atoms in a ^{39}K MOT. The $^{39}K^{+}$ ions are held in the ion trap for a certain hold time (without the 85 Rb MOT, thus making sure $^{85}Rb^{+}$ ions are not formed) and are then extracted onto the CEM for detection. The arrival time distribution of the ^{39}K ions is recorded and found to be distinct from that of the $^{85}Rb^{+}$ ions.

(c) The experiment with $^{39}K^{+}$ ions with the ^{85}Rb MOT is then performed, and the ion arrival time distribution is found to be completely consistent with $^{39}K^{+}$ ions but not with $^{85}Rb^{+}$ ions.

Hence, no confirmed detection of $^{85}Rb^{+}$ ions could be made suggesting very low rates of nRCE. All the experimental results presented in this section suggest that, in an ideal situation with no background gas, a small ensemble of cold atoms, localized at the precise center of the ion trap will always cool a trapped ion via elastic collisions, whatever the ion-atom mass ratio.

To provide more evidence for cooling of ions by localized ensembles of gas, similar experiments were done with $^{85}Rb^{+}$ ions in the presence of ^{133}Cs MOT atoms [11], in a separate experimental chamber [25]. This further validated the claim that ions can be cooled using localized atoms of heavier mass. Figure 3.4 shows the results. An increase in the survival probability of trapped $^{85}Rb^{+}$ ions in the presence of the ^{133}Cs MOT indicates a cooling of $^{85}Rb^{+}$ ions. Figure 3.4(b) shows the ratio between the number of surviving $^{85}Rb^{+}$ ions in the presence and the absence of the ^{133}Cs MOT, obtained by averaging over ten experimental runs. The ratio increases with increasing hold time, and a fit to the ratio using the form $Ae^{k_{\rm eff}(t-1)}$ yields $k_{\rm eff} = 0.053(\pm 0.003)$. This value of $k_{\rm eff}$ is much greater than that for the cooling of $^{39}K^{+}$ ions by ^{85}Rb atoms shown earlier. This is partly because the atom-ion mass ratio (1.565) in this case is lower, resulting in faster cooling compared to the $^{39}K^{+}$-^{85}Rb atom case.

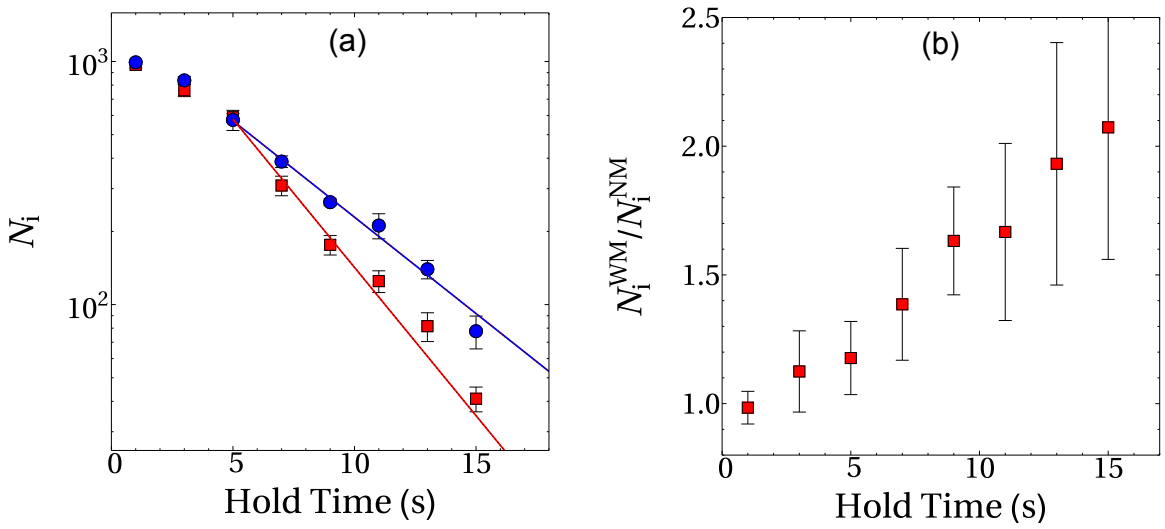

Fig. 3.4 (a) The number of $^{85}Rb^{+}$ ions (N_i) remaining in the ion trap for different values of the hold time either in the presence (blue circles) or the absence (red squares) of the ^{133}Cs MOT. The blue and the red lines are single exponential fits for the respective cases. The error bars represent the width (one s.d.) of the underlying ion number distribution. (b) The ratio between the number of trapped $^{85}Rb^{+}$ ions with ^{133}Cs MOT ($N_i^{\rm WM}$) and with no ^{133}Cs MOT ($N_i^{\rm NM}$) is shown. The experiment and data analysis for this figure was performed by Sourav Dutta.

3.2 Simulations to explain the mechanism of cooling

To study the effect of collisions on the trajectory, kinetic energy and the survival probability of an ion in the ion trap, we use a Monte-Carlo (MC) method to simulate (in Mathematica) the dynamics and the effect of collisions of the ion in the presence of atoms. In the simulations, the ion-ion interactions are neglected, which is a good approximation in the regime of high ion temperatures and the small ion numbers in our experiment. The small number and high temperature of ions ensure that the likelihood of two ions being present in the trap center at the same time is very small because ions move very quickly through the trap center In the outer reaches of the ion trap, the ion-ion collisions are neglected as the volume of the trap makes ion-ion collisions in the outer reaches of the trap very rare.

The simulation procedure proceeds as follows,

(i) At the start of the simulation the ion is stationary, which represents the creation of an ion from a MOT with negligible initial kinetic energy. Its position is chosen randomly, within a sphere of radius 1 mm that is concentric with the ion trap.

(ii) The classical trajectory of ion is then evaluated numerically in the presence of an ion trap potential given by Eqn. 2.7. The duration of this evaluation (t_{i}) is randomly chosen in the range zero to t_{ci}, where t_{ci} is equal to 20 times the inverse of RF frequency.

(iii) The stopping point of the above evaluation becomes the initial condition for an elastic collision of the ion with a MOT atom. The final velocity of the ion is then computed using classical collision theory [10, 72, 73].

(iv) We assume that the collision event is instantaneous with respect to all the relevant time scales and hence the position of the ion does not change during the collision, only the velocity changes. The ion trajectory is again evaluated, with this updated velocity as the initial condition for the times t_{i} to $t_1 = t_{\mathrm{i}} + \tau_{\mathrm{c}}$, where τ_{c} is chosen randomly according to the weights given by the Poisson distribution with a mean of t_{ci}.

(v) After the above evaluation, a trial evaluation is done for times t_1 to $t_1 + t_{\mathrm{ci}}$. This evaluation is done in order to predict the position and time of next collision. The distance of the ion from the center of the ion trap is noted down in a list at regular and small intervals of time from t_1 to $t_1 + t_{\mathrm{ci}}$. Then a weighted random choice is made from the list where the next collision takes place. The weights are proportional to the local atomic density at those points. After this a second weighted choice is made between MOT atoms and background atoms depending on their relative local densities. The background atoms are assumed to have uniform density and a velocity distribution compatible with a room temperature

of 300 K. The MOT atoms have a Gaussian density distribution ($n_0 e^{-r^2/(2\sigma_a^2)}$) having standard a deviation of σ_a and co-centered with the ion trap. The velocity distribution of the MOT atoms is compatible with temperature, T_{MOT}.

(vi) Once the collision point is chosen, steps (iii) to (v) are repeated. This is iterated in order to simulate a large number of collisions. We store the kinetic energy (K.E.) of the ions at regular intervals of $t_{ci}/100$. During each numerical evaluation in the ion trap, we track the position of the ion and stop the simulation if the ion has gone beyond 4 mm in any directions from the center of the ion trap. The time at which such a departure happens is noted down. This gives the exit time of the ion from the ion trap, and the ion is assumed to be lost.

(vii) The whole cycle from (i) to (vi) is repeated 30 times with different initial conditions for the ion position.

This simulation is a faithful representation of the conceptual framework for multiple scattering of ions by atoms and is adapted from the simulations in Ravi et al. [10, 72], with two major differences: (a) the resonant charge exchange collisions are dropped, i.e. only elastic collisions are considered which is consistent with the mixed species experiments, and (ii) collisions with a uniform density background gas are also included.

The results of the simulations mentioned above for three different ions ($^{39}K^+$, $^{85}Rb^+$, and $^{133}Cs^+$) in a gas of ^{85}Rb MOT atoms is shown in figures 3.5 and 3.6. These three cases correspond to different atom-ion mass ratios (m_r = 2.179, 1 and 0.639), corresponding to low, equal and high mass of the ion with respect to the colliding atoms. In all these cases, the ^{85}Rb MOT is assumed to have a Gaussian density distribution with σ_a = 100 μm. The K.E. plotted in the graphs is the mean kinetic energy of the ions between two successive collisions. All the cases mentioned above show cooling in the presence of ^{85}Rb MOT atoms precisely placed at the center of the ion trap.

As seen in the Fig. 3.5, the b.g. atoms will heat the ion, and the MOT atoms will cool the ion. At high background pressures, the ion losses with and without a MOT are the same, as seen experimentally in Fig. 3.3(b). As the background gas (b.g.) density is reduced, cooling due to the MOT overcomes the heating due to the background vapor and therefore lowers the ion kinetic energy as is evident from Fig. 3.5(b), and the ion survives longer as seen in Fig. 3.5(a). When the b.g. density is zero, the ions are held in perpetuity. Fig. 3.5(b) illustrates

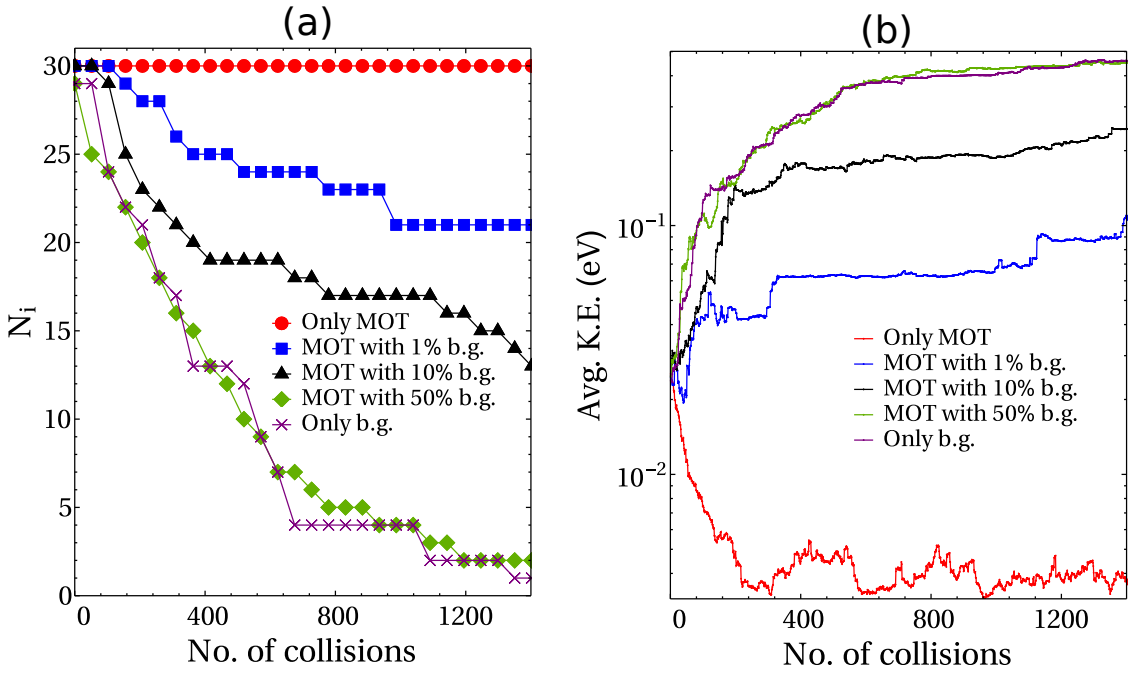

Fig. 3.5 (a) The number of surviving $^{39}K^{+}$ ions in the simulation[1] as a function of the number of collisions each ion experiences. The ions collide with both the background gas of Rb atoms and the ^{85}Rb MOT atoms. (b) The mean kinetic energy of the ions for the simulations in (a). In order to make a comparison with the experiment, we use the potential of the wire trap mentioned in section 2.2 for evaluation of ion trajectories in the ion trap. The ion trap parameters are, $f = 700$ kHz, $V_{\text{outer}} = -5$ V and $V_{\text{inner}} = 85.4$ V.

the competition between the cooling and the heating of the ion for the cases in Fig. 3.5(a), and shows cooling to a steady state temperature when a background vapor of Rb is absent.

From figure 3.6(a), no net change in mean K.E. of $^{85}Rb^{+}$ ions is seen when b.g. alone is considered, consistent with the original theory by Major and Dehmelt [6] for $m_i = m_a$. The addition of the ^{85}Rb MOT, i.e. a localized atomic density at the center of the ion trap, results in a decrease of the mean K.E. suggesting a decrease in the temperature of trapped $^{85}Rb^{+}$ ions. For the case of ^{133} Cs^{+} in ^{85}Rb MOT, a net decrease in the mean K.E. is seen in both cases as shown in Fig. 3.6(b). The case with b.g. is consistent with the original theory by Major and Dehmelt [6] for $m_i > m_a$. The addition of the ^{85}Rb MOT increases the rate at which the mean K.E. decreases, suggesting a faster rate of cooling of the trapped $^{133}Cs^{+}$ ions and a lower final temperature. It is noteworthy that in both cases (a) and (b) above, the simulation also shows that a trapped ion never escapes the ion trap. These simulations support the expectation that an

[1] The Mathematica code for the case "MOT with 10% b.g" is available at https://goo.gl/mzUzvA. The file name is "K39+_Rb85_BG+MOT_0.1_eject.nb". The code for the other cases is the same, except that the parameters are changed.

ion in an ion trap will always be cooled by a localized ensemble of cold gas which is precisely located at the center of the trap for all the mass ratios.

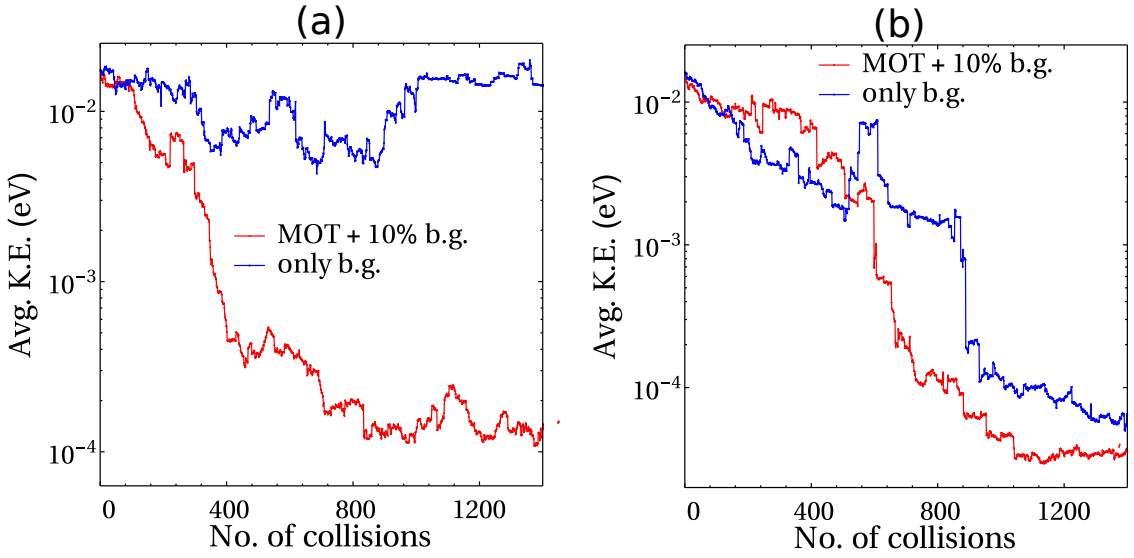

Fig. 3.6 Collisional cooling of ions for different ion-atom mass ratios. (a) The mean kinetic energy of trapped $^{85}Rb^{+}$ ions as a function of the number of collisions with equal mass ^{85}Rb atoms. The blue curve represents the case when collisions with the background gas (b.g.) of Rb alone is considered. The red curve represents the case when collisions with both ^{85}Rb MOT atoms and b.g. are considered. The ion trap parameters used for the $^{85}Rb^{+}$ ion simulations are, $f = 500$ kHz, $V_{\text{outer}} = -5$ V and $V_{\text{inner}} = 80$ V. (b) The mean K.E. of trapped ^{133} Cs^{+} ions as a function of the number of collisions with lighter ^{85}Rb atoms. Again, the blue curve represents the case when collision with the background gas (b.g.) of Rb alone is considered. The red curve represents the case when collisions with both ^{85}Rb MOT atoms and b.g. are considered. The ion trap parameters used for the $^{133}Cs^{+}$ ion simulations are, $f = 500$ kHz, $V_{\text{outer}} = -5$ V and $V_{\text{inner}} = 100$ V.

3.3 Towards efficient cooling of ions

In this section, we present results of simulations done to study the dependence of various parameters on the efficiency of ion cooling by a localized ensemble of atoms having higher mass than the ion. First, we check what happens when we change the size of the atomic cloud, keeping all other parameters constant. As was seen in Fig.3.5(b), the ions attain a steady state mean K.E. when only ^{85}Rb MOT atoms are present. Figure 3.7 shows how the cooling changes if we vary the size of the Gaussian density function of MOT atoms. The mean K.E. of trapped $^{39}K^{+}$ ions as a function of the number of collisions with heavier ^{85}Rb MOT atoms is shown for three different sizes of the ^{85}Rb MOT. Background gas collisions are completely neglected. Beyond a critical MOT size, the point when the spatial extent of the MOT (σ_a) is larger than

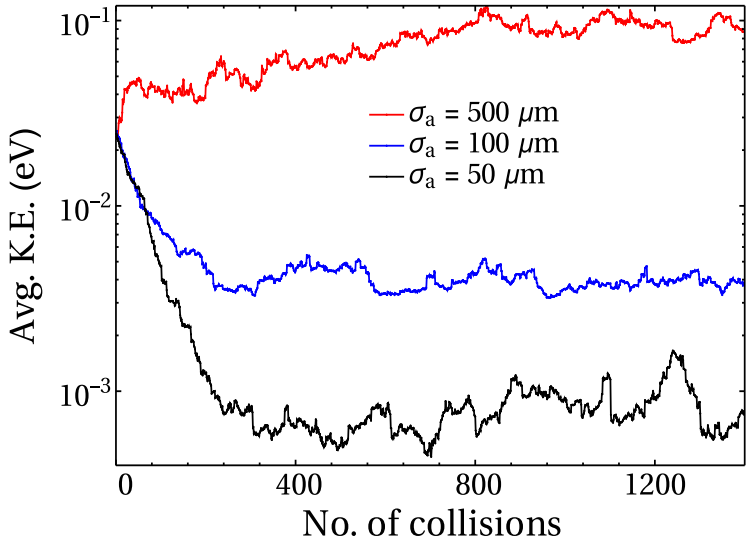

Fig. 3.7 Effect of σ_a of the ^{85}Rb density distribution on the steady state mean K.E. of trapped $^{39}K^+$ ions. The ion trap parameters are same as in Fig. 3.5.

the radius within which the trapped ions are created with speed $v_i \sim 0$, a net increase in the mean K.E. is seen (red curve). This is expected, as now the reservoir of atoms extends beyond the initial trap extent of the ions, and therefore begins to resemble the situation consistent with Major and Dehmelt's theory [6] of ion heating when $m_i < m_a$. Smaller spatial extents of the MOTs (shown as blue and black curves) enable a faster rate of decrease of mean K.E. and result in lower final temperatures[2] of the trapped ions. The steady state temperature (T_s) of the ions is found to be proportional to the σ_a^2 of the MOT Gaussian density function, for given ion trap parameters. Hence reducing the size of the atomic cloud significantly reduces the ion temperature in steady state.

For the case where the mass of the ions is less than the atoms, Major and Dehmelt [6] and other recent work [7–9] have predicted that the ion will always heat up in the presence of a uniform buffer gas of atoms, irrespective of the atom temperature. Our approach with a localized ensemble of atoms tells us that ions will always be cooled irrespective of the mass ratio. However, the steady state value of the ion temperature might change. Hence, we performed simulations for different ion-atom mass ratios (m_r) for the case when only a localized ensemble of atoms is present, and no background gas. Figure 3.8 shows the results the simulations for $^{39}K^+$ ions with m_a varying from 41 to 173. For these simulations, only the mass of the atoms is changed, and all other parameters are kept constant. As expected, the

[2]Whenever we talk about the temperature of the ion, we are referring to the mean K.E of the ion because the energy distribution of the ions is non-thermal and hence temperature cannot be defined in conventional sense. The mean K.E comes closest to the definition of temperature for ions trapped in ion trap.

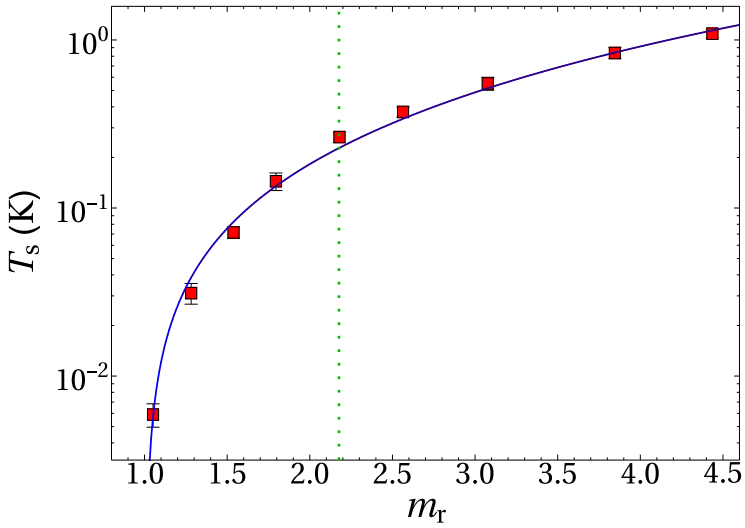

Fig. 3.8 Steady state temperature attained by the $^{39}K^+$ ion with different masses of atoms is shown by the red squares. The blue line is a quadratic fit of the form, $a+bx^2$. The quadratic fit is empirical and is used due to an absence of an analytical theory. Ion trap parameters are same as in Fig. 3.5 except that here we take the ion trap to be ideal corresponding to the equation 2.6 with $d = 10$ mm, in order to get rid of effects due to trap imperfections. The standard deviation of the atomic density Gaussian (σ_a), is 10 μm for all the simulations presented in this figure. The green dotted line indicates the mass ratio for $^{39}K^+$ ions and ^{85}Rb atoms.

steady state temperature is highly dependent on the mass ratio m_r as the cooling rate depends on it.

The s-wave collision threshold for ion-atom collisions scales inversely with the square of the reduced mass, so the ability to cool lighter ions with heavy atoms implies that the s-wave limit of ~ 30 nK for Rb^+ and Rb can now be raised by a factor of ~ 60 to ~ 2 µK for a $^7Li^+$ and ^{87}Rb, which is technically simpler and would usher in the quantum regime for this versatile system. With this goal in mind, we perform simulations for cooling of a $^7Li^+$ ion by a ^{87}Rb MOT. The mass ratio is very high ($m_r = 12.14$), enabling us to see, to what ratio the cooling of lighter ions by the heavier atoms can be stretched. In the simulations, we could attain a steady state temperature of 28 μK for the $^7Li^+$ ion in the presence of ^{87}Rb atoms having a Gaussian density distribution of $\sigma_a = 1$ μm. The size of the atomic cloud chosen can be attained for a cold ensemble of Rb atoms trapped in a dipole trap. The ion trap (Eqn. 2.6) parameters are, $f = 2$ MHz, $V_{rf} = 4.1$ V, $U_0 = 0$ V and $d = 10$ mm. For $^7Li^+$ the RF frequency has to be high as it is a lighter ion compared to K^+ ion. We have kept the RF voltage very small in order to keep the secular frequencies very low ($\omega_x/2\pi = \omega_y/2\pi = 5$ kHz and $\omega_z/2\pi = 10$ kHz). From the Viral theorem [5, 73] the mean kinetic energy is proportional to $\omega_i^2\sigma_i^2$, where ω_i and σ_i are frequency and the standard deviation of the ion position with $i \in (x,y,z)$ respectively. Thus,

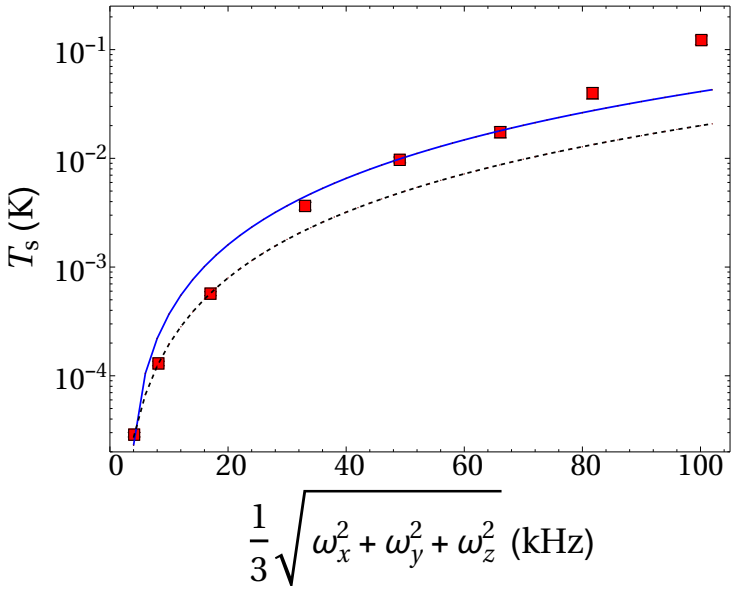

Fig. 3.9 Steady state temperature attained by the $^7Li^+$ ion in the presence of localized ^{85}Rb atoms as a function of the root mean square of the secular frequencies ($\frac{1}{3}\sqrt{\omega_x^2+\omega_y^2+\omega_z^2}$) of the ion trap is shown by the red squares. The blue line is a quadratic fit of the form, $a+bx^2$ to all the data points and black dashed line is the same fit but only to first three data points. The ion trap (Eqn. 2.6) parameters are, $f = 2$ MHz, $d = 10$ mm, $U_0 = 0$ V and a variable V_{rf} in order to change the secular frequency. The MOT size is $\sigma_a = 1$ μm.

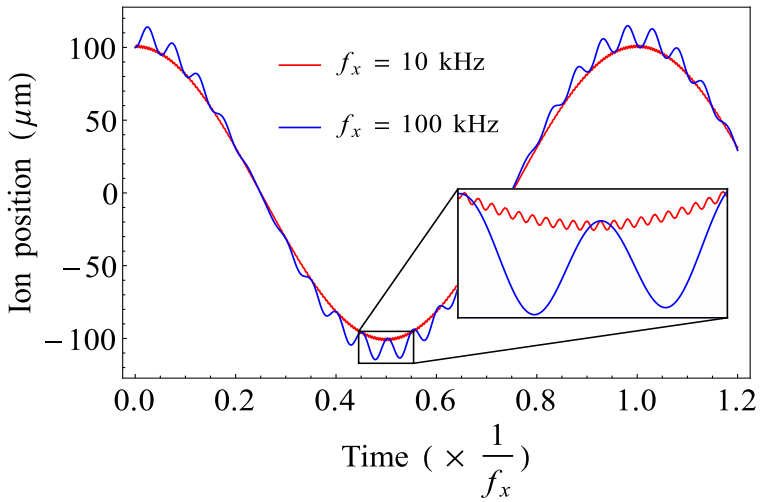

Fig. 3.10 Motion of the $^7Li^+$ ion in ion trap along the x-direction for two different secular frequencies. The x-axis shows time in the units of secular time periods in the x-direction given by $\frac{1}{f_x}$. This figure shows a dependence of the micromotion on the secular frequency.

in order to lower the steady state temperature of the ion, we have to use a very low secular frequency. However, the steady state temperature is not strictly proportional to the square of the secular frequency as can be seen in Fig. 3.9. The proportionality is only maintained till secular frequency ~ 20 kHz. There is a discrepancy because the standard deviation of the ion position also changes when the secular frequency is changed. The increase in standard deviation of the ion position with increase in secular frequency is due to an increase in micromotion amplitude of the ion, as seen in Fig. 3.10. Since the micromotion is responsible for ion heating in the case of lighter ions with respect to the atoms [6, 72, 7–9, 66], the new radius from the center of atomic cloud at which heating and cooling are balanced changes when the micromotion amplitude changes.

From the above observations, an efficient and simple way to cool the ion will be to first place the ion in a stiff trap, with higher ω_i, along with localized ultracold atoms, and then adiabatically reduce the stiffness of the trap (and hence ω_i) to lower the temperature of the ion even further. In the limit $\omega_i \to 0$, the ion will be of the same temperature as the atoms.

3.4 Energy Distribution

The previous sections of this chapter, and related work on collisional cooling of trapped ions with cold atoms by other groups in recent years, have underlined the complexity of the system being studied. The question arises: why is the cooling of a single ion in collisions with atoms invoking so much interest. The simple reason is that the ion is trapped dynamically in a Paul trap, and within this framework the result of a single collision with a cold atom can lead to either heating or cooling of the ion depending on the precise parameters of the collision. It is therefore vital to understand the nature of the cooling process, even at the level of specific trap configuration. Below, we explore the kinetic energy distribution of ions cooled by a localized ensemble of atoms.

Kinetic energy distributions have been used extensively in order to decide whether an ion immersed in a uniform density of cold atoms will cool or heat in recent theoretical and numerical work [7–9]. The complexity mentioned above results in an energy distribution deviating from Maxwell-Boltzmann (MB) distribution and gives an opportunity to study non-MB statistics. In this section, we discuss the K.E distributions obtained from our simulations. The K.E distributions of $^{39}K^{+}$ ion in the presence of a localized ensemble of an atomic gas for various parameters are shown in Fig. 3.11. The procedure to obtain the data points is as follows; Since we are concerned only with the changes in the K.E when a collision between the ion and an atom happens, we track the average of K.E. of the ion between two collisions. This is done for 4000 collisions. One hundred such simulations of 4000 collisions with different

initial conditions are performed and the average K.E. values from these simulations are then binned in order to obtain a probability density. For the binning process, we consider only K.E. values for collisions after attaining a steady state of average K.E where only fluctuations around a mean are seen. To attain such steady state usually less than 1000 collisions are needed.

These distributions are very different from the usual Maxwell-Boltzmann (MB) energy distribution which has a functional form, $C_0\sqrt{E}e^{-\frac{E}{k_BT}}$, where E is energy, T is temperature, k_B is the Boltzmann constant, and C_0 is a scaling parameter. One non-MB distribution which is a generalization of MB distribution, and was predicted in the framework of nonextensive statistical mechanics [74] is a Tsallis distribution having functional form, $C_0\sqrt{E}\left(1+\frac{E}{qk_BT}\right)^{-q}$, where q is a real number. The Tsallis distribution reduces to MB distribution for $q \to \infty$. The mean energy calculated using this distribution diverges for $q < 1$. Hence $q < 1$ is used as a criterion to predict heating of ions in the presence of uniform buffer gas of atoms [7–9]. The mass ratio m_r above which $q < 1$ is called critical mass ratio (CMR). For $m_r >$ CMR, theory and simulations show heating of ion in the presence of uniform buffer gas [7–9]. However, if the atomic gas is localized at the center of the ion trap, cooling of the ion occurs even for $m_r >$ CMR which we have demonstrated using both experiments and simulations. We fit our data to this distribution in order to compare our simulations with the uniform buffer gas simulations. In simulations for the case of a uniform buffer gas, the energy distribution was shown to obey the Tsallis distribution [7–9]. The tail of the Tsallis distributions has the form of a power law (C_0E^{-s}) with $s = q - \frac{1}{2}$ as $\frac{E}{qk_BT} > 1$ for larger values of E compared to the temperature k_BT. For the case of a localized gas, we find that the tail has an exponential decay in addition to the power law, hence we fit to the form $C_0E^{-s}e^{-\frac{E}{\varepsilon_0}}$ where s, C_0 and ε_0 are constants and E is the energy variable. A similar observation was made by Höltkemeier et.al [66, 67] for the case of localized buffer gas. The exponent s tells us how fast the energy distribution is decaying. The higher the value of s, the faster is the decay of energy distribution as we move towards high energy values. The three analytical forms described above are fitted to our distributions from the simulations, results of which are shown in Fig. 3.11.

As can be inferred from Figs. 3.11 (b), (f), (g), and (h), the MB and Tsallis functions start to fit better as the mass ratio starts to become higher, keeping all other parameters constant, but the mean K.E. starts to increase. The fit to a Tsallis function is very good for $m_r = 4.435$, as seen in the Fig. 3.11 (h). The function $E^{-s}e^{-\frac{E}{\varepsilon_0}}$ fits to the tails of all the distributions. As is evident form the Fig. 3.11, the distributions depend not just on atom-ion mass ratio but also on other parameters. An analytical theory which predicts the shape of the distribution will greatly advance this topic. We hope these simulations inspire such a theory in the framework of non-equilibrium statistical mechanics.

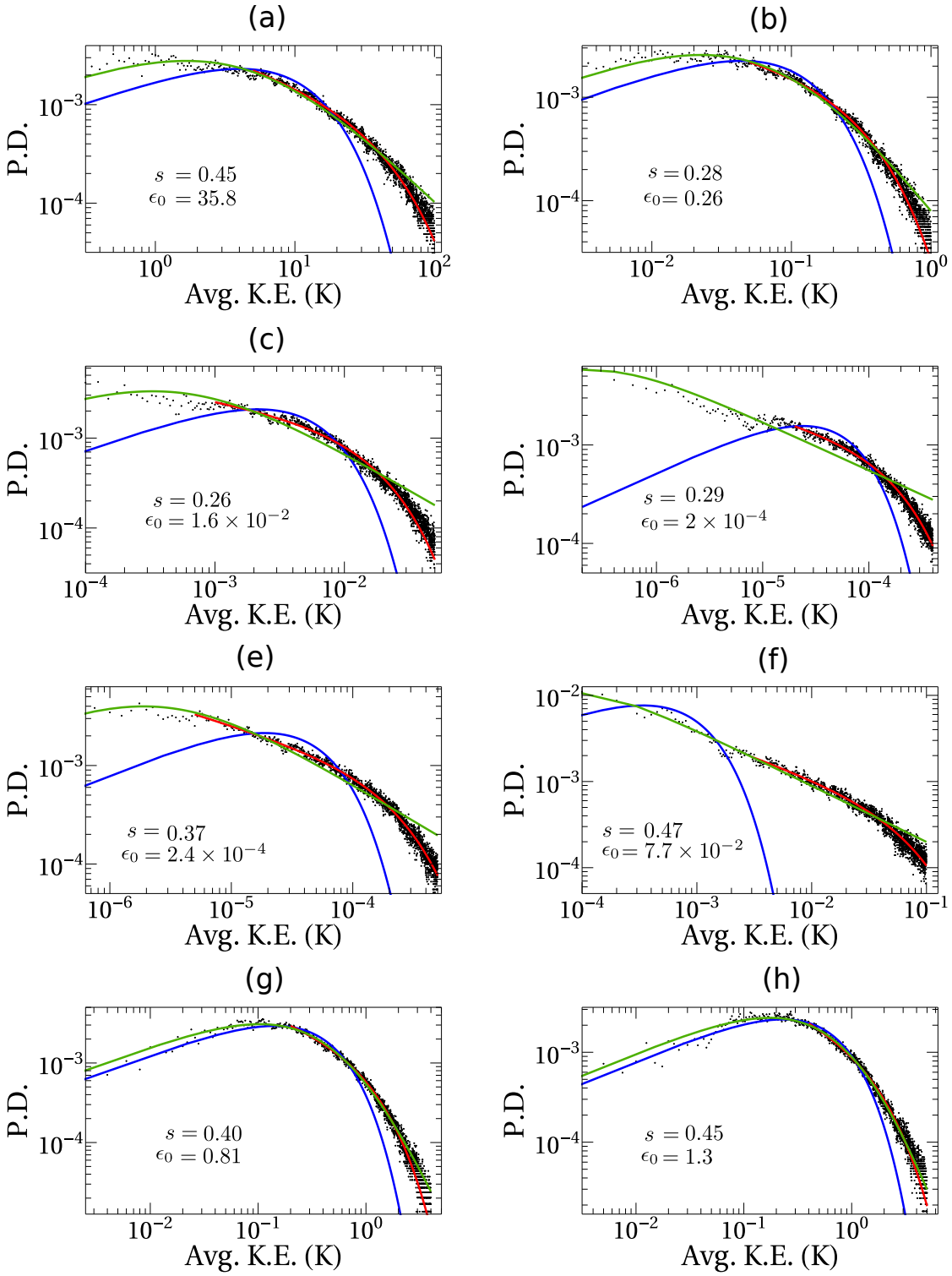

Fig. 3.11 Mean kinetic energy probability distributions of ^{39}K ions trapped in an ideal 3D Paul trap, and in the presence of ultracold atoms. The parameters for the graphs (a)-(h) are given in Table 3.1 below. Black dots show the data from the simulations. The blue curve is a fit to a MB distribution, the green curve is the fit to a Tsallis distribution, and the red curve is a fit to $E^{-s}e^{-\frac{-E}{\epsilon_0}}$. The fitted values of s and ε_0 are mentioned in the graphs. P.D. - Probability Density.

	m_a (u)	$\omega_{x/y}$ (kHz)	ω_z (kHz)	T_a (μK)	σ_a (μm)	$\langle$K.E.$\rangle / k_B$ (mK)
(a)	85	53	107	150	100	26000
(b)	85	53	107	150	10	260
(c)	85	19	38	150	10	15
(d)	85	19	38	500	1	0.18
(e)	85	19	38	10	1	0.18
(f)	60	53	107	150	10	73
(g)	133	53	107	150	10	700
(h)	173	53	107	150	10	1100

Table 3.1 Here, columns 2-6 are for parameters in Fig. 3.11 (a)-(h) and column 7 is mean K.E. in the steady state obtained from the simulations[3]. T_a is the temperature of the atoms.

3.5 Discussion

In this chapter, we presented experiments and simulations for cooling of ions in the presence of higher mass localized atoms. We discussed ways to improve the efficiency of cooling in such a scenario of a heavy ion and light atoms. The cooling is possible in this case because the atoms are localized at the center of the ion trap. Our experiment paves a way towards realizing many possible ion-atom experiments. One such example is cooling of H_2^+ ions using ultracold gas of lithium atoms. Ultracold H_2^+ ions are important for many precision studies [75], and for chemistry at ultracold temperatures. So far, lithium is the lightest atom which can be laser-cooled on a transition with a stable ground state and there is no way to cool H_2^+ ions other than by sympathetic cooling with other precooled species. The mass ratio, in this case, is 3.5 and hence traditional uniform buffer gas techniques will lead to ion heating. We have performed a simulation to study the cooling of H_2^+ by lithium atoms, and the resulting K.E. distribution is shown in the figure 3.12.

In conclusion, the mixing of an ensemble of atoms with ions offers exploration of many interesting phenomenon, some of which we have explored in this chapter. From the studies mentioned in this thesis, we foresee exploration of many physics problems related to statistical physics and physics at ultracold temperatures.

[3]The Mathematica code for the case "(h)" is available at https://goo.gl/mzUzvA. The file name is "K39+_Yt173_onlyMOT0.01mm.nb" for the Monte-Carlo simulation and "K39+_Yt173_onlyMOT0.01mm_KE_dist" for the code which extracts the average K.E. distribution from the simulation data.

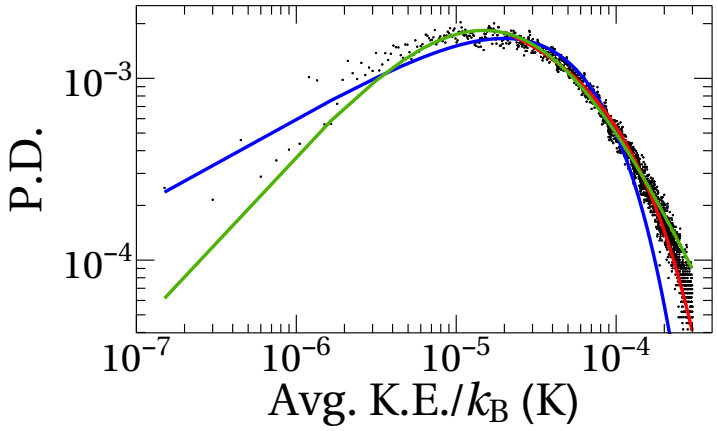

Fig. 3.12 Mean kinetic energy probability distributions of H_2^+ ions in the presence of ultracold ^7Li atoms. The parameters are, $\omega_{x/y} = 34$ kHz, $\omega_z = 68$ kHz, $T_a = 10\ \mu$K, $\sigma_a = 1\ \mu$m, $f = 6$ MHz. Black dots show the data from the simulations. The blue curve is a fit to MB distribution, the green curve is the fit to Tsallis distribution, and the red curve is a fit to $E^{-s}e^{-\frac{E}{\epsilon_0}}$. P.D. - Probability Density. The mean K.E., in this case, is 87 μK.

Chapter 4

Control of resonant light transmission for an atom-cavity system

A resonantly coupled atom-cavity system can be utilized to explore various possibilities, ranging from linear and nonlinear physics [12, 76–78], single photon-atom-cavity systems [33, 79] all the way to multiple atoms [80, 81, 38] in a cavity supported mode. In this chapter, we present a theoretical model to study interactions between multilevel atoms and cavity. This model will be later used to explore the manipulation of the intracavity light mode for an atom-cavity system, where the light is resonant or near resonant with a dipole transition of the atoms contained within the mode volume.

The analysis here is inspired by the optical control experiments described in detail in Sharma et. al. [12], which are performed at room temperature with a cell of atomic vapor in a standing wave cavity. For the control of cavity light using another light beam via multi-level atoms, the phenomenon of optical bistability was exploited in this experiment. Significant work has been done on optical bistability in two-level [76] and three-level systems [82]. Many features (but not all) observed in above studies are explained using the numerical results of Harshawardhan and Agarwal [83]. However, there were significant points of interest experimentally which required theoretical understanding and which resulted in the work discussed in this chapter. Earlier related experimental [76, 82, 84] and theoretical/numerical [83, 85] work is almost exclusively in ring cavity systems. In our work, we perform theoretical calculations for atoms in the Fabry-Pérot cavity. While the ring and standing wave cavity-atom systems have a close equivalence, the extension of such vapor cell experiments to those with cold atoms requires the stationary wave cavity due to the unbalanced light forces in a conventional ring cavity arrangement.

Another major feature of this work is optical control of the intracavity intensity when the atoms are stationary within the cavity mode, that is a *closed system* for the atoms and for an

open system of atoms, where the cavity mode atoms are exchanged with a reservoir of thermal atoms. In a thermal reservoir, the energy levels of atoms without any external light field has a thermal distribution. The two cases mentioned above lead to different behavior, in particular, the timescales for switching are different for the two cases.

4.1 Summary of the vapor cell experiment

In this section, we will give a summary of portions of the vapor cell experiment which are relevant to the calculations mentioned in this chapter. This experiment is described in detail in an article by Sharma et. al. [12]. A schematic of the experimental setup is shown in figure 4.1 (a) and the atomic energy level diagram is shown in figure 4.1 (b). The experiment is performed with a vapor cell of rubidium atoms at room temperature. A symmetric sub-confocal Fabry-Pérot (FP) cavity is constructed around a cylindrical spectroscopy cell that is 75 mm in length and 25 mm in diameter, containing an isotopically enriched sample of ^{87}Rb. The cavity mirrors have a radius of curvature of 250 mm and are separated by $\approx$ 80 mm. The measured finesse $\mathscr{F}$ of the cavity for light on atomic resonance is $\mathscr{F} \approx 100$. An annular piezoelectric transducer

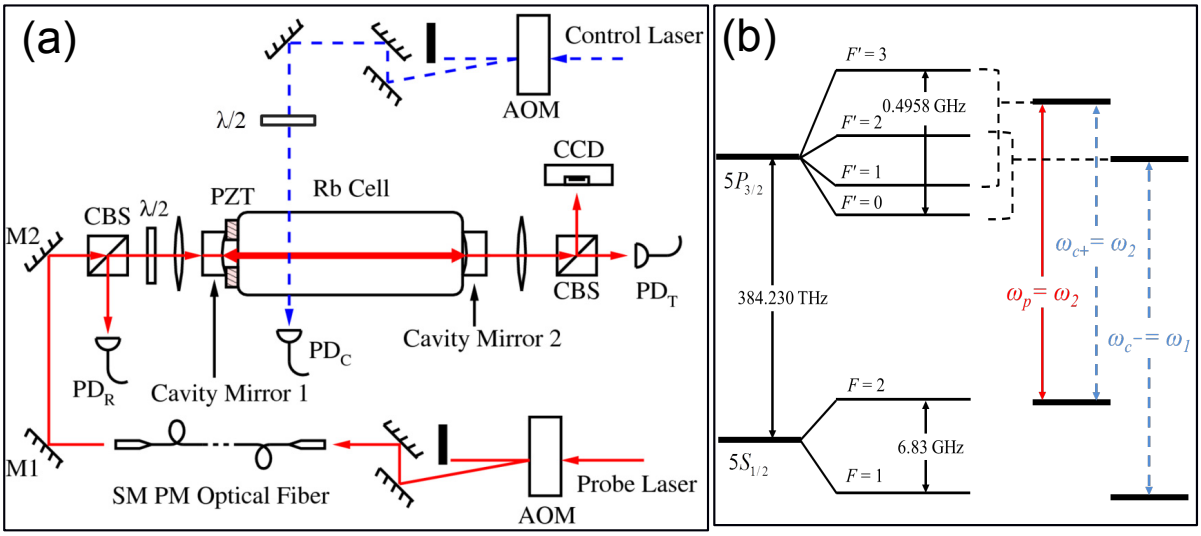

Fig. 4.1 (a) Schematic of the experimental setup for the vapor cell experiment. The FP cavity with the ^{87}Rb cell is shown. The probe beam (solid line) is coupled to the cavity, and the transmission and reflection ports are monitored using the photodiodes PD$_T$ and PD$_R$, respectively. The spatial profile of the transmitted mode is captured using a CCD camera. The control beam (dashed line) intersects the cavity mode over a small spatial region and is monitored using PD$_C$. Switching and intensity modulation of the two beams are done using the AOMs as shown. (b) Energy level diagram of ^{87}Rb atoms present in the vapor cell.

(PZT) is attached to one mirror of the cavity which can be used to change the resonance frequency of the cavity.

At room temperature, the excited state manifold of ^{87}Rb is unresolved due to Doppler broadening. This results in observation of two absorption features, separated by 6.8 GHz corresponding to the frequency difference between the two ground states F = 1 and F = 2. Let us identify ω_1 and ω_2 as the frequencies corresponding to the Doppler absorption maxima of the F = 1 $\leftrightarrow$ F' and F = 2 $\leftrightarrow$ F' manifolds, respectively. The laser beam coupled into the cavity mode is the probe laser beam, with frequency $\omega_p \leftrightarrow \omega_2$ and intensity I_p. The laser beam intersecting the probe laser beam in the cavity mode is the control laser beam, with frequency ω_c (either ω_1 or ω_2) and intensity I_c. The pump and probe beams are both derived from independent lasers, and both lasers are temperature stabilized and have a linewidth of ≈ 2 MHz. Neither laser is actively frequency stabilized. The overall stability of the experiment is sufficient to execute many experimental cycles without significant drift in the laser or cavity parameters. The cavity-mode waist is $\approx 150\ \mu$m. The diameter of the control laser beam is $\leq$ 1 mm and so its intersection with the mode is localized. The intensities of both laser beams can be controlled using acousto-optical modulators (AOMs). The control laser beam intersects the probe beam in the cavity mode with a small volume of intersection.

4.1.1 Bistability and switching

On atomic resonance, the probe light transmitted through the cavity exhibits bistable behavior with respect to the input light intensity. This is observed over the entire Doppler broadened resonance, when the cavity length is adjusted to support transmission. The input probe intensity into the cavity is ramped from low to high (up cycle) and back from high to low (down cycle) by using the AOM in the path. The evolution of the cavity transmitted power (PD_T) as a function of the incident probe power (PD_I) exhibits bistable behavior, as shown in figure 4.2. The lack of active stabilization of the cavity length as well as the laser frequency leads to some scatter in the cavity input-output traces. To overcome this, a seven-point moving average is implemented on the data to obtain the traces presented in figure 4.2. This results in the blunting of the sharp threshold features, but nevertheless illustrates the sharp onset of transmission. In the up cycle, the transmission intensity shows a relatively small linear increase for input light intensity $I < I_{t;u}$. At $I_{t;u}$ a small change in input intensity results in a sharp increase of intracavity light build-up and the cavity consequently transmits light, exhibiting the characteristics of the threshold behavior. Beyond this point, the transmitted light intensity grows linearly with the input intensity, with significantly larger slope than the response below the threshold. In the down cycle, as the input intensity is gradually reduced, the above-threshold linear regime

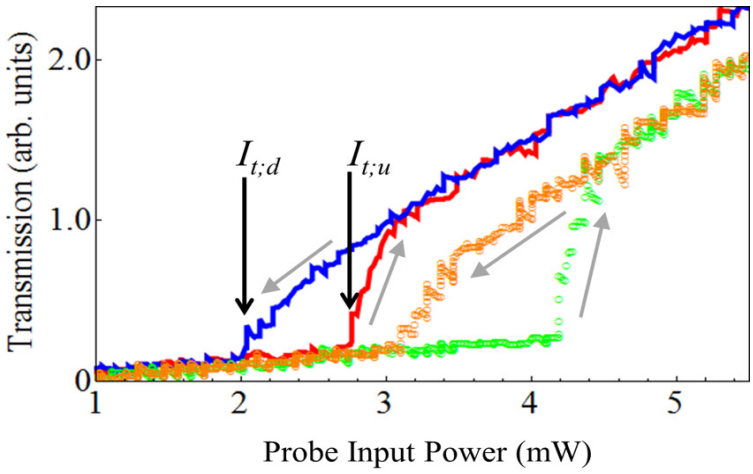

Fig. 4.2 Transmitted light through the cavity, at ω_2, as a function of input light power for up and down cycles. The arrows shows the directions of the input intensity scan. The cavity transmission with increasing input power is the solid red line, while the solid blue line gives the transmission as a function of falling input power, in the absence of the control beam. When the control beam is tuned to ω_1, the hysteresis feature shifts to higher input powers. In the presence of the control light with a power of 10 mW, the new increasing power response is represented by the green circles, while the orange circles give the falling input-power response. The shift in the cavity response, in the presence of the control light, results in the control of the intracavity light intensity.

persists well below $I_{t;u}$, until $I_{t;d}$, below which the transmitted intensity follows the behavior of $I < I_{t;u}$. The intensity build-up in the cavity exhibits hysteresis in the range $I_{t;d} < I < I_{t;u}$.

With the cavity-mode light frequency ω_p on atomic resonance, the addition of another beam of light on atomic resonance, which intersects the cavity mode, can alter the intracavity-mode intensity. Specifically, for $\omega_p = \omega_2$, when $\omega_c = \omega_2$, the same atomic transition, the hysteresis behavior shifts to lower input light power. On the other hand, when $\omega_c = \omega_1$, the hysteresis behavior shifts to higher input probe light power, as shown in figure 4.2. A weak beam of the control laser with frequency $\omega_c = \omega_1$ is sufficient to extinguish the transmission of ω_p completely. Thus the presence of control light inhibits the transmission for any input light intensity that is below the new threshold. For input light intensity above the threshold, the control light causes partial attenuation. The intensity of the control beam determines the degree of attenuation in the range of input intensities of ω_p over which the hysteresis response is seen. The suppression of the cavity transmission of the probe beam by the control beam can be used to fabricate an all-optical negative-logic switch. The intensities of the probe and control beams are chosen so that cavity-mode extinction is seen. The control beam is turned on and off through the control AOM and the cavity output is monitored. When the control is on, the probe transmission is dramatically reduced. The transmission goes back to the initial level

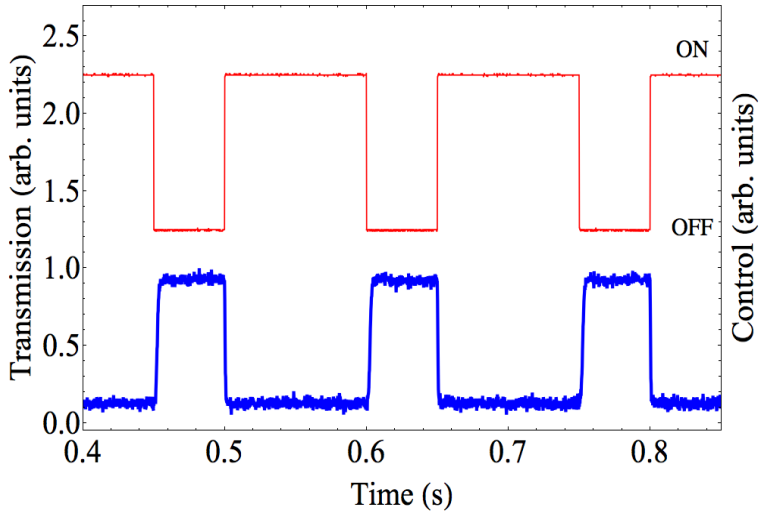

Fig. 4.3 Time trace recording three cycles of switching. The upper trace shows the temporal profile of the control laser and the bottom trace shows the temporal profile of the cavity transmission. The transmission is high when $I_c = 0$ and low when $I_c > I_{c;s}$. For this set of probe and control frequencies, the switch operates in negative logic.

when the control beam is turned off. This results in the optical switching of the probe light by the application of the control beam as shown in figure 4.3. The opposite case of cavity mode enhancement when the control beam has same frequency as the probe beam ($\omega_p = \omega_c = \omega_2$) can be used to fabricate an all-optical positive-logic switch.

The atomic fluorescence from the cavity mode and the intersecting control beam was also monitored during the switching. In the negative-logic partial switching case, we observe enhanced fluorescence in the intersection volume, as shown in figures 4.4(a) and 4.4(c), when the cavity transmission is attenuated. The increased fluorescence is due to the pulling away of the atom-light system from saturation by ω_1 in the region of overlap, resulting in increased absorption of cavity-mode light locally. For the reverse case of positive logic switching, the fluorescence in the intersection volume of the probe and control beams decreases, as shown in figures 4.4(b) and 4.4(c), when the cavity transmission is enhanced. The decreased fluorescence, in this case, is due to the saturating effect of the control beam on the atomic transition which is in resonance with the cavity mode. This results in decreased absorption of cavity-mode light locally.

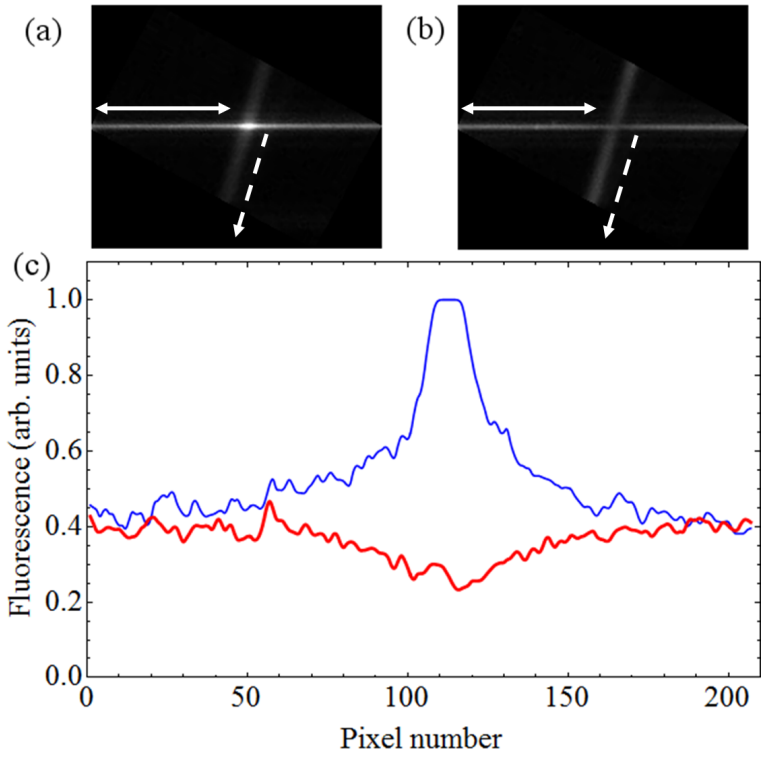

Fig. 4.4 (a) and (b) Image of the intersection region of the cavity mode with the control beam (200 pixels $\approx$ 25 mm). The bold two-headed arrow marks the direction of the cavity mode and the dashed single-headed arrow the control beam. The system is in the partial attenuation regime for this experiment. Illustrated are (a) increased light scattering accompanying probe attenuation, i.e., the two beams on complementary transitions, and (b) decreased light scattering accompanying probe enhancement, i.e., the two beams on the same transition. Also illustrated is (c) the fluorescence intensity in arbitrary units along the cavity mode, from which it is clear that the scattering from the intersection volume is enhanced for the negative-logic configuration (thin blue line) and reduced for the positive-logic case (thick red line).

4.1.2 Transient behavior

The transient behavior of the switching action described above is measured by tuning the probe intensity so that it is switched with high fidelity by the smallest control beam power. Once again ω_p and ω_c are tuned to ω_2 and ω_1, respectively. For the negative-logic switching, the transmission as the control beam is switched off and on is shown in figure 4.5. The transient behavior is not fit well by a single exponential. It was found that a double-exponential function fits the rise and fall behavior well and adding additional fit parameters does not improve the quality of the fit. The fast time constants are $\approx$ 25 μs and the slow time constants are $\approx$ 500 μs. The switching time of the control light AOM is less than 100 ns and therefore does not limit our measurement. The reasons for the complex temporal response will be addressed in

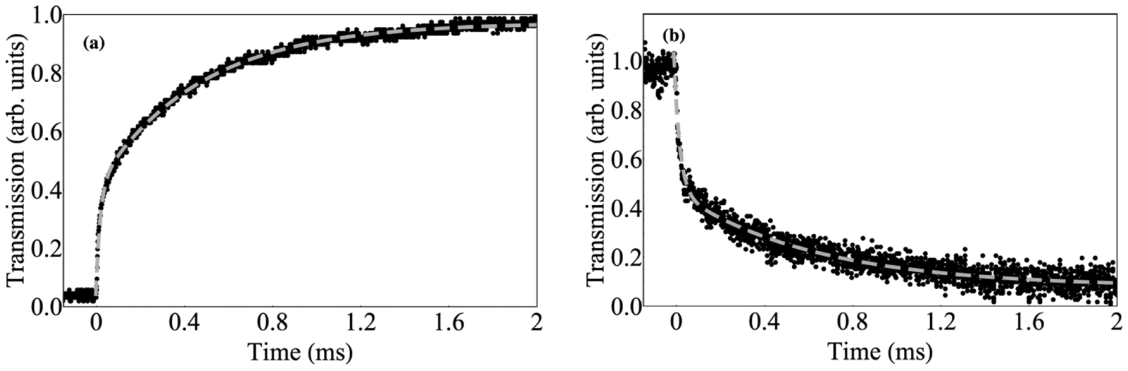

Fig. 4.5 Transient (a) rise and (b) fall response of the cavity output probe light for the negative-logic switching.

subsection 4.3.2 where we will discuss the theory of these phenomena. Complementary to the extinction of light in the cavity mode described above, the light in the cavity mode can be enhanced by a transverse beam, demonstrating the switching of cavity mode in the positive logic. As mentioned in subsection 4.1.1, to do this, the probe and control beams are adjusted to be on the same atomic resonance $\omega_p = \omega_c = \omega_2$, while the experimental arrangement remains the same. Here too the observed time scales are $\approx 500\ \mu$s as shown in figure 4.6.

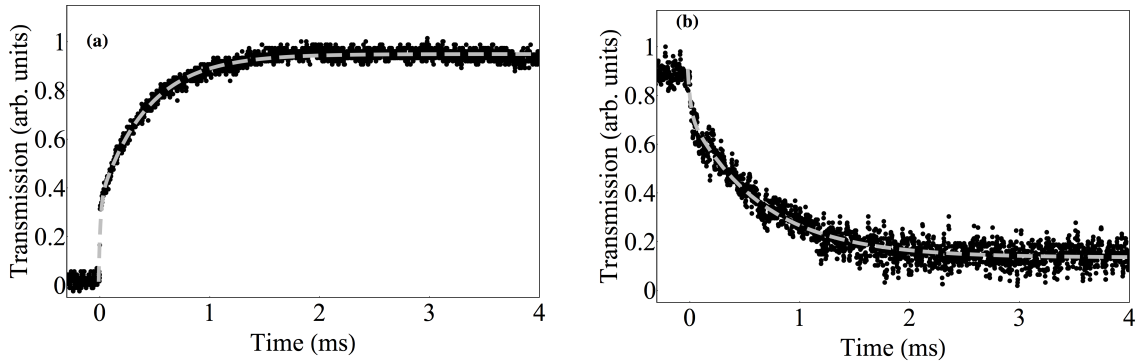

Fig. 4.6 Transient (a) rise and (b) fall response of the cavity output probe light for positive logic switching.

Additionally, figure 4.7 shows the on- and off-resonance build-up and decay of the probe light in the cavity without the control laser which can be used for comparison with the switching times mentioned above. The measurements show that the decay of the light in the cavity mode is rapid ($\approx 1\ \mu$s) both on- and off-resonance. In all cases, the decay rates measured are limited by the response time of the photodiode used. For the rise times, the off-resonance build-up of power in the cavity mode is rapid (measurement limited by the photodiode response time), whereas the on-resonance build-up time constant is $\approx 60\ \mu$s for $\omega_p = \omega_1$ and $\approx 180\ \mu$s for

$\omega_p = \omega_2$. The large on-resonance rise time of the transmitted light and hence the intracavity intensity build-up rate can be directly related to the photon loss from the cavity mode due to resonant scattering of photons by the atoms. It was observed that the time constants for the establishment of the steady-state circulating intensity, and therefore steady transmission, are in the ratio of the transition strengths of the respective ^{87}Rb atomic resonances.

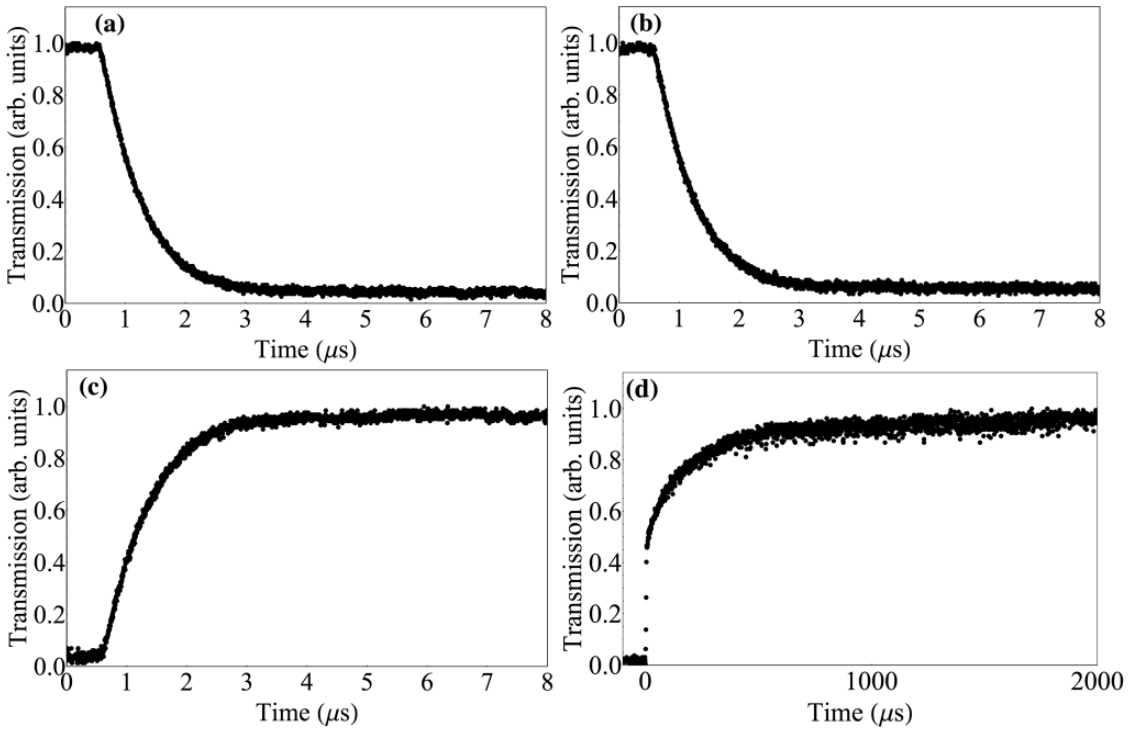

Fig. 4.7 Measured decay and rise of the cavity transmission for the probe, on- and off-resonance. The decay of the steady-state intensity is measured in transmission for (a) the off-resonance case and (b) the on-resonance case. In both cases, the fall time has sub-microsecond time constants. Also shown is the rise in the transmitted intensity (c) off-resonance and (d) on-resonance. Here the rise time constant for the off-resonance case is sub-microsecond, whereas for the on-resonance case it is significantly larger.

The above experimental results needed explanation. In general, it was quite clear that there was a change in level populations when the light fields interacted with the atoms. However, the two time constants for the switching and the fact that the switching times are long was a puzzle. In order to attempt an explanation of all the observed phenomenon, the system was analyzed theoretically. Below we present the result of the analysis.

4.2 2-level atoms interacting with a cavity

Before moving to more complicated calculations, let us consider a simple case of two-level atoms interacting with the cavity. The Hamiltonian for a system of N two-level atoms interacting with a cavity which is probed by a classical probe laser can be written as [55, 86, 87],

$$\hat{H} = \hbar\omega_{\rm cv}\,\hat{a}^\dagger\hat{a} + \hbar\left\{\eta^*\hat{a}e^{-i\omega_{\rm p}t} + \eta\hat{a}^\dagger e^{i\omega_{\rm p}t}\right\} + \sum_{j=1}^{N}\hbar\left\{\frac{\omega_{\rm a}}{2}\hat{\sigma}_j^z + g_j\left(\hat{a}^\dagger\hat{\sigma}_j^- + \hat{a}\hat{\sigma}_j^+\right)\right\},$$

where $\hat{a}$ and $\hat{a}^\dagger$ are photon annihilation and creation operators for the cavity field with commutation relation $[\hat{a},\hat{a}^\dagger]=1$. σ_j^-, σ_j^+, σ_j^z are usual spin-$\frac{1}{2}$ Pauli operators for the $j^{\rm th}$ atom with commutation relations $[\sigma_j^+,\sigma_j^-]=\sigma_j^z$ and $[\sigma_j^z,\sigma_j^\pm]=\pm\sigma_j^\pm$. $g_j = g_0 f'(x_j,y_j,z_j)$ is coupling of $j^{\rm th}$ atom with the cavity mode with $g_0=-\mu\sqrt{\omega_{\rm cv}/(2\hbar\varepsilon_0 V)}$ as the maximum atom-cavity coupling, $f'(x,y,z)=\sqrt{V}f(\vec{r})=e^{-(x^2+y^2)/w_0^2}\cos[kz]$ is mode function of the cavity field derived in section 2.3, $V=\pi w_0^2 L_{\rm c}/4$ is the mode volume of the cavity, $L_{\rm c}$ is cavity length, μ is the transition dipole matrix element between excited and ground state, η is the rate at which classical light is injected into the cavity from the incident probe light. $\omega_{\rm cv}$, $\omega_{\rm a}$, $\omega_{\rm p}$ are frequencies of the cavity (resonance frequency of the cavity when it is empty), atom, and cavity probe respectively and * denotes complex conjugate. The evolution equation for the expectation value for an operator $\hat{X}$ can be evaluated using the Heisenberg equation,

$$\frac{d\langle\hat{X}\rangle}{dt} = \frac{i}{\hbar}\langle[\hat{H},\hat{X}]\rangle, \tag{4.1}$$

where, $[\hat{H},\hat{X}]$ is the commutator of $\hat{X}$ with the Hamiltonian, $\hat{H}$. For the atom-cavity system defined above the evolution equations for the atomic states and the cavity field, after including spontaneous emission rates and cavity loss terms phenomenologically, and assuming the cavity field to be classical denoted by a coherent state $|\alpha\rangle$ result in the set of coupled differential equations [86, 87],

$$\frac{d\langle\hat{a}\rangle}{dt} = -\kappa_{\rm t}\langle\hat{a}\rangle - i\omega_{\rm cv}\langle\hat{a}\rangle - i\sum_{j=1}^{N} g_j\left\langle\hat{\sigma}_j^-\right\rangle - \eta e^{-i\omega_{\rm p}t} \tag{4.2a}$$

$$\frac{d\left\langle\hat{\sigma}_j^-\right\rangle}{dt} = -\left\{\frac{\Gamma}{2} + i\omega_{\rm a}\right\}\left\langle\hat{\sigma}_j^-\right\rangle + ig_j\langle\hat{a}\rangle\left(2\left\langle\hat{\sigma}_{{\rm e},j}\right\rangle - 1\right) \tag{4.2b}$$

$$\frac{d\left\langle\hat{\sigma}_{{\rm e},j}\right\rangle}{dt} = -\Gamma\rho_{{\rm e},j} + i\left\{g_j\langle\hat{a}\rangle^*\left\langle\hat{\sigma}_j^-\right\rangle - g_j\langle\hat{a}\rangle\left\langle\hat{\sigma}_j^-\right\rangle^*\right\}. \tag{4.2c}$$

Here, Γ is the spontaneous emission decay rate from the excited state and we have used the equation $\langle\hat{\sigma}_{e,j}\rangle + \langle\hat{\sigma}_{g,j}\rangle = 1$ to eliminate the ground state population variable. The origin of cavity decay rate κ and cavity driving η is described in the section 2.3 of chapter 2. Transforming the above equations into rotating frame such that $\rho_j = \left\langle\hat{\sigma}_j^-\right\rangle e^{i\omega_p t}$ and $\alpha = \langle\hat{a}\rangle e^{i\omega_p t}$ to get rid of fast oscillations, we get,

$$\frac{d\alpha(t)}{dt} = -\left(\kappa_t - i\Delta_{pc}\right)\alpha(t) - i\sum_{j=1}^{N} g_j\rho_j(t) - \eta \tag{4.3a}$$

$$\frac{d\rho_j(t)}{dt} = -\left\{\frac{\Gamma}{2} - i\Delta_{pa}\right\}\rho_j(t) + ig_j\alpha(t)(2\rho_{e,j}(t) - 1) \tag{4.3b}$$

$$\frac{d\rho_{e,j}(t)}{dt} = -\Gamma\rho_{e,j}(t) + i\left\{g_j\alpha^*(t)\rho_j(t) - g_j\alpha(t)\rho_j^*(t)\right\}, \tag{4.3c}$$

where ρ_j is the coherence between excited and ground state, and $\rho_{e,j} = \langle\hat{\sigma}_{e,j}\rangle$ is the excited state population of the j^{th} atom. Here $\Delta_{pa} = \omega_p - \omega_a$ and $\Delta_{pc} = \omega_p - \omega_{cv}$ are detuning of probe light from atomic transition and cavity resonance respectively. Let's assume that the cavity field is so weak that the atoms remain mostly in ground state, i.e. $\rho_{e,j}(t) \approx 0$. For this case the Eqns. 4.3 in steady state become,

$$-\left(\kappa_t - i\Delta_{pc}\right)\alpha - i\sum_{j=1}^{N} g_j\rho_j - \eta = 0 \tag{4.4a}$$

$$-\left\{\frac{\Gamma}{2} - i\Delta_{pa}\right\}\rho_j - ig_j\alpha = 0. \tag{4.4b}$$

For such a case the cavity field is,

$$\alpha = \frac{-\eta\left\{\frac{\Gamma}{2} - i\Delta_{pa}\right\}}{\left\{\kappa_t - i\Delta_{pc}\right\}\left\{\frac{\Gamma}{2} - i\Delta_{pa}\right\} + g_t^2}. \tag{4.5}$$

For the case $\omega_{cv} = \omega_a$, the intracavity average photon number is,

$$|\alpha|^2 = \frac{|\eta|^2\left(\frac{\Gamma^2}{4} + \Delta_{pa}^2\right)}{\left(\frac{\kappa_t\Gamma}{2} - \Delta_{pa}^2 + g_t^2\right)^2 + \left(\kappa_t + \frac{\Gamma}{2}\right)^2\Delta_{pa}^2}. \tag{4.6}$$

Where, $g_t = \sqrt{\sum_{j=1}^{N} g_j^2}$ is total g for all the atoms. In all the experiments discussed in this thesis, the atoms are not stationary and hence do not have a constant coupling strength, but on average the total coupling strength should not change if the atom number is conserved during the experiment. Hence the more practical exercise will be to take the average of all g_j^2. This

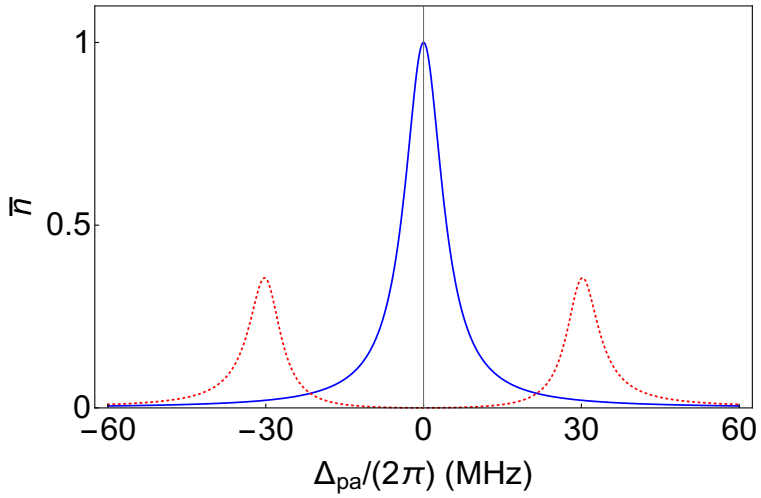

Fig. 4.8 Blue curve and red dotted curve are average intracavity photon numbers without atoms and with atoms (using Eqn. 4.6) present in the cavity respectively. The parameters used here are, $\eta = \kappa_t = 5$ MHz, $\Gamma = 6.06$ MHz, $g_0\sqrt{N_c} = 30$ MHz.

can be achieved by multiplication of g_j^2 at a particular location with the probability of atom to be at that position (proportional to the atomic density at that position) and integrating over whole space, i.e. $\int g_0^2 |f'(x,y,z)|^2 p(x,y,z)\, dx\, dy\, dz$. This integral is same for all the atoms hence summing over all the atoms gives $g_t^2 = g_0^2 N_c$, where

$$N_c = N \int |f'(x,y,z)|^2 p(x,y,z)\, dx\, dy\, dz = \int |f'(x,y,z)|^2 n(x,y,z)\, dx\, dy\, dz \tag{4.7}$$

is an average number of atoms coupled to the cavity. The integral $\int |f'(x,y,z)|^2 n(x,y,z)\, dx\, dy\, dz$ is the overlap integral between cavity mode and atomic density distribution, $n(x,y,z)$. Eqn. (4.6) gives splitting in cavity transmission peak called vacuum Rabi splitting (VRS)/normal mode splitting as shown in figure 4.8. The splitting between two peaks is equal to $2g_t = 2g_0\sqrt{N_c}$. In the framework of quantum mechanics, the splitting is equal to the energy difference between newly formed collective eigenstate of the cavity field and atoms if we restrict to only one excitation in the whole system [88].

The same splitting can also be obtained by coupling N_c stationary atoms with cavity all of which have coupling strength g_0. In such a scenario the coupled differential equations become

very simplified. For example Eqn. 4.3 becomes,

$$\frac{d\alpha(t)}{dt} = -\left(\kappa_t - i\Delta_{pc}\right)\alpha(t) - ig_0 N_c \rho(t) - \eta \tag{4.8a}$$

$$\frac{d\rho(t)}{dt} = -\left\{\frac{\Gamma}{2} - i\Delta_{pa}\right\}\rho(t) + ig_0\alpha(t)(2\rho_e(t) - 1) \tag{4.8b}$$

$$\frac{d\rho_e(t)}{dt} = -\Gamma\rho_e(t) + i\{g_0\alpha^*(t)\rho(t) - g_0\alpha(t)\rho^*(t)\} \tag{4.8c}$$

In this case, we only have to keep track of atomic variables for a single atom because all atoms are identical and the effect of N_c atoms on cavity light is just N_c multiplied by effect due to a single atom. For a large number of atoms with constant density distribution, such an approach of averaging is beneficial for easy computations and conceptual understanding of physics discussed in this chapter. Hence to qualitatively understand the physics, we will follow this approach in the next sections.

4.3 Multilevel atoms in Fabry-Pérot cavity

In this section, we present the model for the system of multi level atoms placed inside a Fabry-Pérot cavity and determine the conditions for optical bistability. The model solves for both, steady state and transient evolution of this system. A four-level atomic system is considered initially, and three- and two- level systems are discussed subsequently. The connection to experiments is made in the later sections by considering the various atomic subsystems for the ^{87}Rb atom, and the model provides a phenomenological interpretation of experimental results summarized in section 4.1. The application of this model to laser cooled atoms [38] or ions [89] coupled to a cavity is addressed. Further, the flow of atoms in and out of the cavity mode is included, so that the transient behavior of the atom-cavity systems can be captured. Comparisons with the experiment are made, and the model successfully replicates the observed transients shown in figures 4.6 and 4.5 of the experiment discussed in section 4.1 and prepares a platform for a variety of experiments.

Consider a cavity which encloses a thermal vapor of atoms. In the model here, we assume that the atomic reservoir is significantly larger than the cavity mode volume. This allows the study of the atom-cavity system in two cases. (a) The closed system, where the atoms contained in the cavity mode are assumed to be stationary, and so the same atoms are always coupled to the cavity. (b) The open system, where the atoms enter and exit the cavity mode volume, with the constraint that the effective number of atoms within the cavity mode is constant. Initially, the calculations are setup for stationary atoms, and the exchange of atoms is incorporated later.

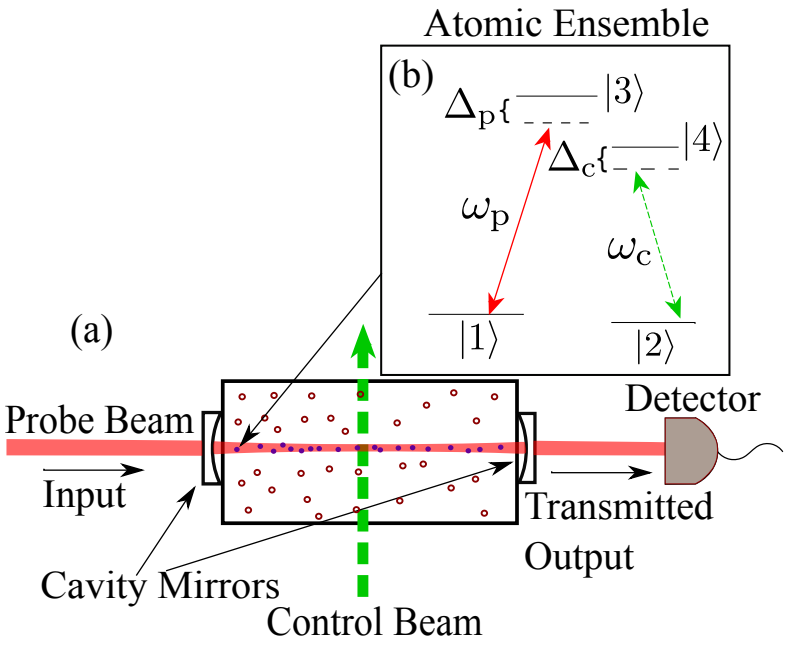

Fig. 4.9 (a) Schematic diagram of the system. The atoms are enclosed in a cell, located within the Fabry-Pérot cavity. The filled circles represent atoms overlapped with the mode, and the empty circles represent the background atom vapor. The incident probe beam, on cavity resonance, is transmitted through the cavity. A transverse control beam (dashed) intersects the cavity mode volume. On atomic resonance, cavity mode light intensity is affected by the presence of the control light beam, which affects the light transmitted through the cavity. The inset (b) shows the atomic level scheme. The probe laser beam is near resonant with transition $|1\rangle \leftrightarrow |3\rangle$ with frequency ω_p and detuning Δ_p, and the control laser beam is near resonant with $|2\rangle \leftrightarrow |4\rangle$ having frequency ω_c and detuning Δ_c.

The schematic conceptualization of the system is illustrated in figure 4.9(a). For specificity, we consider a medium made up of atoms having two ground states $|1\rangle$ and $|2\rangle$. States $|1\rangle$ and $|2\rangle$ are non-degenerate, and cannot decay by any radiative or other processes from one to another. The only process by which the ground state populations of the stationary atoms change is via optical transitions, with the excited states. The two ground states are energetically close to each other when compared to first excited state, such that at room temperature the population is split equally between the two ground states. The excited atomic states are $|3\rangle$ and $|4\rangle$, which are non-degenerate. Dipole allowed transitions are possible between both the excited states and the ground states, and so an excited atom can spontaneously emit a photon and populate either one of these ground states.

As discussed in the previous section, we are concerned with the average effect of many atoms interacting with the cavity mode and therefore consider the effective number of atoms (N_c) coupled to the cavity, to understand phenomenon qualitatively. While the thermal motion

of the atoms also affects the atom-cavity coupling, we assume that on the time scale of the experiment, the average atomic density and velocity distributions do not change. This is the rationale for the coupling of the effective number of atoms with a single atom-cavity coupling constant g_0.

Below we consider mechanisms which transfer the populations from one ground state to another, in the presence of the externally applied light fields, for various atomic level subsystems.

4.3.1 Closed system of atoms

Four level atoms

For the four-level stationary atoms, as shown in figure 4.9 we have an ensemble of atoms placed within the cavity mode. The cavity mode beam (probe beam) with frequency ω_p, is tuned to the $|1\rangle \leftrightarrow |3\rangle$ resonance. The control beam with frequency ω_c is orthogonal to the cavity axis and is tuned to the $|2\rangle \leftrightarrow |4\rangle$ resonance. Identifying the operator $\hat{\sigma}_{ij} \equiv |i\rangle\langle j|$, we can write the Hamiltonian for the four-level atoms with eigenstates $|2\rangle$, $|1\rangle$, $|3\rangle$ and $|4\rangle$ and eigenenergies $\hbar\omega_2 = 0$, $\hbar\omega_1$, $\hbar\omega_3$ and $\hbar\omega_4$, along with the interactions with two fields, consistent with the energy level diagram in figure 4.9(b) as [86, 87, 55],

$$\begin{aligned}\hat{H} = \hbar\left(\hat{\sigma}_{11}\omega_1 + \hat{\sigma}_{33}\omega_3 + \hat{\sigma}_{44}\omega_4\right) + \hbar g_0\left(\hat{a}^\dagger\hat{\sigma}_{13}e^{i\omega_p t} + \hat{a}\hat{\sigma}_{31}e^{-i\omega_p t}\right)\\ + \hbar\left(\Omega^*\hat{\sigma}_{24}e^{i\omega_c t} + \Omega\hat{\sigma}_{42}e^{-i\omega_c t}\right).\end{aligned} \tag{4.9}$$

In the above equation, $g_0 = -\mu_{13}\sqrt{\omega_p/(2\hbar\varepsilon_0 V)}$ is atom-cavity coupling, where μ_{13} is the transition dipole matrix element between $|3\rangle$ and $|1\rangle$, $2\Omega = -\mu_{24}|E_c|/\hbar$ is Rabi frequency for control beam, where μ_{24} is the transition dipole matrix element between $|4\rangle$ and $|2\rangle$, $|E_c|$ is the magnitude of electric field of the control light, and * denotes complex conjugate. The intensity of control beam is kept constant.

As we are not in the single photon regime, it is appropriate to consider the expectation values for the field operators in the cavity mode, where $\alpha = \langle a\rangle$ and $\alpha^* = \langle a^\dagger\rangle$ correspond to the coherent field (semi-classical approximation). Using Eqn. 4.1 and transforming to rotating

frame, we get coupled differential equations similar to Eqn. 4.8,

$$\dot{\alpha} = -\eta - \kappa_t \alpha - i g_0 N_c \rho_{13} \tag{4.10a}$$

$$\dot{\rho}_{13} = -\left(\gamma_{13} + i\Delta_p\right)\rho_{13} + i g_0 \alpha(\rho_{33} - \rho_{11}) \tag{4.10b}$$

$$\dot{\rho}_{33} = -\Gamma\rho_{33} + i g_0(\alpha^*\rho_{13} - \alpha\rho_{13}^*) \tag{4.10c}$$

$$\dot{\rho}_{11} = \frac{\Gamma}{2}\rho_{44} + \frac{\Gamma}{2}\rho_{33} - i g_0(\alpha^*\rho_{13} - \alpha\rho_{13}^*) \tag{4.10d}$$

$$\dot{\rho}_{24} = -\left(\gamma_{24} + i\Delta_c\right)\rho_{24} + i\Omega(\rho_{44} - \rho_{22}) \tag{4.10e}$$

$$\dot{\rho}_{44} = -\Gamma\rho_{44} + i(\Omega^*\rho_{24} - \Omega\rho_{24}^*) \tag{4.10f}$$

$$\dot{\rho}_{22} = \frac{\Gamma}{2}\rho_{44} + \frac{\Gamma}{2}\rho_{33} - i(\Omega^*\rho_{24} - \Omega\rho_{24}^*). \tag{4.10g}$$

Here, Γ is the spontaneous emission decay rate of the excited states, γ_{13} and γ_{24} are the decoherence rates for coherence between states $\{|3\rangle, |1\rangle\}$ and $\{|4\rangle, |2\rangle\}$ respectively. The probe laser detuning from the $|1\rangle \leftrightarrow |3\rangle$ transition is $\Delta_p = (\omega_3 - \omega_1) - \omega_p$, and the control laser detuning from the $|2\rangle \leftrightarrow |4\rangle$ transition is $\Delta_c = (\omega_4 - \omega_2) - \omega_c$. The probe is resonant with the cavity ($\omega_p = \omega_{cv}$).

The objective throughout this work is to solve for the intracavity light intensity α when the states of the atoms interact with the light fields. In this case the application of the cavity mode laser ω_p ($|1\rangle \leftrightarrow |3\rangle$) and the transverse control laser ω_c ($|2\rangle \leftrightarrow |4\rangle$) couples the ground states of the atoms in a manner that shifts the state populations in the atoms. This, in turn, affects the intensity of the light in the cavity mode. The entire coupled system of Eqns. 4.10 can be solved to obtain α, with realistic parameters for the atom and cavity.

For the atom, we have $\rho_{13} = e^{i\omega_p t}\langle|1\rangle\langle 3|\rangle$ and $\rho_{24} = e^{i\omega_c t}\langle|2\rangle\langle 4|\rangle$ for the coherences, and $\rho_{nn} = \langle|n\rangle\langle n|\rangle$ for diagonal terms representing the state populations. We neglect collisional dephasing for all transitions, and set $\gamma_{24} = \gamma_{13} = \frac{\Gamma}{2}$ in Eqns. 4.10. N_c is the effective number of atoms coupled to the cavity at any given time and is taken to be a constant. In the $\dot{\alpha}$ equation, the third term represents the loss of intracavity light due to the presence of spontaneously emitting resonant atoms in the cavity and is proportional to the effective number of atoms (N_c).

In steady state, $\dot{\alpha} = 0$ and $\dot{\rho}_{mn} = 0, \forall(m,n)$ and Eqns. (4.10) becomes a set of linear equations which can be solved algebraically. Eliminating the atomic variables[1] we get a nonlinear equation of degree 3 in α,

$$-\eta - \kappa_t\alpha - \chi\alpha = 0, \tag{4.11}$$

[1]The algebraic manipulation tool of Mathematica program is very helpful here. The Mathematica code for this manipulation is available at https://goo.gl/mzUzvA. The file name is "stationary_4level_steady state hysteresis.nb". This file also contains the code to obtain and plot the data for figure 4.10.

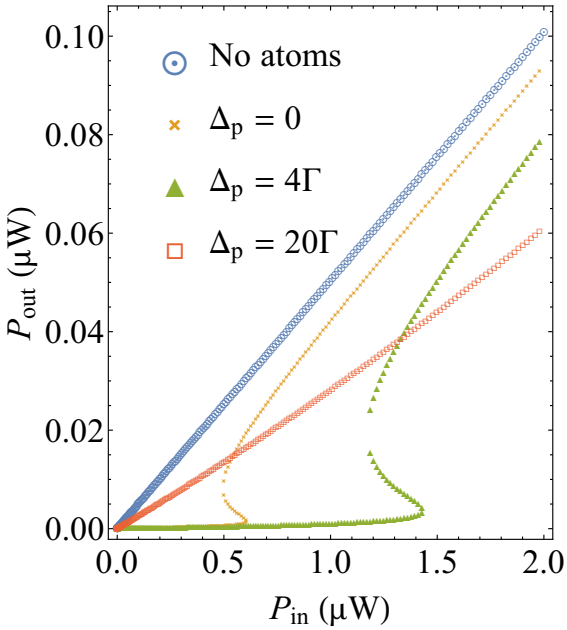

Fig. 4.10 Transmitted power of cavity versus input power after solving Eqn. (4.11) numerically and converting to SI units. The different curves correspond to different detunings of the probe laser from the atomic resonance. When there are no atoms, then the response is linear. As Δ_p changes, the nature of the hysteresis and therefore the region for bistable behavior changes. All curves are for control power corresponding to $\Omega/2\pi = -50$ GHz and detuning $\Delta_c = 0$

where χ is the susceptibility given by,

$$\chi = \frac{2N_c g_0^2(\Gamma - 2i\Delta_p)}{|\alpha|^2 g_0^2\left[(\frac{\Gamma}{|\Omega|})^2 + 16 + 4(\frac{\Delta_c}{|\Omega|})^2\right] + \left(\Gamma^2 + 4\Delta_p^2\right)}.$$

The quadratic dependence on α in the denominator turns Eqn. (4.11) into a cubic equation. The negative sign in front of the third term represents the interaction of cavity field with atoms, which is lossy due to continuous absorption and spontaneous emission. This lossy part corresponds to the real part of the susceptibility, χ. The solution of Eqn. (4.11) allows the existence of 3 steady state values of α for the same η, as shown in figure 4.10.

The part of the solution to Eqn. 4.11 with a negative slope is an unstable solution [90] of the cubic equation. Experimentally, the system transits from one stable solution to another, therefore exhibiting bistability in the regime where multiple solutions exist for a given value of η. In figure 4.10, we have converted the cavity field into power, for comparison with experiments. This is achieved by multiplying intracavity intensity $\frac{c\varepsilon_0}{2}|\alpha|^2\left(\frac{\hbar\omega_{cv}}{2V\varepsilon_0}\right)$ by transmission coefficient $2\kappa_r\tau$ and the area of beam $A = 6.2\times10^{-2}$ mm^2. Here $\sqrt{\frac{\hbar\omega_{cv}}{2V\varepsilon_0}}$ is the proportionality constant between electric field operator inside the cavity and the operators $\hat{a}$ and $\hat{a}^\dagger$, V is the volume of the

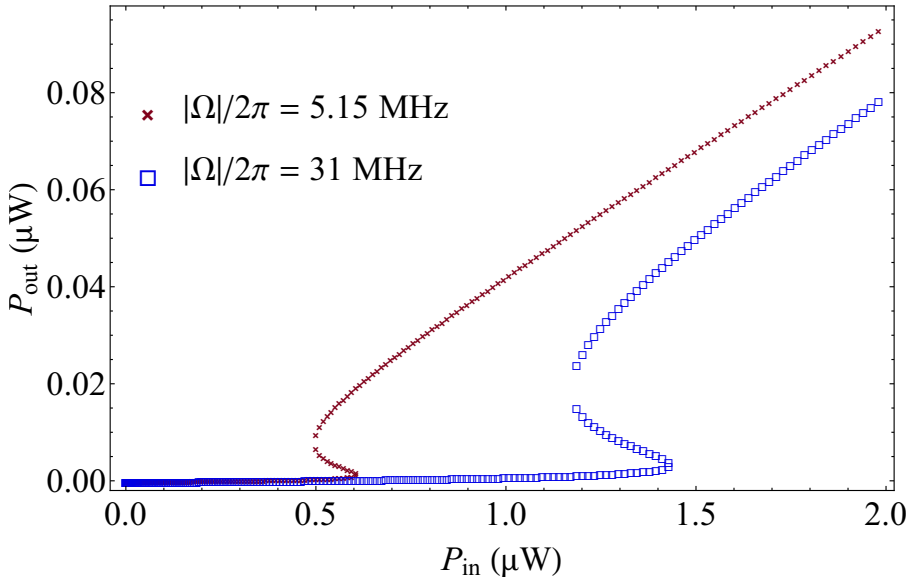

Fig. 4.11 Bistability curves for two different control beam powers with $\Delta_p = 2\Gamma$.

cavity mode and ω_{cv} is cavity resonance frequency. For the calculation, the cavity parameters are $\kappa_t/2\pi = 0.7$ MHz corresponding to the finesse of 2350, $\kappa_r/2\pi = 78$ kHz, $\tau = 0.305$ ns and $N_c = 5 \times 10^4$. The values for atomic transitions are based on the ground states ($|1\rangle$, $|2\rangle$) correspond to $5^2S_{1/2}(F = 2, F = 1)$ and excited states ($|3\rangle$, $|4\rangle$) correspond to $5^2P_{3/2}(F = 1, F = 2)$ respectively of ^{87}Rb D_2 transition and $\Gamma/2\pi = 6.06$ MHz [91]. $\Omega/2\pi = -50$ GHz corresponding to 32 W/m^2 intensity of the control beam, $g_0/2\pi = -40$ kHz. The parameter values above are fairly representative of our general experimental laboratory conditions [38]. The cavity output power as a function of input power, in the presence of transverse control light field with $\Omega/2\pi = -50$ GHz is illustrated in figure 4.10. From the figure, we infer that as the detuning of probe beam from the atomic resonance increases, the region of bistability decreases and beyond a point, for large detunings, the system reduces to the one where no resonant atoms are present in the cavity, and the empty cavity response is obtained. This is evident from Eqn. (4.11), in the limit of large Δ_p.

For large control laser power represented by $\Omega/2\pi \approx -50$ GHz, $16 \gg (\Gamma/\Omega)^2 \geq (\Delta_c/|\Omega|)^2$, the loss in cavity light becomes largely independent of the probe power as can be inferred from above condition and Eqn. (4.11). However, for Ω of the order of Γ the loss of cavity light becomes dependent on control power as seen in figure 4.11). In this range, the intracavity probe light intensity can be significantly altered by changing the ratio of control intensity to cavity input intensity $I_c/I_{in} \approx 10^{-8}$. This shows that a very weak transverse intensity of light, under suitable conditions can control the intracavity light intensity of the probe beam. This regime of control is available only in the region where the bistability is manifested. When the intracavity

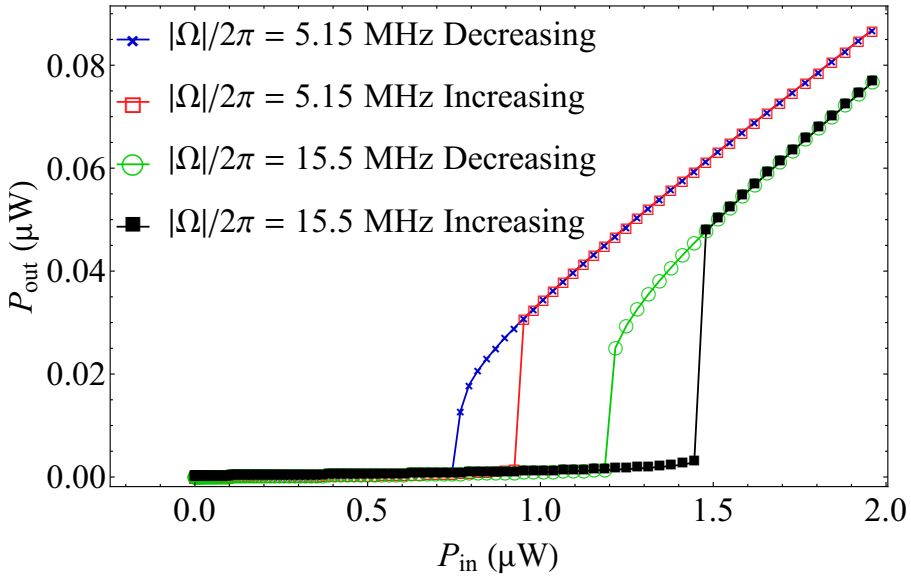

Fig. 4.12 Hysteresis for the two different control beam powers in figure 4.11, with probe beam detuning $\Delta_p = 2\Gamma$. The hysteresis shown here is a result of following the change in output as the input is increased and decreased adiabatically.

intensity is high, and when $\Omega \gg \Gamma$ we obtain a saturated regime, where adding more power to probe or control beam does not alter the intra cavity field significantly.

The set of partial differential equations (Eqns. (4.10)) can be solved in a Mathematica Notebook numerically[2], by adiabatically increasing and then decreasing the input power of probe beam while keeping the power of the control beam at a given value. In this case, the change in the output power can be followed by tracking the intracavity field α and converting it into a transmitted output intensity using the cavity κ_r. The resulting intensity of the transmitted light exhibits hysteresis as seen in figure 4.12. Here, as the control power is increased, the hysteresis features moves to higher values of the probe light intensity. The observed hysteresis is consistent with the steady state solutions that exhibit bistability, and the transmitted light intensity follows the positive slopes of the bistability solution.

Three level atoms

The three-level atom is easily adapted from the earlier four-level atom by eliminating the excited state, $|4\rangle$. The probe beam frequencies and detunings remain the same while the control beam couples $|2\rangle \leftrightarrow |3\rangle$, with detuning $\Delta_c = (\omega_3 - \omega_2) - \omega_c$. The resulting three-level system has two ground states and thus is a Λ system. The rate equations can be derived in a manner

[2]The Mathematica code for this numerical solution can be found at https://goo.gl/mzUzvA. The file name is "stationary_4level_time dependent_ bistability.nb".

analogous to that of Eqns. (4.10), and can be written as,

$$\dot{\alpha} = -\eta - \kappa_t \alpha - i g_0 N_c \rho_{13} \tag{4.12a}$$

$$\dot{\rho}_{13} = -\left(\gamma_{13} + i\Delta_p\right)\rho_{13} + i g_0 \alpha(\rho_{33} - \rho_{11}) - i\Omega\rho_{12} \tag{4.12b}$$

$$\dot{\rho}_{11} = \frac{\Gamma}{2}\rho_{44} + \frac{\Gamma}{2}\rho_{33} - i g_0(\alpha^*\rho_{13} - \alpha\rho_{13}^*) \tag{4.12c}$$

$$\dot{\rho}_{33} = -\Gamma\rho_{33} + i g_0(\alpha^*\rho_{13} - \alpha\rho_{13}^*) + i(\Omega^*\rho_{23} - \Omega\rho_{23}^*) \tag{4.12d}$$

$$\dot{\rho}_{23} = -\left(\gamma_{23} + i\Delta_c\right)\rho_{23} + i\Omega(\rho_{33} - \rho_{22}) - i\alpha g_0\rho_{12}^* \tag{4.12e}$$

$$\dot{\rho}_{12} = -\left(\gamma'_{12} + i[\Delta_c - \Delta_p]\right)\rho_{12} + i\alpha g_0\rho_{23}^* - i\Omega^*\rho_{13} \tag{4.12f}$$

$$\dot{\rho}_{22} = \frac{\Gamma}{2}\rho_{33} - i(\Omega^*\rho_{23} - \Omega\rho_{23}^*), \tag{4.12g}$$

where $\gamma_{13} = \gamma_{23} = \frac{\Gamma}{2}$, and γ'_{12} is the collisional dephasing, between the ground states. This is the general description when the atoms are in motion but still coupled to the cavity mode at all times. For the three-level scheme, we consider the complete set of evolution equations, unlike the four-level case. The coherence term between the ground states $|1\rangle$ and $|2\rangle$ plays a role here due to the common excited state $|3\rangle$. All other notations are the same as those defined alongside Eqns (4.10), in the four-level case. Similar to the four-level case the steady state equation for α can be calculated[3], yielding an equation in α of the form

$$-\eta - \kappa_t\alpha - \tilde{\chi}\alpha = 0, \tag{4.13}$$

where $\tilde{\chi}$ is new susceptibility from atoms given by,

$$\tilde{\chi} = \frac{T_1\alpha + T_2|\alpha|^2\alpha}{T_3|\alpha|^6 + T_4|\alpha|^4 + T_5|\alpha|^2 + T_6}, \tag{4.14}$$

which results in a seventh power equation in α, giving rise to interesting consequences. The corresponding ring cavity analysis [83] also results in a seventh power equation. The values of

[3]The Mathematica code for this is available at https://goo.gl/mzUzvA. The file name is "stationary_3level_steady state hysteresis.nb". This file also contains the code to obtain and plot the data for figure 4.13.

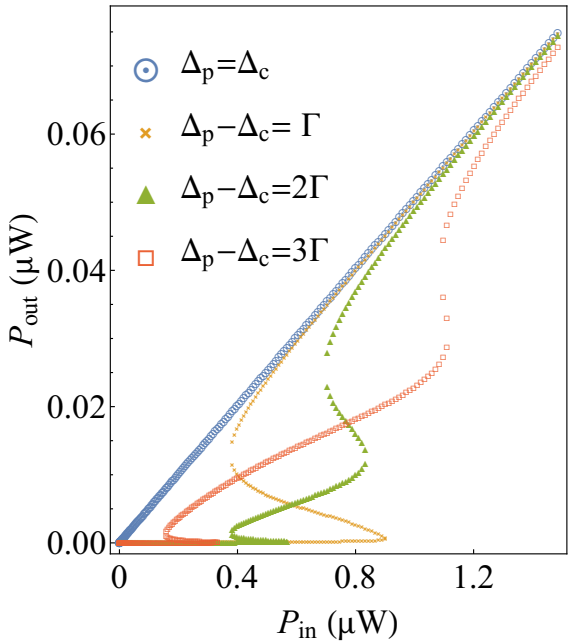

Fig. 4.13 Bistability in the case of a three-level system for different values of detuning. Here $|\Omega|/2\pi = 5.15$ MHz. Unlike the 4 level system, the bistable curves have two distinct regions of negative slope in some cases. The four curves illustrate the different cases of probe and control detuning, as specified in legend.

$T_1, ..., T_6$ are,

$$T_1 = 2g_0^2 N_c |\Omega|^2 \left[\Gamma(\Gamma - 2i\Delta_p)\left(\gamma_{12}'^2 + (\Delta_p - \Delta_c)^2\right) + 2\Gamma|\Omega|^2(\gamma_{12}' + i\Delta_p - i\Delta_c)\right]$$

$$T_2 = 4g_0^4 N_c |\Omega|^2 \left[-2\gamma_{12}'(i\Delta_p + i\Delta_c) + \Gamma(\gamma_{12}' + i\Delta_p - i\Delta_c)\right]$$

$$T_3 = 4\Gamma g_0^6$$

$$T_4 = g_0^4 \left[\Gamma^2\gamma_{12}' + 2\Gamma\Delta_c(\Delta_p - \Delta_c) + 3|\Omega|^2(\Gamma + 4\gamma_{12}')\right]$$

$$T_5 = g_0^2 \Big[\Gamma\left(\Gamma^2 + 4\Delta_c^2\right)\left(\gamma_{12}'^2 + (\Delta_p - \Delta_c)^2\right) + 8|\Omega|^2\left(\Gamma^2\gamma_{12}' + 3\Gamma\gamma_{12}'^2 + 2\Gamma(\Delta_p - \Delta_c)^2 + \gamma_{12}'(\Delta_p + \Delta_c)^2\right) + 12|\Omega|^4(\Gamma + 4\gamma_{12}')\Big]$$

$$T_6 = \Gamma|\Omega|^2\left(\Gamma^2 + 4\Delta_p^2\right)\left(\gamma_{12}'^2 + (\Delta_p - \Delta_c)^2\right) + 4\Gamma|\Omega|^6 + |\Omega|^4[\Gamma^2\gamma_{12}' + 2\Gamma\Delta_p(\Delta_c - \Delta_p)].$$

For a specific case of $g_0 \ll \Omega, \Gamma$, above solution reduces to the one derived in [92] which does not result in hysteresis. The seventh power of α in Eqn. (4.14) gives rise to an input-output relation when the two light frequencies are close to resonance, which is far richer than the case of the four-level system, within the approximations made. A seventh order cavity field solution can result in multi-stability and multiple bistabilities as seen in figure 4.13 and figure 4.14.

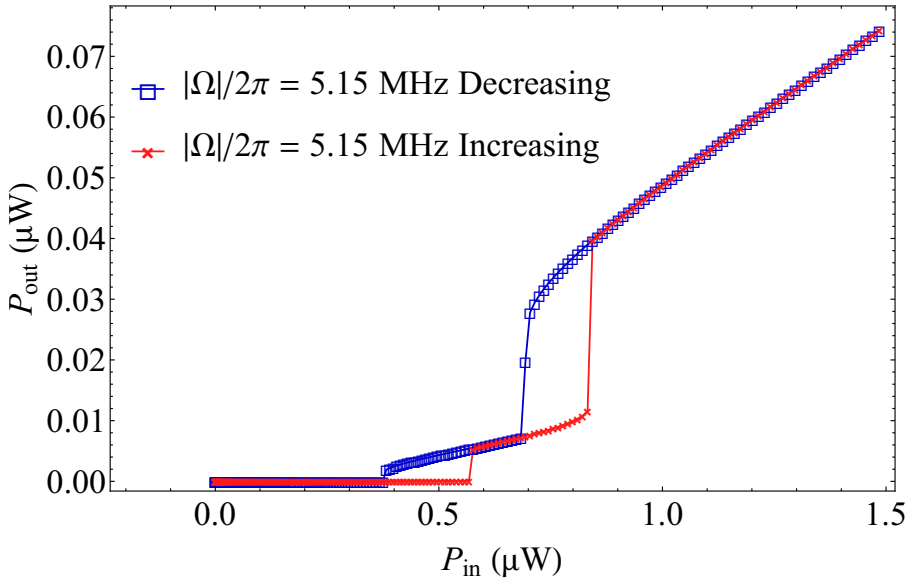

Fig. 4.14 Double hysteresis for the case of $\Delta_p = 0$, $\Delta_c = 2\Gamma$ and $|\Omega|/2\pi = 5.15$ MHz in figure 4.13. The increasing and decreasing legend represents the sense of the change in the input probe power.

When the gas of atoms is dilute and stationary, the assumption $\gamma'_{12} \to 0$ holds and equal detuning, i.e. $\Delta_p = \Delta_c$ implies that $\tilde{\chi} = 0$, resulting in electromagnetically induced transparency (EIT) [93]. This results in Eqn. (4.13) becoming linear in α because the medium becomes transparent in steady state and so the transmitted light depends only on cavity loss. Hence there is no bistability, as has been observed experimentally [94]. For $\Delta_p \neq \Delta_c$ we see bistability, as shown in figure 4.13. Depending on the system parameters, the nature of the solution can be altered such that the adiabatic solution of the curve can exhibit multiple bistable behavior. This is seen in figure 4.13 and figure 4.14.

4.3.2 Open system of atoms

Four level atoms

So far the atoms that have been considered are static, i.e. they do not flow in and out of the cavity mode, which implies zero temperature. We now consider a situation where the resonant atoms are swapped in and out of the cavity mode while maintaining the effective number of atoms within the mode constant with time. Such a system describes the case when the atomic reservoir is much larger than the volume of the cavity mode and that the atoms move into and out of the cavity mode, representing an open system of atoms coupled to the cavity. In this case, the atoms would have a finite temperature to account for their motion. Experimentally

this is satisfied for the schematic illustrated in figure 4.9. In this work, instead of explicitly considering an ab-initio velocity distribution for the temperature, we mimic the temperature by a model which exchanges atoms between the mode and the reservoir at a certain rate, which is consistent with the vapor cell experiment described in section 4.1. At room temperature, the population of the Rb atoms is equally split into the two ground states, and we put this in explicitly in our calculations when we exchange background gas atoms with cavity mode atoms. For such a system, the steady state behavior of the atom-cavity system remains the same while the transient response of the four-level atom-cavity system is significantly affected. Below we formulate the atom-cavity problem by creating a simple exchange model and connect the switching response of light through the cavity to the vapor cell experiment (4.1).

The principle difference with respect to the stationary atom model is that the state of the ensemble (density matrix) in the cavity mode changes, as the atoms interacting with the cavity go out of the cavity mode and background gas atoms are added to the ensemble of atoms inside the cavity. Consider the case when the flow rate of atoms from the cavity mode is $R_{\rm f}$. After time t the fraction of atoms remaining is $e^{-R_{\rm f}t}$. When N_1 atoms with state ρ_1 are mixed with, N_2 atoms with state ρ_2, the statistical mixture of both gives density matrix,

$$\rho = \frac{1}{N_1+N_2}(N_1\rho_1 + N_2\rho_2).$$

If $\rho(t)$ is the density matrix at time t the density matrix after small time τ' is

$$\rho(t+\tau') = e^{-R_{\rm f}\tau'}\rho(t) + (1-e^{-R_{\rm f}\tau'})\rho^0,$$

where ρ^0 is density matrix of external atoms entering the cavity mode. For $\tau' \ll \{1/R_{\rm f}, \tau, 1/\Gamma\}$, $e^{-R_{\rm f}\tau'} \approx 1 - R_{\rm f}\tau'$ and $(1-e^{-R_{\rm f}\tau'}) \approx R_{\rm f}\tau'$. Therefore,

$$\frac{\rho(t+\tau')-\rho(t)}{\tau'} = -R_{\rm f}\rho(t) + R_{\rm f}\rho^0$$

and in the limit $\tau' \to 0$,

$$\frac{d\rho(t)}{dt} = R_{\rm f}[\rho^0 - \rho(t)].$$

For four-level atoms, the equations are same as Eqns. 4.10 with an addition of the term $R_{\rm f}(\rho^0_{nm} - \rho_{nm})$ on the right-hand side for atomic operators $\rho_{nm}, \forall(n,m)$. The corresponding set

of equations with the exchange incorporated are,

$$\dot{\alpha} = -\eta - \kappa_t \alpha - i g_0 N_c \rho_{13} \tag{4.15a}$$

$$\dot{\rho}_{13} = -\left(\gamma_{13} + i\Delta_p\right)\rho_{13} + i g_0 \alpha(\rho_{33} - \rho_{11}) + R_f(\rho^0_{13} - \rho_{13}) \tag{4.15b}$$

$$\dot{\rho}_{33} = -\Gamma\rho_{33} + i g_0(\alpha^*\rho_{13} - \alpha\rho^*_{13}) + R_f(\rho^0_{33} - \rho_{33}) \tag{4.15c}$$

$$\dot{\rho}_{11} = \frac{\Gamma}{2}\rho_{44} + \frac{\Gamma}{2}\rho_{33} - i g_0(\alpha^*\rho_{13} - \alpha\rho^*_{13}) + R_f(\rho^0_{11} - \rho_{11}) \tag{4.15d}$$

$$\dot{\rho}_{24} = -\left(\gamma_{24} + i\Delta_c\right)\rho_{24} + i\Omega(\rho_{44} - \rho_{22}) + R_f(\rho^0_{24} - \rho_{24}) \tag{4.15e}$$

$$\dot{\rho}_{44} = -\Gamma\rho_{44} + i(\Omega^*\rho_{24} - \Omega\rho^*_{24}) + R_f(\rho^0_{44} - \rho_{44}) \tag{4.15f}$$

$$\dot{\rho}_{22} = \frac{\Gamma}{2}\rho_{44} + \frac{\Gamma}{2}\rho_{33} - i(\Omega^*\rho_{24} - \Omega\rho^*_{24}) + R_f(\rho^0_{22} - \rho_{22}). \tag{4.15g}$$

For an atom at room temperature, $\rho^0_{44} = \rho^0_{33} = \rho^0_{13} = \rho^0_{24} \approx 0$ and $\rho^0_{22} = \rho^0_{11} \approx 0.5$. In such a system of atoms, when control light is off (i.e. $\Omega = 0$), the susceptibility is,

$$\chi = \frac{N_c g_0^2 R_f \mathrm{A}(\mathrm{B} - 2i\Delta_p)}{2|\alpha|^2 g_0^2 \mathrm{BC} + R_f \mathrm{A}\left(4\Delta_p^2 + \mathrm{B}^2\right)}, \tag{4.16}$$

where we identify $\mathrm{A} = \Gamma + R_f$, $\mathrm{B} = \Gamma + 2R_f$ and $\mathrm{C} = \Gamma + 4R_f$. Thus the system exhibits bistable behavior, both with and without the presence of the control beam. Here the saturated sample is continuously replaced by a thermal sample hence there is a continuous supply of fresh atoms in ground state $|1\rangle$, which is equivalent to the action of the control beam for the stationary atom case. For $\Omega \neq 0$ we get $\chi = \frac{\mathrm{E}}{\mathrm{F}}$ where,

$$\begin{aligned}
\mathrm{E} &= g_0^2 N_c \mathrm{A}(\mathrm{B} - 2i\Delta_p)\left\{4|\Omega|^2\mathrm{B}^2 + R_f\mathrm{A}\left[4\Delta_c^2 + \mathrm{B}^2\right]\right\} \\
\mathrm{F} &= 2|\alpha|^2 g_0^2 \mathrm{B}\left\{16|\Omega|^2\mathrm{B}^2 + \mathrm{AC}\left[4\Delta_c^2 + \mathrm{B}^2\right]\right\} \\
&\quad + \mathrm{A}\left(4\Delta_p^2 + \mathrm{B}^2\right)\left\{2|\Omega|^2\mathrm{BC} + R_f\mathrm{A}\left[4\Delta_c^2 + \mathrm{B}^2\right]\right)\right\}.
\end{aligned}$$

When the control beam is incident on a small fraction of atoms we see a shift in bistability, as shown in figure 4.15. At input power of 430 μW, in the case when $|\Omega| = 0$, i.e. when there is no intersecting transverse beam, the atom-cavity system is on the upper branch of the stability curve and when $|\Omega| = 1.76$ MHz the stability point exists only on the lower branch of the stability curve, as seen in figure 4.15. On the lower intensity branch, the output is almost zero. Hence the above fact can be used for switching on and off the cavity output by turning off and on the control beam instantaneously. For figure 4.15 parameters different from those used in the computation of figure 4.10 are $\kappa_t/2\pi = 9.36$ MHz corresponding to a finesse of 100, $\kappa_r/2\pi = 44.7$ kHz, $g_0/2\pi = 11.8$ kHz, $\tau = 0.533$ ns, $N_c = 5 \times 10^7$, $\Delta_p = 10\Gamma$. The fraction of

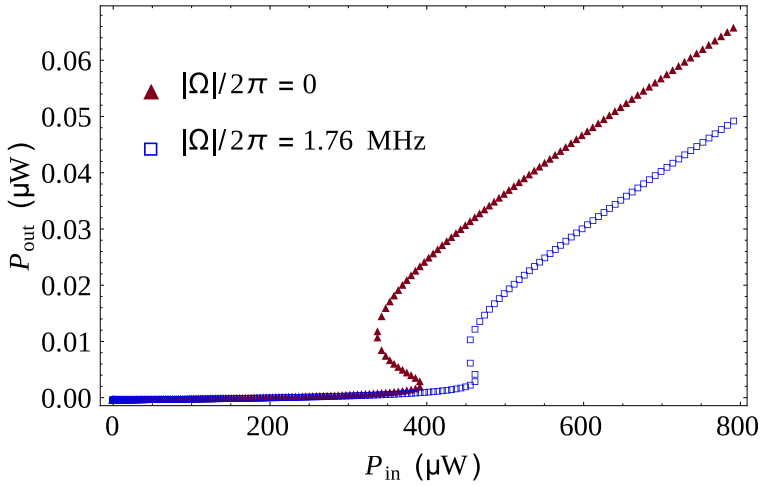

Fig. 4.15 Bistability when atoms are flowing in and out of cavity. The two curves correspond to the condition when the control light is off and on as seen in the legend.

atoms addressed by control beam is 0.025 and $R_f/(2\pi) = 5.5$ kHz. Above parameters are close to the vapor cell experiment (4.1).

The transient behavior of the intracavity intensity, when the control beam is switched on is obtained by tracking the time evolution of the atomic states in the intersection volume of the cavity mode and the transverse beam. This is done by first solving the rate equations numerically (using NDSolve in Mathematica v9.0)[4] till the system reaches steady state with $\Omega = 0$. The second step is to solve the equations again with $\Omega \neq 0$ with initial conditions same as the final conditions of the first step. Finally, the third step is to solve the equations again when the control beam is switched off ($\Omega = 0$) with initial conditions same as the final state of the second step. The second and third steps correspond to switching on and off the control beam. The numerical solutions give time evolution of cavity field. The underlying physics is that the system operating point shifts from the hysteresis solution for the initial condition to that for the final state. In this process, for parameters which closely relate to the switching regime in the vapor cell experiment (4.1), we find that the intracavity intensity shifts from the upper branch of the initial system when $\Omega = 0$ to the lower branch of the final system when $\Omega = 1.76$ MHz. This is the experimentally demonstrated negative logic switching seen in figure 4.2.

For the case when the four-level atoms are static, the transient response time for the switching is rapid (sub-microsecond), consistent with the analysis of Harshawardhan and Agarwal [83]. However, introduction of the exchange to mimic the flow of atoms into and out of the cavity mode keeps readjusting the ground state populations and prevents the intracavity atoms from rapid optical pumping, resulting in large decay times of the cavity mode as can be

[4]The Mathematica code for this is available at https://goo.gl/mzUzvA. The file name is "Non-static_4level_rise and decay times.nb". This file also contains the code to obtain and plot the data for figure 4.16.

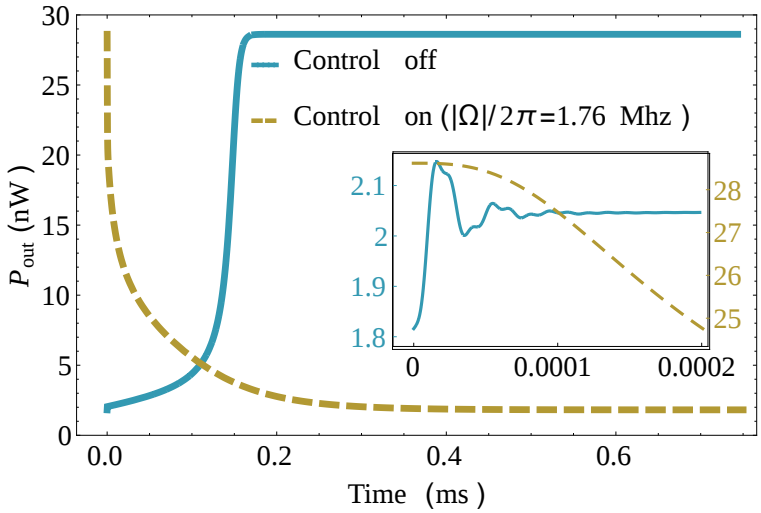

Fig. 4.16 Time evolution of cavity output power when the cavity input laser is switched by the control beam. Here control off is $|\Omega|/2\pi = 0$ and control beam on is $|\Omega|/2\pi = 1.76$ MHz. The input power of 430 μW corresponds to the bistability parameter region in figure 4.15. The sub-ms slow response of the output power is clearly seen. The inset shows the sub-μs response of the transmitted power, where the left ordinate axis is the power in the control off case and right axis is the power for the control on. The time axis is in ms. Clearly the short time behavior is complex.

seen in figure 4.16. The figure shows the time evolution of output power when control beam is suddenly turned on and off. While there are fast fluctuations in the field values, the envelope of the intracavity intensity rise and fall times is of the order of 0.2 ms which is of the order $2\pi/R_f$. This behavior is consistent with the long time responses seen in figure 4.5, and the complex transient behavior prevents the switching times in the experiment from exhibiting single exponential response.

Two-level atoms with decay loss

The special case of the four-level system, where both the probe and control laser are resonant with the $|1\rangle \leftrightarrow |3\rangle$ transition, constitutes the two-level system that is experimentally relevant. For such a system, there is a possibility that an atom in $|3\rangle$ decays to the other ground state $|2\rangle$, but in $|2\rangle$, the atom is no longer optically active and the overall effect of the presence of the other ground state is that of an optical loss mechanism created by the decay from $|3\rangle$. The experimental realization of this is simple and it results in a different response of the cavity transmission. Assuming $\Delta_c = 0$, $\gamma'_{12} = 0$ and all other terms as before, the coupled differential

equations describing the system are,

$$\dot{\alpha} = -\eta - \kappa_t \alpha - i g_0 N_c \rho_{13} \tag{4.17a}$$

$$\dot{\rho}_{13} = -\left(\gamma_{13} + i\Delta_p\right)\rho_{13} + i g_0 \alpha(\rho_{33} - \rho_{11}) + i\tilde{\Omega}(\rho_{33} - \rho_{11}) + R_f(\rho^0_{13} - \rho_{13}) \tag{4.17b}$$

$$\dot{\rho}_{33} = -\Gamma\rho_{33} + i g_0(\alpha^*\rho_{13} - \alpha\rho^*_{13}) + i(\tilde{\Omega}^*\rho_{13} - \tilde{\Omega}\rho^*_{13}) + R_f(\rho^0_{33} - \rho_{33}) \tag{4.17c}$$

$$\dot{\rho}_{11} = \frac{\Gamma}{2}\rho_{33} - i g_0(\alpha^*\rho_{13} - \alpha\rho^*_{13}) - i(\tilde{\Omega}^*\rho_{13} - \tilde{\Omega}\rho^*_{13}) + R_f(\rho^0_{11} - \rho_{11}) \tag{4.17d}$$

$$\dot{\rho}_{22} = \frac{\Gamma}{2}\rho_{33} + R_f(\rho^0_{22} - \rho_{22}). \tag{4.17e}$$

Where, $\tilde{\Omega} = \Omega e^{i(\omega_p - \omega_c)t}$. For the case $\omega_c = \omega_p$, when the intracavity field is enhanced corresponding to positive logic switching described in section 4.1, χ becomes,

$$\chi = \frac{N_c g_0 R_f A(g_0 + \Omega/\alpha)(B - 2i\Delta_p)}{2BC|g_0\alpha + \Omega|^2 + R_f A\left[4\Delta_p^2 + B^2\right]}, \tag{4.18}$$

where A, B and C are defined earlier. Once again there exists a cubic equation in α, which is the type of solution that supports bistability and hysteresis. Here the equations have been written with the exchange rate of atoms incorporated. Solving for the same atom-cavity parameters as used for the four-level open system, we see that in this case, the control beam pumps atoms out of the cavity light cycle and hence reduce probe loss. The shift in the bistable region of the output response to lower input intensity, shown in figure 4.17 confirms this. The corresponding hysteresis plot can be readily imagined, and the positive logic or cavity mode enhancement

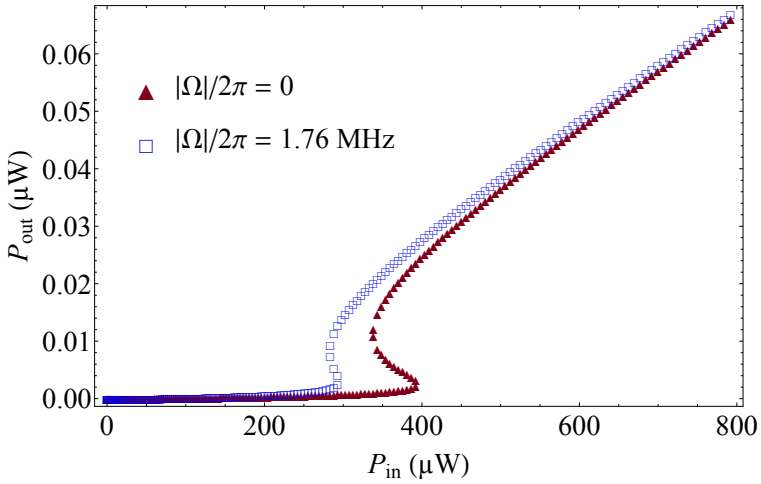

Fig. 4.17 Bistability for atoms with exchange when control beam is in resonance with levels $|1\rangle$ and $|3\rangle$, making it a two-level system with loss. Here the fraction of atoms addressed by control beam is 0.2, all other parameters are same as the values used for figure 4.15

experiments shown in figure 4.6 follow from the processes described above. Without undue repetition, we can observe from figure 4.17 that, in a region of input power values of the probe, the application of the appropriate intensity of control laser can promote the transmission from low intensity to high intensity in positive switching logic. The transient properties are similar to that of the four-level case with non-static atoms, as can and should be expected and in line with the experimental observations.

4.3.3 Discussion

As can be seen from the results above, the division of the problem into a closed and open atomic ensemble interacting with the cavity mode expresses itself in the transient response of the controlled intracavity light intensity. The theoretical solutions obtained can be explicitly tested in experiments since the values for the atomic transitions and fields used in the explicit solutions are close to the experimental values for Rb. We expect that the generic features of the results here are independent of the particular atomic system and cavity parameters. We now discuss the simplifications and extensions of this work to experiments. The ^{87}Rb energy levels considered in the above calculations are the $5S_{1/2}$, $F = 1,2$ and the $5P_{3/2}$, $F' = 1,2$, so that there are no closed optical transitions in the system. This choice represents the most general four-level system. In the vapor cell experiment, majority of the experiments were performed by tuning the lasers to the maxima of the Doppler broadened absorption, and therefore close to the $5P_{3/2}$, $F' = 3,4$. Further, the Doppler spread and the velocity dependent coupling of the atoms to the cavity in the open system case, which is expected to contribute to the details of the experimental results, has not been considered in the model. While the effort has been to keep the agreement between theoretical parameters and experiment as close as possible, significant departures between the analysis in this article and the experimental realization discussed in section 4.1 exist. Therefore while qualitative agreement can be expected between the theory here and the vapor cell experiment (4.1), the present work does not attempt to provide detailed quantitative agreement.

Closed system of atoms

A viable candidate for a closed system of atoms can be a cold atom ensemble that is contained within the mode volume of the cavity as illustrated in the figure 4.18. For such a system, using state prepared atoms, a number of situations with four, three and two-level atomic systems can be studied, with a small number of atoms present in the cavity mode. The simulations for this case above have been done with $N_c = 5 \times 10^4$ atoms and the lasers plus the detection technologies required are readily available. In all cases with the closed system, resonant light

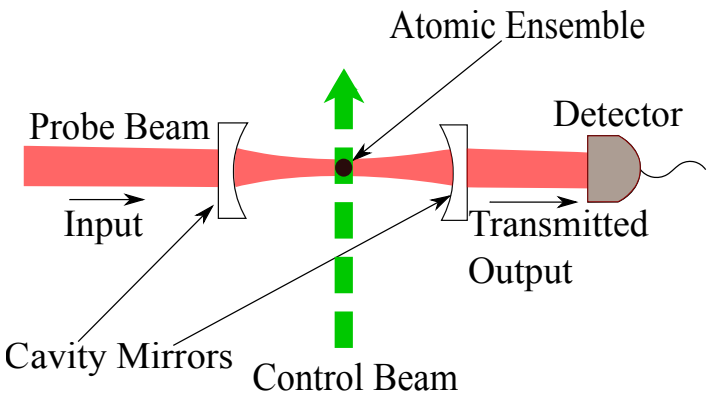

Fig. 4.18 Schematic diagram for closed system of atoms. The black spot can represent an ensemble of laser cooled and trapped atoms or ions, or atoms in a dipole trap.

in the cavity mode will lead to optical pumping into the alternate ground state and lead the system into transparency. Therefore to control the intracavity light field, it is essential to have a non-zero transverse field which allows the atom to interact with the cavity field.

When weak control light is incident on the atoms connecting an excited state with the former dark ground state, the optical pumping effects are reversed, and a simultaneous non-zero population of both ground states manifests. In a specific range of system parameters which depend on the detunings and intensities of the two fields, steady state bistability of the transmitted light intensity is observed. This can be used to control the transmitted light intensity through the cavity and in the limit of weak fields and small atom numbers can be used as a very sensitive all-optical switch. The choice of doing this with either the four-level atom or the three-level atom exists.

Due to negligible Doppler broadening for laser-cooled atoms, the three-level system is practically realizable. The solution for this system is particularly rich, as seen in 4.3.1 . As the relative detunings are altered, complex output to input intensity dependencies show up, resulting in multiple bistabilities in some cases. The parameter space for observation of multiple bistabilities needs careful adjustment of intensity and detunings, an example of this is seen in figure 4.13 and figure 4.14. It might be possible to exploit the multiple bistabilities regime for a 2^{+}-level all-optical switch, where instead of just the turning on and off of the cavity field, intermediate, stable intracavity light intensities are possible. This would open up new possibilities for the precise control of the degree of atom-cavity field interaction, by manipulation of the control light field.

The transient response of the intracavity light field for the closed system depends on the atom-cavity coupling, the reflectivity of the cavity mirrors and the cavity mode volume. The transient response, in this case, is of the order of a microsecond (Fig 4.19), for both the rise and

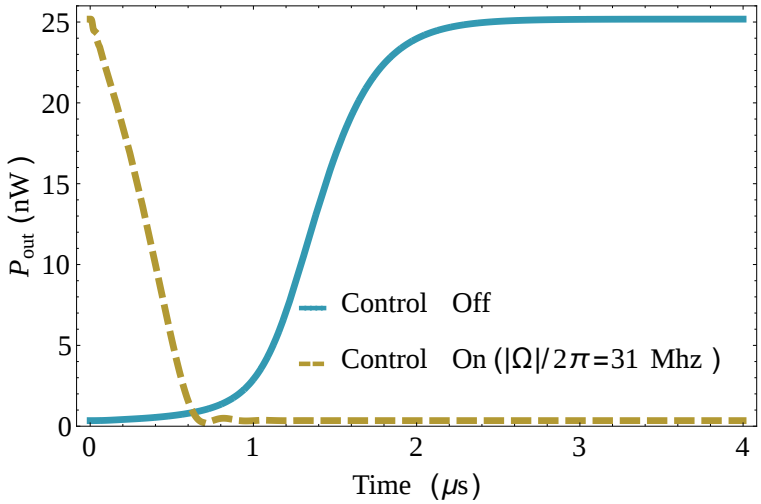

Fig. 4.19 Fast Switching times for closed 4 level system. Here control off is $|\Omega|/2\pi = 0$ and control beam on is $|\Omega|/2\pi = 31$ MHz. The input power of 1 μW corresponds to the lower part of the second bistability curve in figure 4.11 when control is on and the no atoms curve in figure 4.10 when control is off.

fall times of the intracavity intensity, when solved for the experimental parameters of Ray et. al. [38]. A significant fraction of the physics discussed here is possible in our experimental setup with cold atoms in the cavity [38]. While a cold atom ensemble also has its losses and flows, our ability to state prepare the system allows it to be used partially in the manner treated in the present manuscript.

Open system of atoms

When the atoms from the reservoir move in and out of the cavity mode volume, the atomic subsystem is open. How the exchange of atoms affects the experimental measurement can be studied with a vapor cell placed inside a cavity, which is much larger than the mode volume. The cell can be placed in either a ring cavity [77, 94] or a standing wave Fabry-Pérot cavity [12, 92, 95], as discussed here.

In this system, we have a significantly larger number of atoms in the cavity mode at any given time, consistent with the vapor pressure at room temperature. In addition, the cavity decay rates for photons are much higher since the cavity has very high losses, i.e. κ_t is very high. Further, the atom-cavity coupling g is much lower in this case than that for the cold atoms.

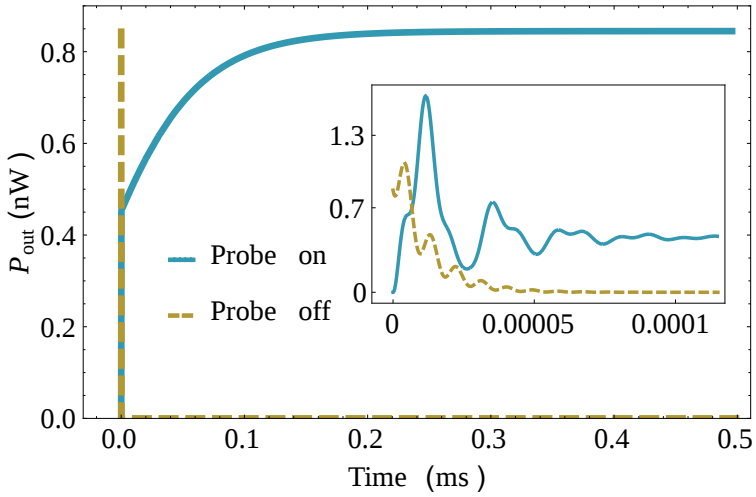

Fig. 4.20 Rise and decay of transmitted intensity when cavity laser is switched on and off respectively. The input power of 300 μW corresponds to the lower branch of hysteresis curve in figure 4.15 with $\Omega = 0$.

Of the many connections that the model makes with the vapor cell experiment (4.1), a key one is in the understanding of the long rise time (≈ 0.2 ms) for the cavity field, when resonant probe light is suddenly switched on, in the absence of control beam. This long rise time is due to the inclusion of atom flow in and out from the cavity mode volume, as seen in figure 4.20. If the flow of atoms is not incorporated, then the field buildup in the cavity is two orders of magnitude faster (2 μs). When the probe field is physically switched off, the decay of the cavity field is very rapid. Both the rise and the decay of the resonant probe field is shown in figure 4.20. In both the rise and decay, fast oscillations are seen in the time evolution. From this, it is clear that the transient response of the resonant atom-cavity system is critically altered by the movement of atoms in and out of the cavity mode. The constant R_f for the calculations is extracted from the vapor cell experiment (4.1) and then introduced into the evolution equations for the atom-field system to obtain the results reported here.

For the open system, even when the control beam is off, the atom-cavity bistability is observed similar to the experimental observations shown in figure 4.2. This is due to the continuous flow of ground state atoms in the cavity mode volume, which has the effect of continuously maintaining the atomic population in both atomic ground states. The effect of the control beam is that the particular value of input light intensity, where the cavity field solution becomes bistable shifts, (a) to higher input light power values, when the control is on the complementary transition (full four-level system), and (b) to lower light input powers when the control is on the same transition as the probe (two-level system with decay).

The observation that for high intracavity intensity of the probe light, even relatively large intensities of the control light is unable to switch the probe transmission off, is explained by

the intracavity intensity jumping between the upper branches of the hysteresis curve, resulting in small changes in the intracavity intensity, and therefore the transmitted light intensity. It is, therefore, clear that the switching of the cavity light intensity as described in section 4.1 is possible only in a window of parameter space, which can be calculated using the methods described here.

A particularly challenging problem posed by the experiment (4.1) was a large time constant for the decay of the cavity mode intensity when the control beam is switched on, in the negative logic case. The measured time constant was ≈ 0.5 ms. This was explained by invoking the exchange of thermal atoms between the cavity mode and the thermal reservoir. From the analysis here we find that the decay time for the cavity field on transverse switching, for the open system as shown in figures 4.16 and 4.20 is in agreement with the experimental result shown in figures 4.5 and 4.6. This large decay time reduces by orders of magnitude (0.6 μs) for the closed system as seen in figure 4.19.

4.4 Nonlinearity in VRS

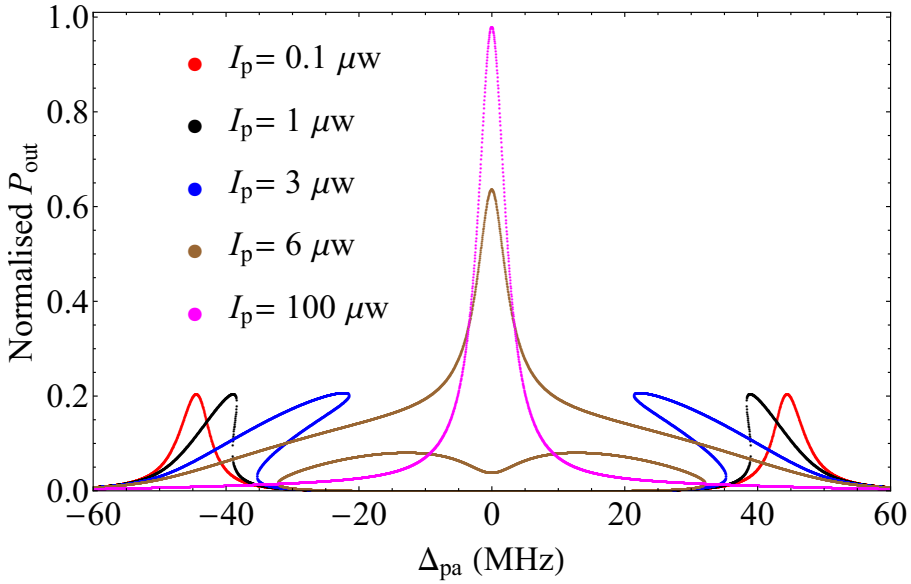

Fig. 4.21 Change in VRS when probe power is increased. The output power in each case is normalized with respect to the maximum of empty cavity transmission of the probe. The parameters used here are, $\kappa_t/2\pi = 2.5$ MHz corresponding to finesse of 656, $\kappa_r/2\pi = 78$ kHz, $g/2\pi = 201$ kHz, $N_c = 5 \times 10^4$, and $\omega_{cv} = \omega_a$.

In section 4.2 we derived a linear equation for cavity field assuming the probe intensity is so small that the atoms remain mostly in ground state. The result of the analysis was the emergence

of splitting in cavity transmission called vacuum Rabi splitting (VRS) when detuning of the probe light was scanned. In contrast, we dealt with nonlinear equations for the intracavity field in section 4.3 which resulted in the phenomenon of bistability when input probe power was scanned. In this section, we extend our calculations to explore nonlinearity in VRS for a system of two-level atoms and Fabry-Pérot cavity. Solving Eqn. 4.8 fully in steady state we get susceptibility,

$$\chi = \frac{2g_0^2 N_c(2i\Delta_{pa} + \Gamma)}{8|\alpha|^2 g_0^2 + \Gamma^2 + 4\Delta_{pa}^2}. \tag{4.19}$$

Combining this equation with Eqn. 4.11 gives a cubic equation for α giving more than one solution for same Δ_p similar to the case of bistability in section 4.3. As can be seen in figure 4.21 the transmission of probe beam shows bistable behavior for high powers of the probe beam. For extremely high power (greater than 100 μW) of the probe beam, the atoms become saturated, and the probe transmission approaches empty cavity transmission. Such of behavior was first observed by Gripp et.al. [96, 97] and was recently used to demonstrate fast optical switching by Dutta et.al. [14].

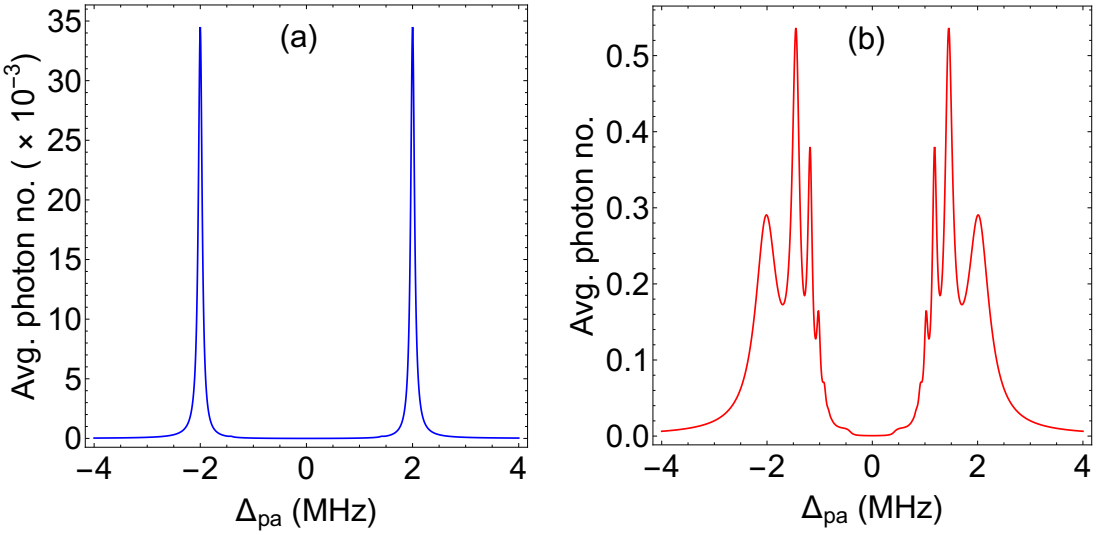

Fig. 4.22 Average intracavity photon number for the case of single atom in the cavity when the detuning of the probe is changed using full quantum calculation. (a) Shows normal VRS for $\eta = 0.1$ MHz. (b) Extra peaks start to appear corresponding to multi-photon absorptions when probe strength is increased to $\eta = 1.5$ MHz. Other parameters used here are, $\kappa_t/2\pi = 0.5$ MHz, $\Gamma/2\pi = 0.5$ MHz, $g/2\pi = 2$ MHz, and $\omega_{cv} = \omega_a$. The computation for this graph was done using QuTiP [98], a Quantum toolbox in Python programming language

There are two reasons for such behavior, first is the saturating effects of the cavity light and second is multi-photon absorption to the higher energy collective eigenstate of the atom-cavity system. Such multi-photon resonances appear when we perform a full quantum calculation as opposed to the semiclassical calculations in above sections which blur the discreetness of photons. We performed such computation for a single two-level atom, results of which are shown in figure 4.22. Such computations are feasible for only systems with small Hilbert space (few atoms and few photons) hence we use single atom as opposed to a multi-atom scenario of previous calculations. The observations [99–101] of multiple peaks from figure 4.22 (b) is considered to be a feature of atom-cavity interaction which can only be explained through quantization of cavity field and hence is direct evidence for field quantization.

4.5 Conclusions

In this chapter, we studied the atom-cavity system's ability to transmit resonant light in detail. The solutions for 4-level, 3-level, and 2-level atoms were solved for realistic atom-cavity parameters. The solutions were constructed for the case when the atoms are stationary in the cavity mode and generalized to the case when the atoms are exchanged with a reservoir. It is shown that the motion of the atoms is reflected in the transient properties of the transmitted light through the cavity. All the key features of the vapor cell experiment (4.1) are qualitatively understood on the basis of the theoretical analysis here. The possibility of adapting these systems for the study of multiple-bistability, multistability and with cold atom ensembles are exciting prospects for the future experiments. In addition, we extended our calculations for the atom-cavity system to study nonlinearity in frequency space.

Chapter 5

Lasing by driven atoms coupled to a cavity

We now discuss the interaction of fluorescing and continuously driven MOT atoms with the cavity mode. Cooled and trapped atoms are spatially localized, natural linewidth limited and have high local densities, which allows spectral and spatial overlap with cavity modes. When a large number of these atoms are contained within the cavity mode volume, and the atom-cavity system is brought into resonance, collective strong coupling of atoms and light alters the transmission properties of resonant probe light through the cavity [102, 35, 103, 104, 38, 12, 13, 39]. This manifests in a change from a single transmission peak per spatial electromagnetic (EM) mode with a Lorentzian lineshape for an empty cavity, to zero transmission of the probe on atomic resonance. Further scanning the probe light around the atomic transition, symmetric red and blue detuned transmission peaks are observed as discussed in section 4.2. The atom numbers in the present experiment are such that the collective strong coupling regime of atom-cavity mode interaction is accessible. We then pose the question, what is the effect of externally driven atoms on the coupled atom-cavity system? The answer is surprisingly different from the non-driven system. On scanning the cavity length, the system now emits light out of the cavity at red and blue detuning of the cavity with respect to the atomic resonance frequency. Evidence of lasing for the red detuning is obtained from the series of experiments discussed below. The lasing here is not due to population inversion in the gain medium but due to multiphoton processes as discussed in section 5.3. The lasing is seeded by spontaneous emission from the driven atoms and not by an external seed/probe laser. When this system is probed with a probe laser coupled to the cavity, Fano-like resonances and line narrowing are seen for the probe, which is much narrower than all the line widths that are natural to the system. All the observations put together provide irrefutable evidence of lasing by the driven atom-cavity system.

In recent times, understanding lasing with different gain mechanisms [105, 86, 106–110, 79, 111, 112] has accelerated. For example, one such process relies on quantum interference between probability amplitudes in multilevel atoms and does not require population inversion [105, 86]. Raman processes between different hyperfine levels and its sublevels [106–108], and levels involving external degrees of freedom [109, 110] have been exploited as gain mechanisms. Lasing from just a single atom [79] considerably enhanced our understanding of lasing action at the microscopic level. Much progress in understanding the role of collective effects on lasing [110–112] has been made. William *et.al* [108] showed lasing using three different gain mechanisms, Mollow gain, Raman transition between Zeeman sublevels and gain due to four-wave mixing, all of which were achieved with the same gain medium. Raman transition between Zeeman sublevels as gain was used by the same group to demonstrate random laser without any cavity and seed laser [113]. In the experiments here we demonstrate that continuous lasing seeded by spontaneous emission from the driven, non-inverted population of atoms in the cavity mode is possible and robust under reasonable experimental conditions. The gain mechanism for the lasing action is a result of multi-photon scattering [114, 16]. However, unlike previous work [108, 16], we observe lasing action even when the cavity is not driven by a seed laser. Lezama *et.al* [115] have earlier seen lasing in an atomic beam experiment, in a regime where atom-cavity coupling was very small for any co-operative effect to manifest.

5.1 The experiment

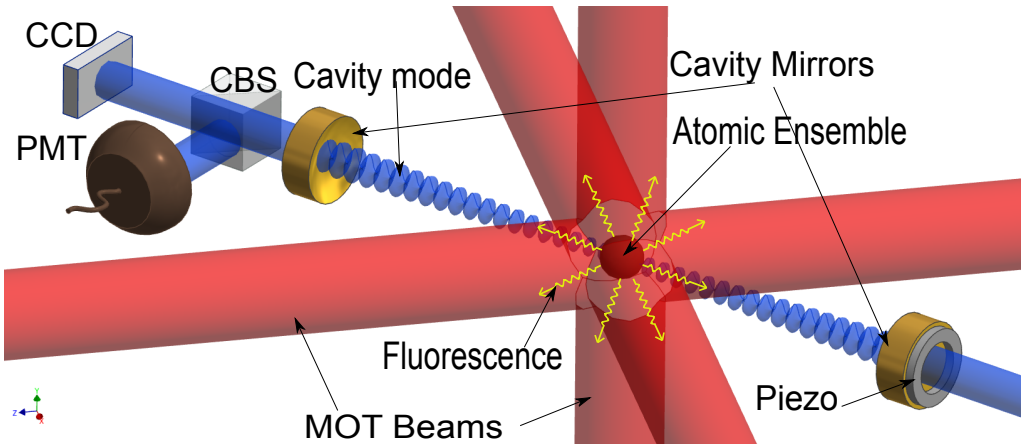

Fig. 5.1 Experimental schematics. ^{85}Rb atoms are cooled by the six red MOT beams and trapped with the help of magnetic gradient. The center of MOT beams and center of the cavity formed by the two mirrors overlap. PMT - Photomultiplier tube, CBS - Common beam splitter, CCD- Charge-coupled device camera.

The experimental schematic is as shown in the Fig. 5.1, ^{85}Rb atoms are cooled and trapped in a Magnet-optical trap (MOT). The center of the MOT and center of the enclosing Fabry-Pérot cavity are overlapped [116, 38]. The atomic ensemble is constantly illuminated by the six MOT light beams of 10 mm diameter and frequency red detuned by 13 MHz from the atomic transition (3-4′ transition of D2 line [91]). The magnetic field gradient of the MOT is 22 G/cm. No probe light is incident on the cavity mirrors apart from the experiments reported in Figs. 5.7 and 5.8. The atom-cavity is in collective strong coupling regime, i.e., $g_0\sqrt{N_c} > \Gamma, \kappa_t$ [103, 117]. Here $g_0/2\pi = 201$ kHz is maximum single atom coupling strength, $\Gamma/2\pi = 6.06$ MHz is atomic exited state decay rate, $2\kappa_t/2\pi = 9.5 \pm 0.1$ MHz is cavity full width at half maximum (FWHM), and N_c is an *effective number of atoms coupled to the cavity* which can be computed using overlap integral of the cavity mode and the observed atomic density profile as discussed in section 4.2. The free spectral range of the cavity is 3.28 GHz, the waist size of TEM_{00} cavity mode is 78 μm, and the spacing between the TEM modes is 180 MHz. Using an annular piezoelectric transducer (PZT) attached to one cavity mirror, the length of the cavity and hence

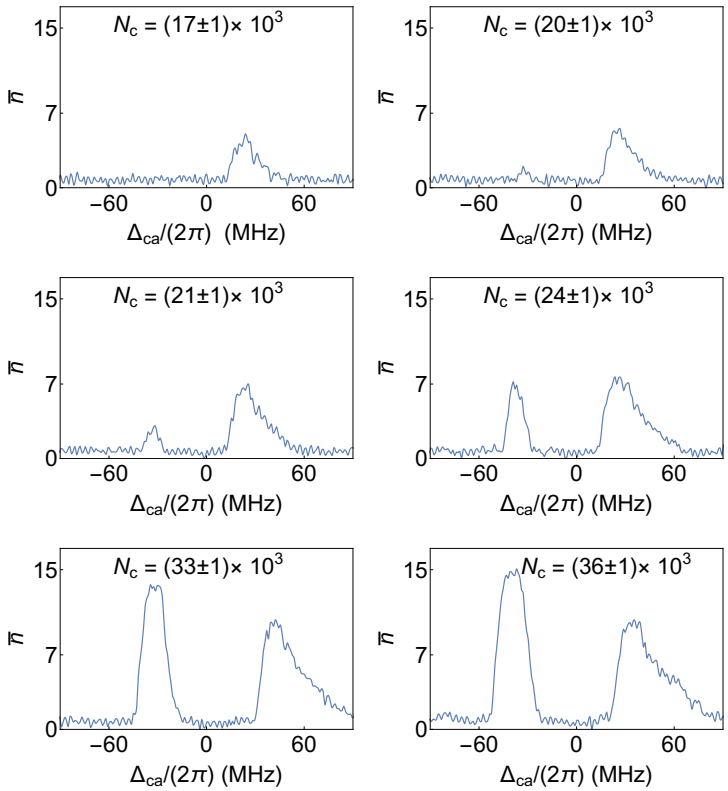

Fig. 5.2 Change in emission from the cavity when the atom number coupled to the cavity is varied. Total intensity of all cooling laser beams is 36 mW/cm^2 for all the measurements. $\Delta_{ca} = \omega_{cv} - \omega_a$ is detuning of empty cavity resonance from atomic transition and $\bar{n}$ is average intracavity photon number.

its resonance frequency (ω_{cv}) can be tuned. On scanning ω_{cv} around the atomic transition, with frequency ω_a (3-4′ transition of D2 line [91], which is also the cooling transition for the MOT), two peaks are observed in cavity emission. The cavity emission is monitored using a Photo Multiplier Tube (PMT) and a CCD camera. One peak is red detuned, and the other peak is formed blue detuned to the atomic transition at ω_a as shown in Fig. 5.2. The power of light coming out of the cavity measured in the PMT is converted to the average number of photons in the cavity, $\bar{n}$ by the expression, $\bar{n} = \frac{P_{out}}{2\hbar\omega_{cv}\kappa_r}$, where P_{out} is the power of light out of the cavity, $\omega_{cv}/(2\pi)$ is the frequency of cavity resonance, and $2\kappa_r/(2\pi)$ is the measured rate of transmission from one of the cavity mirror (the method to measure κ_r is given in subsection 2.3.4). Both these peaks show TEM_{00} spatial mode structure imaged in the camera, i.e., the cavity output has Gaussian intensity profile. Other spatial modes also show similar two peaked behavior. The peak heights and frequencies of both the peaks depend on N_c and power in the MOT beams. The red detuned peak is only visible above a critical number of atoms ($N_c \sim 20 \times 10^3$) and grows rapidly to dominate the blue detuned peak for atom number $N_c \sim 27 \times 10^3$ as seen from the Fig. 5.3(b). In addition, from Fig. 5.2 the peaks are seen to broaden as N_c increases. It should be noted that the width of the red detuned peak is narrower than the blue detuned peak in all the measurements. The dependence of the peak separation as a function of N_c, when the cavity length is scanned across the atom-cavity resonances is illustrated in Fig. 5.3(a). The blue dots show corresponding vacuum Rabi splitting (VRS) calculated for the same number of atoms and cavity parameters when the cavity is on the atomic resonance, and external weak probe light scans the atom-cavity system. From this close

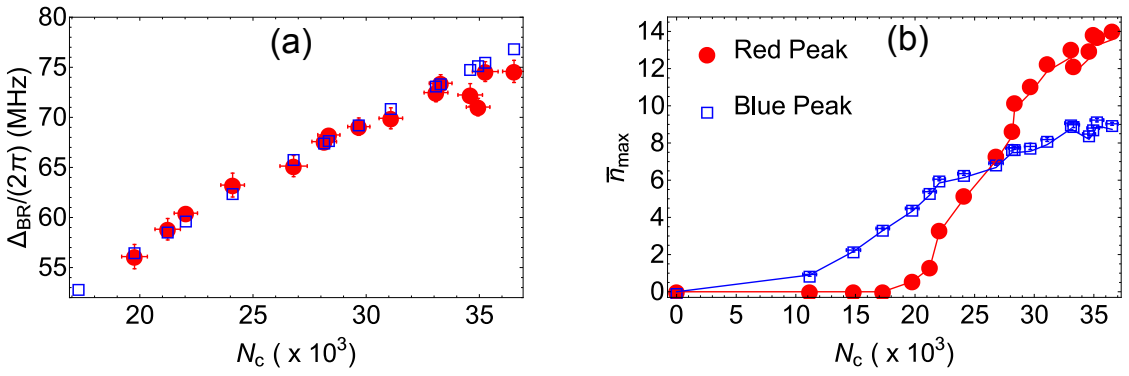

Fig. 5.3 (a) Red dots with error bars show the change in peak separation of the cavity emission with N_c. Blue empty squares are corresponding calculated VRS ($2g_0\sqrt{N_c}$) values. $\Delta_{BR}/(2\pi)$ - The frequency separation between the maximum of red and blue detuned peaks (b) Variation in the height of red and blue detuned peaks. In the range of measurement, the red peak shows a threshold behavior with atom number whereas the blue peak does not. $\bar{n}_{max}$ - Maximum intracavity photon number for the red and blue detuned peaks. Total intensity of all cooling laser beams is 36 mW/cm^2 for all the measurements.

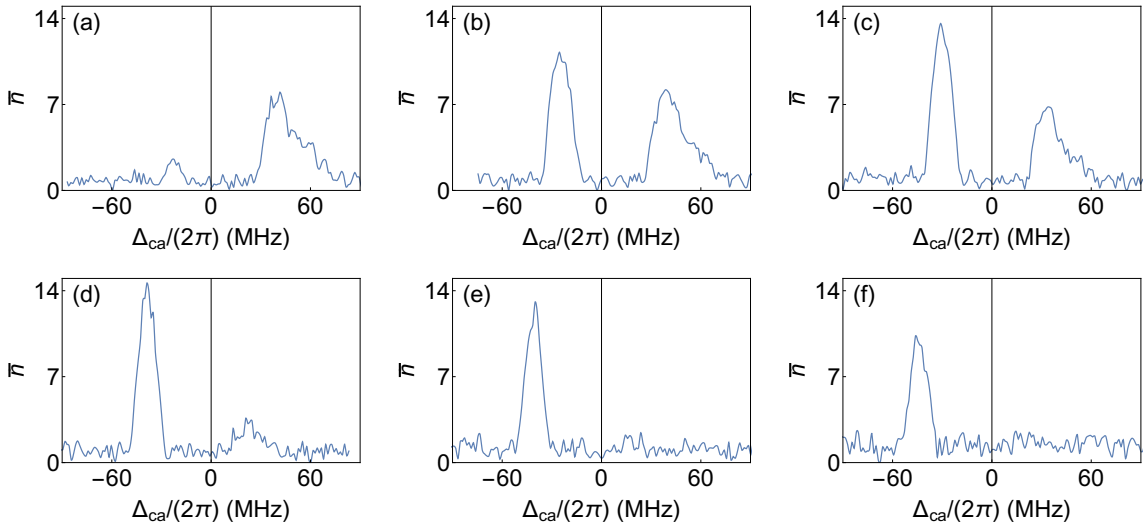

Fig. 5.4 Change in emission from the cavity when total intensity of MOT laser is varied. Intensities and atoms coupled (N_c) are (a) 22 mW/cm^2 and $(35 \pm 1) \times 10^3$, (b) 30 mW/cm^2 and $(33 \pm 1) \times 10^3$, (c) 36 mW/cm^2 and $(29 \pm 1) \times 10^3$, (d) 45 mW/cm^2 and $(24 \pm 1) \times 10^3$, (e) 60 mW/cm^2 and $(21 \pm 1) \times 10^3$, (f) 75 mW/cm^2 and $(23 \pm 1) \times 10^3$ respectively.

agreement between the measured frequency split and the VRS calculation we can see that the observed split depends on $g_0\sqrt{N_c}$, similar to VRS, and hence we conclude that the observed splitting and the atom-cavity collective strong coupling are very closely related. However, this is the case only beyond a certain atom number in the cavity mode. Below a critical value of N_c, the red-detuned peak disappears while the blue detuned peak persists, as seen in Fig. 5.3(b). Here a clear threshold is seen in the measured heights of the red detuned peak, while the blue detuned peak shows no threshold over the measurement range. It is also evident from Fig. 5.3(a) and Fig. 5.3(b) that the agreement with the VRS calculation starts degrading at the larger values of N_c, which coincides with the tendency towards saturation of the red detuned peak height. The intensity of the MOT beams for these measurements was 36 mW/cm^2. The atom number is varied by changing the pressure of background atoms from which the ultracold atoms are loaded by laser cooling using the MOT beams. This is done by changing the intensity of deep blue LED's mounted on the vacuum system. Blue wavelengths are very efficient at desorbing alkali atoms from the glass viewports and result in changes in vapor pressure. The detuning $\Delta_{ca}/(2\pi)$ is calibrated by monitoring the transmission of a laser beam which is frequency stabilized to the atomic transition through the cavity. For this, the scanning parameters are kept the same and there are no atoms in the cavity. The calibration between the voltage applied to the PZT and shift in frequency of the cavity resonance which is scanned is achieved by measuring the spectrum of a frequency stabilized laser with 20 MHz sidebands using the experimental cavity scan.

Given the qualitative difference in the nature of the red and blue detuned peaks, and the fact that the red detuned peak shows threshold behavior, indicative of lasing it is important to determine the effect of driving the MOT atoms deeper into saturation on the two peaks. For very low power the red detuned peak vanishes and when the power in MOT laser is high the blue detuned peak vanishes as can be seen in Fig. 5.4. Increasing the power increases total atom number but also increases the spatial size of the atomic cloud in MOT. The increase in size is attributed to an increase in temperature of the MOT atoms [118–120]. The increase in size lowers N_c, and as fewer atoms overlap the cavity mode, the rate of fluorescence into the cavity decreases reducing the size of the blue detuned peak. Lower number of N_c should also result in reduction of red detuned peak according to Fig. 5.3(b). However, when the atoms are driven harder two factors play a role in higher amplitude of red detuned peak, (a) the relative fluorescence into the Mollow sidebands of the fluorescence spectrum increases (see Fig. A.2 of Appendix A) and (b) the rate of stimulated emission for red detuned peak increases as will be clear in the section which discusses the gain mechanism for lasing in red detuned peak. However, once the lasing starts to saturate, the effects of the increase in the size of atomic cloud and reduction in N_c lead to a reduction in amplitude of red detuned peak as can be seen from Figs. 5.4(e) and 5.4(f). This provides experimental evidence of crucial differences between the blue and red detuned emission peaks.

5.2 Signatures of lasing

The threshold behavior seen only in the red detuned peak in Fig. 5.3(b) is suggestive of lasing in this driven atomic system coupled to the cavity mode. In lasing one mode experiences large gain compared to others as stimulated emission ensures that the dominant mode wins. As a check for lasing by the atom-cavity system, we check for purity of the state of light that comes out of the cavity. The first check is for the polarization state of the cavity emitted light using a polarizer (Thorlabs LPNIRE100-B) with variable polarization angle in between the cavity mirror and the PMT. Fig. 5.5(a) shows the change in peak height of both red and blue detuned peaks as the polarization angle is changed. The polarization of the red detuned peak is considerably purer than that of the blue detuned peak. From the fits to data, the visibility for the red detuned peak is around 95 % and for the blue detuned peak is around 43 %. The small systematic change in amplitude with polarizer angle is due to the slight decrease in atom number as the measurement progressed. In addition, Fig. 5.5(b) shows that the shape of the blue detuned peak depends on polarizer angle. The peak and the wings of the blue detuned peak show different polarizations. This shows that the light out of the cavity for the red peak is strongly polarized and indicative of a single cavity mode present. On the other hand, the

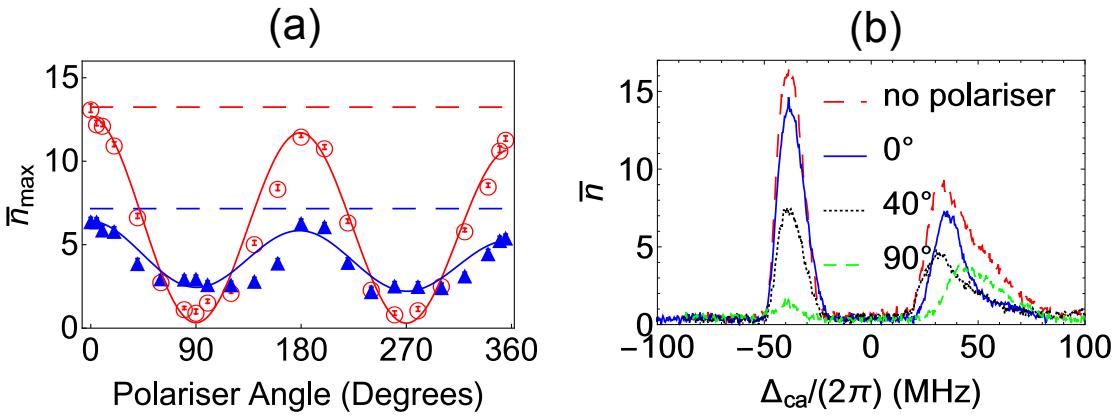

Fig. 5.5 (a) Polarization diagnosis of the light coming out of the cavity. Blue filled triangles denote the height of the blue detuned peak, and red empty circles denote the height of the red detuned peak. Red dashed and blue dashed are peak values when we don't have a polarizer in the cavity output path multiplied by transmission coefficient of the polarizer. The smooth curves are obtained by fitting cosine function multiplied by a linear function, $\left(\mathrm{a}+\mathrm{b}\cos\left[\frac{\pi}{180}x\right]\right)(1-\mathrm{c}x)$. The linear function is used to correct for the systematic effect of atom number decrease during long measurements. Cavity output profile for different polarizer angles, (b) no polarizer (c) 0 degrees (d) 40 degrees (e) 90 degrees. Here, the total intensity of MOT cooling laser beams is 36 mW/cm^2 and $N_c = (26 \pm 1) \times 10^3$ for all the measurements.

blue detuned peak has multiple polarization states in coexistence, which is indicative of no mode competition and therefore is detected as a mixture of several simultaneously existing polarization states. The consistent explanation for this is that the light out of the cavity for the red peak is lasing. All the data mentioned above was for TEM_{00} spatial mode as there are no nearby spatial modes within the cavity linewidth which will compete with the TEM_{00} spatial mode, the only competition is between the polarization states of the spatial mode. The existence of single spatial mode is verified by imaging the spatial mode of light emitted by the cavity. However, for higher spatial modes there is competition between the cylindrical and rectangular modes which are nearly degenerate as can be seen explicitly from Fig. 5.6. Again, similar to the polarization states, a single dominant spatial mode is observed for the red detuned peak while the blue detuned cavity emission peak shows multiple spatial modes of similar intensities. Experimentally, the purity of polarization and the spatial mode is strong evidence in support of lasing in the case of the red detuned peak. The sharp threshold for the red detuned peak and the rapid increase in peak height as the atom number is increased is characteristic of lasing behavior arising due to non-linear response with an increase in gain [15].

To determine the frequency at which the gain occurs, we pass a probe beam through the cavity and monitor the transmission. Fig. 5.7(a) shows the transmitted intensity when the frequency of the probe beam is scanned while keeping the cavity detuning fixed on the red

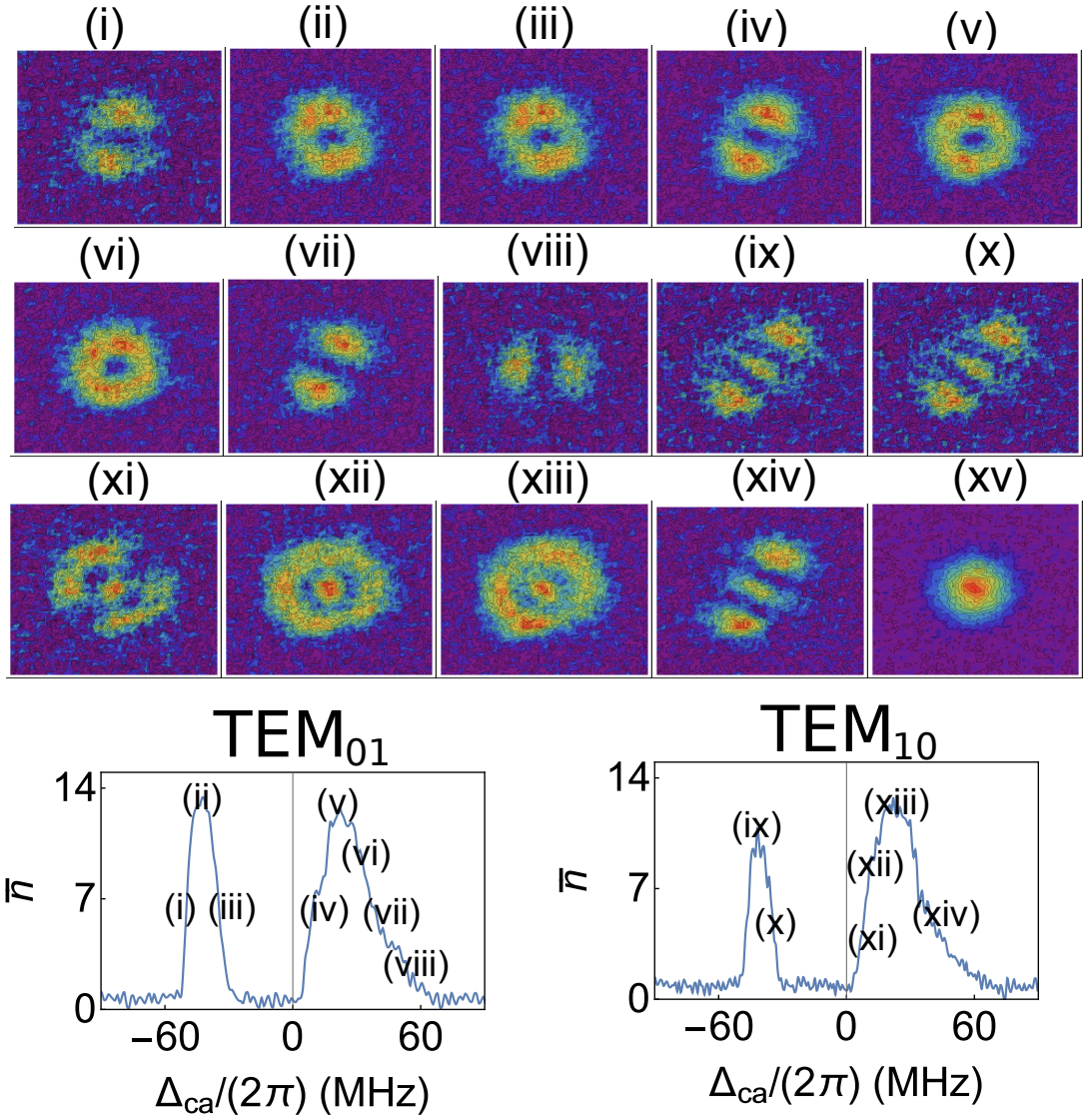

Fig. 5.6 Modes of the cavity as seen on a CCD camera at various detunings of the cavity. Letters (a)-(h) are for TEM_{01} mode, and (i)-(n) are for TEM_{10} mode. (o) Shows an instance of TEM_{00} mode. Here, the power of MOT cooling laser is 36 mW/cm^2, and for TEM_{00} mode $N_c = (33 \pm 1) \times 10^3$, it will be lower for higher order modes.

detuned peak of the last panel in Fig. 5.2(a). The blue trace represents the output with MOT atoms, and the red trace is the output when there are no atoms in MOT (the magnetic field of the MOT is switched off). As is evident from the differences in the transmission in Fig. 5.7, the probe beam experiences gain which is more than the total losses when interacting with atoms inside the cavity. The shift between blue and the red curve is due to lasing without any probe laser as we make sure that the cavity detuning is fixed on the red peak of the

last panel in Fig. 5.2(a). In addition to gain, the blue trace also shows a Fano-like profile indicating interference between two or multiple probability amplitudes for emission [121] which suppresses the lasing action. Fig. 5.7(b) shows line narrowing even in the absence of Fano profile 5.5 MHz red of the red detuned peak of the last panel in Fig. 5.2(a). A similar experiment on the blue detuned peak attenuates and shows a tendency to broaden the transmitted light.

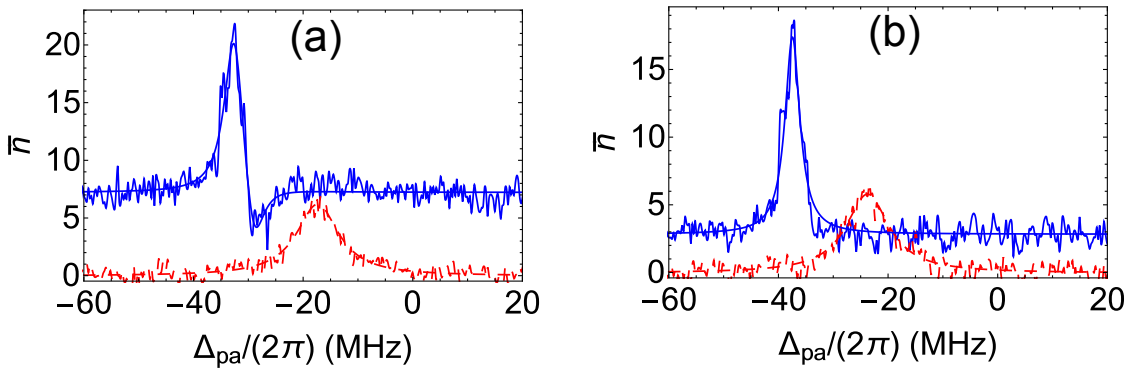

Fig. 5.7 The blue trace shows cavity probe transmission when driven atoms are present in the cavity, and the broken red trace is probe transmission curve without atoms. (a) This figure shows a gain and Fano-type structure in the presence of atoms. The cavity length is such that we are near the top of the red detuned peak of Fig. 5.2(e). We can see a gain in the probe at around 33 MHz. The blue curve in the background is fit to the sum of a Lorentzian and a inverted Lorentzian both of FWHM 4.5 MHz, and the red dashed curve for the empty cavity is a Lorentzian with FWHM of 9.5 MHz. (b) This figure shows line narrowing and gain without the Fano structure when the cavity is slightly red of the red detuned peak of Fig. 5.2(e). A Lorentzian fit to the blue trace gives FWHM of 3.3 MHz and is shown as the blue curve. Here, the total intensity of MOT cooling laser beams is 36 mW/cm^2 and $N_c = (33 \pm 1) \times 10^3$ for all the measurements.

5.3 Gain mechanism and collective strong coupling

The phenomenon of gain in probe beam when two-level atoms are strongly driven by another drive laser is well known. B. R. Mollow was first to predict such gain mechanism [122] using semi-classical arguments and phenomenologically including atomic decay rates. Haroche *et.al* [123] reported similar calculations in the same year. This was later observed in an experiment with sodium beam by Wu *et.al* [16]. Grynberg *et.al* [114] later proposed a microscopic description for gain in the above experiments and calculated the cross-section of various relevant multiphoton processes using perturbation theory. For this, they analyzed processes involving spontaneous emission of one and two photons. For the parameters they considered, out of

all the photon scattering processes in which only one photon is spontaneously emitted, the scattering processes leading to absorption of the probe photon dominates. Hence, single photon emission processes always lead to net absorption of the probe photon. They then showed that processes resonant in dressed state picture which involve spontaneous emission of two photons result in both absorption and amplification of the probe beam (see Fig. A.3 of Appendix A for diagrammatic representation of the processes.). However, these have equal cross-sections and hence cancel out. This balance is changed by interference between resonant and non-resonant absorption probability amplitudes involving emission of two spontaneous emission photons. This interference leads to a term in the cross section for absorption proportional to $|\Omega|^4(\omega_d - \omega_p)/\Delta_{da}^3$, where $\omega_p/(2\pi)$ is frequency of the probe laser, $\omega_d/(2\pi)$ is frequency of the drive laser, $\Delta_{da} = (\omega_d - \omega_a)$ is detuning of drive laser from the atomic transition, and $2\Omega/(2\pi)$ is Rabi frequency of the drive laser. For $\Delta_{da}(\omega_d - \omega_p) < 0$ this interference term will have a negative sign and hence will reduce the absorption cross section for the probe photon. In this case, the non-resonant processes leading to probe photon amplification were negligible compared to non-resonant processes leading to probe photon absorption hence was neglected resulting in no change in the amplification cross section. This decrease in absorption for a probe photon can lead to net amplification which is the source of gain in such systems. Additionally, this reduction in absorption is proportional to $|\Omega|^4$, i.e. $\propto I_d^2$, where I_d is the intensity of the drive beam, which explains the rapid increase in red detuned peak in Fig. 5.4. The mechanism for the gain in our experiment is similar to the description of Grynberg *et.al* [114], with the additional consideration that the cavity-atom collective strong coupling regime introduces certain differences discussed below.

In the regime defined by collective strong coupling, weak probe transmission through the cavity is split into two peaks when resonant atoms are present in the cavity due to VRS [102, 103, 117, 104]. Fig. 5.8(a) is a measurement of such a split for which the MOT lasers were switched off, and all the atoms were in the ground state [38]. Here, if the cavity resonance frequency is matched with the atomic frequency we see symmetric splitting on the red and the blue side of the atomic resonance. However, if the cavity resonance is blue (red) detuned with respect to the atomic frequency the blue (red) detuned VRS peak is bigger than red (blue) detuned one [117] and blue (red) peak shifts away (towards) from atomic frequency. However, when the drive laser with a frequency different from atomic transition is switched on, symmetry is broken because of unequal gain and loss. Fig. 5.8(b,c,d) shows such a scenario. For Fig. 5.8(b), when the MOT drive lasers are present, the frequency spectrum remains unchanged, but the heights are completely different, indicating an unequal total loss. The drive (MOT cooling laser) is to the red side of atomic frequency. For Fig. 5.8(c) even though the cavity resonance is set to the blue of the atomic resonance, the red detuned peak is dominant. In the

absence of drive laser, the height of blue detuned peak would have increased, and the height of red detuned peak would have diminished. However, due to Mollow gain in the the red detuned probe and Mollow loss in the blue detuned probe in the presence of the red detuned drive we see the opposite in Fig. 5.8(c) with respect to what is expected in the case when the atoms are not optically driven. Equal height for the two peaks is obtained when the cavity resonance is 8 MHz detuned towards blue of atomic frequency as shown in Fig. 5.8(d). In addition to this, there also seems to be gain around -13 MHz which is the drive frequency. This is because of coherent energy exchange between drive and cavity. The observations mentioned above are compared with the results of a semi-classical theory in the discussion section.

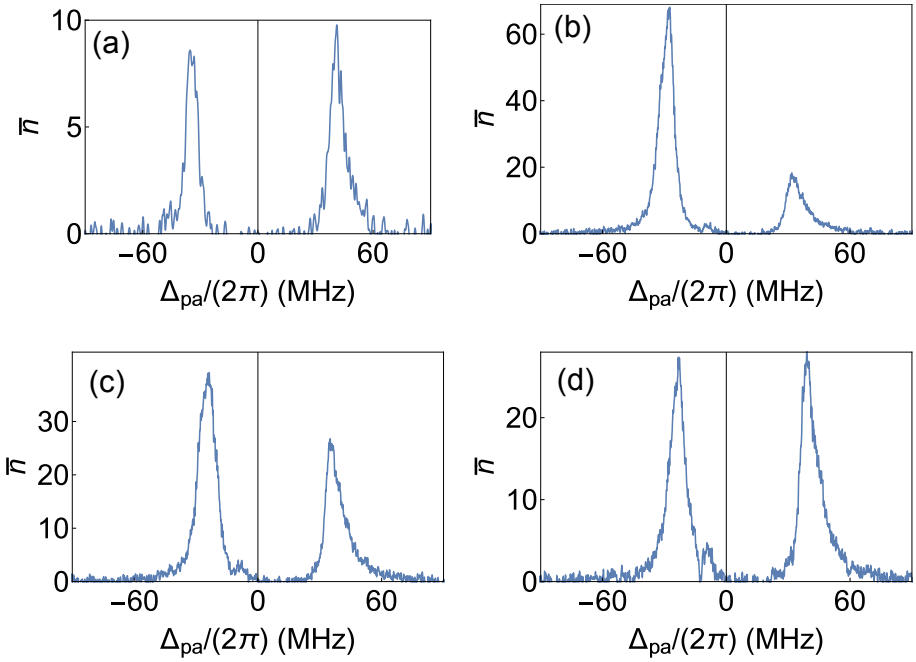

Fig. 5.8 Probe transmission spectra when atoms are present inside the cavity. (a) Without MOT laser and cavity freq same as atomic. (b) With MOT laser and cavity freq. same as atomic freq. (c) With MOT laser and cavity freq. towards blue of atomic freq. (d) With MOT laser and cavity freq. more towards blue of atomic freq to make the heights of the peak same. For (a)-(d) $N_c = (25 \pm 1) \times 10^3$ and power in MOT laser is 36 mW/cm^2

In addition to gain in the probe, we also observe lasing without any seeding (no probe light). This is because of the coupling of light into the cavity by the fluorescing atoms. B. R. Mollow was first to calculate the fluorescence spectrum of a two level atom driven by a strong monochromatic laser [124]. Such a spectrum can be computed from fluctuations of atomic coherence [55]. The details of this computation are given in Appendix A, and the results are shown in the Fig. A.1 of Appendix A. There is some light at $\sim$ 30 MHz red of the atomic

transition. This resonance fluorescence provides the seed which is then amplified by the driven atoms.

5.4 Theoretical Model for gain in probe light

The interpretation of the observed gain rests on the theoretical work of B. R. Mollow [122] and Grynberg *et.al* [114] which was for a free-space probe beam and hence their theoretical modeling did not include a cavity. Additionally, Grynberg *et.al* [114] in their full quantum calculations assumed $4|\Omega/\Delta_{\mathrm{da}}|^2 \ll 1$ in order to perform the calculations using perturbation theory. In our experiment, $4|\Omega/\Delta_{\mathrm{da}}|^2 \sim 1$ hence the perturbation approach is not possible, and a full quantum calculation is very challenging. Hence, in order to quantitatively compare our experiment with a theory, we modeled our experimental system using the semi-classical theory of light-matter interactions adapted from the calculations of B. R. Mollow [122]. The model contains all the essential elements required to show gain consistent with the experimental observations. We consider 2-level atoms coupled to one of the modes of a Fabry-Pérot cavity, which is probed by a monochromatic laser of frequency $\omega_{\mathrm{p}}/(2\pi)$ and the atoms are driven by a single drive laser with frequency $\omega_{\mathrm{d}}/(2\pi)$. The probe and drive light fields are assumed to be classical. The Hamiltonian for a system of driven N two-level atoms interacting with a cavity driven by a probe laser can be written as [55, 86, 87],

$$\hat{H} = \hbar\omega_{\mathrm{cv}}\,\hat{a}^{\dagger}\hat{a} + \hbar\left\{\eta^{*}\hat{a}e^{-i\omega_{\mathrm{p}}t} + \eta\hat{a}^{\dagger}e^{i\omega_{\mathrm{p}}t}\right\} + \sum_{j=1}^{N}\hbar\left\{\frac{\omega_{\mathrm{a}}}{2}\hat{\sigma}_j^{z} + g_j\left(\hat{a}^{\dagger}\hat{\sigma}_j^{-} + \hat{a}\hat{\sigma}_j^{+}\right)\right\} + \sum_{j=1}^{N}\hbar\left\{\Omega^{*}\hat{\sigma}_j^{-}e^{i\omega_{\mathrm{d}}t} + \Omega\hat{\sigma}_j^{+}e^{-i\omega_{\mathrm{d}}t}\right\}. \tag{5.1}$$

Where, the various quantities are defined in section 4.2.

Rate equations

The evolution equation for the expectation value for an operator $\hat{X}$ can be evaluated using the Heisenberg equation 4.1. In addition to this unitary evolution, we introduce non-unitary decay rates κ_{t} and Γ phenomenologically for cavity field and atoms respectively. This approach is similar to the one taken by B. R. Mollow [122]. For the calculation here, the cavity field is assumed to be classical and is denoted by a coherent state $|\alpha\rangle$. Eqn. 4.1 for system variables

give,

$$\frac{d\alpha(t)}{dt} = -\kappa_t\alpha(t) - i\omega_{cv}\alpha(t) - i\sum_{j=1}^{N} g_j\rho_j(t) - \eta e^{-i\omega_p t} \tag{5.2a}$$

$$\frac{d\rho_j(t)}{dt} = -\left\{\frac{\Gamma}{2} + i\omega_a\right\}\rho_j(t) + i(g_j\alpha(t) + \Omega e^{-i\omega_d t})(2\rho_{e,j}(t) - 1)$$

$$\frac{d\rho_{e,j}(t)}{dt} = -\Gamma\rho_{e,j}(t) + i\left\{(g_j\alpha^*(t) + \Omega^* e^{i\omega_d t})\rho_j(t) - (g_j\alpha(t) + \Omega e^{-i\omega_d t})\rho_j^*(t)\right\} \tag{5.2b}$$

where $\rho_j = \left\langle \sigma_j^- \right\rangle$ is coherence of the j^{th} atom, $\alpha = \langle \hat{a} \rangle$ is field amplitude inside the cavity and $\rho_{e,j} = \left\langle \sigma_{e,j} \right\rangle$ is excited state population.

As multiple frequencies are involved, we transform the time-dependent equations (5.2) into Fourier space. For the cavity field and atomic coherences the Fourier transforms are, $\alpha(t) = \int_{-\infty}^{\infty}\tilde{\alpha}(\omega)e^{-i\omega t}d\omega$ and $\rho_j(t) = \int_{-\infty}^{\infty}\tilde{\rho}_j(\omega)e^{-i\omega t}d\omega$ respectively. As $\rho_{e,j}(t)$ is always real, its Fourier transform takes the form, $\rho_{e,j}(t) = \int_{-\infty}^{\infty}\frac{1}{2}(\tilde{\rho}_{e,j}(\omega)e^{-i\omega t} + \tilde{\rho}_{e,j}^*(\omega)e^{i\omega t})d\omega$ with the relation $\tilde{\rho}_{e,j}^*(-\omega) = \tilde{\rho}_{e,j}(\omega)$. This relation can be verified by replacing ω with $-\omega$ in Fourier relation of $\rho_{e,j}(t)$. The inverse transforms are, $\tilde{\alpha}(\omega) = \int_{-\infty}^{\infty}\alpha(t)e^{-i\omega t}dt$, $\tilde{\rho}_j(\omega) = \int_{-\infty}^{\infty}\rho_j(t)e^{i\omega t}dt$. $\tilde{\rho}_{e,j}(\omega) = \int_{-\infty}^{\infty}\rho_{e,j}(t)e^{i\omega t}dt$ and $\tilde{\rho}_{e,j}^*(\omega) = \int_{-\infty}^{\infty}\rho_{e,j}(t)e^{-i\omega t}dt$. To transform Eqns. 5.2 into Fourier space we multiply Eqn. (5.2a) and Eqn. (5.2b) by $e^{i\omega t}$, and multiply Eqn. (5.2c) by $e^{-i\omega t}$. Integrating w.r.t time, $\int_{-\infty}^{\infty}dt$ gives a set of equations,

$$-i\omega\tilde{\alpha}(\omega) = -\kappa_t\tilde{\alpha}(\omega) - i\omega_{cv}\tilde{\alpha}(\omega) - i\sum_{j=1}^{N} g_j\tilde{\rho}_j(\omega) - \eta\,\delta(\omega - \omega_p) \tag{5.3a}$$

$$-i\omega\tilde{\rho}_j(\omega) = -\left\{\frac{\Gamma}{2} + i\omega_a\right\}\tilde{\rho}_j(\omega) + ig_j\left\{2(\tilde{\alpha}\odot\tilde{\rho}_{e,j}^*)(\omega)_- - \tilde{\alpha}(\omega)\right\}$$
$$+ i\Omega\left\{2\tilde{\rho}_{e,j}^*(\omega_d - \omega) - \delta(\omega - \omega_d)\right\} \tag{5.3b}$$

$$i\omega\tilde{\rho}_{e,j}^*(\omega) = -\Gamma\tilde{\rho}_{e,j}^*(\omega) + ig_j\left\{(\tilde{\alpha}^*\odot\tilde{\rho}_j)(\omega)_- - (\tilde{\alpha}\odot\tilde{\rho}_j^*)(\omega)_+\right\}$$
$$+ i\left\{\Omega^*\tilde{\rho}_j(\omega_d - \omega) - \Omega\tilde{\rho}_j^*(\omega_d + \omega)\right\}. \tag{5.3c}$$

Here, the definition of Dirac delta function $\delta(\omega - \omega') = \int_{-\infty}^{\infty}e^{-i(\omega-\omega')t}dt$ is used.
$(\tilde{\alpha}\odot\tilde{\rho}_j^*)(\omega)_\pm = \int\tilde{\alpha}(\omega_1)\tilde{\rho}_j^*(\omega_1 \pm \omega)d\omega_1$ are convolution functions where $\odot$ denotes convolu-

tion operation and are derived as follows,

$$\begin{aligned}
&\int_{-\infty}^{\infty} \alpha(t)\rho_{e,j}(t)e^{i\omega t}dt \\
&= \frac{1}{2}\int_{-\infty}^{\infty}\int_{-\infty}^{\infty}\int_{-\infty}^{\infty} \tilde{\alpha}(\omega_1)e^{-i\omega_1 t}\left[\tilde{\rho}_{e,j}(\omega_2)e^{-i\omega_2 t}+\tilde{\rho}^*_{e,j}(\omega_2)e^{i\omega_2 t}\right]e^{i\omega t}dt\ d\omega_1\ d\omega_2 \\
&= \frac{1}{2}\int_{-\infty}^{\infty}\int_{-\infty}^{\infty} \tilde{\alpha}(\omega_1)\left[\tilde{\rho}_{e,j}(\omega_2)\delta(\omega_2+\omega_1-\omega)+\tilde{\rho}^*_{e,j}(\omega_2)\delta(\omega_2-\omega_1+\omega)\right]d\omega_1\ d\omega_2 \\
&= \frac{1}{2}\int_{-\infty}^{\infty} \tilde{\alpha}(\omega_1)\left[\tilde{\rho}_{e,j}(\omega-\omega_1)+\tilde{\rho}^*_{e,j}(\omega_1-\omega)\right]d\omega_1 \\
&= \int_{-\infty}^{\infty} \tilde{\alpha}(\omega_1)\tilde{\rho}^*_{e,j}(\omega_1-\omega)d\omega_1 = (\tilde{\alpha}\odot\tilde{\rho}^*_{e,j})(\omega)_-,
\end{aligned} \tag{5.4}$$

$$\begin{aligned}
&\int_{-\infty}^{\infty} \alpha(t)\rho^*_j(t)e^{-i\omega t}dt \\
&= \int_{-\infty}^{\infty}\int_{-\infty}^{\infty}\int_{-\infty}^{\infty} \tilde{\alpha}(\omega_1)e^{-i\omega_1 t}\tilde{\rho}^*_j(\omega_2)e^{i\omega_2 t}e^{-i\omega t}dt\ d\omega_1\ d\omega_2 \\
&= \int_{-\infty}^{\infty}\int_{-\infty}^{\infty} \tilde{\alpha}(\omega_1)\tilde{\rho}^*_j(\omega_2)\delta(\omega_2-\omega_1-\omega)d\omega_1\ d\omega_2 \\
&= \int_{-\infty}^{\infty} \tilde{\alpha}(\omega_1)\tilde{\rho}^*_j(\omega_1+\omega)d\omega_1\ = (\tilde{\alpha}\odot\tilde{\rho}^*_j)(\omega)_+.
\end{aligned} \tag{5.5}$$

and similarly,

$$\int_{-\infty}^{\infty} \alpha^*(t)\rho_j(t)e^{-i\omega t}dt = (\tilde{\alpha^*}\odot\tilde{\rho}_j)(\omega)_-. \tag{5.6}$$

These derivations are similar to the proof of Fourier convolution theorem [125].

In absence of a cavity, the equations for atomic variables are,

$$-\left\{\frac{\Gamma}{2}+i\Delta_{da}\right\}\tilde{\rho}(\omega_d)+i\Omega\{2\tilde{\rho}^*_e(0)-1\}=0 \tag{5.7a}$$

$$-\Gamma\tilde{\rho}^*_e(0)+i\{\Omega^*\tilde{\rho}(\omega_d)-\Omega\tilde{\rho}^*(\omega_d)\}=0. \tag{5.7b}$$

In the absence of a cavity all the atoms behave in same way. This is because all are driven equally by the classical drive field. Hence, the j subscript is removed as the atom-field interaction strength is same for all the atoms. The atomic coherence oscillates only at the driving frequency ω_d and all other frequency components are zero. $\Delta_{da}=\omega_d-\omega_a$ is detuning of drive laser from the atomic transition. Solving for the coherence term and excited state

population in the absence of cavity gives,

$$\tilde{\rho}(\omega_{\mathrm{d}}) = \frac{-2i\Omega(2i\Delta_{\mathrm{da}}+\Gamma)}{\Gamma^2+4\Delta_{\mathrm{da}}^2+8|\Omega|^2} \tag{5.8}$$

and

$$\tilde{\rho}_{\mathrm{e}}(0) = \frac{4|\Omega|^2}{\Gamma^2+4\Delta_{\mathrm{da}}^2+8|\Omega|^2}. \tag{5.9}$$

Perturbative calculation

For our experiment, $\Omega^2 \gg g_0^2|\alpha|^2$ and hence the effect of the cavity on the atoms is very small and adds only small perturbations to values in (5.8) and (5.9). The perturbed atomic variables can be written as, $\tilde{\rho}_j(\omega) = \tilde{\rho}(\omega_{\mathrm{d}})\delta(\omega-\omega_{\mathrm{d}}) + \tilde{\varepsilon}_j(\omega)$, $\tilde{\rho}_{\mathrm{e},j}(\omega) = \tilde{\rho}_{\mathrm{e}}(0)\delta(\omega) + \tilde{\varepsilon}_{\mathrm{e},j}(\omega)$and $\tilde{\rho}^*_{\mathrm{e},j}(\omega) = \tilde{\rho}_{\mathrm{e}}(0)\delta(\omega) + \tilde{\varepsilon}^*_{\mathrm{e},j}(\omega)$. Here, ε is perturbation to density matrix elements of atoms due to interaction with the cavity. Keeping only the unperturbed part in the convolution functions of Eqns. 5.3 gives a set of linear equations,

$$-i\omega\tilde{\alpha}(\omega) = -\kappa_{\mathrm{t}}\tilde{\alpha}(\omega) - i\omega_{\mathrm{cv}}\tilde{\alpha}(\omega) - i\sum_{j=1}^{N} g_j\tilde{\rho}_j(\omega) - \eta\,\delta(\omega-\omega_{\mathrm{p}}) \tag{5.10a}$$

$$\begin{aligned}-i\omega\tilde{\rho}_j(\omega) = &-\left\{\frac{\Gamma}{2}+i\omega_{\mathrm{a}}\right\}\tilde{\rho}_j(\omega) + ig_j\tilde{\alpha}(\omega)\{2\tilde{\rho}_{\mathrm{e}}(0)-1\} \\ &+i\Omega\left\{2\tilde{\rho}^*_{\mathrm{e},j}(\omega_{\mathrm{d}}-\omega) - \delta(\omega-\omega_{\mathrm{d}})\right\}\end{aligned} \tag{5.10b}$$

$$\begin{aligned}i\omega\tilde{\rho}^*_{\mathrm{e},j}(\omega) = &-\Gamma\tilde{\rho}^*_{\mathrm{e},j}(\omega) + ig_j\{\tilde{\alpha}^*(\omega_{\mathrm{d}}+\omega)\tilde{\rho}(\omega_{\mathrm{d}}) - \tilde{\alpha}(\omega_{\mathrm{d}}-\omega)\tilde{\rho}^*(\omega_{\mathrm{d}})\} \\ &+i\left\{\Omega^*\tilde{\rho}_j(\omega_{\mathrm{d}}-\omega) - \Omega\tilde{\rho}^*_j(\omega_{\mathrm{d}}+\omega)\right\}.\end{aligned} \tag{5.10c}$$

In zero$^{\mathrm{th}}$ order of the atomic terms, the cavity field gets an additional term,

$$i\sum_{j=1}^{N} g_j\tilde{\rho}_j(\omega) = i\sum_{j=1}^{N} g_j\left\{\tilde{\rho}(\omega_{\mathrm{d}})\delta(\omega-\omega_{\mathrm{d}}) + \tilde{\varepsilon}_j(\omega)\right\} \approx i\sum_{j=1}^{N} g_j\tilde{\rho}(\omega_{\mathrm{d}})\delta(\omega-\omega_{\mathrm{d}}) \tag{5.11}$$

This requires $\omega_{\mathrm{p}} = \omega_{\mathrm{d}}$ as seen in Eqn. (5.11) and results in an elastic exchange of energy from drive field to cavity field via atoms and the cavity will gain photons even if it is not driven by an external field.

For other frequencies the perturbation term $\tilde{\varepsilon}_j(\omega)$ is important. Hence we proceed to derive it using Eqn. (5.10). Eqn. (5.10b) can be rewritten as,

$$\begin{aligned}
&-\left\{\frac{\Gamma}{2}+i\Delta_{\rm a}(\omega)\right\}\tilde{\varepsilon}_j(\omega)+ig_j\tilde{\alpha}(\omega)\left\{2\tilde{\rho}_{\rm e}(0)-1\right\}+i\Omega\left\{2\tilde{\varepsilon}^*_{{\rm e},j}(\omega_{\rm d}-\omega)\right\}\\
&=\left(\left\{\frac{\Gamma}{2}+i\Delta_{\rm a}(\omega)\right\}\tilde{\rho}(\omega_{\rm d})-i\Omega\left\{2\tilde{\rho}_{\rm e}(0)-1\right\}\right)\delta(\omega-\omega_{\rm d})
\end{aligned}\tag{5.12}$$

where $\Delta_{\rm a}(\omega)=\omega_{\rm a}-\omega$. The right-hand side of above equation is zero for all ω from the definition of the δ function and using Eqn. 5.7. This gives,

$$-\left\{\frac{\Gamma}{2}+i\Delta_{\rm a}(\omega)\right\}\tilde{\varepsilon}_j(\omega)+ig_j\tilde{\alpha}(\omega)\left\{2\tilde{\rho}_{\rm e}(0)-1\right\}+i\Omega\left\{2\tilde{\varepsilon}^*_{{\rm e},j}(\omega_{\rm d}-\omega)\right\}=0.\tag{5.13}$$

Using Eqn. (5.13) and $\tilde{\varepsilon}^*_{{\rm e},j}(\omega_{\rm d}-\omega)\approx 0$ gives first order correction term for $\tilde{\rho}_j(\omega)$,

$$\tilde{\varepsilon}_j(\omega_{\rm p})=-ig_j\frac{\tilde{\alpha}(\omega_{\rm p})\left\{-2\tilde{\rho}_{\rm e}(0)+1\right\}}{\left\{\frac{\Gamma}{2}-i\Delta_{\rm pa}\right\}}=-ig_j\tilde{\alpha}(\omega_{\rm p}){\rm C}_1(\omega_{\rm p}).\tag{5.14}$$

This is similar to the value of $\tilde{\rho}(\omega)$ used to calculate the VRS (see Eqn. 4.6) but with an extra factor of $\{-2\tilde{\rho}_{\rm e}(0)+1\}$. This factor comes because of change in population difference between excited and ground state and effectively reduces the coupling and hence the VRS as the cavity field sees fewer atoms in the ground state.

Now for excited state population if we don't neglect the term, $\tilde{\varepsilon}^*_{{\rm e},j}(\omega_{\rm d}-\omega)$,

$$\begin{aligned}
&(i\omega_{\rm d}-i\omega+\Gamma)[\tilde{\rho}_{\rm e}(0)\delta(\omega_{\rm d}-\omega)+\tilde{\varepsilon}^*_{{\rm e},j}(\omega_{\rm d}-\omega)]\\
&=ig_j\left\{\tilde{\alpha}^*(2\omega_{\rm d}-\omega)\tilde{\rho}(\omega_{\rm d})-\tilde{\alpha}(\omega)\tilde{\rho}^*(\omega_{\rm d})\right\}+i\left\{\Omega^*\tilde{\rho}_j(\omega)-\Omega\tilde{\rho}^*_j(2\omega_{\rm d}-\omega)\right\}
\end{aligned}\tag{5.15}$$

Rearranging terms,

$$\begin{aligned}
&(i\omega_{\rm d}-i\omega+\Gamma)\tilde{\varepsilon}^*_{{\rm e},j}(\omega_{\rm d}-\omega)-ig_j\left\{\tilde{\alpha}^*(2\omega_{\rm d}-\omega)\tilde{\rho}(\omega_{\rm d})-\tilde{\alpha}(\omega)\tilde{\rho}^*(\omega_{\rm d})\right\}\\
&-i\left\{\Omega^*\tilde{\varepsilon}_j(\omega)-\Omega\tilde{\varepsilon}^*_j(2\omega_{\rm d}-\omega)\right\}\\
&=\left[-(i\omega_{\rm d}-i\omega+\Gamma)\tilde{\rho}_{\rm e}(0)+i\left\{\Omega^*\tilde{\rho}_j(\omega_{\rm d})-\Omega\tilde{\rho}^*_j(\omega_{\rm d})\right\}\right]\delta(\omega_{\rm d}-\omega).
\end{aligned}\tag{5.16}$$

Again the right hand side is zero for all ω. The complete set of equations to calculate $\tilde{\varepsilon}_j(\omega_\mathrm{p})$ at the cavity probe frequency can be derived from (5.13) and (5.16) and are given by,

$$-\left\{\frac{\Gamma}{2}+i\Delta_\mathrm{a}(\omega_\mathrm{p})\right\}\tilde{\varepsilon}_j(\omega_\mathrm{p})+ig_j\tilde{\alpha}(\omega_\mathrm{p})\{2\tilde{\rho}_\mathrm{e}(0)-1\}+i\Omega\left\{2\tilde{\varepsilon}^*_{\mathrm{e},j}(\omega_\mathrm{d}-\omega_\mathrm{p})\right\}=0 \tag{5.17a}$$

$$-[i(\omega_\mathrm{d}-\omega_\mathrm{p})+\Gamma]\tilde{\varepsilon}^*_{\mathrm{e},j}(\omega_\mathrm{d}-\omega_\mathrm{p})+ig_j\left\{\tilde{\alpha}^*(2\omega_\mathrm{d}-\omega_\mathrm{p})\tilde{\rho}(\omega_\mathrm{d})-\tilde{\alpha}(\omega_\mathrm{p})\tilde{\rho}^*(\omega_\mathrm{d})\right\}$$
$$+i\left\{\Omega^*\tilde{\varepsilon}_j(\omega_\mathrm{p})-\Omega\tilde{\varepsilon}^*_j(2\omega_\mathrm{d}-\omega_\mathrm{p})\right\}=0 \tag{5.17b}$$

$$-\left\{\frac{\Gamma}{2}+i\Delta_\mathrm{a}(2\omega_\mathrm{d}-\omega_\mathrm{p})\right\}\tilde{\varepsilon}_j(2\omega_\mathrm{d}-\omega_\mathrm{p})+ig_j\tilde{\alpha}(2\omega_\mathrm{d}-\omega_\mathrm{p})\{2\tilde{\rho}_\mathrm{e}(0)-1\}$$
$$+i\Omega\left\{2\tilde{\varepsilon}^*_{\mathrm{e},j}(\omega_\mathrm{p}-\omega_\mathrm{d})\right\}=0 \tag{5.17c}$$

$$-[i(\omega_\mathrm{p}-\omega_\mathrm{d})+\Gamma]\tilde{\varepsilon}^*_{\mathrm{e},j}(\omega_\mathrm{p}-\omega_\mathrm{d})+ig_j\left\{\tilde{\alpha}^*(\omega_\mathrm{p})\tilde{\rho}(\omega_\mathrm{d})-\tilde{\alpha}(2\omega_\mathrm{d}-\omega_\mathrm{p})\tilde{\rho}^*(\omega_\mathrm{d})\right\}$$
$$+i\left\{\Omega^*\tilde{\varepsilon}_j(2\omega_\mathrm{d}-\omega)-\Omega\tilde{\varepsilon}^*_j(\omega)\right\}=0. \tag{5.17d}$$

If the cavity is only driven at one frequency, ω_p, $\alpha(2\omega_\mathrm{p}-\omega)=0$ in above equations. From (5.17) it can be seen that in addition to oscillating at the frequency ω_p the atomic coherence also oscillates at frequencies $\omega_\mathrm{p}\pm\Delta_\mathrm{pd}$, where $\Delta_\mathrm{pd}=\omega_\mathrm{p}-\omega_\mathrm{d}$. This was an assumption made by B. R. Mollow in his article [122] for solving free space scenario of the same problem as ours. We arrive at it using Fourier transforms. Hence, for non-zero $\tilde{\varepsilon}^*_{\mathrm{e},j}(\omega_\mathrm{d}-\omega)$ we get,

$$\tilde{\varepsilon}_j(\omega_\mathrm{p})=-ig_j\tilde{\alpha}(\omega_\mathrm{p})[\mathrm{C}_1(\omega_\mathrm{p})+\mathrm{C}_2(\omega_\mathrm{p})] \tag{5.18}$$

Where $\mathrm{C}_1(\omega_\mathrm{p})$ is same as in (5.14) and the value of $\mathrm{C}_2(\omega_\mathrm{p})$ is,

$$\mathrm{C}_2(\omega_\mathrm{p})=\frac{\mathrm{E}}{\mathrm{FG}} \tag{5.19}$$

Where ,
$\mathrm{E}=-16|\Omega|^2(\Gamma-i\Delta_{dp})\left[\Gamma^2-2i\Gamma\Delta_{dp}+4\Delta_\mathrm{pa}(\Delta_\mathrm{pa}-\Delta_{dp})\right]$,
$\mathrm{F}=(\Gamma-2i(\Delta_\mathrm{pa}+\Delta_{dp}))\left(\Gamma^2+8|\Omega|^2+4\Delta^2_\mathrm{pa}\right)$ and
$\mathrm{G}=\left[(\Gamma-i\Delta_{dp})\left(4\Delta^2_\mathrm{pa}+(\Gamma-2i\Delta_{dp})^2\right)+8|\Omega|^2(\Gamma-2i\Delta_{dp})\right]$.
Finally, $\tilde{\alpha}(\omega_\mathrm{p})$ takes the form,

$$\tilde{\alpha}(\omega_\mathrm{p})=\frac{-\eta-i\tilde{\rho}(\omega_\mathrm{d})\delta(\omega_\mathrm{d}-\omega_\mathrm{p})\sum_{j=1}^{N}g_j}{\left\{\kappa_\mathrm{t}-i\Delta_{pc}\right\}+g_\mathrm{t}^2[\mathrm{C}_1(\omega_\mathrm{p})+\mathrm{C}_2(\omega_\mathrm{p})]}. \tag{5.20}$$

The average photon number in the cavity, $\bar{n} = |\alpha|^2$ can be calculated using this semi-classical theory of atom-light interaction[1]. Fig. 5.9 shows cavity transmission spectrum as a function of the frequency of probe laser using Eqn. 5.20. From Fig. 5.9 it is evident that for red detuning the probe laser experiences gain and for blue detuning experiences loss. This is completely consistent with the experimental observations in Fig. 5.7. When the gain of probe laser from the atoms exceed the loss from the atom-cavity system, we see lasing as shown in Fig. 5.9(b) providing a consistency check for the lasing of the red-detuned peak. In addition, the parameters in our calculations are such that $4|\Omega|^4 < |\Delta_{da}|^3\Gamma$ and $4|\Omega|^2 < |\Delta_{da}|^2$, where 2Ω is Rabi frequency of the drive laser, Δ_{da} is detuning of drive laser from the atomic transition and Γ is decay rate of the atomic excited state due to spontaneous emission. This is opposite to the conditions necessary for gain in probe beam according to [114] and [122] respectively, where the system was required to be driven hard. However, here the presence of cavity enhances the interaction, and we see gain even without the very demanding requirements on parameters in the earlier experiments.

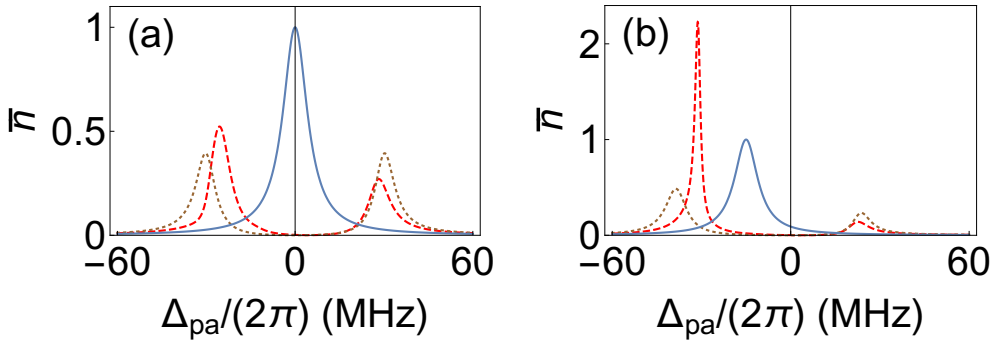

Fig. 5.9 Probe transmission through the cavity as a function of detuning from the atomic transition. Blue is empty cavity transmission, the dotted brown curve is the VRS, and red dashed curve shows probe transmission when atoms are driven by classical light. The two graphs are for different detuning of the cavity from atomic transition, (a) $\Delta_{ca}/(2\pi) = 0$ and (b) $\Delta_{ca}/(2\pi) = -15$ MHz. Other parameters are, the strength of drive field is $\Omega/(2\pi) = 6$ MHz, the strength of probe field is $\eta/(2\pi) = 4.75$ MHz, atom-cavity collective strong coupling is $g_t/(2\pi) = 30$ MHz, $\Gamma/(2\pi) = 6$ MHz, cavity FWHM is $2\kappa_t/(2\pi) = 9.5$ MHz, and $\Delta_{pa}/(2\pi) = -13$ MHz.

[1]The Mathematica code for the algebraic manipulation leading to Eqn. 5.20 is given at https://goo.gl/mzUzvA. The file name is "Driven atoms_plus_cavity_analysis.nb". This file also contains the code to obtain and plot the data for Fig. 5.9.

5.5 Further discussions

Most of the concepts discussed in the sections preceding this concentrated on the origin of the red detuned peak observed in the experiment. In this section, we discuss the origin of the blue detuned peak observed in the experiment. On changing the detuning of the cavity with respect to the atomic transition, the collective eigenstate (VRS) also shifts in frequency. When the cavity is blue detuned with respect to the atomic transition, the red VRS peak shifts towards the atomic transition and the blue peak shifts away from the atomic transition. This makes it possible for the red VRS peak to be in resonance with the MOT cooling laser which is 13 MHz red detuned from the atomic transition when the detuned cavity resonance is to the blue side. As can be inferred from Fig. A.1 of Appendix A, the atomic fluorescence is dominant at MOT/drive laser frequency. Hence, the combined system of atoms and cavity becomes resonant for most of the florescent light, when the cavity is blue detuned with respect to the atomic transition. This explains the observation of the blue peak in the experiment as shown in the Figs. 5.2, 5.4 and 5.5. This blue peak is unpolarized as the fluorescence can be of any polarization.

Comparing the numbers in the above calculations and the experiment, the total intensity of all the MOT beams and dipole moment for isotropic beam case gives $\Omega/(2\pi) \approx 6$ MHz as an estimate. However, theoretical treatment is for single drive beam whereas there are six beams, all with different polarization and non-zero relative phase differences between them. The calculation, therefore, is a lower estimate of the light-atom interaction, since sub-Doppler cooling mechanisms will try to localize atoms towards intensity maxima formed by the six MOT beams increasing effective value of Ω [120]. Also, for the analysis, we have assumed the cavity field to be very weak, such that the atomic coherence, ρ is only first order in cavity field, α. There is a possibility of gain to be higher order in α which has not been considered here. Hence exact quantitative comparison is not possible with the present model, but qualitatively we do not expect the physics behind the observations to change.

5.6 Conclusion

In conclusion, when a MOT of actively driven atoms is in collective strong coupling regime with a Fabry-Pérot cavity, lasing is seen in the red detuned emitted light from the atom-cavity system. The lasing for a stabilized cavity and MOT atom number is continuous in nature. This driving field is the same as the MOT light which cools and traps the atoms and results in continuous operation of the laser from the coupled atom-cavity system. The lasing is seen for the red detuned peak because symmetry is broken in favor of the red detuned peak due to the

MOT light, which also confines the atoms effectively and couples it to the cavity mode. In principle, the lasing could be achieved on the blue detuned peak if the driving frequency and the trap mechanism were not connected and the driving light was blue detuned with respect to the atomic transition. The observed phenomena are therefore generic to the driven atom-cavity system and have potential to be of interest for basic studies and for applications. To analyze the basic processes of this phenomena a semiclassical theory of light-matter interaction is presented, where the role of Mollow gain and dispersion due to the collective strong coupling of atoms to the cavity and the change in the dynamics of the system is explained. Here, we took the decay of the atomic excited state phenomenologically similar to B. R. Mollow [122]. Theoretically, it would be a useful exercise to perform a full quantum and multimode calculation including the vacuum modes similar to Grynberg *et.al* [114]. The vacuum modes and the drive field can be then integrated out similar to the approach of open quantum optics [86] giving an effective non-linear interaction between the photons in the cavity and the atoms. Such an approach will provide more information regarding the properties of laser observed in our experiment. Future work can be taken up to observe the properties of this type of non-linear laser, such as photon statistics, phase diffusion and squeezing, as predicted by single mode theories of Zakrzewski *et.al* [126–128] and Agarwal [129, 130]

Chapter 6

Towards coupling of ultracold molecules to a cavity

In the introduction we enumerated several motivations for creation of molecules at ultracold temperatures. Among these, our primary motivation is to study interactions between molecules [131] and between molecules and atoms [17, 132, 46] where quantum statistics will play a significant role. To study interactions between these molecules, it would be advantageous to couple these molecules to the cavity or to mix the molecules with the atoms coupled to the cavity. Such a atom-molecule-cavity system might be useful in the future for creating the molecules in a particular state, detecting them non-destructively either directly using cavity or via an atom-cavity coupling.

In order to study the interactions mentioned above, we need state prepared molecules at ultracold temperatures. An efficient and simple way is to create them from ultracold atoms. There are two processes which are used to create molecules from a ultracold ensemble of atoms. One is using magnetic field via magnetically tunable Feshbach resonances [41] and second is via photoassociation (PA) using light [42]. The PA process has been very useful for creating diatomic molecules [133], for doing spectroscopy of these molecules [47], and for measuring atomic constants [134–136].

To make a start in this direction, we perform experiments to study the creation of diatomic molecules from ultracold atoms using light coupled to a cavity via the process of photoassociation. In principle, cavity offers two advantages; first is to increase the intensity of light and second is to increase the light-matter interaction strength compared to free space interactions. PA experiments with cavity and other related experiments will be described in the sections 6.1 and 6.2. In the process of molecule creation, we also observe atomic losses not related to the PA process which result in molecule creation. These losses have to be understood and distinguished from the PA process. The possible distinctions will be discussed in section 6.4.

In section 6.5, we will explore techniques to detect molecules using cavity. The experiments mentioned in this chapter are done with a magneto-optical trap (MOT) of ultracold ^{85}Rb atoms. At the initial stages of the experiment, MOT of ^{40}K was used to look for signatures of molecule creation using light coupled to a cavity. However, as the density of atoms in ^{40}K MOT was small, the signal for molecular creation was very weak. Hence we moved to a MOT of ^{85}Rb atoms which had an order of magnitude higher density. The features described in section 6.2 were also observed for ^{40}K atoms.

6.1 Photoassociation spectroscopy

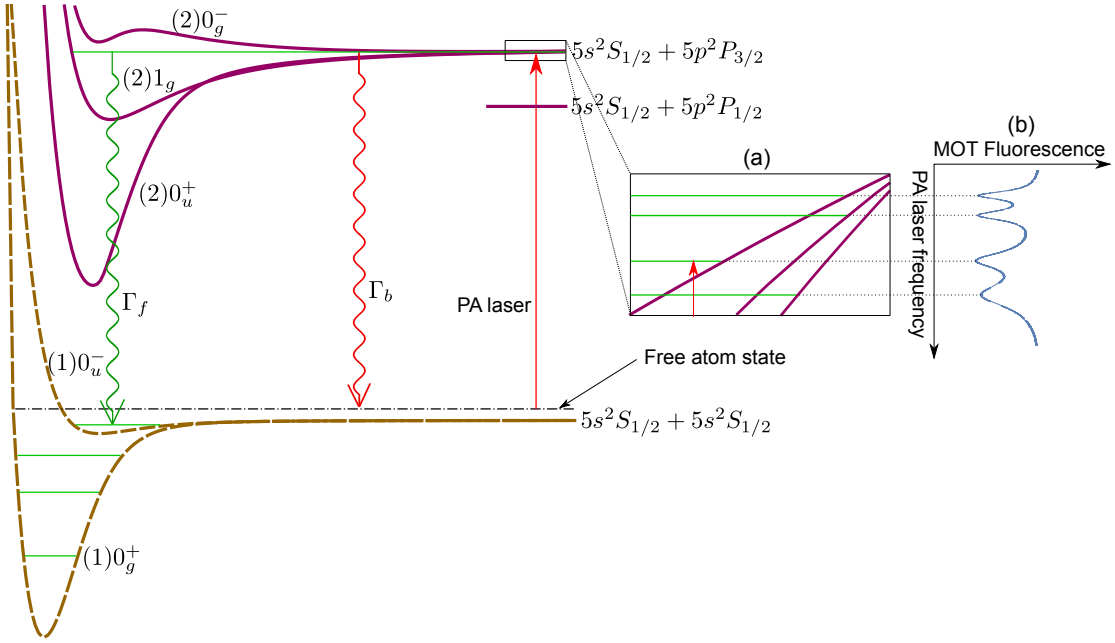

Fig. 6.1 The process of photoassociation and relevant potential energy curves of Rb atom. An excited state molecule is formed when two atoms which are close to each other are exposed to a photon from a PA laser. The frequency of this PA laser (red solid line) is such that it is in resonance with one of the vibrational level (shown by green color lines) of an exited state potential. This excited state molecule either decays due to spontaneous emission back to free atom state with rate Γ_f or to a bound vibrational level of one of the ground state potential with rate Γ_b. The wavy lines show spontaneous emission paths. (a) Shows a zoomed in part of the potential energy curves and the high lying vibrational levels of the excited state potentials near the asymptote. (b) Shows the variation in MOT atom number when the PA laser frequency is scanned near the vibrational levels of the excited state potential.

In this section, we present the results of photoassociation (PA) spectroscopy via the method of atomic trap loss spectroscopy. Figure 6.1 is a representative schematic figure showing the

process of PA. In the method of atomic trap loss spectroscopy, the creation of molecules is inferred from loss of atoms. In a MOT, there is always a balance of atom loss due to collisions and atom gain due to the constant loading of atoms from background thermal gas of atoms due to laser cooling. This balance helps in maintaining a steady state of atom number. After introducing a laser to perform the process of PA an additional loss process occurs for the MOT atoms as these atoms are converted to electronically excited molecules, these excited molecules either decay to ground bound state molecules or free atoms which may or may not be trapped in the MOT. Hence, the steady state atom number drops giving us an indirect evidence of molecule creation. The creation of molecules is possible only at specific wavelengths of light due to discrete nature of molecular states, and hence we see resonances when the light wavelength is scanned. Few such resonances are shown in figure 6.2. The resonances in figure 6.2 are observed by free space illumination of atoms with PA light, i.e. without coupling the light to a cavity. As a demonstration of the feasibility of molecule creation in cavity we also performed spectroscopy using PA light coupled to a cavity, the result is shown in figure 6.3. Here, we have taken data at only a few detunings because unlike the free space case scanning the wavelength

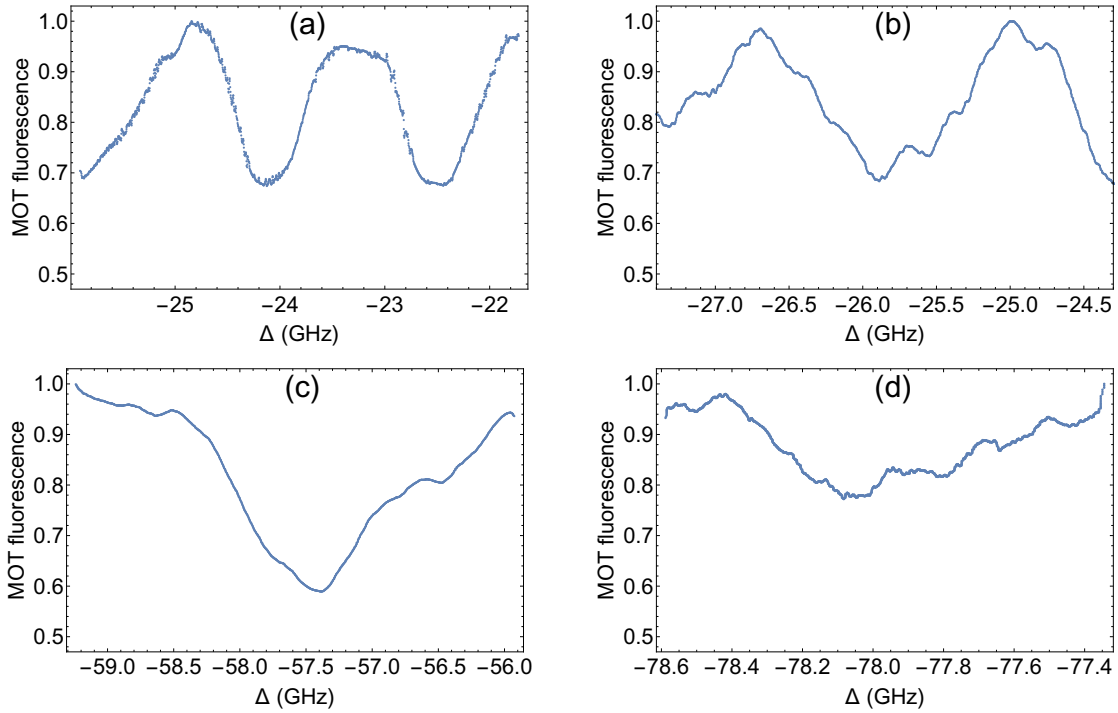

Fig. 6.2 The scans of the experiments which show $^{85}Rb_2$ molecular resonances. The y-axis shows normalized fluorescence from MOT atoms, the fluorescence is a measure of atom number in the MOT, and $\Delta = \omega_{pa} - \omega_a$ is detuning of PA laser from the cooling transition of ^{85}Rb atom (3-4′ transition of D2 line [91]). Here, ω_{pa} is the frequency of PA laser and ω_a is the frequency of the atomic transition. The wavelength of the PA laser is monitored using a wavemeter.

of the PA laser which is locked to the cavity is not possible in our experimental setup. The technique for locking of PA laser to the cavity is explained in section 2.3.5.

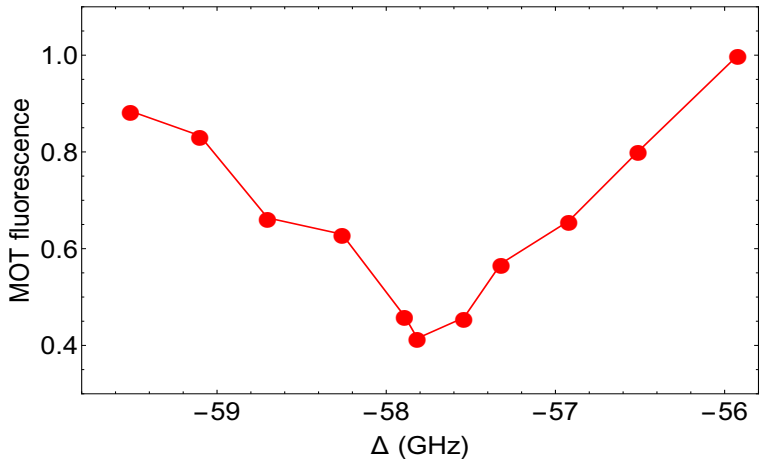

Fig. 6.3 The scan of an experiment which show $^{85}Rb_2$ molecular resonance at -57.5 GHz when PA light is coupled to the cavity. The corresponding free space spectroscopy is shown in figure 6.2(c).

6.2 Dependence of atomic number in MOT on the intensity of far detuned light

6.2.1 Far detuned light coupled to a cavity

To clearly understand the differences between PA process with and without cavity it is essential to know the dependence of atom loss on the intensity of the far detuned ($\sim$ few GHz) PA light. To understand this dependence we performed experiments where the intensity of PA light was varied, and the corresponding change in MOT fluorescence was recorded. The data for these experiments show unexpected behavior which is complex. The atom number shows non-monotonic behavior with respect to (w.r.t.) a monotonic increase in intensity. This behavior is not restricted to the molecular PA resonances but is a generic feature of the system when the light is red detuned w.r.t. the atomic transition whether or not on PA resonance as shown in figure 6.4. As can be seen in figure 6.4, the fluorescence first decreases and then increases and drops suddenly as the intensity of laser light is further increased. The expected behavior is monotonic decrease in fluorescence as the atom number decreases due to light-induced losses in atomic ensemble. Qualitatively the behavior remains same for different detunings but the features shift towards high intensity values. As seen in figure 6.5 the blue detuned light induces entirely different behavior. Initially the atomic fluorescence shows slight tendency

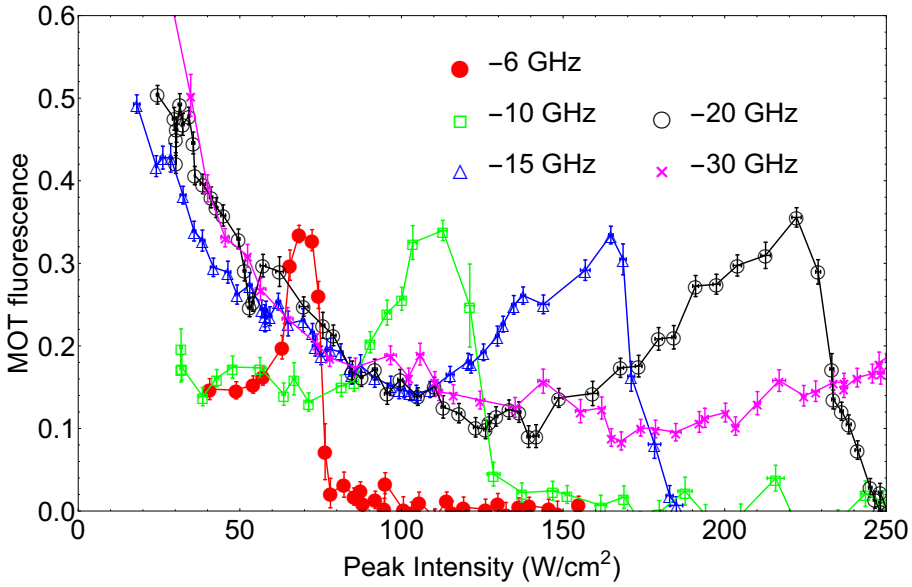

Fig. 6.4 Dependence of MOT fluorescence on the intensity of light coupled to the cavity when the light is red detuned w.r.t. the atomic transition. The MOT fluorescence for all the data points is normalized w.r.t. MOT fluorescence without the cavity light. The detuning of cavity light mentioned in the plot legends is w.r.t. the cooling transition of the atom.

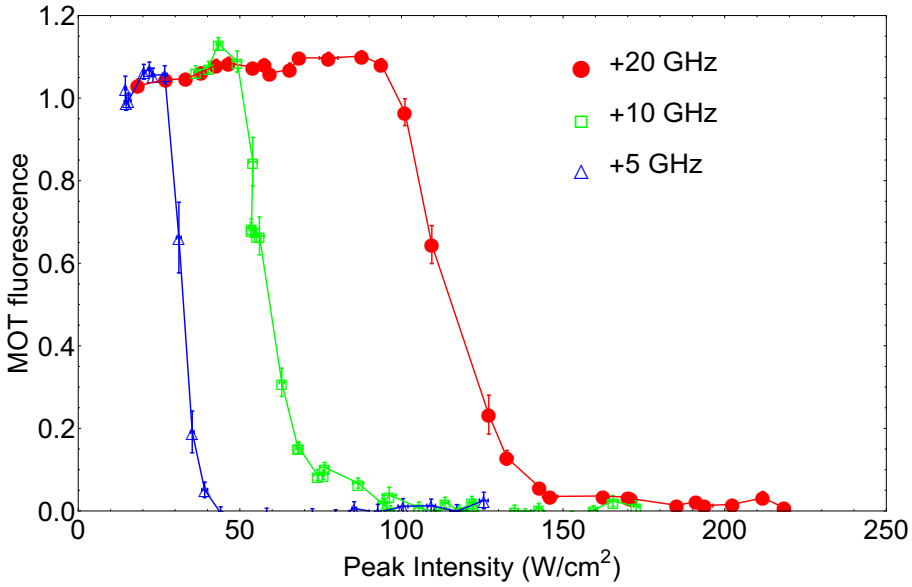

Fig. 6.5 Dependence of MOT fluorescence on the intensity of light coupled to the cavity when the light is blue detuned w.r.t. the atomic transition.

to increase and then drops suddenly. Similar to red detuned case, qualitatively the behavior remains same for different detunings, but the slope and location for the sudden drops change.

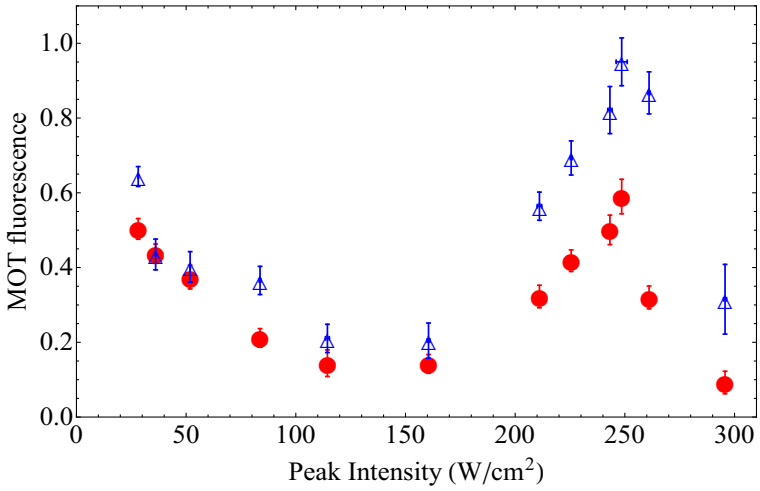

Fig. 6.6 This graph shows a correspondence between detected fluorescence and atom number when cavity light is present. Red filled circles show the amount of fluorescence from atoms when cavity light is present, and empty triangles show the amount of fluorescence from atoms immediately after the cavity light is suddenly blocked. The cavity light detuning w.r.t. the atomic cooling transition is -21.7 GHz. This detuning is chosen to avoid a molecular resonance as can be inferred from figure 6.2(a).

The experimental setup for intensity scans when the laser is locked to the cavity is explained in section 2.3.5.

In order to check whether the change in amount of fluorescence from the MOT atoms mentioned above is due to change in atom number, a separate experiment is performed. In this experiment, the light coupled to the cavity is suddenly blocked, and the fluorescence is immediately recorded. This experiment is repeated for several values of cavity light intensities, and the result is shown in figure 6.6. For atoms in the MOT, the time required to attain steady-state atom number is more than 5 seconds, the measurement is only limited by the PMT response time ($\sim$ 100 μs) and hence the fluorescence just after blocking of the cavity light is a correct measure of atom number in the presence of the cavity light. As can be seen from figure 6.6 the non-monotonic behavior is indeed shown by the atom number. The atomic number is seen to almost increase to the without cavity light atom number for the point of maximum fluorescence in figure 6.6. The difference in fluorescence just before and after blocking of cavity light in this experiment is likely to be due to AC Stark shifts which reduce the amount of light scattered by the atoms from the MOT lasers. AC stark shift is a phenomenon in which an oscillating electric field interacting with an atomic transition shifts the energies of states involved in the transition [55]. In our experiment this oscillating electric field is provided by the cavity light.

6.2.2 Photoassociation with cavity coupled light

In order find out the intensity dependence of the photoassociation process, we perform intensity scans at the molecular resonances and compare them with scans when the cavity light is detuned away to the immediate higher and lower frequency off-resonant detunings about the measured molecular resonance. Scans away from the molecular resonance at both red and blue detunings of the molecular resonance are performed in order to distinguish the effect of molecule formation from detuning-dependent changes observed in the above subsection. The results are shown in figure 6.7. In this figure, the red and the blue points represent the off resonance detunings and the black points are the on molecular resonance data. The red and

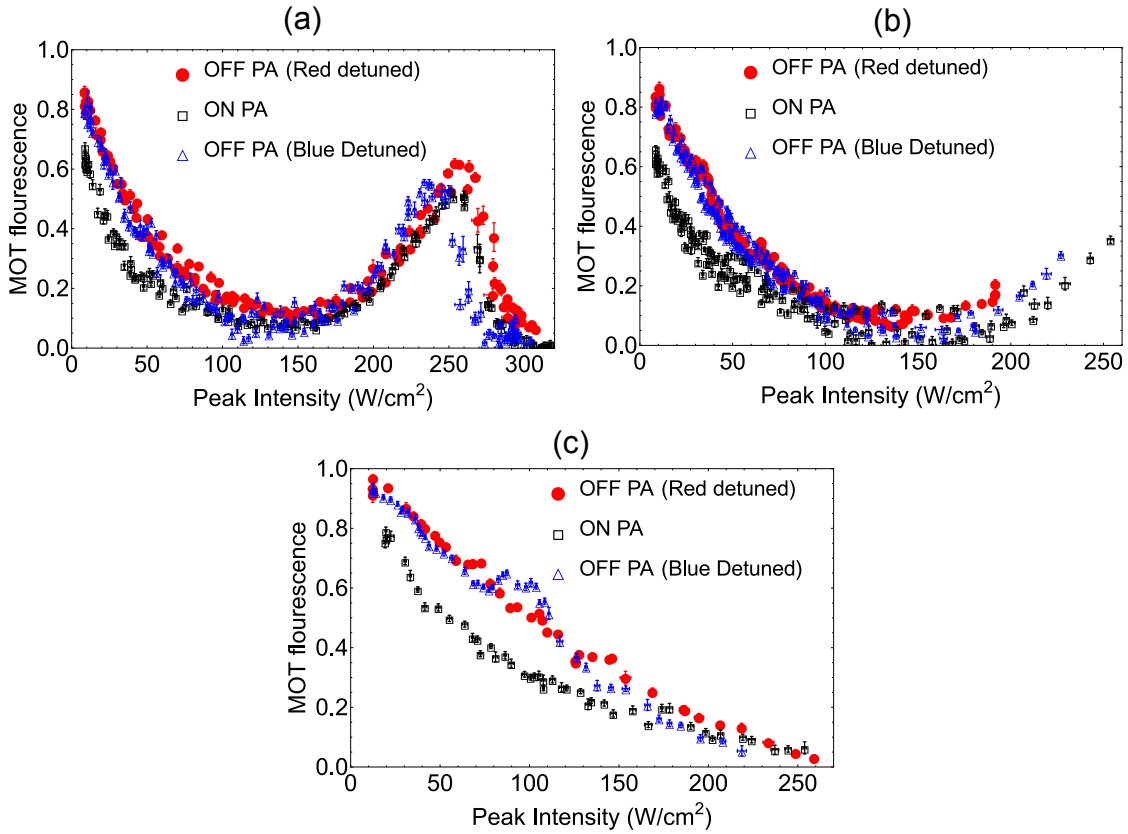

Fig. 6.7 Dependence of MOT fluorescence on the intensity of PA light coupled to the cavity near molecular resonances. In all of the graphs, empty black squares show intensity scan exactly at the PA resonance, filled red circles and empty blue triangles show intensity scans away from the molecular resonances but are red and blue detuned w.r.t. molecular resonance respectively. The detunings for [red, on resonance, blue] are, (a) [-23.29 GHz, -22.49 GHz, -21.50 GHz], (b) [-24.79 GHz, -24.19 GHz, -23.49 GHz], and (c) [-59.81 GHz, -57.91 GHz, -56.21 GHz]. The spectroscopy signal for the resonances in (a) and (b) is shown in figure 6.2(a) and for (c) is shown in figure 6.2(c).

the blue points represent light induced processes on the atomic system which does not result in molecular formation while the black is from molecular formation in addition to the light induced processes. It is therefore the difference between the blue/red and the black data points which represents the change due to molecular formation by PA. Additionally, from figure 6.7 it can be seen that initially for a very low intensity of PA light the molecule formation rate is low which increases as the PA light intensity is increased. This rate becomes maximum for an intermediate value of intensity and further increasing the intensity reduces the molecular formation rate as the density is reduced to a very low value by the PA process and other competing processes not related to PA. Towards the end, the competing processes become so strong that there is no signal for molecule formation even when the atom number increases. The best conversion rate for molecule formation is obtained for figure 6.7(c) as this molecular resonance is more detuned away from the atomic transition than the resonances of figure 6.7(a) and figure 6.7(b). The observations of this section and figure 6.3 show that despite the presence of other competing processes it is possible to create molecules efficiently using light coupled to a cavity.

6.2.3 Far detuned light in free space

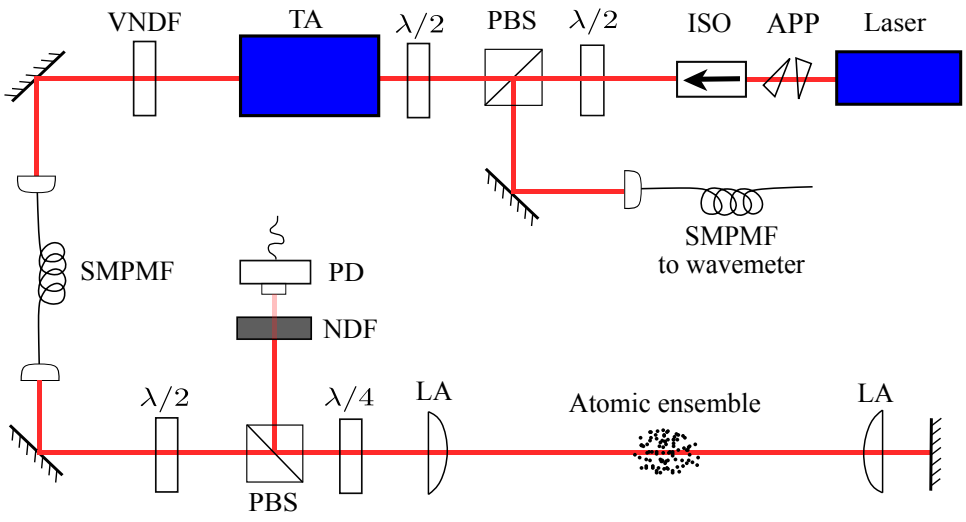

Fig. 6.8 This is the experimental arrangement for free space PA light. The photodiode (PD) is used for monitoring the power of retroreflected light beam. NDF - neutral density filter, NDF - variable neutral density filter, PBS - polarizing beam splitter, PD - photo diode, LA - plano convex lens, APP - anamorphic prism pair, ISO - optical isolator, to amplify the power, SMPMF - single mode polarization maintaining fiber, $\lambda/2$ - half wave plate, $\lambda/4$ - quarter wave plate.

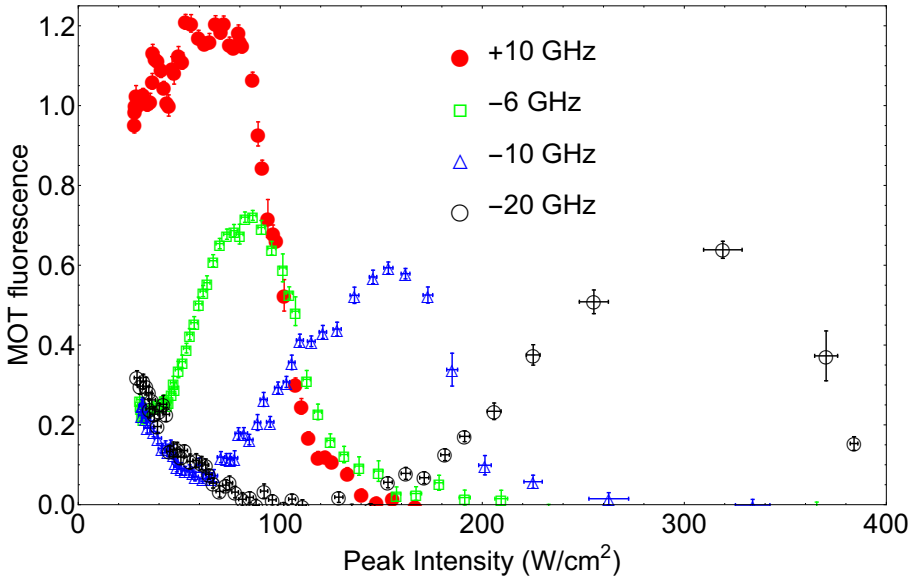

Fig. 6.9 Dependence of MOT fluorescence on the intensity of free space detuned light (not coupled to a cavity). The MOT fluorescence for all the data points is normalized w.r.t. MOT fluorescence without the detuned light. The detuning of detuned laser light mentioned in the plot legends is w.r.t. the cooling transition of the atom.

In order to determine whether the effect we observe for far detuned intense light coupled to the cavity is an effect due to the presence of a cavity or not we perform experiments similar to the experiments of the previous sections but with free space light. In order to mimic the spatial profile of cavity light in free space, we focus the light at the center of the atomic cloud. The experimental arrangement for this is shown in figure 6.8. A convex lens of 30 cm focal length focuses the light at the center of the atomic ensemble, the $1/e^2$ radius of this light at the focus is $\sim 80\ \mu$m. Using a combination of a convex lens and a mirror the light is again reflected back. This retroreflected light interferes with the original light beam forming a standing wave. This ensures similarity between the free space light and cavity coupled light.

Observations with free space far detuned light are shown in figure 6.9. Here, qualitatively the features observed are similar to the features observed for cavity coupled light. These observations tell us that the intensity dependent features observed are not due to a process which requires a cavity and can be observed even for a focused free space light. One more question that can be asked is, what role does standing wave place in the process leading to the observed feature? The answer is nuanced. Qualitatively the large variations in the MOT atom numbers are seen whether the light is retro-reflected or not. However particular details of the MOT number variations change, as seen in figures 6.9 and 6.10. No retroreflection ensure no standing wave. The experiment was performed for both circular and linear polarized light and

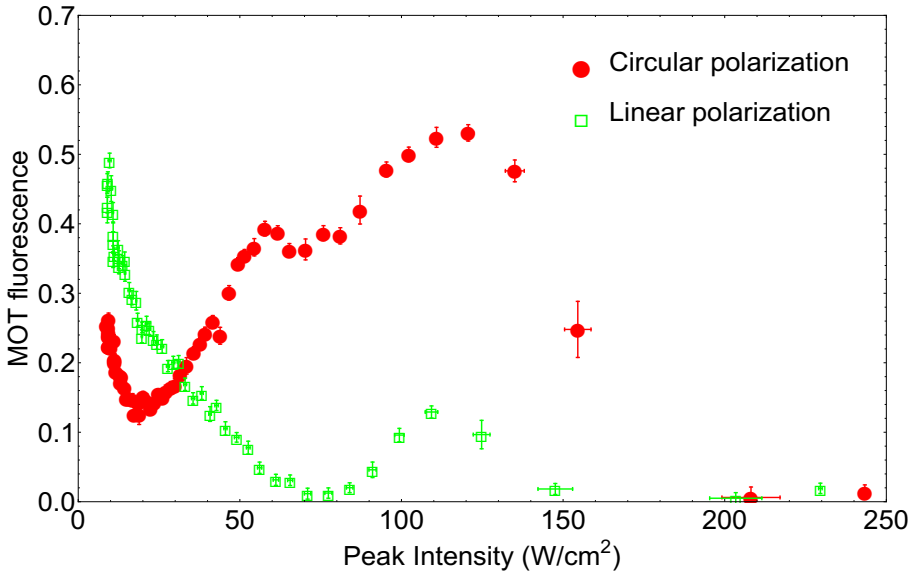

Fig. 6.10 Dependence of MOT fluorescence on the intensity of circularly and linearly polarized free space detuned light without the standing wave. The MOT fluorescence for all the data points is normalized w.r.t. MOT fluorescence without the detuned light. The detuning of detuned laser light w.r.t. to the atomic transition is -10 GHz.

as seen in figure 6.10, the rise in atom number after the initial dip is more prominent in the circularly polarized case.

6.3 Dependence of atomic density in MOT on the intensity of far detuned light

In the above section, we discussed how the atom number changes when a far detuned light of high intensity is interacting with ultracold atoms trapped in a MOT. In this section, we will discuss the change in density profile when such a light is incident on the atomic ensemble. This will enable us to further understand the phenomenon we observe. Moreover, knowing the correct density distribution of atoms is essential for PA with cavity because the process of PA is proportional to the square of the atomic density and the intensity of cavity light concentrated in a small volume. So, the knowledge of atomic density at the center of the cavity is essential for observing the process of PA. In addition to PA process, other atomic loss processes which arise due to atomic collisions also depend on the atomic density, and accurate calculation of rates for these processes will require accurate knowledge of atomic density profile.

6.3.1 Experimental observations

Figures 6.11 and 6.12 show few instances of spatial dependence of fluorescence from MOT atoms for relevant intensities of red-detuned and blue-detuned light respectively. In figure 6.11(d) when the atom number is maximum after initial decrease (see figure 6.4) the density profile shows flat top and the overall width of the atomic cloud increases. This change in density profile is due to (a) heating of atoms as a result of scattering of cavity light photons

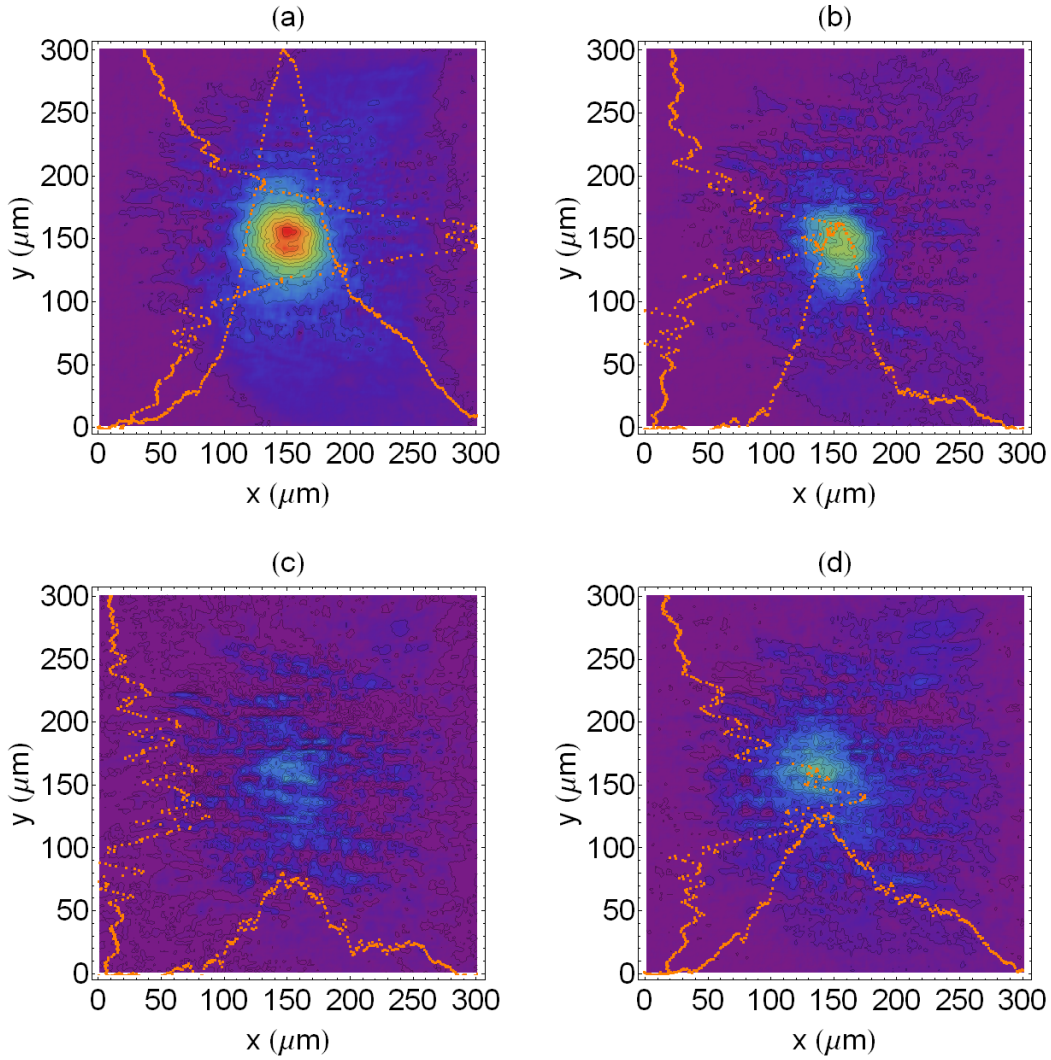

Fig. 6.11 Spatial dependence of fluorescence of MOT atoms for different intracavity intensities of red-detuned light. (a) No cavity light is present, (b) Cavity Light with peak intensity 10 W/cm^2, (c) Cavity Light with peak intensity 100 W/cm^2, (d) Cavity Light with peak intensity 165 W/cm^2. The detuning of this cavity coupled laser light w.r.t. to the atomic transition is -15 GHz. The orange traces show 1D density profiles along x and y axes obtained by taking mean along y and x axis respectively. See figure 6.4 for corresponding atom number dependence.

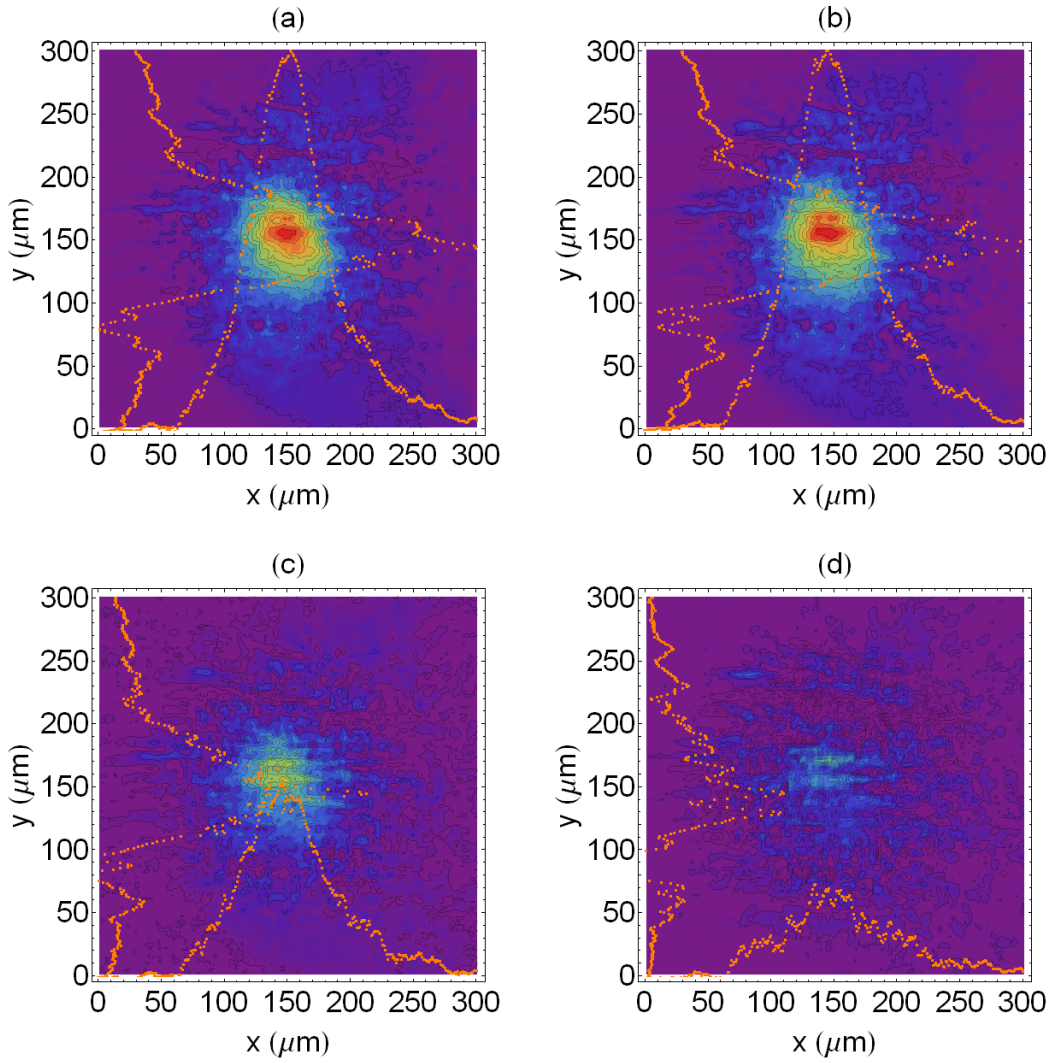

Fig. 6.12 Spatial dependence of fluorescence of MOT atoms for different intracavity intensities of blue-detuned light. (a) No cavity light is present, (b) Cavity Light with peak intensity 45 W/cm^2, (c) Cavity Light with peak intensity 55 W/cm^2, (d) Cavity Light with peak intensity 67 W/cm^2. The detuning of this cavity coupled laser light w.r.t. to the atomic transition is +10 GHz. See figure 6.5 for corresponding atom number dependence.

by the atoms and (b) due to AC Stark shift of atomic levels from the cavity light which reduces the scattering from MOT beams reducing the visibility of the atoms in the cavity mode volume. This can be inferred from figure 6.13 which shows density profile just before and after the cavity light is blocked (see figure 6.6 for corresponding atom number variation). As the scattering processes are very fast ($\sim 1\ \mu$s) the density profile changes instantaneously without any noticeable change in the atom number which comparatively takes few orders of magnitude more time to change. The change in density profile recorded by the CCD camera is limited by

the frame rate of the camera. In our case, the frame rate is 30 Hz which is fast compared to the loading rate of the MOT.

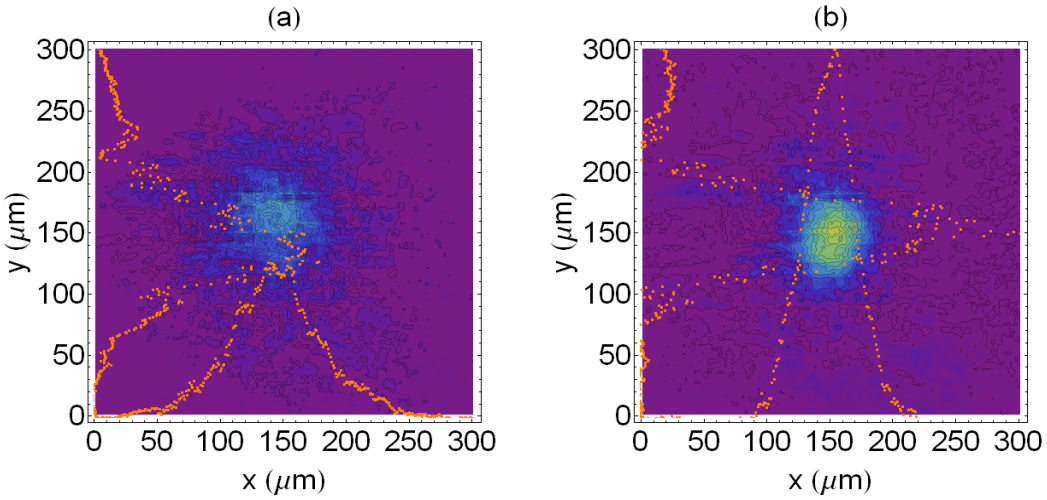

Fig. 6.13 Spatial dependence of fluorescence of MOT atoms. (a) Just before suddenly blocking the cavity light. (a) Just after suddenly blocking the cavity light. The detuning of PA laser light w.r.t. to the atomic transition is -21.7 GHz, and intensity is 250 W/cm^2. See figure 6.6 for corresponding atom number variation

6.3.2 Simulations for density profile

Effect of MOT light on atoms

From section 2.1 we saw that the force on an atom trapped in the MOT can be written as,

$$\vec{F} = -\vec{\beta}_{3D} \circ \vec{v} - \vec{\zeta}_{3D} \circ \vec{r} \tag{6.1}$$

where $\circ$ denotes a Hadamard (element wise) product of the vectors. Similarly, the rate of photon scattering by a MOT atom from the MOT light is given by [55],

$$\mathscr{R} = \frac{3I_r\Gamma}{1+4|\Delta|^2/\Gamma^2+6I_r}. \tag{6.2}$$

Here, Γ is excited state decay rate of atoms, $I_r = I/I_{sat}$ is the ratio of intensity per MOT beam to saturation intensity [55], Δ is detuning of MOT light from resonance. The random scattering of photons by the atoms lead to a random walk of atoms inside the MOT beams, this leads to spreading of atoms away from the center of the atoms and gives the atomic cloud a characteristic size. This random walk leads to diffusion of the atoms with a diffusion constant,

$\mathscr{D}_{\mathrm{MOT}} = \hbar^2 k^2 \mathscr{R}$ [54], where $k = 2\pi/\lambda$ is wavenumber and λ the wavelength of light. Assuming isotropic scattering from the atoms, the diffusion constant in each direction becomes, $\mathscr{D}_{\mathrm{MOT}}/3$. For a particle trapped in a harmonic trap undergoing diffusion which is the case for MOT atoms following Eqn. 6.1, the temperature is given by [137],

$$T_{\mathrm{MOT}} = \frac{\mathscr{D}_{\mathrm{MOT}}}{3\beta_{3\mathrm{D}} m_{\mathrm{a}} k_{\mathrm{B}}} \tag{6.3}$$

and the standard deviation in distance from trap center is given by,

$$\sigma^i_{\mathrm{mot}} = \sqrt{\frac{\mathscr{D}_{\mathrm{MOT}}}{3\beta_{3\mathrm{D}} m_{\mathrm{a}} \zeta^i_{3\mathrm{D}}}} \tag{6.4}$$

for $i \in (x, y, z)$. Here m_{a} is the mass of the atom, k_{B} is Boltzmann's constant, and $\zeta^i_{3\mathrm{D}}$ is the trap stiffness in i direction. For simplicity, we take equal trap stiffness ($\zeta_{3\mathrm{D}}$) in all direction for the purpose of the simulations, this gives $\sigma^x_{\mathrm{mot}} = \sigma^y_{\mathrm{mot}} = \sigma^z_{\mathrm{mot}} = \sigma_{\mathrm{mot}}$. The density of atoms in this simple case of diffusion with harmonic confinement is Gaussian with standard deviation σ_{mot} mentioned above.

Now, if we add the interaction of atoms with the cavity light the scenario is altered due to multiple factors, (a) the scattering of photons from this cavity light will add into diffusion, (b) the dipole force due to cavity light will change the confining of atoms, and (c) the AC Stark effect will change the MOT parameters inside the cavity mode volume. Before starting to find the atomic density for such a scenario, we study the effect on the atomic variables when two lasers of different frequencies interact with the same two-level atom.

A two-level atom interacting with two light fields

Similar to Eqn. 5.1 we can write a Hamiltonian for such a scenario,

$$\hat{H} = \frac{\hbar\omega_{\mathrm{a}}}{2}\hat{\sigma}^z + \hbar\left\{\Omega^*_{\mathrm{m}}\hat{\sigma}^- e^{i\omega_{\mathrm{m}}t} + \Omega_{\mathrm{m}}\hat{\sigma}^+ e^{-i\omega_{\mathrm{m}}t}\right\} + \hbar\left\{\Omega^*_{\mathrm{cv}}\hat{\sigma}^- e^{i\omega_{\mathrm{cv}}t} + \Omega_{\mathrm{cv}}\hat{\sigma}^+ e^{-i\omega_{\mathrm{cv}}t}\right\}. \tag{6.5}$$

Here, the subscripts m and cv are for MOT laser light and cavity light respectively. We assume the strength of cavity light is constant because we are in high intensity regime where change in cavity light intensity due to the presence of atoms is negligible. The time dependent equations

for the atomic variables become,

$$\begin{aligned}\frac{d\rho(t)}{dt} &= -\left\{\frac{\Gamma}{2}+i\omega_{\mathrm{a}}\right\}\rho(t)+i(\Omega_{\mathrm{m}}e^{-i\omega_{\mathrm{m}}t}+\Omega_{\mathrm{cv}}e^{-i\omega_{\mathrm{cv}}t})(2\rho_{\mathrm{e}}(t)-1)\\ \frac{d\rho_{\mathrm{e}}(t)}{dt} &= -\Gamma\rho_{\mathrm{e}}(t)+i\left\{(\Omega_{\mathrm{m}}^{*}e^{i\omega_{\mathrm{m}}t}+\Omega_{\mathrm{cv}}^{*}e^{i\omega_{\mathrm{cv}}t})\rho(t)-(\Omega_{\mathrm{m}}e^{-i\omega_{\mathrm{m}}t}+\Omega_{\mathrm{cv}}e^{-i\omega_{\mathrm{cv}}t})\rho^{*}(t)\right\}.\end{aligned} \tag{6.6a}$$

As multiple frequencies are involved, we will have to Fourier transform the above equations similar to Eqns. 5.3. This gives,

$$\begin{aligned}-i\omega\tilde{\rho}(\omega) &= -\left\{\frac{\Gamma}{2}+i\omega_{\mathrm{a}}\right\}\tilde{\rho}(\omega)-i\Omega_{\mathrm{cv}}\left\{2\tilde{\rho}_{\mathrm{e}}^{*}(\omega_{\mathrm{cv}}-\omega)-\delta(\omega-\omega_{\mathrm{cv}})\right\}\\ &\quad -i\Omega_{\mathrm{m}}\left\{2\tilde{\rho}_{\mathrm{e}}^{*}(\omega_{\mathrm{m}}-\omega)-\delta(\omega-\omega_{\mathrm{m}})\right\} \qquad (6.7a)\\ i\omega\tilde{\rho}_{\mathrm{e}}^{*}(\omega) &= -\Gamma\tilde{\rho}_{\mathrm{e}}^{*}(\omega)-i\left\{\Omega_{\mathrm{cv}}^{*}\tilde{\rho}(\omega_{\mathrm{cv}}-\omega)-\Omega_{\mathrm{cv}}\tilde{\rho}^{*}(\omega_{\mathrm{cv}}+\omega)\right\}\\ &\quad -i\left\{\Omega_{\mathrm{m}}^{*}\tilde{\rho}(\omega_{\mathrm{m}}-\omega)-\Omega_{\mathrm{m}}\tilde{\rho}^{*}(\omega_{\mathrm{m}}+\omega)\right\}. \qquad (6.7b)\end{aligned}$$

The susceptibility of atoms for the MOT light and the cavity light will be proportional to the Fourier components $\tilde{\rho}(\omega_{\mathrm{m}})$ and $\tilde{\rho}(\omega_{\mathrm{cv}})$ of the atomic coherence respectively [90], i.e., the components oscillating at the respective frequencies. Hence, we will solve for these Fourier components using Eqns. 6.7. The Fourier components will follow following algebraic equations,

$$-\left\{\frac{\Gamma}{2}-i\Delta_{\mathrm{cv}}\right\}\tilde{\rho}(\omega_{\mathrm{cv}})-i\Omega_{\mathrm{cv}}\left\{2\tilde{\rho}_{\mathrm{e}}^{*}(0)-1\right\}-i\Omega_{\mathrm{m}}\left\{2\tilde{\rho}_{\mathrm{e}}^{*}(\Delta_{\mathrm{mc}})\right\}=0 \tag{6.8a}$$

$$-\left\{\frac{\Gamma}{2}-i\Delta_{\mathrm{m}}\right\}\tilde{\rho}(\omega_{\mathrm{m}})-i\Omega_{\mathrm{cv}}\left\{2\tilde{\rho}_{\mathrm{e}}^{*}(-\Delta_{\mathrm{mc}})\right\}-i\Omega_{\mathrm{m}}\left\{2\tilde{\rho}_{\mathrm{e}}^{*}(0)-1\right\}=0 \tag{6.8b}$$

$$-\Gamma\tilde{\rho}_{\mathrm{e}}^{*}(0)-i\left\{\Omega_{\mathrm{cv}}^{*}\tilde{\rho}(\omega_{\mathrm{cv}})-\Omega_{\mathrm{cv}}\tilde{\rho}^{*}(\omega_{\mathrm{cv}})\right\}-i\left\{\Omega_{\mathrm{m}}^{*}\tilde{\rho}(\omega_{\mathrm{m}})-\Omega_{\mathrm{m}}\tilde{\rho}^{*}(\omega_{\mathrm{m}})\right\}=0 \tag{6.8c}$$

$$\begin{aligned}&\left\{i\Delta_{\mathrm{mc}}-\Gamma\right\}\tilde{\rho}_{\mathrm{e}}^{*}(-\Delta_{\mathrm{mc}})-i\left\{\Omega_{\mathrm{cv}}^{*}\tilde{\rho}(\omega_{\mathrm{m}})-\Omega_{\mathrm{cv}}\tilde{\rho}^{*}(\omega_{\mathrm{cv}}-\Delta_{\mathrm{mc}})\right\}\\ &-i\left\{\Omega_{\mathrm{m}}^{*}\tilde{\rho}(\omega_{\mathrm{m}}+\Delta_{\mathrm{mc}})-\Omega_{\mathrm{m}}\tilde{\rho}^{*}(\omega_{\mathrm{cv}})\right\}=0 \qquad (6.8d)\\ &-\left\{i\Delta_{\mathrm{mc}}+\Gamma\right\}\tilde{\rho}_{\mathrm{e}}^{*}(\Delta_{\mathrm{mc}})-i\left\{\Omega_{\mathrm{cv}}^{*}\tilde{\rho}(\omega_{\mathrm{cv}}-\Delta_{\mathrm{mc}})-\Omega_{\mathrm{cv}}\tilde{\rho}^{*}(\omega_{\mathrm{m}})\right\}\\ &-i\left\{\Omega_{\mathrm{m}}^{*}\tilde{\rho}(\omega_{\mathrm{cv}})-\Omega_{\mathrm{m}}\tilde{\rho}^{*}(\omega_{\mathrm{m}}+\Delta_{\mathrm{mc}})\right\}=0 \qquad (6.8e)\end{aligned}$$

$$-\left\{\frac{\Gamma}{2}-i\Delta_{\mathrm{m}}-i\Delta_{\mathrm{mc}}\right\}\tilde{\rho}(\omega_{\mathrm{m}}+\Delta_{\mathrm{mc}})-i\Omega_{\mathrm{cv}}\left\{2\tilde{\rho}_{\mathrm{e}}^{*}(-2\Delta_{\mathrm{mc}})\right\}-i\Omega_{\mathrm{m}}\left\{2\tilde{\rho}_{\mathrm{e}}^{*}(-\Delta_{\mathrm{mc}})\right\}=0 \tag{6.8f}$$

$$-\left\{\frac{\Gamma}{2}-i\Delta_{\mathrm{cv}}+i\Delta_{\mathrm{mc}}\right\}\tilde{\rho}(\omega_{\mathrm{cv}}-\Delta_{\mathrm{mc}})-i\Omega_{\mathrm{cv}}\left\{2\tilde{\rho}_{\mathrm{e}}^{*}(\Delta_{\mathrm{mc}})\right\}-i\Omega_{\mathrm{m}}\left\{2\tilde{\rho}_{\mathrm{e}}^{*}(2\Delta_{\mathrm{mc}})\right\}=0. \tag{6.8g}$$

Here, we neglect the higher order beat terms as those will be small, $\Delta_{\mathrm{cv}}=\omega_{\mathrm{cv}}-\omega_{\mathrm{a}}$ and $\Delta_{\mathrm{m}}=\omega_{\mathrm{m}}-\omega_{\mathrm{a}}$ are detunings of cavity and MOT light from atomic transition respectively, and

$\Delta_{mc} = \omega_m - \omega_{cv}$ is detuning of MOT laser from the cavity light. To calculate approximate effects, lets neglect terms which are higher than order one of first order beating terms and as $\Omega_{cv} \gg \Omega_m$ for the intensities we use in the experiments, $\Omega_{cv}\{2\tilde{\rho}_e^*(0)-1\} - i\Omega_m\{2\tilde{\rho}_e^*(\Delta_{mc})\} \approx \Omega_{cv}\{2\tilde{\rho}_e^*(0)-1\}$. This simplifies the Eqns. 6.8 to,

$$-\left\{\frac{\Gamma}{2} - i\Delta_{cv}\right\}\tilde{\rho}(\omega_{cv}) - i\Omega_{cv}\{2\tilde{\rho}_e^*(0)-1\} = 0 \tag{6.9a}$$

$$-\left\{\frac{\Gamma}{2} - i\Delta_{m}\right\}\tilde{\rho}(\omega_{m}) - i\Omega_{cv}\{2\tilde{\rho}_e^*(-\Delta_{mc})\} - i\Omega_m\{2\tilde{\rho}_e^*(0)-1\} = 0 \tag{6.9b}$$

$$-\Gamma\tilde{\rho}_e^*(0) - i\{\Omega_{cv}^*\tilde{\rho}(\omega_{cv}) - \Omega_{cv}\tilde{\rho}^*(\omega_{cv})\} - i\{\Omega_m^*\tilde{\rho}(\omega_m) - \Omega_m\tilde{\rho}^*(\omega_m)\} = 0 \tag{6.9c}$$

$$\{i\Delta_{mc} - \Gamma\}\tilde{\rho}_e^*(-\Delta_{mc}) - i\Omega_{cv}^*\tilde{\rho}(\omega_m) - i\Omega_m\tilde{\rho}^*(\omega_{cv}) = 0 \tag{6.9d}$$

$$-\{i\Delta_{mc} + \Gamma\}\tilde{\rho}_e^*(\Delta_{mc}) - i\Omega_{cv}\tilde{\rho}^*(\omega_m) - i\Omega_m^*\tilde{\rho}(\omega_{cv}) = 0 \tag{6.9e}$$

Solving above equations we get[1],

$$\begin{aligned}\tilde{\rho}(\omega_m) &= \left\{\frac{-4\Omega_m\left(\Delta_m + \frac{2\Omega_{cv}^2}{\Delta_{cv}}\right)}{\Gamma^2 + 4\left(\frac{2\Omega_{cv}^2}{\Delta_{cv}} + \Delta_m\right)^2 + 8\Omega_m^2}\right\} + i\left\{\frac{2\Gamma\Omega_m}{\Gamma^2 + 4\left(\frac{2\Omega_{cv}^2}{\Delta_{cv}} + \Delta_m\right)^2 + 8\Omega_m^2}\right\} \\ &= \left\{\frac{-4\Omega_m\left(\Delta_m + \Delta_{ac}\right)}{\Gamma^2 + 4\left(\Delta_m + \Delta_{ac}\right)^2 + 8\Omega_m^2}\right\} + i\left\{\frac{2\Gamma\Omega_m}{\Gamma^2 + 4\left(\Delta_m + \Delta_{ac}\right)^2 + 8\Omega_m^2}\right\}\end{aligned} \tag{6.10}$$

$$\begin{aligned}\tilde{\rho}(\omega_{cv}) &= \left\{\frac{-\Omega_{cv}\left[\Gamma^2 + 4\left(\frac{2\Omega_{cv}^2}{\Delta_{cv}} + \Delta_m\right)^2\right]}{\Delta_{cv}\left[\Gamma^2 + 4\left(\frac{2\Omega_{cv}^2}{\Delta_{cv}} + \Delta_m\right)^2 + 8\Omega_m^2\right]}\right\} + i\left\{\frac{\Gamma\Omega_{cv}\left[\Gamma^2 + 4\left(\frac{2\Omega_{cv}^2}{\Delta_{cv}} + \Delta_m\right)^2\right]}{2\Delta_{cv}^2\left[\Gamma^2 + 4\left(\frac{2\Omega_{cv}^2}{\Delta_{cv}} + \Delta_m\right)^2 + 8\Omega_m^2\right]}\right\} \\ &= p_d\left\{\frac{-\Omega_{cv}}{\Delta_{cv}} + i\frac{\Gamma\Omega_{cv}}{2\Delta_{cv}^2}\right\}.\end{aligned} \tag{6.11}$$

While deriving the above functional form, we used the identities, $\left|\frac{\Gamma}{\Delta_{cv}}\right| \ll 1$, $\left|\frac{\Omega_{cv}}{\Delta_{cv}}\right| \ll 1$, and $|\Delta_{cv}| \gg |\Delta_m|$ for far detuned cavity light. From the Eqn. 6.10 we can see that for the atomic coherence oscillating at MOT laser frequency, an additional term $\frac{2\Omega_{cv}^2}{\Delta_{cv}}$ gets added to the detuning of MOT laser. This addition is nothing but AC Stark shift due to the cavity light [55]. For Eqn. 6.11 an additional term p_d gets multiplied to the atomic coherence oscillating at cavity laser frequency. $p_d = \rho_g - \rho_e$ is population difference between excited state and ground state and is due to saturating effect of MOT light. The saturating effect of cavity light is very less

[1]The Mathematica code for the algebraic manipulation leading these equations is given at https://goo.gl/mzUzvA. The file name is "2-level_two light fields.nb".

as $\frac{\Omega_{cv}^2}{\Delta_{cv}^2} \ll 1$. Hence, the functioning of the MOT will depend on the intensity of cavity light where the atom is located. This will require adding Stark shift term to the detuning term in constants β_{3D}, ζ_{3D}, and $\mathscr{D}_{MOT}$. The Stark shifted constants will be denoted as β'_{3D}, ζ'_{3D}, and $\mathscr{D}'_{MOT}$. Also, all the cavity terms which denote scattering and dipole trapping due to cavity will get multiplied by p_d.

Effect of cavity light on motion of atoms.

On a coarser level, the intensity variation of light can be approximated as, $I(x,y) = 2I_0 e^{-\frac{2(x^2+y^2)}{w_0^2}}$. Here, $w_0 = 78\ \mu$m is cavity waist and $I_0 = \frac{I_t}{2}$ intensity per beam. The peak intensity for the cavity is I_t. We average over the standing wave formed along the cavity axis (z) as it will just add details at a very fine level, and the feature we observe in the experiment is present even if there is no standing wave. The above density profile will result in a dipole potential, $\mathscr{U}(x,y) = \frac{\hbar\Omega_{cv}^2}{\Delta_{cv}} e^{-\frac{2(x^2+y^2)}{w_0^2}}$. Where $2\Omega_{cv}$ is Rabi frequency due to cavity light. Similar to the MOT light, the diffusion co-efficient due to scattering from cavity light is, $\mathscr{D}_0(x,y) = \Gamma\hbar^2 k^2 s(x,y)$, where

$$s(x,y) = \frac{\Omega_{cv}^2}{\Delta_{cv}^2} e^{-\frac{2(x^2+y^2)}{w_0^2}} \tag{6.12}$$

is position dependent saturation parameter of cavity light. In addition to this diffusion, the atom also undergoes random motion due to fluctuations in dipole force. The diffusion co-efficient due to this fluctuation is given by [138],

$$\mathscr{D}_d(x,y) = \frac{\Gamma\hbar^2 s(x,y)}{2}\left\{k^2 + |\alpha(x,y)|^2\left[1 + \frac{32\Delta_{cv}^2 s(x,y)^3}{\Gamma^2}\right]\right\} \tag{6.13}$$

where, $|\alpha(x,y)|^2 = 4\frac{x^2+y^2}{w_0^4}$. We obtain the above simplified form using $|s(x,y)|_{max} = \frac{\Omega_{cv}^2}{\Delta_{cv}^2} \ll 1$. Hence, total diffusion co-efficient due to cavity light in x/y direction is, $\mathscr{D}_{cv}^{x/y}(x,y) = \mathscr{D}_d(x,y)/2 + \mathscr{D}_0(x,y)/3$ and in z direction along cavity axis is, $\mathscr{D}_{cv}^{z}(x,y) = \mathscr{D}_0(x,y)/3$. In the above subsection, we saw how saturation effects from MOT light will change atomic susceptibility to cavity light. Hence the dipole potential becomes $\mathscr{U}'(x,y) = \mathscr{U}(x,y)p_d(x,y)$ and the diffusion co-efficient becomes $\mathscr{D}'_{cv}(x,y) = \mathscr{D}_{cv}(x,y)p_d(x,y)$.

Monte-Carlo Simulations

For an atom which is moving in fields of MOT light and cavity light, the problem of calculating the density and the momentum distributions analytically is very challenging. Hence, we compute the distributions using Monte Carlo simulations for the Brownian motion of the atoms.

The equations of motion for the atoms including the stochastic terms are [139],

$$dx(t) = \frac{p_x(t)}{m_\mathrm{a}} dt \tag{6.14a}$$

$$dy(t) = \frac{p_y(t)}{m_\mathrm{a}} dt \tag{6.14b}$$

$$dz(t) = \frac{p_z(t)}{m_\mathrm{a}} dt \tag{6.14c}$$

$$dp_x(t) = -\beta'_{3\mathrm{D}}[x(t),y(t),z(t)]\frac{p_x(t)}{m_\mathrm{a}}dt - \left\{\zeta'_{3\mathrm{D}}[x(t),y(t),z(t)] + 4\frac{\mathscr{U}'[x(t),y(t)]}{w_0^2}\right\}x(t)dt + d\mathscr{W}_x[x(t),y(t)] \tag{6.14d}$$

$$dp_y(t) = -\beta'_{3\mathrm{D}}[x(t),y(t),z(t)]\frac{p_y(t)}{m_\mathrm{a}}dt - \left\{\zeta'_{3\mathrm{D}}[x(t),y(t),z(t)] + 4\frac{\mathscr{U}'[x(t),y(t)]}{w_0^2}\right\}y(t)dt + d\mathscr{W}_y[x(t),y(t)] \tag{6.14e}$$

$$dp_z(t) = -\beta'_{3\mathrm{D}}[x(t),y(t),z(t)]\frac{p_z(t)}{m_\mathrm{a}}dt - \zeta'_{3\mathrm{D}}[x(t),y(t),z(t)]z(t)dt + d\mathscr{W}_z[x(t),y(t)]. \tag{6.14f}$$

Where m_a is the mass of the atom, p_x, p_y and p_z are momentum in x, y and z direction respectively, $d\mathscr{W}_x[x(t),y(t)]$ is a Wiener process (Brownian motion) [139] with zero drift and volatility (standard deviation) given by, $\sqrt{2\mathscr{D}'_{\mathrm{MOT}}[x(t),y(t)]/3 + 2\mathscr{D}'^{lx}_{\mathrm{cv}}[x(t),y(t)]}$ in x-direction.

Simulating[2] the above equations for cavity light detuning of -10 GHz and $+10$ GHz, the density profile of the atoms becomes non-Gaussian as seen in figure 6.14 and figure 6.15 for red and blue detuning respectively. For density profile in x and y-direction, the dipole force dominates initially, and hence the atoms are attracted towards the cavity center. After reaching a maximum at peak intensity 120 W/cm^2, the diffusion starts to negate the dipole force and reduces the peak density when the peak intensity is increased. From figure 6.14(b) it can be seen that as there is no dipole force in the z direction, the density profile always becomes broader as the peak intensity in the cavity is increased. However, as the dipole force pushes the atoms out of the cavity mode for the blue-detuned light the density of atoms in the cavity always decreases as seen in figure 6.15.

[2]The Mathematica code for one of the simulation is given at https://goo.gl/mzUzvA. For the case where the cavity detuning is -10 GHz, the file name is "3D_MOT+cavity_10Ghz_red detuned.nb".

In this section we saw that the high intensity far detuned focused light in our experiment interferes with the operation of a MOT. This leads to change in density profile of atoms which should be taken into account for calculating atomic losses which depend on the density of the atoms. However, from figure 6.14 and figure 6.15 we can see that the change in density of atoms near center is not substantial for explain the dramatic changes seen in our experiment. Nevertheless, the density profiles will be part of the whole picture which explains the features observed in the experiment.

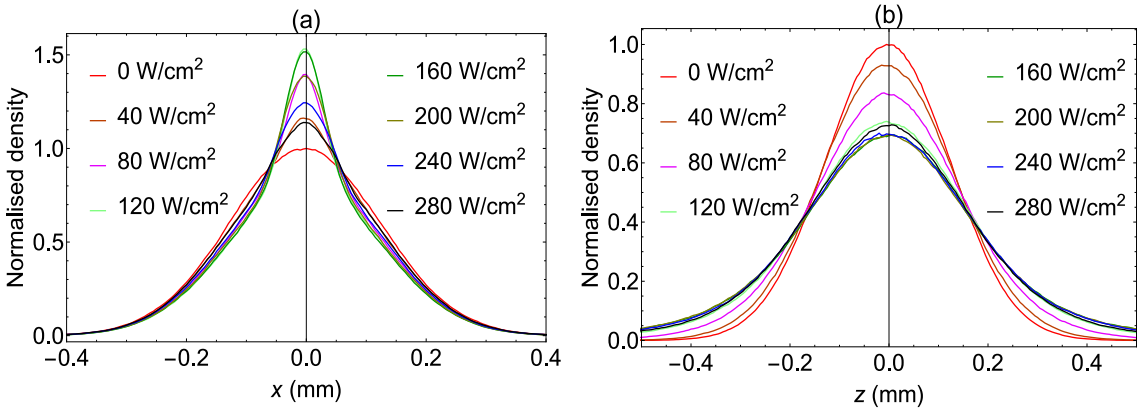

Fig. 6.14 Atomic density profile for different peak intensities of red-detuned light in the cavity, (a) for x-direction and (b) for z-direction. The parameters used are $I_r = 2$, $\Gamma/(2\pi) = 6$ MHz, $\Delta_m/(2\pi) = 12$ MHz, $\lambda = 780$ nm, $B_0 = 22$ G/cm, $\mu = 0.1\mu_B$ where μ_B is Bohr magneton, $\Delta_{cv} = -10$ GHz, and $w_0 = 78$ μm. β_{3D} and ζ_{3D} obtained from the calculations of this section and section 2.1 are multiplied by 3.4 and 0.64 respectively in order to obtain the experimental values of $\sigma_{MOT} = 0.125$ mm and $T_{MOT} = 160\mu$K for MOT size and temperature respectively. The density profile in the y-direction is same as the density profile in x-direction due to symmetry in the equations.

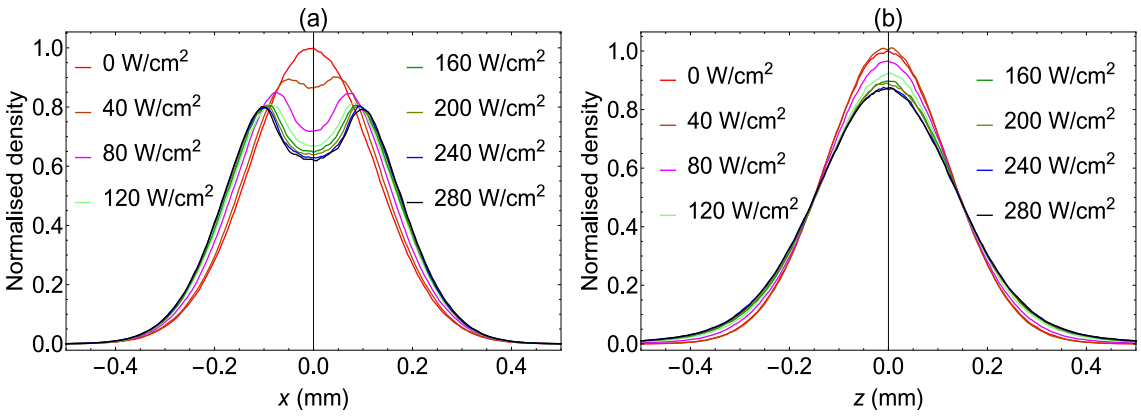

Fig. 6.15 Atomic density profile for different peak intensities of blue-detuned light in the cavity, (a) for x-direction and (b) for z-direction. The parameters used are same as mentioned in figure 6.14 with an exception of, $\Delta_{cv} = +10$ GHz.

6.4 Probable cause of atom loss in the presence of far detuned light

Although the experiments and analysis presented here offer some insight, they are not enough to completely explain the intensity dependence we observe for the atom number in the presence of far detuned light. However, we can provide some tentative explanations and future directions of investigations. In the presence of such a far (red) detuned light, there can be inelastic collisions which transfer energy from internal states to the external motion of atoms [140, 141]. The main processes in such a case are, absorption and emission of photons at different points on excited state potential energy curve of the molecule formed by the atoms, $\mathscr{A} + \mathscr{A} + \hbar\omega \rightarrow \mathscr{A}_2^* \rightarrow \mathscr{A} + \mathscr{A} + \hbar\omega'$ [140, 141]. Here $\mathscr{A}$ are atoms, and * denotes excited state. ω is the light frequency in the presence of which collision is happening. ω' is the frequency of emitted photon. The difference in energy of absorbed and emitted photon ($\hbar[\omega - \omega']$) goes into external motion of atoms. Second is fine structure changing collisions, $\mathscr{A} + \mathscr{A} + \hbar\omega \rightarrow \mathscr{A}^*(P_{3/2}) + \mathscr{A} \rightarrow \mathscr{A}^*(P_{1/2}) + \mathscr{A} = \mathscr{A} + \mathscr{A} + \hbar\omega'$ [140, 141]. The energy released in such a process is sufficient to eject the atoms out of the MOT. For ^{85}Rb, cross-section for such processes was measured using a low intensity (~ 10 mW/cm^2) seed laser [142] till the detuning of 0.5 GHz from the atomic transition. The intensities and detunings in our case are one order of magnitude more than then the parameters in [142] hence direct comparison is not possible. The theoretical analysis of such phenomena is very involved [140, 141] and has not been performed here. If a loss rate which depends on intensity is found and is denoted by $\mathscr{L}[I(x,y),\Delta_{cv}]$ cm^3/s, the total loss rate will be $\gamma = \int \mathscr{L}[I(x,y)]\ n[x,y,z,I(x,y),\Delta_{cv}]^2\ dx\ dy\ dz$, where $n[x,y,z,I(x,y),\Delta_{cv}]$ is

position dependent density shown in figure 6.14. Hence, the total loss rate will depend in a major way on the overlap integral of cavity intensity profile and density profile of atoms, which changes when total light intensity inside the cavity is changed as seen in the previous section.

Figures 6.16 and 6.17 help shed some light on the phenomena leading to the intensity dependence observed in the experiments. For these graphs, the intensity for each case was

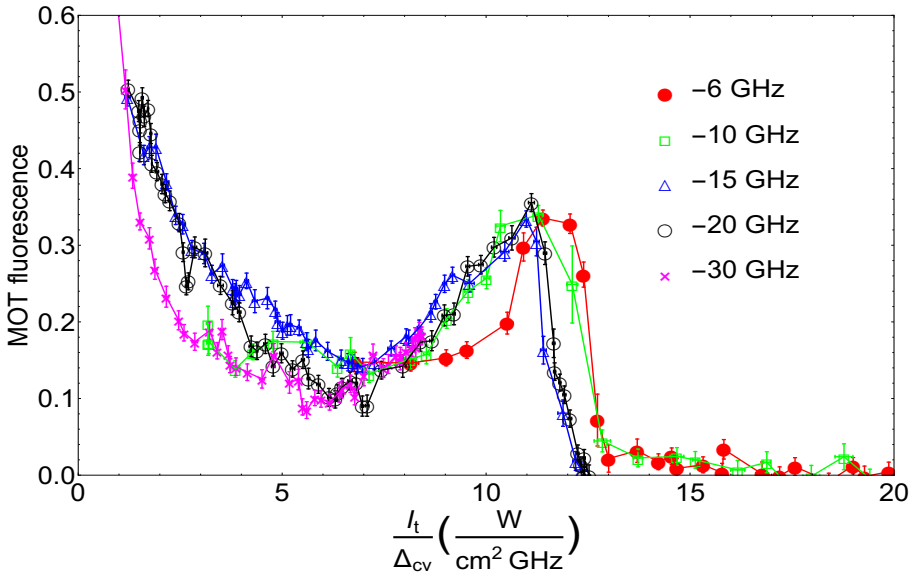

Fig. 6.16 Dependence of MOT fluorescence on the ratio, $I_t/|\Delta_{cv}|$ for red-detuned light in cavity corresponding to figure 6.4

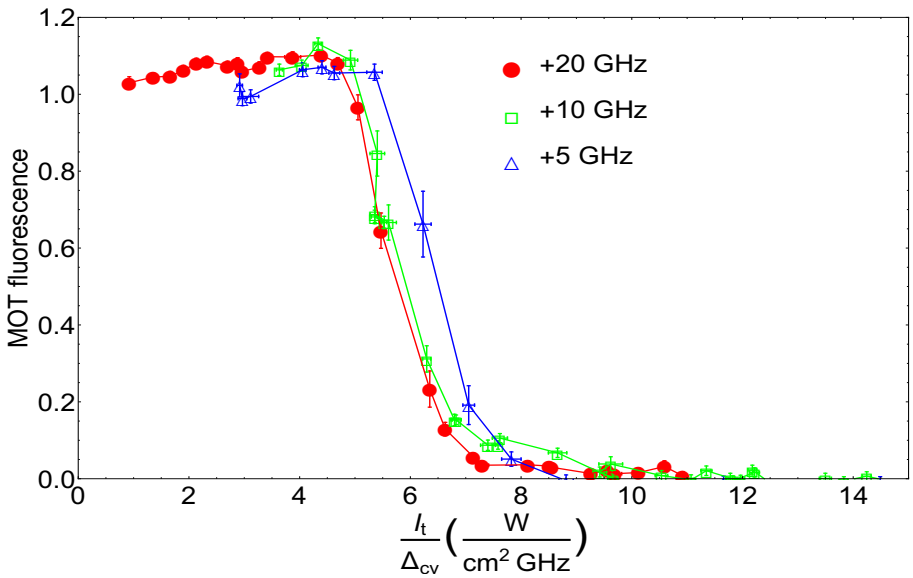

Fig. 6.17 Dependence of MOT fluorescence on the ratio, $I_t/|\Delta_{cv}|$ for blue-detuned light in cavity corresponding to figure 6.5

divided by the absolute value of the detuning of the cavity light from the atomic transition. In this case, the overlap of the feature is good, and hence we can at the least say that the phenomena leading to the feature we observe is proportional to the inverse of the detuning from the atomic transition in first order. In other words the various measurements of the MOT fluorescence at different detunings show a universal scaling behavior with I_t/Δ_{cv}.

The I_t/Δ_{cv} proportionality is shown by AC Stark shift. Hence, the AC Stark shift due to the high intensity far detuned light might play a role in the phenomenon leading to the feature we observe. To see whether the detuning by the AC stark shift puts the atomic system in resonance with other transitions of the Rb atom we explicitly put light in the experiment to ascertain on the effects of resonant scattering due to other atomic levels. We detune the focused light described in section 6.2.3 of free space light, near the atomic cooling transition (3-4′ transition of D2 line [91]). The figure 6.18 shows MOT fluorescence as a function of the frequency of this focused light from the cooling transition. The observations show a monotonic decrease in MOT fluorescence as we approach the cooling transition (from -30 to -15 MHz detuning). Beyond -30 MHz to -80 MHz the MOT intensities show a 20% variation. This is small compared to the variations seen when we put MOT fluorescence light in terms of the scaled AC Stark shift (The intensity 400 W/cm^2 corresponds to an AC Stark shift of 80 MHz for the cooling transition under the present experimental conditions). The intensity of the focused light used for obtaining figure 6.18 was 100 mW/cm^2. For comparison, the total intensity in MOT cooling beams is 45 mW/cm^2. A similar experiment with detuning of focused light near the repump transition (2-3′ transition of D2 line [91]) of the atoms in MOT was performed to mimic the case of the AC Stark shifting of the repump transition. No change in the fluorescence of atoms is seen when the frequency of this is scanned near the repump transition. This experiment confirms that the volume occupied by the focused beam is too small to have much effect on MOT loading rate, atom numbers, and MOT fluorescence. These experiments lead to the conclusion that when the detunings that are generated in our experiment by the AC stark shift are imposed with an external light field on our MOT (no light field in the far detuned regime), the effect of this field on the fluorescing atoms of the MOT is insufficient to explain the large variations seen for the far detuned experiments. This means that the other levels of the Rb atom do not play a decisive role in the intensity dependent fluorescence signal seen in our experiment.

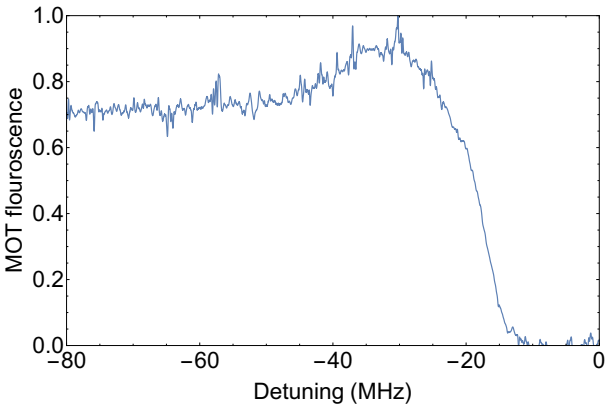

Fig. 6.18 Dependence of MOT fluorescence on the frequency of near-resonant focused light. The x-axis shows the detuning of this focused light from the cooling transition of ^{85}Rb atom (3-4′ transition of D2 line [91]). The MOT fluorescence for all the data points is normalized w.r.t. MOT fluorescence without this near focused near-resonant light.

6.5 Towards detecting molecules using cavity

In the previous sections, we discussed experiments for the creation of ultracold molecules using near detuned light from the dissociation limit coupled to the cavity. As we saw, there are number of effects that manifest, over and above the creation of molecules. Clearly, while there remain a number of aspects which require understanding in the formation process, it is clear that cold molecules and cavity geometries are compatible. In this section, we explore techniques to detect ultracold molecules using cavity, which is another big challenge to overcome experimentally. Unlike atoms, detection of molecules using resonant light is not very straightforward. A large number of vibrational and rotational levels in molecules create a problem for imaging of the molecules using fluorescence or absorption. When a molecule prepared in particular ro-vibrational level absorbs a photon and goes to an excited state, there are multiple ro-vibrational levels to which the molecule can go into after a single spontaneous emission decay. If it goes to another ro-vibrational level the molecule is lost to further imaging by the light which was resonant with the initial ro-vibrational state. There are few molecules that can be detected using florescence imaging [143]. However, these molecules are very few and cooling of them to ultracold temperatures require elaborate techniques as demonstrated in a recent work [144, 145]. The techniques that are used in most of the experiments are, ionize the molecules and detect the resulting ion on an ion detector [47–49] or, reconvert the molecules back to atoms and detect the atoms [50–53]. These techniques result in the destruction of the molecule, and the molecule is not available for further study. Hence, a detection technique which does not destroy the molecule and does not bleach the molecule from the transition of choice will

be very beneficial in performing experiments involving the molecules. Here we explore the utility of a cavity for cold molecule detection due to enhanced light molecule interaction which enables detection through dispersive effects rather than absorption effects. We discuss various advantages and disadvantages of detecting molecules using cavity. A non-destructive technique will significantly advance the study of ultracold molecules and is an important problem to solve. Recently, a non-destructive detection technique using Rydberg atoms was proposed for ultracold polar molecules [146]. Here, we focus on a theoretical exploration of general detection techniques which use light as the measuring medium. The key reason for this is that the introduction of other interacting species will interfere with the study of interactions between molecules and atoms/ions.

6.5.1 Finding a suitable molecular transition for detection

Before discussing the detection techniques, we will first identify molecular transitions which will enable efficient detection of the molecules. For studies involving molecules, it is desirable to create all of the molecules in a single ro-vibrational level. Also, the molecule creation process should be efficient. For Rb_2, $v_e = 59$ vibrational level of $(2)0_g^-$ excited long range state is convenient for creating the molecules using photoassociation. The are various advantages of choosing this level. There are no close by vibrational levels of states $(2)0_u^+$ and $(2)1_g$ which will interfere with creating molecules in this state and the transition is narrow as can be seen from the PA spectrum of Cline et.al [147]. Also, 97.5 % [3] of molecules created in this state which decay to molecular ground state will decay to $v_g = 40$ vibrational level of $(1)0_u^-$ enabling us to create most of the molecules in a single vibrational state. The transition $|v_g = 40\rangle \leftrightarrow |v_e = 60\rangle$ has the highest dipole moment of 5.65×10^{-30} C·m and hence is a suitable transition for detection of the molecules involving single transition. For simplicity, we will ignore the angular momentum states of the molecules. For detection schemes which involve two transitions, the transitions $|v_g = 40\rangle \leftrightarrow |v_e = 31\rangle$ and $|v_g = 39\rangle \leftrightarrow |v_e = 31\rangle$ can be used as both of them have fairly good values of dipole moments, the dipole moments are 1.79×10^{-30} C·m and 5.49×10^{-30} C·m respectively.

Most experimental studies of ultracold molecules require that the molecules occupy the lowest vibrational level. There are numerous experiments which have been successful in creating molecules in the vibrational ground state [149, 52, 150–155]. Here, we will mention the relevant parameters for the vibrational ground state of Rb_2 molecule. The lowest ground state of this molecule is $v_g = 0$ vibrational level of $(1)0_g^+$ electronic ground state. This ground state has the highest dipole moment of 1.29×10^{-29} C·m with $v_e = 11$ vibrational level of $(2)0_u^+$

[3] We arrive at this number by performing calculations for transition rates using ab initio calculations of A. R. Allouche et.al [148]. For further details see the PhD thesis of Jyothi S. [59].

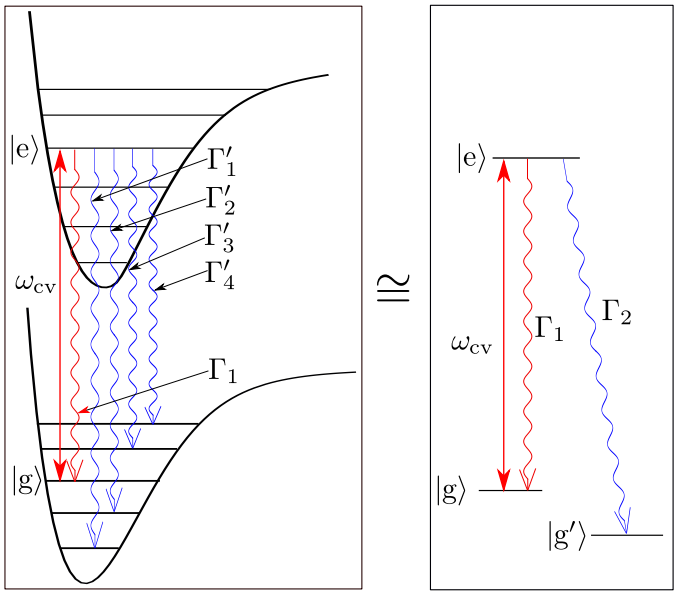

Fig. 6.19 Representative energy level diagram showing equivalence of the molecular levels and a 3-level atomic system for the purpose of detection using VRS. The straight red line denotes coupling of the cavity photon and the wavy lines denote spontaneous emission processes with the corresponding rates shown. Here, $\Gamma_2 = \Gamma_1' + \Gamma_2' + \Gamma_3' + \Gamma_4'$ is the total rate of spontaneous emission to ground vibrational levels other than $|g\rangle$.

electronically excited state. The transitions $\left|v_g = 0\right\rangle \leftrightarrow |v_e = 9\rangle$ and $\left|v_g = 1\right\rangle \leftrightarrow |v_e = 9\rangle$ are suitable for Raman processes involving two transitions, the dipole moments are 1.14×10^{-29} C·m and 1.00×10^{-29} C·m respectively.

6.5.2 Detection through VRS

In section 4.2 we saw how when multiple atoms are coupled to the cavity, the single peak of transmission of a probe light from the cavity splits into two peaks called vacuum Rabi splitting (VRS). This split is proportional to square root of the atom number and hence measuring the split tells us how many atoms are present in the cavity. The analysis done in section 4.2 was for a two-level atom in which the decay due to spontaneous emission does not take the atoms out of the transition coupled to the cavity. For molecules, this would not be the case due to the presence of multiple vibrational levels. This leakage can also occur for atoms, but the atoms can pe put back into the ground state coupling to the cavity using another repump laser [38]. Having such a repump laser is not practical for the molecules due to a large number of ground states in molecules unlike alkali atoms where there are only two ground states [38]. We can nevertheless try to see if molecules can be detected using VRS if the effect leading to VRS is faster than the rate of photon absorption. If this is the case, the molecules can be detected

without changing the number of molecules coupled to the cavity substantially. In order to see if this is feasible, we consider a equivalent case of a 3-level atom with two ground states coupled to a cavity where the cavity is resonant with one of the transitions, and there is no repump light present as shown in figure 6.19. We studied a similar system in section 4.3.1. The coupled differential equations is such a case are,

$$\frac{d\alpha(t)}{dt} = -\left(\kappa_t - i\Delta_{pc}\right)\alpha(t) - ig_0 N_c \rho(t) - \eta \tag{6.15a}$$

$$\frac{d\rho(t)}{dt} = -\left\{\frac{\Gamma_t}{2} - i\Delta_{pa}\right\}\rho(t) + ig_0\alpha(t)(\rho_e(t) - \rho_g(t)) \tag{6.15b}$$

$$\frac{d\rho_e(t)}{dt} = -\Gamma_t\rho_e(t) + ig_0\left\{\alpha^*(t)\rho(t) - \alpha(t)\rho^*(t)\right\} \tag{6.15c}$$

$$\frac{d\rho_g(t)}{dt} = \Gamma_1\rho_e(t) - ig_0\left\{\alpha^*(t)\rho(t) - \alpha(t)\rho^*(t)\right\} \tag{6.15d}$$

$$\frac{d\rho_{g'}(t)}{dt} = \Gamma_2\rho_e(t). \tag{6.15e}$$

Here, $|e\rangle$ denotes excited state, $|g\rangle$ is ground state forming a dipole transition with $|e\rangle$ which is resonant with the cavity, $|g'\rangle$ is the second ground state which is not interacting with any light and which is dark with respect to the cavity light, Γ_1 and Γ_2 are decay rate of the excited state to the ground states $|g\rangle$ and $|g'\rangle$ respectively, and $\Gamma_t = \Gamma_1 + \Gamma_2$ is the total decay rate of the excited state. $|g'\rangle$ represents all the dark ground states of molecules as can be seen from figure 6.19, the major role of this dark ground state is to bleach the atom/molecule [4] from the transition interacting with the cavity so whether it is just one dark ground state or many, it is the same for calculations in this section. Similar to the methods of chapter 4, the above time-dependent differential equations can be numerically integrated[5] to obtain the power of light transmitted by the atom-cavity system. Here, the detuning of the probe laser is adiabatically increased, and the corresponding change in cavity output power is monitored. The results are shown in figure 6.20. The detuning of the probe laser is scanned in steps totaling 200 steps. The 200 steps take 0.1 ms to finish, hence the scan rate is 10 kHz. The maximum output of cavity is 10 pW, this corresponds to 4×10^7 photons per second. So, the maximum photons available for detection at each point in the scan for figure 6.20(a) are 10 if the detection efficiency is 50%, this gives 50 ns as minimum time duration between two photons, this time duration is equal to the typical dead time of single-photon avalanche photodetectors (APD) [156] making such a

[4] Here we write atom or molecule because the theoretical modeling involving dark states is valid for both atoms and molecules.

[5] The Mathematica code for this is available at https://goo.gl/mzUzvA. The file name is "3_level_VRS_time dependent.nb".

detection feasible. The maximum photon occupancy in the cavity mode for these parameters is three.

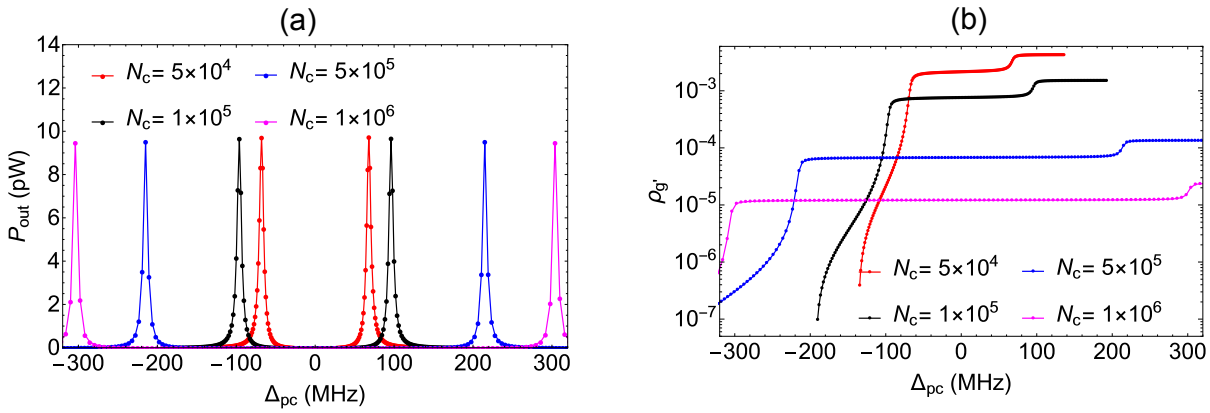

Fig. 6.20 (a) The output of the cavity-atom system showing VRS for various atom numbers. (b) Probability for the atom to go into the dark ground state $|g'\rangle$. At the start of the scan, all atoms/molecules are assumed to be in state $|g\rangle$. The parameters used here are, power of light input to the cavity $P_{in} = 0.26$ nW, $\Gamma_1/2\pi = 301.6$ kHz, $\Gamma_2/2\pi = 7.5$ MHz, $g_0/2\pi = 304$ kHz, $\kappa_t/2\pi = 7.81$ MHz, loss rate from input mirror of cavity $\kappa_{r1} = 0.1\kappa_t$, and loss rate from output mirror of cavity $\kappa_{r2} = 0.8\kappa_t$. Here, $|e\rangle$ is $v_e = 60$ vibrational level of $(2)0_g^-$ electronically excited state, $|g\rangle$ is $v_g = 40$ vibrational level of $(1)0_u^-$ electronic ground state as explained in subsection 6.5.1, and $|g'\rangle$ is everything else including the free atom states. The distance between the two mirrors is 11.8 mm, and the radius of curvature of the mirrors is 10 mm, this gives a waist size of 30 μm for the cavity mode at the center of the cavity. These cavity parameters are taken from the experimental work of Albert et.al [89].

From figure 6.20(b) it can be seen that for a larger number of atoms/molecules the leakage into the dark ground state ($|g'\rangle$) is smaller. This is because the higher atom/molecule number will ensure increased distance of VRS peaks from the atomic/molecular resonance and hence the probability of photon absorption by single atoms/molecule reduces. For collective strong coupling of $2g_0\sqrt{N_c}/(2\pi) = 136$ MHz, 0.45% atoms/molecules will be lost to the dark ground state per scan and for $2g_0\sqrt{N_c}/(2\pi) = 608$ MHz, 2.5×10^{-3}% atoms/molecules will be lost. These numbers tell us that such a detection scheme is feasible. The most important parameter here is, the ratio of loss rate from the output mirror of the cavity to total loss rate from the cavity mirrors, $\frac{\kappa_{r2}}{\kappa_t}$. In order to keep the absorption and spontaneous emission of a photon by single atoms/molecules low, we need to keep the photon occupancy of the cavity on the lower side. This results in lower flux of photons out of the cavity, consequently reducing the detection efficiency. Hence, to ensure optimal detection, the loss from cavity mirrors other than the loss due to leakage from output mirror should be minimized. Therefore the strategy is to have ultra-high reflectivity input mirror and a moderately reflective output mirror such that most of

the losses from the mirrors are due to transmission rather than absorption and scattering losses. This means the ratio $\frac{\kappa_{r2}}{\kappa_t}$ should be very high. For example if we keep the output photon flux and other parameters same, a low ratio of $\frac{\kappa_{r2}}{\kappa_t} = 0.01$ will result in loss of 40% atoms/molecules in the case of $2g_0\sqrt{N_c}/(2\pi) = 136$ MHz and a loss of 0.19% atoms/molecules in the case of $2g_0\sqrt{N_c}/(2\pi) = 608$ MHz atoms/molecules per scan. In addition, having a larger value of κ_t is advantageous in this case because a larger value of κ_t means the photon comes out of the cavity faster reducing its probability of getting absorbed and the steady state inside the cavity is achieved faster, enabling a faster scan. For example, if we keep the above-mentioned ratio, output photon flux, and other parameters same, $\kappa_t = 20$ MHz will result in a loss of 0.2% in the case of $2g_0\sqrt{N_c}/(2\pi) = 136$ MHz and a loss of 1.5×10^{-3}% atoms/molecules in the case of $2g_0\sqrt{N_c}/(2\pi) = 608$ MHz per scan and, $\kappa_t = 0.5$ MHz will result in loss of 1.5% atoms/molecules in the case of $2g_0\sqrt{N_c}/(2\pi) = 136$ MHz and a loss of 8×10^{-3}% atoms/molecules in the case of $2g_0\sqrt{N_c}/(2\pi) = 608$ MHz per scan. However, we cannot keep on increasing κ_t because this will result in very broad cavity linewidth which will engulf the VRS.

6.5.3 Detection through cavity EIT

The phenomenon of electromagnetically induced transparency (EIT) [93] is a good prospect for detection of molecules using cavity. It is a well-known fact that there is a steep dispersive effect, and little or no absorption near the EIT peak [93]. This could be exploited for the detection of molecules. The presence of a cavity will enhance this effect for multiple molecules. To start with, we will first analyze the case of three-level atoms coupled to the cavity and later extend the analysis to the molecules. The three levels with two ground states ($|\mathrm{g}\rangle$ and $|\mathrm{g}'\rangle$) form a lambda system [93]. For EIT, another light field which couples the earlier dark ground state ($|\mathrm{g}'\rangle$) to excited state is required. We will call this light field control beam. In a frame rotating at probe frequency, the atomic Hamiltonian for such a case is,

$$\hat{H} = \hbar \sum_{j=1}^{N} \left[-\Delta_{\mathrm{pa}} \hat{\sigma}^j_{\mathrm{ee}} + (-\Delta_{\mathrm{pa}} + \Delta_{\mathrm{ra}}) \hat{\sigma}^j_{\mathrm{g'g'}} + g_j (\hat{a}^\dagger \hat{\sigma}^j_{\mathrm{ge}} + \hat{a} \hat{\sigma}^j_{\mathrm{eg}}) + (\Omega^* \hat{\sigma}^j_{\mathrm{g'e}} + \Omega \hat{\sigma}^j_{\mathrm{eg'}}) \right]. \quad (6.16)$$

Here, 2Ω is Rabi frequency for control beam, $\hat{\sigma}^j_{mn} = (|m\rangle \langle n|)^j$ denotes the atomic operators for j^{th} atom, $\Delta_{\mathrm{pa}} = \omega_{\mathrm{p}} - (\omega_{\mathrm{e}} - \omega_t extg)$ is the probe laser detuning from the $|\mathrm{g}\rangle \leftrightarrow |\mathrm{e}\rangle$ transition, and $\Delta_{\mathrm{ra}} = \omega_{\mathrm{r}} - (\omega_{\mathrm{e}} - \omega_{\mathrm{g'}})$ is the control laser detuning from the $|\mathrm{g}'\rangle \leftrightarrow |\mathrm{e}\rangle$ transition. See

section 4.2 for remaining definitions. Using Eqn. 4.1 the equations of motion are,

$$\dot{\alpha} = -\eta - \alpha(\kappa_t - i\Delta_{pc}) - i\sum_{j=1}^{N} g_j \rho^j_{ge} \tag{6.17a}$$

$$\dot{\rho}^j_{ge} = (-\frac{\Gamma_t}{2} + i\Delta_{pa})\rho^j_{ge} - i\alpha g_j(\rho^j_{gg} - \rho^j_{ee}) - i\rho^j_{gg'}\Omega \tag{6.17b}$$

$$\dot{\rho}^j_{gg'} = (-\gamma_{gg'} + i\Delta_{pa} - i\Delta_{ra})\rho^j_{gg'} + i\alpha g_j \rho^j_{eg'} - i\rho^j_{ge}\Omega^* \tag{6.17c}$$

$$\dot{\rho}^j_{g'e} = (-\frac{\Gamma_t}{2} + i\Delta_{ra})\rho^j_{g'e} - i\alpha g_j \rho^j_{g'g} - \Omega(\rho^j_{g'g'} - \rho^j_{ee}) \tag{6.17d}$$

$$\dot{\rho}^j_{gg} = \Gamma_1 \rho^j_{ee} - i\alpha^* g_j \rho^j_{ge} + i\alpha g_j \rho^j_{eg} \tag{6.17e}$$

$$\dot{\rho}^j_{g'g'} = \Gamma_2 \rho^j_{ee} + i\rho^j_{eg'}\Omega - i\rho^j_{g'e}\Omega^* \tag{6.17f}$$

$$\dot{\rho}^j_{ee} = -\Gamma_t \rho^j_{ee} + i\alpha^* g_j \rho^j_{ge} - i\alpha g_j \rho^j_{eg} - \rho^j_{eg'}\Omega + i\rho^j_{g'e}\Omega^*. \tag{6.17g}$$

Here, $\Delta_{pc} = \omega_p - \omega_{cv}$ is detuning of probe laser from the cavity resonance, $\gamma_{gg'}$ is the decoherence rate for the coherence between the two ground states $\{|g\rangle, |g'\rangle\}$. In steady state, $\dot{\alpha} = 0$ and $\dot{\rho}_{mn} = 0, \forall(m,n)$ and Eqns. 6.17 become a set of linear equations which can be solved algebraically. Eliminating the atomic variables we get,

$$\begin{aligned} -\eta - \alpha(\kappa_t - i\Delta_{pc}) &= i\sum_{j=1}^{N} g_j \rho^j_{ge} \\ &= i\alpha \sum_{j=1}^{N} \chi_j \\ &= i\alpha \frac{2g_0^2 N_c(\Delta_{ra} - \Delta_{pa})}{2|\Omega|^2 + (2\Delta_{pa} + i\Gamma_t)(\Delta_{ra} - \Delta_{pa})} \\ &= i\alpha\chi. \end{aligned} \tag{6.18}$$

Where, $\chi_j = \frac{2g_j^2(\Delta_{ra} - \Delta_{pa})}{2|\Omega|^2 + (2\Delta_{pa} + i\Gamma_t)(\Delta_{ra} - \Delta_{pa})}$ is linear susceptibility of j^{th} atom and χ is total linear susceptibility. In deriving the above equation, we have assumed that the intra-cavity light amplitude is very small compared to other parameters, i.e. $g_0|\alpha| \ll \Omega, \Gamma_t$ and hence we are in a linear regime. We also assume there is no decoherence for the coherence between the two ground states, i.e. $\gamma_{gg'} = 0$, this approximation is valid for a dilute gas. The average photon number inside the cavity can then be written as,

$$\bar{n} = |\alpha|^2 = \frac{\eta^2}{(\Delta_{pc} - \chi_1)^2 + (\kappa_t - \chi_2)^2} \tag{6.19}$$

where,

$$\chi_1 = \frac{4g_0^2 N_c(\Delta_{ra}-\Delta_{pa})\left(|\Omega|^2-\Delta_{pa}(\Delta_{ra}-\Delta_{pa})\right)}{\Gamma_t^2(\Delta_{ra}-\Delta_{pa})^2+4\left(|\Omega|^2-\Delta_{pa}(\Delta_{ra}-\Delta_{pa})\right)^2}$$

and

$$\chi_2 = -\frac{2\Gamma_t g_0^2 N_c(\Delta_{ra}-\Delta_{pa})^2}{\Gamma_t^2(\Delta_{ra}-\Delta_{pa})^2+4\left(|\Omega|^2-\Delta_{pa}(\Delta_{ra}-\Delta_{pa})\right)^2}$$

are real and imaginary parts of χ respectively. χ_1 results in the dispersive effects and χ_2 results in change of total loss rate for cavity field. For $\Delta_{ra}=0$ and $\Delta_{pa}=\Delta_{pc}=\Delta$,

$$\chi_1 = -\frac{4g_0^2 N_c\Delta\left(|\Omega|^2+\Delta^2\right)}{\Gamma_t^2\Delta^2+4\left(|\Omega|^2+\Delta^2\right)^2} \text{ and } \chi_2 = -\frac{2\Gamma_t g_0^2 N_c\Delta^2}{\Gamma_t^2\Delta^2+4\left(|\Omega|^2+\Delta^2\right)^2}.$$

In the limit of $\Delta^2 \ll |\Omega|^2, 4\frac{|\Omega|^4}{\Gamma_t^2}$, i.e. small detuning of probe laser near the EIT peak, the intracavity photon number ($\bar{n}$) reduces to[6],

$$\bar{n} = |\alpha|^2 = \frac{\eta^2}{\kappa_t^2}\frac{d^2}{\Delta^2+d^2}. \tag{6.20}$$

This is a Lorentzian function with full width at half maxima (FWHM), $2d = \frac{2|\Omega|^2\kappa_t}{\sqrt{\Gamma_t g_0^2\kappa_t N_c+\left(g_0^2N_c+|\Omega|^2\right)^2}}$.

For $|\Omega|^2 \gg \Gamma_t\kappa_t$, the FWHM reduces to,

$$2d = \frac{2\kappa_t}{(\frac{g_0^2N_c}{|\Omega|^2}+1)}. \tag{6.21}$$

This expression gives us a simple dependence of FWHM on the atom number and greater the atom number lower the linewidth of the Lorentzian. Importantly, the dependence is linear in N_c unlike the square root dependence of VRS making this method of atom/molecule number detection more sensitive. Such a linewidth narrowing was predicted a long time ago by Lukin et.al [157]. It was observed for thermal atoms coupled to ring cavity [158], laser-cooled atoms coupled to Fabry-Pérot cavity [159], and for laser-cooled ions coupled to Fabry-Pérot cavity [160].

Here, the lambda system for the atoms/ions was a closed system, and there was no leakage to any other dark state. However, this will not be the case for molecules due to the presence of a large number of ground states. To see if the Eqn. 6.21 holds true for such a leaky system we perform time-dependent numerical simulations of partial differential equations 6.17 with

[6]The Mathematica code for the algebraic manipulation leading to this equation is given at https://goo.gl/mzUzvA. The file name is "3_level_EIT_Steady state_algebra.nb".

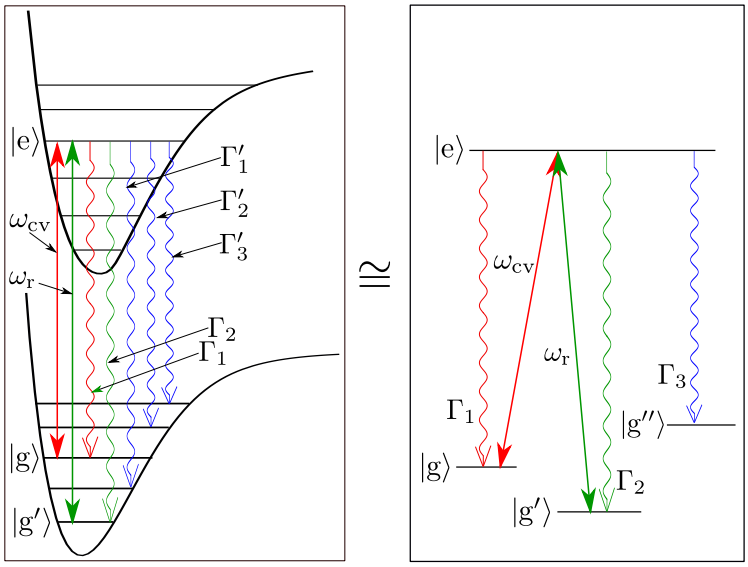

Fig. 6.21 Representative energy level diagram showing equivalence of the molecular levels and a 4-level atomic system for the purpose of detection using EIT. The straight red line denotes coupling of the cavity photon, the straight green line denote coupling of the control laser, and the wavy lines denote spontaneous emission processes with the corresponding rates shown. Here, $\Gamma_3 = \Gamma_1' + \Gamma_2' + \Gamma_3'$ is the total rate of spontaneous emission to ground vibrational levels other than $|g\rangle$ and $|g'\rangle$.

an additional decay Γ_3 to the dark ground state $|g''\rangle$. The total decay rate from excited state becomes $\Gamma_t = \Gamma_1 + \Gamma_2 + \Gamma_3$ and all other parameters remain the same. An equivalence diagram between molecular levels and atomic levels is shown in the figure 6.21.

For such a scenario, the EIT peaks obtained by performing a numerical integration[7] are shown in figure 6.22 for different atom numbers. Here, for collective strong coupling of $2g_0\sqrt{N_c}/(2\pi) = 13.65$ MHz, 2.9% atoms/molecules will to lost to the dark ground state per scan and for $2g_0\sqrt{N_c}/(2\pi) = 136$ MHz, 3×10^{-3}% atoms/molecules will to lost. Here, we have kept the scan duration to be 1 ms because it takes more time to reach steady state in this case of detection using EIT. Additionally, at the end of the scan, very few atoms/molecules go to the state $|g'\rangle$ as can be seen from figure 6.23. If we compare this detection scheme with the scheme of detection through VRS for the same $g_0\sqrt{N_c}$, this detection is a significant improvement in terms of efficiency. For same collective strong coupling, the loss rate per scan here is two orders of magnitude better, and hence detection of a smaller number of molecules is possible. For such an EIT-based detection scheme, having smaller κ_t is better because the EIT window is usually small. For example, if we keep the output photon flux and other parameters

[7]The Mathematica code for this is available at https://goo.gl/mzUzvA. The file name is "4level_time dependent_EITscan.nb".

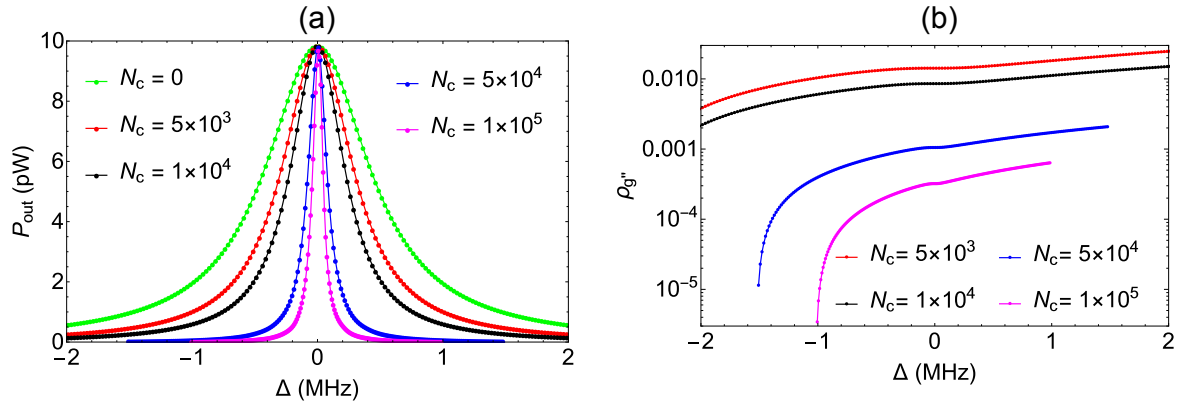

Fig. 6.22 (a) The output of the cavity-atom system showing the EIT peak for various atom numbers. Dots show the results of time-dependent numerical simulation of the scan and the lines are obtained using the simple Eqn. 6.21. (b)The probability for the atom to go into the dark ground state $|g''\rangle$. At the start of the scan, all atoms/molecules are assumed to be in state $|g\rangle$. The parameters used here are, the power of light input to the cavity $P_{in} = 40$ pW, $\Gamma_1/2\pi = 30.4$ kHz, $\Gamma_2/2\pi = 284.5$ kHz, $\Gamma_3/2\pi = 6.14$ MHz, $g_0/2\pi = 96.5$ kHz, $\kappa_t/2\pi = 0.5$ MHz, $\Omega = 10$ MHz, loss rate from the input mirror of the cavity $\kappa_{r1} = 0.1\kappa_t$, and loss rate from the output mirror of the cavity $\kappa_{r2} = 0.8\kappa_t$. Here, $|e\rangle$ is $v_e = 31$ vibrational level of $(2)0_g^-$ electronically excited state, $|g\rangle$ and $|g'\rangle$ are $v_g = 40$ and $v_g = 39$ vibrational levels of $(1)0_u^-$ electronic ground state respectively as explained in subsection 6.5.1, and $|g''\rangle$ is everything else including the free atom states. Cavity parameters are same as in figure 6.20.

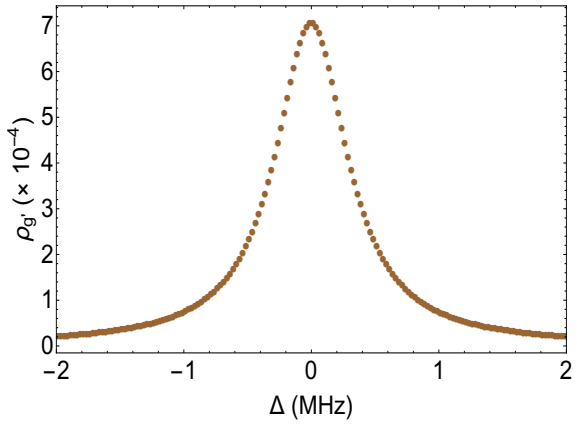

Fig. 6.23 The probability for the atom/molecule to be in ground state $|g'\rangle$ during the detection scan. Here, $2g_0\sqrt{N_c}/(2\pi) = 13.65$ MHz and other parameters are same as in figure 6.22.

same, $\kappa_t = 2.5$ MHz will result in a loss of 46% in the case of $2g_0\sqrt{N_c}/(2\pi) = 13.65$ MHz and a loss of 15×10^{-3}% atoms/molecules in the case of $2g_0\sqrt{N_c}/(2\pi) = 136$ MHz per scan. Although small κ_t is desirable in this case, we cannot lower it arbitrarily because the linewidth of the probe laser will also require lowering. Similar to the case of detection using VRS,

here too the ratio $\frac{\kappa_{r2}}{\kappa_t}$ should be on the higher side to avoid high intracavity photon number occupation.

It is a well-established fact that the phenomenon of EIT is accompanied by the phenomenon of slowing of light [93]. Hence, we expect an increase in trapping times for the photon inside the cavity as observed in few previous experiments [161, 159]. This phenomenon of slow light can be used to detect the molecules placed inside the cavity. We explore a simple detection scheme. The scheme is to keep $\Delta_{pa} = \Delta_{pc} = \Delta_{ra} = 0$, switch on the probe laser and let the system reach the steady state [8] such that we get a constant light intensity output of the cavity, the second step is to suddenly switch off the probe laser and observe the decay of the cavity output light. The results of numerical simulations[9] are shown in figure 6.24.

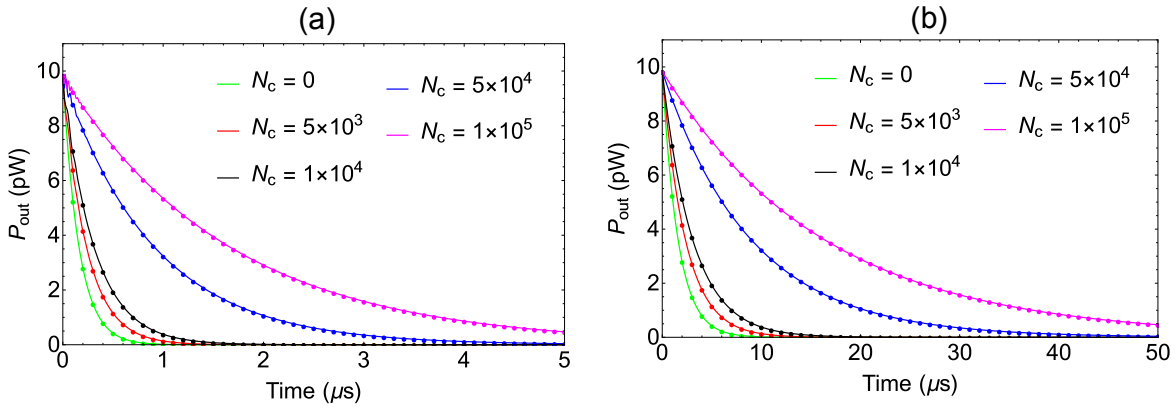

Fig. 6.24 The output of the cavity-atom system showing a slowing of cavity light decay for various atom numbers. (a) $\kappa_t/(2\pi) = 0.5$ MHz and (b) $\kappa_t/(2\pi) = 0.05$ MHz. All other parameters are same as figure 6.22. Dots show the results of time-dependent numerical simulation of the decay and the lines are obtained using an exponential form, $I_0 e^{-2d\times t}$ where 2d is taken from Eqn. 6.21 and t is the time variable.

Generally, a Lorentzian in frequency space is exhibits an exponential decay in the time domain, we expect the decay curves to be exponential with the decay rates, $2d$ of Eqn. 6.21. This is indeed what we see from the full numerical simulations as seen in figure 6.24. For this detection scheme, smaller value of κ_t is very advantageous because lower the value of κ_t higher the decay time and higher the observation time as seen in figure 6.24(b) for $\kappa_t = 0.05$ MHz. As seen from figure 6.24(a) for $\kappa_t = 0.5$ MHz, the observation time is very short. Hence, very few photons will be collected during a single decay due to a finite dead time of an APD. However, multiple such detection cycles can be performed, results of which can be added up.

[8] Time required to reach steady state is 1 ms for the atom number 5×10^5. It will be lower for smaller atom number

[9] The Mathematica code for this is available at https://goo.gl/mzUzvA. The file name is "4level_time dependent_EIT_slowlight.nb".

For example, observation of one decay event in case of $\kappa_t = 0.5$ MHz gives a maximum of 1 photon detection per 50 ns, so for 10 detection cycles, we get a maximum of 10 detections per observation point if the total points are 20 for 1 μs decay. Similarly, in the case of $\kappa_t = 0.05$ MHz, we get a maximum of 10 detections per observation point if the total points are 20 for 10 μs decay [10] if a maximum of 1 photon is detected per 50 ns. Hence comparing the two cases with respect to total measurement time and total photon flux, 10 decay events in case of $\kappa_t = 0.5$ MHz and 1 decay event in case of $\kappa_t = 0.05$ MHz gives same detection efficiency.

For this detection scheme, the condition $\Delta_{pa} = \Delta_{ra}$ is always satisfied. Hence, we expect complete transparency and very little absorption of photons. For 10 detection cycles in case of $\kappa_t = 0.5$ MHz, 1.6×10^{-2}% atoms/molecules are lost for $2g_0\sqrt{N_c}/(2\pi) = 13.65$ MHz and 5×10^{-4}% atoms/molecules are lost for $2g_0\sqrt{N_c}/(2\pi) = 136$ MHz. In contrast, for single detection cycles in case of $\kappa_t = 0.05$ MHz, 1.6×10^{-3}% atoms/molecules are lost for $2g_0\sqrt{N_c}/(2\pi) = 13.65$ MHz and 7×10^{-5}% atoms/molecules are lost for $2g_0\sqrt{N_c}/(2\pi) = 136$ MHz. From above numbers, we can say that the detection involving lower κ_t is more efficient. However, less than one atom/molecule is lost during each detection cycle in each case so detection scheme with $\kappa_t = 0.5$ MHz is already very efficient and it is not required to make the detection scheme more efficient. Less loss for this detection scheme implies more flexibility for the ratio $\frac{\kappa_{r2}}{\kappa_t}$. For example, if we fix the output photon flux, $\kappa_t = 0.5$ MHz, and other parameters, a low ratio of $\frac{\kappa_{r2}}{\kappa_t} = 0.01$ will result in loss of 0.16% atoms/molecules in the case of $2g_0\sqrt{N_c}/(2\pi) = 13.6$ MHz and a loss of 5×10^{-3}% atoms/molecules in the case of $2g_0\sqrt{N_c}/(2\pi) = 136$ MHz atoms/molecules for the 10 decay events.

In terms of detection efficiency, the detection of molecules through delay in decay times mentioned above is best of all the detection schemes which we explored. However, the condition $\Delta_{pa} = \Delta_{ra} = 0$ should always be satisfied, and any fluctuations around this condition will hinder the detection as the EIT effect is very sensitive near this condition as can be seen from narrow linewidths of figure 6.22. In the presence of such fluctuation higher value of κ_t will be more advantageous due to large linewidths in this case. The condition $\Delta_{pa} = \Delta_{ra}$ will be mostly satisfied if both the probe and the control beams are derived from the same laser. This is feasible for the molecular levels analyzed in this section as the frequency difference between the two ground states $|g\rangle$ and $|g'\rangle$ is only 338.74 MHz. Large wavelength difference between the two ground states will require more elaborate techniques [162] for locking of probe and control frequency. This will be the case when the molecules are in the lowest vibrational level. For example, the frequency difference between the lowest two vibrational levels of the state $(1)0_g^+$ of Rb_2 molecule is 1.724 THz. This is a disadvantage for molecules in their vibrational ground state. There are also advantages for such molecules. One advantage is, the dipole moments

[10] This will require 500 ns integration window when counting photons.

are better by one order of magnitude as discussed in subsection 6.5.1, this means g_0 is one order of magnitude better and hence will enable detection of two orders of magnitude fewer atoms as can be inferred from the term $g_0^2 N_c$ in Eqn. 6.21. Hence, for the cavity parameters of figures 6.22 and 6.24 a minimum of 50 molecules can be detected whereas a minimum of 5000 molecules could be detected in $\nu_g = 40$ level.

6.6 Conclusion

In this chapter, we explored techniques for molecule creation and detection using a cavity. Creation of diatomic molecules from ultracold atoms using light coupled to a cavity was experimentally demonstrated. During these experiments, we also observed some unexpected features for atom loss as a function of the intensity of cavity light. These features resulted from phenomena which compete with the process of creation of molecules. Even if the exact reason for the intensity dependence is not known, it is evident from all the analysis that for creating molecules by the process of PA, it is better to be very far detuned ($>$ 50 GHz) from the atomic transition in order to avoid the strong competing processes. If for some reason the molecule creation process has to happen for the detunings 1-50 GHz, the intensity should be selected so as to maximize the process of PA. For this intensity selection, experiments similar to ones discussed in subsection 6.2.2 should be performed.

In section 6.5 we explored techniques with the help of numerical simulations and theoretical analysis for detecting molecules using a cavity. We found out that the detection of molecules using the EIT feature is not just feasible but also very efficient. The next step to advance these detection techniques will be to test them first on ultracold atoms as this is technically easier. Once this is demonstrated, the detection scheme can be extended to molecules.

Chapter 7

Summary and future prospects

7.1 Summary of results

The initial work reported in the thesis related to the development of a MOT for potassium atoms which was combined with an existing MOT of rubidium atoms. This was done with a motivation of studying interactions between atoms, ions, and molecules of different species. The first use of these ultracold potassium atoms was to efficiently create potassium ions which could be trapped in an ion trap. The cooling of these potassium ions by ultracold and localized rubidium atoms was then demonstrated in an experiment. This is the first demonstration of the cooling of ions by gas of atoms which are heavier than the ions. Such cooling is not possible by a uniform gas of atoms heavier than the ions, it requires a gas localized at the center of the ion trap for cooling the ions. Monte-Carlo simulations to explain the mechanisms behind this cooling process were performed, and methods to increase the efficiency of such cooling process was explored using these simulations. Also, the dependence of steady-state temperature on various parameters was investigated using these Monte-Carlo simulations.

Next, we explored several atom-cavity configurations with the intention of exploiting some of these to detect interactions between atoms, ions, and molecules. First, we performed a theoretical study of the nonlinear phenomenon of optical bistability for a system of multi-level atoms coupled to a Fabry-Pérot cavity. The analysis for exploitation of this phenomenon to study switching of light using light was performed for both ultracold atoms and thermal atoms. Using this analysis, we were able to explain the results of a vapor cell optical bistability and switching experiment.

We then performed experiments to study the effects of atom driving on the atom-cavity system. The atoms were driven by a classical laser light interacting with the atoms. We observed emission of light from the cavity for such a system. For red detuning of the cavity with respect to atomic transition, we observed features of lasing for the light emitted by the

cavity. For light which probes the cavity when driven atoms are present inside the cavity, we observe gain and line narrowing. This observation provides irrefutable evidence for lasing in this system. The seed photon for starting this lasing action is provided by the fluorescence of the atoms.

One of the motivations of working with a cavity in this thesis was to develop techniques to create and detect ultracold molecules using a cavity. For this purpose, we coupled high intensity light to a cavity which we used to demonstrate the creation of diatomic molecules from ultracold atoms through the process of photoassociation (PA). In addition to loss due to molecule production, we also observed atomic losses for far detuned light from the atomic transition which showed some surprising behavior. This surprising behavior was a non-monotonic change in atom loss as the intensity of the far detuned light is increased. We performed several experiments to explore the phenomena leading to these losses and performed analyses of probable phenomena which can lead to these losses. We also performed experiments for optimizing the process of molecule creation in the presence of these losses and observed that it is possible to create molecules efficiently if we choose the right intensity and a detuning further away from the atomic resonance frequency of the PA light which makes the molecules.

Detection of molecules without destroying or bleaching them from a particular state is a long standing problem. We hope to resolve this problem by developing techniques to detect molecules using a cavity. For this purpose, we explored methods to detect diatomic molecules using cavity without destroying or bleaching them. The effects of three detection techniques on the state of the molecules were analyzed. The three detection techniques were, detection using VRS signal in collective-strong coupling regime, detection using linewidth narrowing in the case of cavity EIT phenomenon, and detection through the effect of slowing of light in case of cavity EIT phenomenon. From these analyses, it was found that the detection technique which uses slowing of light in EIT phenomenon is the most efficient detection method. The calculations also showed that this method is feasible for detecting ultracold Rb_2 molecules.

7.2 Future prospects

The work discussed in this thesis opens up many prospects for the future. We discuss few of them in this section.

7.2.1 Prospects for studying of Molecule-Molecule interactions

One of the goals of the techniques developed in this thesis was to study molecule-molecule interactions at ultracold temperatures where the quantum statistics of atoms which make up

the molecules will play a significant role. The idea is to study the behavior of composite particles where the quantum statistics of the components play a role. For example, the diatomic molecules $^{39}K_2$ and $^{40}K_2$ are very good candidates to study composite bosons as they are bosonic molecule made up of two bosonic atoms and two fermionic atoms respectively. Elastic scattering cross sections of both the molecules can be extracted from loss rates of a molecule trap. The difference in cross sections will mainly be due to the bosonic or fermionic composition of the molecules as the potentials due to electronic interaction will be same. Below we discuss briefly molecule-molecule interaction and suggest a way forward to study such interactions both theoretically and experimentally. The discussion is in the spirit of posing hard questions for the future, where several critical concepts are not yet well formulated.

Theoretical considerations

Theoretically, it needs to be figured out under what conditions the molecule-molecule interaction for the diatomic molecules is two-body interaction and under what conditions it is a four-body interaction. We discuss various possibilities below. An effective two-body scattering interaction can occur if the potential between the molecules is very repulsive and the molecules are at ultracold temperatures, and hence the molecules do not come close enough. For such a case the internal structure of the molecules should not play a role, and the interaction would be similar to the interaction of two structureless particles. For this case, the quantum statistics of the constituent atoms will not play a role, and only quantum statistics of the molecule as a whole will matter. Similar to the atomic case the s-wave collisions for fermionic molecules will be absent [163, 164]. An extension of this scenario will be molecular structure as a perturbation to the two-body interaction. This perturbation will result due to the dependence of intermolecular potential on the orientation of the molecules when they approach each other. The effect of this perturbation will be to change the scattering cross-section with respect to the earlier case of two-body collision of structureless particles. There is no qualitative difference between the above two cases. The cases mentioned above require knowledge of interaction potential between the molecules which can be found by doing ab-initio calculations of electronic energies as a function of the distance between the atomic nuclei [165].

An interesting case to study will be for molecules which can come close to each other such that particle exchange between the molecules is a possibility. For such a four-body interaction the quantum statistics of the constituent atoms will play a significant role in the interaction. The following questions can be asked in the study of molecule-molecule interactions. How does the system transitions from a two-body case to a four body case? How do the internal state and the bond length of the molecules affect the four-body interactions?

Practical considerations

Here we discuss the experimental aspects of a possible molecule-molecule interaction study. For alkali atoms the number of electrons is odd. Hence the electronic wavefunction should be anti-symmetric. Now, depending on the spin of nucleus the wavefunction of nuclear motion is symmetric or anti-symmetric. For example, ^{39}K has spin 3/2 which gives an anti-symmetric nuclear wavefunction and hence the overall wavefunction is symmetric and the atom is bosonic, for ^{40}K the spin is 4 making the nuclear wavefunction symmetric and the atom fermionic. The spin wavefunction of all four nuclei in the two diatomic molecules should be either symmetrized or anti-symmetrized. Using the method of *Young Tableau* [163] we can find the number of possible symmetric and anti-symmetric wavefunctions for a given spin and particle number. For the four particles in the two diatomic molecules having spin 3/2, there are 29 symmetric and 1 anti-symmetric states. For spin 4 there are 429 symmetric and 126 anti-symmetric states. This tells us that the spin wavefunction will be symmetric in majority of the cases, and hence the symmetry has to be followed by the nuclear motional wavefunction, anti-symmetric for ^{39}K and symmetric for ^{40}K. For spin lower than 3/2 all spin wavefunctions are symmetric. From the above discussion we can see that the experiments will require separating various spin states and picking only one type.

Earlier, we mentioned that the molecules $^{39}K_2$ and $^{40}K_2$ could be used to study molecule-molecule interaction where quantum statistics of atoms which make up the molecules might play a crucial role. K is an alkali atom, so for tightly bound K_2 the *s* orbital is filled and hence the potential for two molecules in the ground state should be repulsive corresponding to the case of two-body interaction discussed earlier. Hence, we expect a very small difference in rates. The difference can increase for long bond molecules, but the inelastic collision cross sections for vibrational quenching are very high and will lead to rapid loss of molecules from the trap overpowering elastic collisions [131, 46, 166]. These quenching cross sections might also depend on the symmetry of atoms [20, 167] and hence require experimental investigation. To avoid these quenching effects, we need molecules in the ro-vibrational ground state. These molecules can be created from ultracold atoms by photoassociation or magnetoassociation and then can be transferred to the ro-vibrational ground state using STIRAP (stimulated Raman adiabatic process) [149, 52, 150–155]. Molecules with unfilled orbitals and hence better electron affinities are good candidates to study this problem as the potential should be attractive and hence the probability of atom exchange process might increase considerably [168]. *Ytterbium* is also a good candidate for this purpose as it has a long lived excited state [169]. The excited state potential between the molecules will mostly be attractive allowing the molecules to come closer.

To perform the studies mentioned above, the current experimental apparatus will require many modifications and additions. The study of molecule-molecule interaction will require trapping of molecules for a long time. The trapping can be achieved using a far-off resonant dipole trapping laser [170]. To obtain long trapping times and high density of atoms for efficient creation of molecules from the atoms the pressure in the experimental chamber has to be very low. The low pressure in case of potassium atoms can be achieved by having two vacuum chambers with two MOT's where a 3D MOT in one chamber is loaded from a 2D MOT in another chamber [171]. Additionally, the molecules created from ultracold atoms are not created in ro-vibrational ground state. However, the molecules can be transferred to the ro-vibrational ground state using the adiabatic Raman process of STIRAP [151]. For the STIRAP process to be efficient, the linewidth of the lasers performing the process should be of the order of few kHz. This linewidth can be achieved by locking the laser to an ultrastable cavity [162]. The development of such a locking scheme will be required in the future.

7.2.2 Other prospects

As mentioned in the summary of results section we were able to demonstrate cooling of ions by a localized ensemble of atoms whose mass is more than the mass of the ions. In spite of this cooling, we were not able to keep the ions trapped in the ion trap for a long duration of time because of heating from uniform density background gas of thermal atoms. So, in order to fully utilize the potential of cooling, in this case, it is essential to build an experiment where the pressure due to background gas is very low. Also, from simulations, we found out that the size of ultracold atomic cloud limits both the cooling rate and steady state temperature. Hence, such an experiment can be performed with a colder ensemble of dipole trapped atoms to increase the efficiency of cooling. Hence, the building of an experiment with better vacuum and smaller size of atomic cloud can be carried out in the future to have ions at a steady state temperature.

In chapter 5, we saw that the light used for cooling and trapping of atoms also induces lasing if the atoms are placed inside a Fabry-Pérot cavity. One of the evidence for lasing was provided by gain and line narrowing for a laser probing the system of a cavity and driven atoms. We used a semiclassical theory of light-matter interaction to explain this observation. In the present work, we have not performed the analysis using full quantum theory for such a system. In future, such an analysis can be performed which will not only explain the threshold effect of lasing but also give details about the photon statistics of light emitted by the cavity. Also, in future, experiments can be performed to observe the photon statistics, phase diffusion, squeezing, and many more phenomena some of which are predicted by the single mode theories of Zakrzewski *et.al* [126–128] and Agarwal [129, 130]. A multimode quantum theory will be required to fully understand the properties of such a laser which can be attempted in future.

We started the study of the atom-cavity system with the goal of understanding the system and using this understanding to devise methods to detect interactions between different species and detection of molecules using the cavity. We made some progress for detection of molecules using cavity when we performed a theoretical analysis for three techniques in chapter 6 and found out that detection through the slowing of light in cavity EIT process is the most efficient technique. In order to further advance these techniques, they can be first tested with ultracold atoms as they are already present in our experimental apparatus. For this purpose, we need a frequency stabilized cavity. The locking of the cavity is an ongoing project. After this is done, the detection techniques can be tested using ultracold ^{85}Rb atoms. The detection of molecules using these methods will require lots of additional development to the apparatus. The cavity mirrors might require changing, and greater efficiency of creation and trapping of ultracold molecules will be needed.

References

[1] Harold J. Metcalf and Peter van der Straten. *Laser Cooling and Trapping*. Graduate Texts in Contemporary Physics. Springer New York, New York, NY, 1999.

[2] D. Leibfried, R. Blatt, C. Monroe, and D. Wineland. Quantum dynamics of single trapped ions. *Reviews of Modern Physics*, 75(1):281–324, March 2003.

[3] Rainer Blatt and David Wineland. Entangled states of trapped atomic ions. *Nature*, 453(7198):1008–1015, June 2008.

[4] S. Jyothi, Tridib Ray, N. Bhargava Ram, and S.A. Rangwala. Hybrid ion, atom and light trap. In *Ion Traps for Tomorrow's Applications*. IOS Press, July 2015.

[5] Fouad G. Major, Viorica N. Gheorghe, and Günther Werth. *Charged Particle Traps*, volume 37. Springer-Verlag, Berlin/Heidelberg, 2005.

[6] F. G. Major and H. G. Dehmelt. Exchange-Collision Technique for the rf Spectroscopy of Stored Ions. *Physical Review*, 170(1):91–107, June 1968.

[7] Ralph G. DeVoe. Power-Law Distributions for a Trapped Ion Interacting with a Classical Buffer Gas. *Physical Review Letters*, 102(6), February 2009.

[8] Christoph Zipkes, Lothar Ratschbacher, Carlo Sias, and Michael Köhl. Kinetics of a single trapped ion in an ultracold buffer gas. *New Journal of Physics*, 13(5):053020, May 2011.

[9] Kuang Chen, Scott T. Sullivan, and Eric R. Hudson. Neutral Gas Sympathetic Cooling of an Ion in a Paul Trap. *Physical Review Letters*, 112(14), April 2014.

[10] K. Ravi, Seunghyun Lee, Arijit Sharma, G. Werth, and S.A. Rangwala. Cooling and stabilization by collisions in a mixed ion-atom system. *Nature Communications*, 3:1126, October 2012.

[11] Sourav Dutta, Rahul Sawant, and S. A. Rangwala. Collisional Cooling of Light Ions by Cotrapped Heavy Atoms. *Physical Review Letters*, 118(11), March 2017.

[12] Arijit Sharma, Tridib Ray, Rahul V. Sawant, G. Sheikholeslami, S. A. Rangwala, and D. Budker. Optical control of resonant light transmission for an atom-cavity system. *Physical Review A*, 91(4), April 2015.

[13] Rahul Sawant and S. A. Rangwala. Optical-bistability-enabled control of resonant light transmission for an atom-cavity system. *Physical Review A*, 93(2), February 2016.

[14] Sourav Dutta and S. A. Rangwala. All-optical switching in a continuously operated and strongly coupled atom-cavity system. *Applied Physics Letters*, 110(12):121107, March 2017.

[15] William T. Silfvast. *Laser Fundamentals*. Cambridge University Press, January 2004.

[16] F. Y. Wu, S. Ezekiel, M. Ducloy, and B. R. Mollow. Observation of Amplification in a Strongly Driven Two-Level Atomic System at Optical Frequencies. *Physical Review Letters*, 38(19):1077–1080, May 1977.

[17] D. S. Petrov. Three-body problem in Fermi gases with short-range interparticle interaction. *Physical Review A*, 67(1), January 2003.

[18] Arne Härter, Artjom Krükow, Andreas Brunner, Wolfgang Schnitzler, Stefan Schmid, and Johannes Hecker Denschlag. Single Ion as a Three-Body Reaction Center in an Ultracold Atomic Gas. *Physical Review Letters*, 109(12), September 2012.

[19] Pascal Naidon and Shimpei Endo. Efimov physics: a review. *Reports on Progress in Physics*, 80(5):056001, May 2017.

[20] D. S. Petrov, C. Salomon, and G. V. Shlyapnikov. Weakly Bound Dimers of Fermionic Atoms. *Physical Review Letters*, 93(9), August 2004.

[21] Immanuel Bloch, Jean Dalibard, and Wilhelm Zwerger. Many-body physics with ultracold gases. *Reviews of Modern Physics*, 80(3):885–964, July 2008.

[22] G. Bollen. Ion traps - Precision measurements and more. *The European Physical Journal A*, 15(1):237–243, September 2002.

[23] R. Blatt and C. F. Roos. Quantum simulations with trapped ions. *Nature Physics*, 8(4):277–284, April 2012.

[24] Stefan Willitsch. Ion-atom hybrid systems. In *Ion Traps for Tomorrow's Applications*. IOS Press, July 2015.

[25] K. Ravi, S. Lee, A. Sharma, G. Werth, and S. A. Rangwala. Combined ion and atom trap for low-temperature ion-atom physics. *Applied Physics B*, 107(4):971–981, June 2012.

[26] Andrew T. Grier, Marko Cetina, Fedja Oručević, and Vladan Vuletić. Observation of Cold Collisions between Trapped Ions and Trapped Atoms. *Physical Review Letters*, 102(22), June 2009.

[27] Christoph Zipkes, Stefan Palzer, Carlo Sias, and Michael Köhl. A trapped single ion inside a Bose-Einstein condensate. *Nature*, 464(7287):388–391, March 2010.

[28] I. Sivarajah, D. S. Goodman, J. E. Wells, F. A. Narducci, and W. W. Smith. Evidence of sympathetic cooling of Na^+ ions by a Na magneto-optical trap in a hybrid trap. *Physical Review A*, 86(6), December 2012.

[29] Lothar Ratschbacher, Christoph Zipkes, Carlo Sias, and Michael Köhl. Controlling chemical reactions of a single particle. *Nature Physics*, 8(9):649–652, July 2012.

[30] R. Côté, V. Kharchenko, and M. D. Lukin. Mesoscopic Molecular Ions in Bose-Einstein Condensates. *Physical Review Letters*, 89(9), August 2002.

[31] Robin Côté. From Classical Mobility to Hopping Conductivity: Charge Hopping in an Ultracold Gas. *Physical Review Letters*, 85(25):5316–5319, December 2000.

[32] Serge Haroche and Jean-Michel Raimond. *Exploring the Quantum*. Oxford University Press, August 2006.

[33] J. M. Raimond, M. Brune, and S. Haroche. Manipulating quantum entanglement with atoms and photons in a cavity. *Reviews of Modern Physics*, 73(3):565–582, August 2001.

[34] Andreas Reiserer and Gerhard Rempe. Cavity-based quantum networks with single atoms and optical photons. *Reviews of Modern Physics*, 87(4):1379–1418, December 2015.

[35] M. G. Raizen, R. J. Thompson, R. J. Brecha, H. J. Kimble, and H. J. Carmichael. Normal-mode splitting and linewidth averaging for two-state atoms in an optical cavity. *Physical Review Letters*, 63(3):240–243, July 1989.

[36] Peter F. Herskind, Aurélien Dantan, Joan P. Marler, Magnus Albert, and Michael Drewsen. Realization of collective strong coupling with ion Coulomb crystals in an optical cavity. *Nature Physics*, 5(7):494–498, July 2009.

[37] Guoqing Yang, Wen-ju Gu, Gaoxiang Li, Bichen Zou, and Yifu Zhu. Quantum nonlinear cavity quantum electrodynamics with coherently prepared atoms. *Physical Review A*, 92(3), September 2015.

[38] Tridib Ray, Arijit Sharma, S. Jyothi, and S. A. Rangwala. Temperature measurement of laser-cooled atoms using vacuum Rabi splitting. *Physical Review A*, 87(3), March 2013.

[39] Sourav Dutta and S. A. Rangwala. Nondestructive detection of ions using atom-cavity collective strong coupling. *Physical Review A*, 94(5), November 2016.

[40] Lincoln D Carr, David DeMille, Roman V Krems, and Jun Ye. Cold and ultracold molecules: science, technology and applications. *New Journal of Physics*, 11(5):055049, May 2009.

[41] Thorsten Köhler, Krzysztof Góral, and Paul S. Julienne. Production of cold molecules via magnetically tunable Feshbach resonances. *Reviews of Modern Physics*, 78(4):1311–1361, December 2006.

[42] Kevin M. Jones, Eite Tiesinga, Paul D. Lett, and Paul S. Julienne. Ultracold photoassociation spectroscopy: Long-range molecules and atomic scattering. *Reviews of Modern Physics*, 78(2):483–535, May 2006.

[43] D. DeMille. Quantum Computation with Trapped Polar Molecules. *Physical Review Letters*, 88(6), January 2002.

[44] G. Pupillo, A. Micheli, H. P. Büchler, and P. Zoller. Condensed Matter Physics with Cold Polar Molecules. In *Cold molecules: Creation and applications*. CRC Press, June 2009.

[45] R. V. Krems. Cold controlled chemistry. *Physical Chemistry Chemical Physics*, 10(28):4079, 2008.

[46] Goulven Quéméner, Pascal Honvault, Jean-Michel Launay, Pavel Soldán, Daniel E. Potter, and Jeremy M. Hutson. Ultracold quantum dynamics: Spin-polarized K + K_2 collisions with three identical bosons or fermions. *Physical Review A*, 71(3), March 2005.

[47] William C. Stwalley and He Wang. Photoassociation of Ultracold Atoms: A New Spectroscopic Technique. *Journal of Molecular Spectroscopy*, 195(2):194–228, June 1999.

[48] C. Gabbanini, A. Fioretti, A. Lucchesini, S. Gozzini, and M. Mazzoni. Cold Rubidium Molecules Formed in a Magneto-Optical Trap. *Physical Review Letters*, 84(13):2814–2817, March 2000.

[49] Fredrik K. Fatemi, Kevin M. Jones, Paul D. Lett, and Eite Tiesinga. Ultracold ground-state molecule production in sodium. *Physical Review A*, 66(5), November 2002.

[50] J. Herbig. Preparation of a Pure Molecular Quantum Gas. *Science*, 301(5639):1510–1513, September 2003.

[51] K. Winkler, G. Thalhammer, F. Lang, R. Grimm, J. Hecker Denschlag, A. J. Daley, A. Kantian, H. P. Büchler, and P. Zoller. Repulsively bound atom pairs in an optical lattice. *Nature*, 441(7095):853–856, June 2006.

[52] F. Lang, K. Winkler, C. Strauss, R. Grimm, and J. Hecker Denschlag. Ultracold Triplet Molecules in the Rovibrational Ground State. *Physical Review Letters*, 101(13), September 2008.

[53] J. J. Zirbel, K.-K. Ni, S. Ospelkaus, T. L. Nicholson, M. L. Olsen, P. S. Julienne, C. E. Wieman, J. Ye, and D. S. Jin. Heteronuclear molecules in an optical dipole trap. *Physical Review A*, 78(1), July 2008.

[54] P. D. Lett, W. D. Phillips, S. L. Rolston, C. E. Tanner, R. N. Watts, and C. I. Westbrook. Optical molasses. *Journal of the Optical Society of America B*, 6(11):2084, November 1989.

[55] Daniel A. Steck. *Quantum and Atom Optics*. June 2011.

[56] S. Chang and V. Minogin. Density-matrix approach to dynamics of multilevel atoms in laser fields. *Physics Reports*, 365(2):65–143, July 2002.

[57] C. Fort, A. Bambini, L. Cacciapuoti, F.S. Cataliotti, M. Prevedelli, G.M. Tino, and M. Inguscio. Cooling mechanisms in potassium magneto-optical traps. *The European Physical Journal D - Atomic, Molecular and Optical Physics*, 3(2):113–118, August 1998.

[58] Tridib Ray. *Progression towards study of interactions with composite systems at ultracold temperature*. PhD thesis, Raman Research Institute, Bangalore, 2015.

[59] Jyothi S. *Exploring molecular ion formation, trapping and detection in hybrid system*. PhD thesis, Raman Research Institute, Bangalore, 2015.

[60] Robert Williamson III. *Magneto-optical trapping of potassium isotopes*. PhD thesis, University of Wisconsin- Madison, Madison, 1997.

[61] B. E. A. Saleh and M. C. Teich. *Fundamentals of Photonics*. Wiley, March 2007.

[62] Daniel A. Steck. *Classical and Modern Optics*. February 2012.

[63] G. Nogues, A. Rauschenbeutel, S. Osnaghi, M. Brune, J. M. Raimond, and S. Haroche. Seeing a single photon without destroying it. *Nature*, 400(6741):239–242, July 1999.

[64] A. Reiserer, S. Ritter, and G. Rempe. Nondestructive Detection of an Optical Photon. *Science*, 342(6164):1349–1351, December 2013.

[65] Eric D. Black. An introduction to Pound-Drever-Hall laser frequency stabilization. *American Journal of Physics*, 69(1):79–87, January 2001.

[66] Bastian Höltkemeier, Pascal Weckesser, Henry López-Carrera, and Matthias Weidemüller. Buffer-Gas Cooling of a Single Ion in a Multipole Radio Frequency Trap Beyond the Critical Mass Ratio. *Physical Review Letters*, 116(23), June 2016.

[67] Bastian Höltkemeier, Pascal Weckesser, Henry López-Carrera, and Matthias Weidemüller. Dynamics of a single trapped ion immersed in a buffer gas. *Physical Review A*, 94(6), December 2016.

[68] S. Jyothi, Tridib Ray, and S. A. Rangwala. Phase-sensitive radial extraction and mass spectrometry of trapped ions in a compact geometry. *Applied Physics B*, 118(1):131–138, January 2015.

[69] T. Arpornthip, C. A. Sackett, and K. J. Hughes. Vacuum-pressure measurement using a magneto-optical trap. *Physical Review A*, 85(3), March 2012.

[70] R. Côté and A. Dalgarno. Ultracold atom-ion collisions. *Physical Review A*, 62(1), June 2000.

[71] L. L. Yan, L. Liu, Y. Wu, Y. Z. Qu, J. G. Wang, and R. J. Buenker. Charge transfer and association of Na^+ with ^{87}Rb atoms from extremely low to intermediate energies. *Physical Review A*, 88(1), July 2013.

[72] Ravi Krishnamurthy. *Trapping and cooling of ions and the study of ion atom Interactions*. PhD thesis, Raman Research Institute, Bangalore, 2012.

[73] Seunghyun Lee. *Study of trapped ion collisions with cold atoms and cold molecules*. PhD thesis, Raman Research Institute, Bangalore, 2014.

[74] Constantino Tsallis. Possible generalization of Boltzmann-Gibbs statistics. *Journal of Statistical Physics*, 52(1-2):479–487, July 1988.

[75] P. Blythe, B. Roth, U. Fröhlich, H. Wenz, and S. Schiller. Production of Ultracold Trapped Molecular Hydrogen Ions. *Physical Review Letters*, 95(18), October 2005.

[76] Hyatt Gibbs. *Optical Bistability: Controlling Light With Light*. Elsevier, December 2012.

[77] Hai Wang, David Goorskey, and Min Xiao. Controlling the cavity field with enhanced Kerr nonlinearity in three-level atoms. *Physical Review A*, 65(5), May 2002.

[78] L. A. Orozco, H. J. Kimble, A. T. Rosenberger, L. A. Lugiato, M. L. Asquini, M. Brambilla, and L. M. Narducci. Single-mode instability in optical bistability. *Physical Review A*, 39(3):1235–1252, February 1989.

[79] J. McKeever, A. Boca, A. D. Boozer, J. R. Buck, and H. J. Kimble. Experimental realization of a one-atom laser in the regime of strong coupling. *Nature*, 425(6955):268–271, September 2003.

[80] Hilton W. Chan, Adam T. Black, and Vladan Vuletić. Observation of Collective-Emission-Induced Cooling of Atoms in an Optical Cavity. *Physical Review Letters*, 90(6), February 2003.

[81] Yanhua Wang, Jiepeng Zhang, and Yifu Zhu. Observation of dressed intracavity dark states. *Physical Review A*, 85(1), January 2012.

[82] Amitabh Joshi and Min Xiao. Optical Multistability in Three-Level Atoms inside an Optical Ring Cavity. *Physical Review Letters*, 91(14), October 2003.

[83] W. Harshawardhan and G. S. Agarwal. Controlling optical bistability using electromagnetic-field-induced transparency and quantum interferences. *Physical Review A*, 53(3):1812–1817, March 1996.

[84] Hong Chang, Haibin Wu, Changde Xie, and Hai Wang. Controlled Shift of Optical Bistability Hysteresis Curve and Storage of Optical Signals in a Four-Level Atomic System. *Physical Review Letters*, 93(21), November 2004.

[85] Lü Xin-You, Li Jia-Hua, Liu Ji-Bing, and Luo Jin-Ming. Optical bistability via quantum interference in a four-level atomic medium. *Journal of Physics B: Atomic, Molecular and Optical Physics*, 39(24):5161–5171, December 2006.

[86] Marlan O. Scully and M. Suhail Zubairy. *Quantum Optics*. Cambridge University Press, September 1997.

[87] D.F. Walls and Gerard J. Milburn, editors. *Quantum Optics*. Springer Berlin Heidelberg, Berlin, Heidelberg, 2008. DOI: 10.1007/978-3-540-28574-8.

[88] Howard J. Carmichael. *Statistical Methods in Quantum Optics 2*. Theoretical and Mathematical Physics. Springer Berlin Heidelberg, Berlin, Heidelberg, 2008. DOI: 10.1007/978-3-540-71320-3.

[89] M. Albert, J. P. Marler, P. F. Herskind, A. Dantan, and M. Drewsen. Collective strong coupling between ion Coulomb crystals and an optical cavity field: Theory and experiment. *Physical Review A*, 85(2), February 2012.

[90] Robert W. Boyd. *Nonlinear Optics*. Academic Press, January 2003.

[91] Daniel A. Steck. *Rubidium 85 D Line Data*. September 2013.

[92] Bichen Zou and Yifu Zhu. Light controlling light in a coupled atom-cavity system. *Physical Review A*, 87(5), May 2013.

[93] Michael Fleischhauer, Atac Imamoglu, and Jonathan P. Marangos. Electromagnetically induced transparency: Optics in coherent media. *Reviews of Modern Physics*, 77(2):633–673, July 2005.

[94] Amitabh Joshi, Andy Brown, Hai Wang, and Min Xiao. Controlling optical bistability in a three-level atomic system. *Physical Review A*, 67(4), April 2003.

[95] Xiaogang Wei, Jiepeng Zhang, and Yifu Zhu. All-optical switching in a coupled cavity-atom system. *Physical Review A*, 82(3), September 2010.

[96] J. Gripp, S. L. Mielke, L. A. Orozco, and H. J. Carmichael. Anharmonicity of the vacuum Rabi peaks in a many-atom system. *Physical Review A*, 54(5):R3746–R3749, November 1996.

[97] J. Gripp, S. L. Mielke, and L. A. Orozco. Evolution of the vacuum Rabi peaks in a detuned atom-cavity system. *Physical Review A*, 56(4):3262–3273, October 1997.

[98] J.R. Johansson, P.D. Nation, and Franco Nori. QuTiP 2: A Python framework for the dynamics of open quantum systems. *Computer Physics Communications*, 184(4):1234–1240, April 2013.

[99] M. Brune, F. Schmidt-Kaler, A. Maali, J. Dreyer, E. Hagley, J. M. Raimond, and S. Haroche. Quantum Rabi Oscillation: A Direct Test of Field Quantization in a Cavity. *Physical Review Letters*, 76(11):1800–1803, March 1996.

[100] I. Schuster, A. Kubanek, A. Fuhrmanek, T. Puppe, P. W. H. Pinkse, K. Murr, and G. Rempe. Nonlinear spectroscopy of photons bound to one atom. *Nature Physics*, 4(5):382–385, May 2008.

[101] Lev S. Bishop, J. M. Chow, Jens Koch, A. A. Houck, M. H. Devoret, E. Thuneberg, S. M. Girvin, and R. J. Schoelkopf. Nonlinear response of the vacuum Rabi resonance. *Nature Physics*, 5(2):105–109, February 2009.

[102] Michael Tavis and Frederick W. Cummings. Exact Solution for an N-Molecule-Radiation-Field Hamiltonian. *Physical Review*, 170(2):379–384, June 1968.

[103] R. J. Thompson, G. Rempe, and H. J. Kimble. Observation of normal-mode splitting for an atom in an optical cavity. *Physical Review Letters*, 68(8):1132–1135, February 1992.

[104] Gessler Hernandez, Jiepeng Zhang, and Yifu Zhu. Vacuum Rabi splitting and intracavity dark state in a cavity-atom system. *Physical Review A*, 76(5), November 2007.

[105] J Mompart and R Corbalán. Lasing without inversion. *Journal of Optics B: Quantum and Semiclassical Optics*, 2(3):R7–R24, June 2000.

[106] Geert Vrijsen, Onur Hosten, Jongmin Lee, Simon Bernon, and Mark A. Kasevich. Raman Lasing with a Cold Atom Gain Medium in a High-Finesse Optical Cavity. *Physical Review Letters*, 107(6), August 2011.

[107] L Hilico, C Fabre, and E Giacobino. Operation of a "Cold-Atom Laser" in a Magneto-Optical Trap. *Europhysics Letters (EPL)*, 18(8):685–688, April 1992.

[108] William Guerin, Franck Michaud, and Robin Kaiser. Mechanisms for Lasing with Cold Atoms as the Gain Medium. *Physical Review Letters*, 101(9), August 2008.

[109] D. Kruse, C. von Cube, C. Zimmermann, and Ph. W. Courteille. Observation of Lasing Mediated by Collective Atomic Recoil. *Physical Review Letters*, 91(18), October 2003.

[110] S. Slama, S. Bux, G. Krenz, C. Zimmermann, and Ph. W. Courteille. Superradiant Rayleigh Scattering and Collective Atomic Recoil Lasing in a Ring Cavity. *Physical Review Letters*, 98(5), February 2007.

[111] Justin G. Bohnet, Zilong Chen, Joshua M. Weiner, Dominic Meiser, Murray J. Holland, and James K. Thompson. A steady-state superradiant laser with less than one intracavity photon. *Nature*, 484(7392):78–81, April 2012.

[112] Matthew A. Norcia and James K. Thompson. Cold-Strontium Laser in the Superradiant Crossover Regime. *Physical Review X*, 6(1), March 2016.

[113] Q. Baudouin, N. Mercadier, V. Guarrera, W. Guerin, and R. Kaiser. A cold-atom random laser. *Nat Phys*, 9(6):357–360, June 2013.

[114] Gilbert Grynberg and Claude Cohen-Tannoudji. Central resonance of the Mollow absorption spectrum: physical origin of gain without population inversion. *Optics Communications*, 96(1-3):150–163, February 1993.

[115] A. Lezama, Yifu Zhu, Manoj Kanskar, and T. W. Mossberg. Radiative emission of driven two-level atoms into the modes of an enclosing optical cavity: The transition from fluorescence to lasing. *Physical Review A*, 41(3):1576–1581, February 1990.

[116] Tridib Ray, S. Jyothi, N. Bhargava Ram, and S. A. Rangwala. A thin wire ion trap to study ion–atom collisions built within a Fabry-Perot cavity. *Applied Physics B*, 114(1-2):267–273, January 2014.

[117] G. S. Agarwal. Spectroscopy of strongly coupled atom-cavity systems: A topical review. *Journal of Modern Optics*, 45(3):449–470, March 1998.

[118] K. Kowalski, V. Cao Long, K. Dinh Xuan, M. Głódź, B. Nguyen Huy, and J. Szonert. Magneto-optical Trap: Fundamentals and Realization. *Computational Methods in Science and Technology*, Special Issue(02):115–129, 2010.

[119] Wolfgang Petrich, Michael H. Anderson, Jason R. Ensher, and Eric A. Cornell. Behavior of atoms in a compressed magneto-optical trap. *Journal of the Optical Society of America B*, 11(8):1332, August 1994.

[120] C. G. Townsend, N. H. Edwards, C. J. Cooper, K. P. Zetie, C. J. Foot, A. M. Steane, P. Szriftgiser, H. Perrin, and J. Dalibard. Phase-space density in the magneto-optical trap. *Physical Review A*, 52(2):1423–1440, August 1995.

[121] Andrey E. Miroshnichenko, Sergej Flach, and Yuri S. Kivshar. Fano resonances in nanoscale structures. *Reviews of Modern Physics*, 82(3):2257–2298, August 2010.

[122] B. R. Mollow. Stimulated Emission and Absorption near Resonance for Driven Systems. *Physical Review A*, 5(5):2217–2222, May 1972.

[123] Serge Haroche and Francis Hartmann. Theory of Saturated-Absorption Line Shapes. *Physical Review A*, 6(4):1280–1300, October 1972.

[124] B. R. Mollow. Power Spectrum of Light Scattered by Two-Level Systems. *Physical Review*, 188(5):1969–1975, December 1969.

[125] George B. Arfken, Hans J. Weber, and Frank E. Harris. *Mathematical Methods for Physicists: A Comprehensive Guide*. Academic Press, December 2011.

[126] Jakub Zakrzewski, Maciej Lewenstein, and Thomas W. Mossberg. Theory of dressed-state lasers. I. Effective Hamiltonians and stability properties. *Physical Review A*, 44(11):7717–7731, December 1991.

[127] Jakub Zakrzewski, Maciej Lewenstein, and Thomas W. Mossberg. Theory of dressed-state lasers. II. Phase diffusion and squeezing. *Physical Review A*, 44(11):7732–7745, December 1991.

[128] Jakub Zakrzewski, Maciej Lewenstein, and Thomas W. Mossberg. Theory of dressed-state lasers. III. Pump-depletion effects. *Physical Review A*, 44(11):7746–7758, December 1991.

[129] G.S. Agarwal. Theory of the laser operating due to gain on three-photon Mollow side band. *Optics Communications*, 80(1):37–41, December 1990.

[130] G. S. Agarwal. Dressed-state lasers and masers. *Physical Review A*, 42(1):686–688, July 1990.

[131] Goulven Quéméner and Naduvalath Balakrishnan. Quantum calculations of H_2-H_2 collisions: From ultracold to thermal energies. *The Journal of Chemical Physics*, 130(11):114303, March 2009.

[132] Marko T. Cvitaš, Pavel Soldán, Jeremy M. Hutson, Pascal Honvault, and Jean-Michel Launay. Ultracold Li + Li_2 Collisions: Bosonic and Fermionic Cases. *Physical Review Letters*, 94(3), January 2005.

[133] A. Fioretti, D. Comparat, A. Crubellier, O. Dulieu, F. Masnou-Seeuws, and P. Pillet. Formation of Cold Cs_2 Molecules through Photoassociation. *Physical Review Letters*, 80(20):4402–4405, May 1998.

[134] H. Wang, J. Li, X. T. Wang, C. J. Williams, P. L. Gould, and W. C. Stwalley. Precise determination of the dipole matrix element and radiative lifetime of the ^{39}K 4p state by photoassociative spectroscopy. *Physical Review A*, 55(3):R1569–R1572, March 1997.

[135] R. F. Gutterres, C. Amiot, A. Fioretti, C. Gabbanini, M. Mazzoni, and O. Dulieu. Determination of the ^{87}Rb 5p state dipole matrix element and radiative lifetime from the photoassociation spectroscopy of the Rb_2 0_g^- ($P_{3/2}$) long-range state. *Physical Review A*, 66(2), August 2002.

[136] C. Amiot, O. Dulieu, R. F. Gutterres, and F. Masnou-Seeuws. Determination of the Cs_2 0_g^- $(P_{3/2})$ potential curve and of Cs $6P_{1/2,3/2}$ atomic radiative lifetimes from photoassociation spectroscopy. *Physical Review A*, 66(5), November 2002.

[137] G. E. Uhlenbeck and L. S. Ornstein. On the Theory of the Brownian Motion. *Physical Review*, 36(5):823–841, September 1930.

[138] C. Cohen-Tannoudji. Atomic Motion in Laser Light. In J.-M. Raimond, J. Zinn-Justin, and J. Dalibard, editors, *Fundamental Systems in Quantum Optics: Les Houches lectures*, Les Houches. Elsevier Science Publisher, 1992.

[139] Kurt Jacobs. *Stochastic Processes for Physicists: Understanding Noisy Systems*. Cambridge University Press, February 2010.

[140] Kalle-Antti Suominen. Theories for cold atomic collisions in light fields. *Journal of Physics B: Atomic, Molecular and Optical Physics*, 29(24):5981–6007, December 1996.

[141] John Weiner, Vanderlei S. Bagnato, Sergio Zilio, and Paul S. Julienne. Experiments and theory in cold and ultracold collisions. *Reviews of Modern Physics*, 71(1):1–85, January 1999.

[142] D. Hoffmann, P. Feng, R. S. Williamson, and T. Walker. Excited-state collisions of trapped Rb 85 atoms. *Physical Review Letters*, 69(5):753–756, August 1992.

[143] Benjamin K. Stuhl, Brian C. Sawyer, Dajun Wang, and Jun Ye. Magneto-optical Trap for Polar Molecules. *Physical Review Letters*, 101(24), December 2008.

[144] J. F. Barry, D. J. McCarron, E. B. Norrgard, M. H. Steinecker, and D. DeMille. Magneto-optical trapping of a diatomic molecule. *Nature*, 512(7514):286–289, August 2014.

[145] Matthew H. Steinecker, Daniel J. McCarron, Yuqi Zhu, and David DeMille. Improved Radio-Frequency Magneto-Optical Trap of SrF Molecules. *ChemPhysChem*, 17(22):3664–3669, November 2016.

[146] M. Zeppenfeld. Nondestructive detection of polar molecules via Rydberg atoms. *EPL (Europhysics Letters)*, 118(1):13002, April 2017.

[147] R. A. Cline, J. D. Miller, and D. J. Heinzen. Study of Rb_2 Long-Range States by High-Resolution Photoassociation Spectroscopy. *Physical Review Letters*, 73(19):2636–2636, November 1994.

[148] Abdul-Rahman Allouche and Monique Aubert-Frécon. Transition dipole moments between the low-lying $\Omega_{g,u}^{\pm}$ states of the Rb_2 and Cs_2 molecules. *The Journal of Chemical Physics*, 136(11):114302, March 2012.

[149] J. Deiglmayr, A. Grochola, M. Repp, K. Mörtlbauer, C. Glück, J. Lange, O. Dulieu, R. Wester, and M. Weidemüller. Formation of Ultracold Polar Molecules in the Rovibrational Ground State. *Physical Review Letters*, 101(13), September 2008.

[150] Johann G. Danzl, Manfred J. Mark, Elmar Haller, Mattias Gustavsson, Russell Hart, Jesus Aldegunde, Jeremy M. Hutson, and Hanns-Christoph Nägerl. An ultracold high-density sample of rovibronic ground-state molecules in an optical lattice. *Nature Physics*, 6(4):265–270, April 2010.

[151] K. Aikawa, D. Akamatsu, M. Hayashi, K. Oasa, J. Kobayashi, P. Naidon, T. Kishimoto, M. Ueda, and S. Inouye. Coherent Transfer of Photoassociated Molecules into the Rovibrational Ground State. *Physical Review Letters*, 105(20), November 2010.

[152] Tetsu Takekoshi, Lukas Reichsöllner, Andreas Schindewolf, Jeremy M. Hutson, C. Ruth Le Sueur, Olivier Dulieu, Francesca Ferlaino, Rudolf Grimm, and Hanns-Christoph Nägerl. Ultracold Dense Samples of Dipolar RbCs Molecules in the Rovibrational and Hyperfine Ground State. *Physical Review Letters*, 113(20), November 2014.

[153] Peter K. Molony, Philip D. Gregory, Zhonghua Ji, Bo Lu, Michael P. Köppinger, C. Ruth Le Sueur, Caroline L. Blackley, Jeremy M. Hutson, and Simon L. Cornish. Creation of Ultracold $^{87}Rb^{133}Cs$ Molecules in the Rovibrational Ground State. *Physical Review Letters*, 113(25), December 2014.

[154] Jee Woo Park, Sebastian A. Will, and Martin W. Zwierlein. Ultracold Dipolar Gas of Fermionic $^{23}Na^{40}K$ Molecules in Their Absolute Ground State. *Physical Review Letters*, 114(20), May 2015.

[155] Mingyang Guo, Bing Zhu, Bo Lu, Xin Ye, Fudong Wang, Romain Vexiau, Nadia Bouloufa-Maafa, Goulven Quéméner, Olivier Dulieu, and Dajun Wang. Creation of an Ultracold Gas of Ground-State Dipolar $^{23}Na^{87}Rb$ Molecules. *Physical Review Letters*, 116(20), May 2016.

[156] Robert H. Hadfield. Single-photon detectors for optical quantum information applications. *Nature Photonics*, 3(12):696–705, December 2009.

[157] Mikhail D. Lukin, Michael Fleischhauer, Marlan O. Scully, and Vladimir L. Velichansky. Intracavity electromagnetically induced transparency. *Optics Letters*, 23(4):295, February 1998.

[158] Hai Wang, D. J. Goorskey, W. H. Burkett, and Min Xiao. Cavity-linewidth narrowing by means of electromagnetically induced transparency. *Optics Letters*, 25(23):1732, December 2000.

[159] Jiepeng Zhang, Gessler Hernandez, and Yifu Zhu. Slow light with cavity electromagnetically induced transparency. *Optics Letters*, 33(1):46, January 2008.

[160] Magnus Albert, Aurélien Dantan, and Michael Drewsen. Cavity electromagnetically induced transparency and all-optical switching using ion Coulomb crystals. *Nature Photonics*, 5(10):633–636, September 2011.

[161] Yukiko Shimizu, Noritsugu Shiokawa, Noriaki Yamamoto, Mikio Kozuma, Takahiro Kuga, L. Deng, and E. W. Hagley. Control of Light Pulse Propagation with Only a Few Cold Atoms in a High-Finesse Microcavity. *Physical Review Letters*, 89(23), November 2002.

[162] K. Aikawa, J. Kobayashi, K. Oasa, T. Kishimoto, M. Ueda, and S. Inouye. Narrow-linewidth light source for a coherent Raman transfer of ultracold molecules. *Optics Express*, 19(15):14479, July 2011.

[163] J. J. Sakurai. *Modern Quantum Mechanics*. Pearson Education India, 2006.

[164] Claude Cohen-Tannoudji and David Guéry-Odelin. *Advances in Atomic Physics: An Overview*. World Scientific, 2011.

[165] Hélène Lefebvre-Brion and Robert W. Field. *The Spectra and Dynamics of Diatomic Molecules*. Elsevier Academic Press, 2004.

[166] Björn Drews, Markus Deiß, Krzysztof Jachymski, Zbigniew Idziaszek, and Johannes Hecker Denschlag. Inelastic collisions of ultracold triplet Rb2 molecules in the rovibrational ground state. *Nature Communications*, 8:14854, March 2017.

[167] D. S. Petrov, C. Salomon, and G. V. Shlyapnikov. Scattering properties of weakly bound dimers of fermionic atoms. *Physical Review A*, 71(1), January 2005.

[168] Alexandr V. Avdeenkov and John L. Bohn. Ultracold collisions of oxygen molecules. *Physical Review A*, 64(5), October 2001.

[169] Mateusz Borkowski, Roman Ciuryło, Paul S. Julienne, Rekishu Yamazaki, Hideaki Hara, Katsunari Enomoto, Shintaro Taie, Seiji Sugawa, Yosuke Takasu, and Yoshiro Takahashi. Photoassociative production of ultracold heteronuclear ytterbium molecules. *Physical Review A*, 84(3), September 2011.

[170] T. Takekoshi, B. M. Patterson, and R. J. Knize. Observation of Optically Trapped Cold Cesium Molecules. *Physical Review Letters*, 81(23):5105–5108, December 1998.

[171] Vandna Gokhroo, G Rajalakshmi, R Kollengode Easwaran, and C S Unnikrishnan. Sub-Doppler deep-cooled bosonic and fermionic isotopes of potassium in a compact $2D^+$ - 3D MOT set-up. *Journal of Physics B: Atomic, Molecular and Optical Physics*, 44(11):115307, June 2011.

Appendix A

A.1 Mollow Spectrum

In this section, we summarize the calculation for computing the florescence spectrum of atoms driven hard by classical laser light. For a two-level atom driven by a classical laser light with Rabi frequency 2Ω, the time-dependent equations in rotating frame for atomic variables similar to ones mentioned in chapter 4 and 5 are,

$$\begin{aligned}
\frac{d\rho(t)}{dt} &= -\left\{\frac{\Gamma}{2} - i\Delta_{da}\right\}\rho(t) + i\Omega\left\langle\sigma_z(t)\right\rangle \\
\frac{d\rho^*(t)}{dt} &= -\left\{\frac{\Gamma}{2} + i\Delta_{da}\right\}\rho^*(t) - i\Omega\left\langle\sigma_z(t)\right\rangle \\
\frac{d\left\langle\sigma_z(t)\right\rangle}{dt} &= -\Gamma\left[\sigma_z(t)+1\right] + 2i\left\{\Omega^*\rho_j(t) - \Omega\rho_j^*(t)\right\}
\end{aligned} \tag{A.1}$$

Here, $\langle\sigma_z(t)\rangle$ is the population difference in excited state and ground state of the atom. It can be proved using optical Wiener–Khinchin theorem that the incoherent part of the fluorescence spectrum is proportional to the Fourier transform of fluctuations in atomic dipole moment [124, 55]. This fluctuation can be denoted by, $\delta C(\tau) = \langle\delta\sigma^+(t)\delta\sigma^-(t+\tau)\rangle_{t\to\infty} = \langle\sigma^+(t)\sigma^-(t+\tau)\rangle_{t\to\infty} - |\langle\sigma^-\rangle|^2_{t\to\infty}$. Where, $\delta\sigma = \delta\sigma - \langle\sigma\rangle_{t\to\infty}$ denotes deviation from steady-state mean value $\langle\sigma\rangle_{t\to\infty}$. When we subtract the steady state components from Eqns. A.1 we get optical block equations for these deviations. The equations for deviations can be written in matrix form as follows,

$$\frac{d}{dt}\begin{bmatrix}\delta\rho(t)\\ \delta\rho^*(t)\\ \langle\delta\sigma_z(t)\rangle\end{bmatrix} = 2\begin{bmatrix}-\Gamma+2i\Delta_{da} & 0 & 2i\Omega\\ 0 & -\Gamma-2i\Delta_{da} & -2i\Omega\\ 2i\Omega & -2i\Omega & -2\Gamma\end{bmatrix}\begin{bmatrix}\delta\rho(t)\\ \delta\rho^*(t)\\ \langle\delta\sigma_z(t)\rangle\end{bmatrix} = \mathbf{P}\begin{bmatrix}\delta\rho(t)\\ \delta\rho^*(t)\\ \langle\delta\sigma_z(t)\rangle\end{bmatrix} \tag{A.2}$$

Now, using the quantum regression theorem the two-point correlation function for fluctuations can be written as [55], $\delta C(\tau) = \mathrm{Tr}_A\left[\delta\sigma^-\delta\Lambda(\tau)\right]$. Here, Tr_A is trace operation over the

atomic Hilbert space and $\frac{\partial \delta\Lambda(\tau)}{\partial \tau} = \mathbf{P}\delta\Lambda(\tau)$ with the initial condition [55]:

$$\delta\Lambda(0) = \rho(t\to\infty)\delta\sigma^{+} = \begin{bmatrix} \frac{1}{2}\left[\langle\sigma_z\rangle + 1 - 2|\rho|^2\right] \\ -(\rho^*)^2 \\ -\rho^*(1+\langle\sigma_z\rangle) \end{bmatrix}_{t\to\infty}. \tag{A.3}$$

The solution for $\delta\Lambda(\tau)$ is now very easy and is given by, $\delta\Lambda(\tau) = e^{\mathbf{P}\tau}\delta\Lambda(0)$. The correlation function $\delta C(\tau)$ is then simply the first element of the vector $\delta\Lambda(\tau)$. The incoherent part of the spectrum can then be found by taking Fourier transform of correlation function in lab frame of reference,

$$S(\omega_s)_{inc} = \frac{1}{2\pi}\int_{-\infty}^{\infty} e^{i\omega_s\tau}e^{i\omega_a\tau}\delta C(\tau)\ d\tau. \tag{A.4}$$

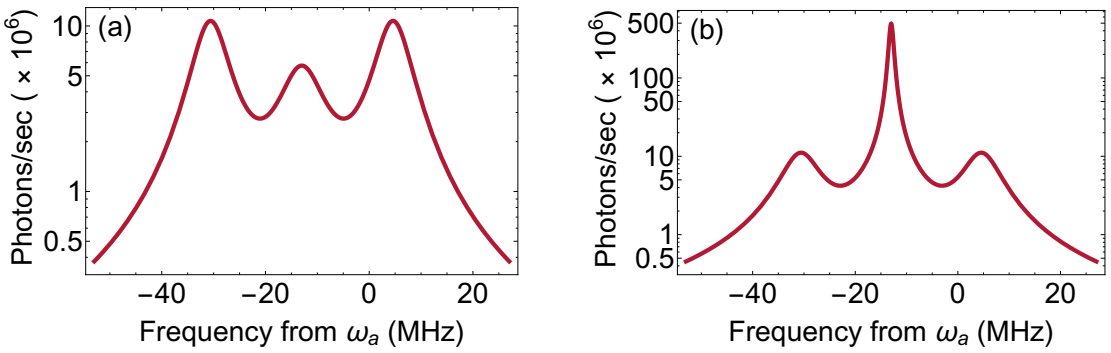

Fig. A.1 (a) Numerically computed incoherent part of the Mollow spectrum on a log scale. (b) Mollow spectrum on a log scale including the coherent part of scattering. The parameters used are, $\Omega/(2\pi) = 6$ MHz, $\Delta_{pa}/(2\pi) = -13$ MHz, $N_c = 22\times10^3$, $\Gamma/(2\pi) = 6.06$ and MOT laser linewidth 1 MHz. Most of the light emitted is at MOT laser/drive frequency. The y-axis shows the rate of photon emission into the cavity at that particular wavelength. This rate is upper bound on the actual rate because in the calculation of the rate we assume that all the atoms are at the center of the cavity and hence all the light emitted by the atoms which fall on the cavity mirrors come back to the center and form the cavity mode. Also, the emission from atoms is assumed to be isotropic. Hence the rate is $\zeta\times$ total rate of photon emission, where $\zeta = 0.009$ depends on the solid angle subtended by the mirrors at the center of the cavity. The red sideband and blue sideband have center frequencies -30.6 MHz $\approx (\Delta_{pa} - \sqrt{4\Omega^2+\Delta_{pa}^2})/(2\pi)$ MHz and 4.6 MHz $\approx (\Delta_{pa} + \sqrt{4\Omega^2+\Delta_{pa}^2})/(2\pi)$ respectively

We compute $\delta\Lambda(\tau)$ numerically[1] and the resulting spectrum is shown in figure A.1a. This is just the incoherent scattering part, to get a full spectrum we need to add the coherent part

[1]The Mathematica code for this is available at https://goo.gl/mzUzvA. The file name is "mollow_spectrum.nb".

also [124, 55], $S(\omega_s) = S(\omega_s)_{inc} + S(\omega_s)_{coh}$. The coherent part comes from light scattered exactly at the drive laser frequency. Assuming that the drive laser light is Lorentzian with a linewidth of 1 MHz the complete spectrum is shown in figure A.1b. The ratio between total incoherent and total coherent part of scattered light is $\frac{8\Omega^2}{\Gamma^2+4\Delta_{da}^2}$ [55], this ratio is used in the plotting of Fig. A.1.

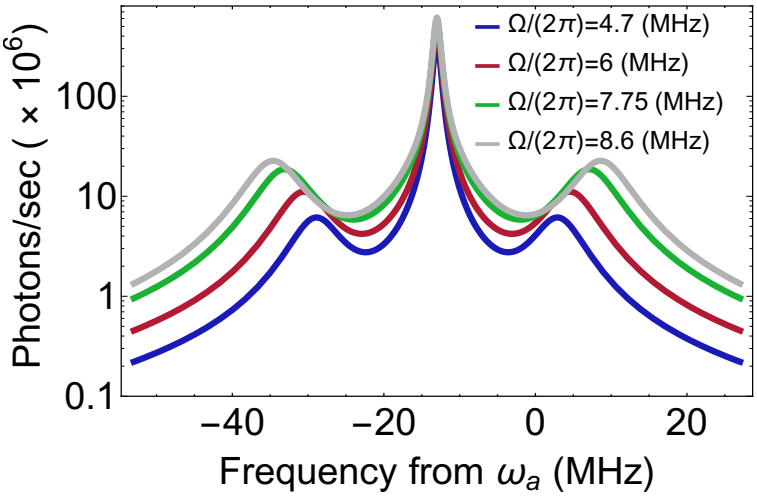

Fig. A.2 Mollow spectrum for different powers of the drive beam.

A.2 Multiphoton processes

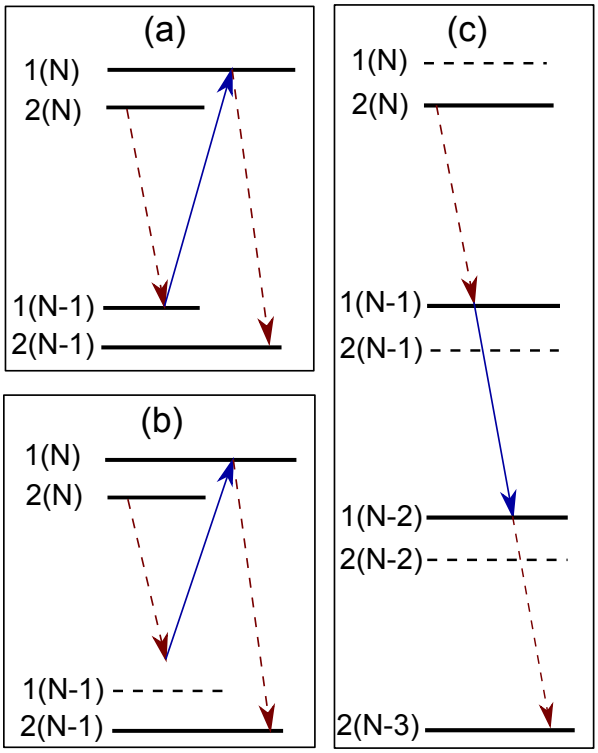

Fig. A.3 Multi-photon processes taken from Grynberg *et.al* [114] relevant for lasing described in chapter 5. (a) Resonant absorption of the probe photon. (b) Non-resonant absorption of the probe photon. (c) Resonant amplification of the probe photon. Here the brown dashed lines with an arrow represent spontaneous emission of the photons and solid blue lines represent a photon of the probe laser. The levels 1(N) and 2(N) are combined dressed states of the 2-level atom and strong drive field dressing the atoms [55]. The solid lines are for levels which participate in the process shown and dashed lines are for levels which do not participate in the process.

Appendix B

Frequently used mathematical symbols in the thesis

Γ	spontaneous emission rate from the excited state
F	force
k	wave-number
λ	wavelength of light
I_{sat}	saturation intensity of the atomic transition
Δ	detuning of light from the atomic transition
$\hbar$	Plank's constant
β	damping term for atoms in MOT
ζ	MOT trap stiffness
β_{3D}	3D damping term for atoms in MOT
ζ_{3D}	3D MOT trap stiffness
w_0	$1/e^2$ radius of cavity light intensity Gaussian
$\omega_{\text{cv}}/(2\pi)$	resonance frequency of the cavity
$\kappa_{\text{t}}/(2\pi)$	total loss rate of the cavity
$\kappa_{\text{r}}/(2\pi)$	transmission rate of the cavity mirrors
$\mathscr{F}$	Finesse of the cavity
m_{r}	ratio of atom mass to ion mass
g_0	maximum atom-cavity coupling strength
$\hat{H}$	Hamiltonian of the system
$\hat{a}$	annihilation operator for a photon
$\hat{a}^\dagger$	creation operator for a photon

$\omega_p/(2\pi)$	frequency of light probing the cavity
$\omega_a/(2\pi)$	frequency of the atomic transition
$\hat{\sigma}$	atomic operators
ρ_g	ground state element of atomic density matrix (population in ground state)
ρ_e	excited state element of atomic density matrix (population in excited state)
ρ	coherence term of atomic density matrix (dipole element)
ρ_{nn}	element of atomic density matrix for state n (population in n state)
ρ_{nm}	coherence term between the states n and m
γ	decoherence rate
Δ_{pc}	detuning of probe light from the cavity resonance
Δ_{pa}	detuning of probe light from the atomic transition
α	cavity light field strength
η	rate at which classical light is injected into the cavity
χ	atomic susceptibility
2Ω	Rabi frequency of classical light interacting with the atomic transition
N	total number of atoms
P_j	suffix to denote any parameter P for j^{th} atom
N_c	effective number of atoms coupled to the cavity
g_t	total atom-cavity coupling strength
ν	vibrational level of the molecules
$\bar{n}$	average photon number